DEUTSCHES ELEKTRONEN — SYNCHROTRON

DESY 92-041
March 1992

HELENA
A Beauty Factory in Hamburg

ISSN 0418-9833

NOTKESTRASSE 85 · D - 2000 HAMBURG 52

To be sure that your preprints are promptly included in the
HIGH ENERGY PHYSICS INDEX,
send them to (if possible by air mail):

DESY
Bibliothek
Notkestraße 85
W-2000 Hamburg 52
Germany

DESY-IfH
Bibliothek
Platanenallee 6
O-1615 Zeuthen
Germany

DESY 92-041
March 1992

HELENA
A Beauty Factory in Hamburg

ISSN 0418-9833

Abstract

A high-luminosity asymmetric energy e^+e^- collider, operated at the $\Upsilon(4S)$ energy, provides the best opportunity to study CP violation as a means of testing the consistency of the Standard Model. If the phenomenon of CP violation is explained by the Standard Model through the non-zero angles and phase of the Cabibbo-Kobayashi-Maskawa matrix, then there are precise relations between the CKM parameters and the various measurable CP violating asymmetries in B meson decay. Should these consistency relations fail, the origin of CP violation must lie outside of the Standard Model framework. The measurement would then lead to the first observation of physics beyond the Standard Model.

The B Factory will also carry out a varied, high quality program of studies of other aspects of the physics of b quarks, as well as high precision measurements in τ and charm physics.

The peak luminosity of $3{\cdot}10^{33}$ $\mathrm{cm}^{-2}\mathrm{s}^{-1}$ necessary for such a physics program can be achieved with a double ring e^+e^- collider that fits into the PETRA tunnel at DESY, and that can be constructed using presently existing techniques.

We describe the design of a universal magnetic detector that is optimized for the observation of CP violation, but also allows for a wide additional physics program.

The combination of collider and detector can be built within 4 years for an estimated cost of 175 MDM and 104 MDM, respectively.

This document presents the result of studies carried out with enthusiastic participation of physicists from a variety of institutions:

DESY-F, Hamburg, Germany

H. Albrecht, G. Bohm*, H. Ehrlichmann, E. Michel, H. Nowak*, S. Nowak*, M. Reidenbach, W. Reinsch, H. Schröder, H.D. Schulz, M. Walter*, R. Wurth

DESY-M, Hamburg, Germany

K. Balewski, B. Dwersteg, A. Febel, A. Gamp, G. Hemmie, S. Herb, R.-D. Kohaupt, J. Rümmler, H. Hartwig, G. Jacobs, J.-P. Jensen, H. Kaiser, J. Kouptsidis, D. Krämer, M. Marx, G. Meyer, H. Musfeld, H. Narciss, B. Oentrich, S. Pätzold, A. Piwinski, D. Proch, J. Sekutowicz, K. Sinram, H. Wümpelmann, F. Willeke

Institut für Physik, Universität Dortmund, Germany

H. Kolanoski, R. Mankel, B. Spaan, D. Wegener

II. Institut für Experimentalphysik, Universität Hamburg, Germany

W. Schmidt-Parzefall

Institut für Hochenergiephysik, Universität Heidelberg, Germany

P. Hanke, J. Stiewe

Max-Planck-Institut für Kernphysik, Heidelberg, Germany

S. Ball, C. Geyer, W. Hofmann, B. Holzer, E. Jaeschke, S. Khan, K.T. Knöpfle, M. Spahn, J. Spengler

CERN, Geneva, Switzerland

P. Grosse-Wiesmann

Institut für Experimentelle Kernphysik, Universität Karlsruhe, Germany

K. Strahl

*DESY, IfH Zeuthen

Institut J. Stefan and Oddelek za fiziko, Univerza v Ljubljani, Ljubljana, Slovenia

V. Cindro, G. Kernel, S. Korpar, P. Križan, E. Križnič, A. Stanovnik, M. Starič

Institute of Theoretical and Experimental Physics, Moscow, Russia

M. Danilov, A. Droutskoy, B. Fominykh, A. Nepeipivo, A. Rostovtsev, I. Tichomirov, Yu. Zaitsev

Max-Planck-Institut für Physik, Werner-Heisenberg-Institut, München, Germany

R. Kotthaus, E. Lorenz

LAL-Orsay, France

G. Wormser

Carleton University, Ottawa, Ontario, Canada

H. Kapitza

Univ. Paris VI & VII, Paris, France

J. Chauveau

Centre d'Etudes Nucléaires, Saclay, France

R. Aleksan

PSI, Villigen, Switzerland

R. Horisberger

Contents

References to literature, chapters, sections and tables in the text are specific to the Part where they occur unless explicitly stated otherwise.

INTRODUCTION

Physics motivation

Over the last decade dedicated research programs in B physics – the physics of the heavy fifth quark – were carried out at two facilities, the CESR e^+e^- storage ring at Cornell and the DORIS ring at DESY. Results from these two machines had a major impact in shaping our present understanding of fundamental forces, as summarized in the Standard Model. The depth and richness of the physics revealed in the CESR and DORIS energy range was far beyond the expectations of the protagonists of this field and competes favorably with most other recent enterprises in particle physics. However, it has also become clear that some of the very fundamental questions in this new realm of B physics are beyond the reach of those present machines. The most exciting prospect – the observation of the violation of CP symmetry in the B system – requires improvements in the achievable interaction rates by orders of magnitude. Such machines are now technically feasible, and detailed studies of next–generation facilities for B physics are being performed in nearly all major accelerator centers around the world. In this document, we present a design study for a B factory at DESY which optimally exploits the existing infrastructure – in particular the PETRA tunnel – and which would guarantee the continuation of the successful research program initiated by the ARGUS group.

High luminosity versus high energy frontier

A B factory – like other "factory" machines – explores the high luminosity frontier of elementary particle physics, and tries to probe new physics in precision measurements at modest energies and to examine rare processes. The history of physics with kaons provides the most viable demonstration of this concept – minute effects at low energies are shown to probe interactions and fields at multi–TeV mass scales, which cannot be reached in direct production experiments. Of course, the mainstream of particle physics is still directed towards the other frontier – the high energy frontier. There are, however, indications that the rewards gained at this frontier may turn out to be quite limited. The Standard Model – which will remain one of the lasting achievements of our century – describes the most fundamental layer of nature so far discovered with remarkable precision. The number of fundamental quark and lepton families is most likely limited to 3, as shown by LEP and SLC. With the exception of the t quark and the Higgs particle, no more fundamental particles are expected. At the same time, the Standard Model has too many arbitrary parameters to be truly fundamental. However, given that no indication for physics beyond the Standard Model has ever been noticed, new accelerators providing the next step towards higher energies are no longer guaranteed to find new physics.

On the other hand, the b quark is probably the most heavy charge $-1/3$ quark ever. It is the heaviest object to form true bound states with other quarks, which allows to study the strong interaction potential between quarks and the still unresolved low–energy phenomenon of quark confinement; in hadrons with t quarks any level structure is completely smeared out because of the short life-

time of these heavy quarks. Future studies of quarks and leptons and of their interactions will therefore not require higher energies, but need higher reaction rates which can be achieved at "factory" accelerators. Factories are facilities producing large rates of certain particles; compared to energy–frontier machines, they represent modest scale efforts. Among the various factories under discussion, a wide consensus exists that a B factory provides an outstandingly large physics potential.

In this situation, it seems appropriate that the high–energy physics community would invest most but definitely not all of their resources in the struggle for ever higher energies. The remaining resources should be invested in factories, challenging the luminosity frontier. The hope being that a closer and more precise look at the physics within the energy scale of the Standard Model will lead to hints sufficient to develop a more fundamental theory.

Observation of CP violation

The highlight and key measurement at a B factory is the observation of CP violation. C stands for charge conjugation, but actually means the symmetry of nature between particles and antiparticles. P means the symmetry of nature, when viewed as a mirror image. All known basic laws of physics remain invariant, when particles are exchanged by their antiparticles and looked at through a mirror. Thus nature is expected to be CP invariant. But it is not. The universe consists of matter and not of antimatter. Elementary particles were discovered which do not respect the CP symmetry. In 1964 Cronin, Fitch and collaborators in their Nobel price winning work observed that K^0 mesons in a few permille of the cases decay in a CP violating way. Until now the origin of this phenomenon is not understood. In 1972 Kobayashi and Maskawa proposed that the Standard Model of those days could be generalized to describe 3 generations of quarks – which by then were not yet discovered – by enlarging the Cabibbo matrix to a 3 x 3 matrix. This matrix is known as the CKM matrix. They also noted that if the CKM matrix was not entirely real, but contained some imaginary part, this would automatically lead to CP violation. For a complete determination of all relevant parameters of the Standard Model, the direct observation of CP violation in B decays is indispensable; the kaon data alone do not provide sufficient constraints.

Mass generation and the CKM matrix

Closely related to the question of CP violation and the structure of the CKM matrix is another, even deeper question, namely the understanding of the mechanisms by which the masses of quarks and leptons are generated. The Standard Model makes the assumption that the mass of a particle is given by the product of a dimensionless coupling constant with the Higgs field strength. The Higgs field and its field quantum, the Higgs particle, are the main research goals of the next generation of high energy colliders, the LHC and SSC. Closely related to this issue is the question of the origin of the quark coupling constants, and of the relation between the mass eigenstates and the flavor eigenstates of quarks. Here the CKM matrix plays an essential role, since it connects the individual

couplings. Thus the next super colliders and a B factory address aspects of the same fundamental physics.

For a complete determination of the CKM matrix a large number of different measurements has to be performed, which can only be accomplished with a B factory. While the physics of the CKM matrix is already enough justification for a B factory, its physics potential is much richer, as will be discussed in detail in part I of this study. Especially the charm and τ–physics is competitive with the stated goals of charm– and τ–factories.

Asymmetric e^+e^-–collider

The concept of an asymmetric e^+e^- collider, operated at the CMS-energy of the $\Upsilon(4S)$ resonance, emerged at DESY and independently also at other places. Such a machine would enable the measurement of interference effects in weak decays, providing a direct measure of the CP violating part of the CKM matrix. In an asymmetric storage ring, electrons and positrons collide with different energies to give the B mesons, produced almost at rest in the CMS, a well defined Lorentz boost in the lab-system. The B meson decay lengths are then measurable and reveal a time dependent interference pattern.

Collider design

The design of a B factory collider is based on progress in the technology of storage rings. Detailed simulation calculations for the CP violation experiment have lead to the definition of the specifications required for the machine, which are given in part II of the study.

A luminosity of at least 10^{33} cm^{-2}s^{-1} must be reached. In order to achieve this safely, the proposed machine is designed for a luminosity of

$$\mathcal{L} = 3 \cdot 10^{33} \text{ cm}^{-2}\text{s}^{-1}.$$

For the CP violation measurement an asymmetry with beam energies of $E_1 = 9.33$ GeV and $E_2 = 3.0$ GeV is adequate. Although a B factory will operate mostly on or near the $\Upsilon(4S)$, some related questions, such as the study of B_s mesons, may require slightly higher energy and larger asymmetries up to $E_1 = 14$ GeV and $E_2 = 2$ GeV; in this case the requirement for the luminosity is relaxed to about $3 \cdot 10^{32}$ cm^{-2}s^{-1}.

Several ideas have been considered how these specifications could be met: Normal conducting and superconducting linear colliders and various storage ring configurations were studied in detail. We conclude that a large ring on large ring collider is the only scheme which guarantees to meet the required specifications at a reasonable cost. The same conclusion was reached by all groups which have studied B factory concepts at other laboratories. The various designs have by now converged, and a consensus exists about the best technical solutions.

The machine resulting from this study, HELENA, is designed to reach a luminosity 100 times larger than DORIS II. This increase is essentially accomplished by an increase in the bunch collision frequency. The luminosity per bunch collision stays the same. DORIS has a collision frequency of 1 MHz, whereas HELENA has 83 MHz.

All new features of this machine design are consequences of the task to create an environment where such a high collision frequency is possible. In particular, it turned out that an asymmetric machine is advantageous to reach this goal. Unequal beam energies allow for an efficient magnetic beam separation, avoiding parasitic bunch crossings due to the small bunch distances. With the separation scheme described in this document, combined with a carefully optimized set of radiation masks, backgrounds and doses in the detector remain at tolerable levels.

HELENA in the PETRA tunnel

The PETRA ring has a circumference ideally suited for an asymmetric B factory. The B factory requires the construction of two new rings in the PETRA tunnel, a high energy ring, HER, and a low energy ring LER. In addition the PETRA machine, the injector for HERA and HELENA, must stay in the PETRA tunnel.

The study presented here shows that a B factory using the PETRA tunnel is feasible and meets the required specifications.

Detector design

The design of a universal detector for a B factory, while less challenging than the machine design, represents nevertheless a non-trivial task. To cover the broad physics program, the detector must be equally suited for high-multiplicity $B\overline{B}$ events, for annihilation events, for $\tau\bar{\tau}$ events with few high-momentum particles, and for two-photon events with their low-momentum tracks. Optimum use of the particularly precious $B\overline{B}$ events implies full 4 π coverage, identification of pions, kaons, protons as well as leptons over nearly the full momentum range, and precision tracking close to the beam pipe to resolve B decay vertices.

The detector presented in section III of this document fulfils all these requirements. Essential parts of the concept are the asymmetric layout, which guarantees uniform coverage and resolution in the centre-of-mass frame of the reaction, and the use of Helmholtz coils to generate the main analysing field, resulting in improved access to the calorimeter as well as in cost savings. The low-density main drift chamber has a small inner radius and a design optimized for the mostly low-momentum B decay products; its unconventional shape optimizes the acceptance and momentum resolution and minimizes the obstruction of outer dectector components due to supports and end plates. Further main elements are the silicon vertex detector, the ring imaging Čerenkov counter for particle identification, the scintillators for triggering, the homogeneous CsI calorimeter, and the multi-layer muon detection system. The performance of the detector is illustrated with detailed simulations of the most important benchmark reactions.

50 fb^{-1} is the target

After some years of operation, HELENA will have accumulated a data sample corresponding to an integrated luminosity of 50 fb^{-1}. The following description of the physics potential of HELENA is based on a collected data sample of this size.

If approved, HELENA would contribute significantly to the scientific output of high energy physics of DESY and Europe.

Part I

Physics Motivation

The scientific program of HELENA covers an exceptionally rich research field which is accessible due to the favourable energy range and high luminosity of such a machine.

1. B Mesons and the CKM Matrix

The important role of B mesons for the measurement of CKM matrix elements.

The elements of the CKM matrix are fundamental parameters of the Standard Model. They can not be predicted by present theory but might be the key to a more advanced theory. Most of the elements of the CKM matrix can only be measured by high precision experiments with B mesons. Even the CKM matrix elements involving the very heavy top quark are only accessible through B mesons. Most important, the self-consistency of the CKM approach and its description of CP violation can be put to a stringent test by the observation of CP violation in the B system.

The CKM matrix is closely related to the mass generating mechanism.

While the CKM matrix has previously been considered as a basic property of the Weak Interaction, in a more modern view, the CKM matrix is introduced as a consequence of the mechanism of mass generation of the elementary particles. Much of the present effort in particle physics is focused on this problem, and the study of b quarks is likely to provide important clues.

2. Beauty Spectroscopy

Many of the bound states of the heavy b quark are yet undiscovered. Of prime importance is the yet missing discovery of the ground state of the $b\bar{b}$ system. Furthermore the region of higher excited $b\bar{b}$ states has still to be explored.

The $b\bar{b}$ system provides information on $q\bar{q}$ interactions

For this research program HELENA provides ideal conditions. Since the top quark will be too heavy to live long enough to form bound states, the beauty quark is the quark which gives the most valuable spectroscopic information for our understanding of the strong interaction.

3. Charm Physics

A precise knowledge of charm decays is essential.

Many questions of charm physics are still unresolved. Charm decays offer the possibility to study the simultaneous action of both weak and strong interactions. Last not least, a good understanding of charm physics is essential for high precision experiments with beauty.

4. The Heavy Lepton Tau

Heavy leptons are a good searching ground for new physics.

The heavy lepton τ and its neutrino ν_τ are still much less known than the other leptons, the muon and the electron. Many theoretical models predict effects of new physics proportional to the mass squared of the lepton involved. Thus, from the heavy lepton the largest effects could be expected. HELENA will produce by far more τ leptons than any other machine and will therefore offer an excellent environment for this research program.

5. Two Photon Physics

$\gamma\gamma$ physics may give access to glue balls and $4q$ states.

Through interaction of the photon clouds of the colliding electrons and positrons, various hadronic states are produced. This allows to search for new types of hadrons such as glue balls and 4 - quark states which are theoretically expected but have so far not been unambiguously identified.

The above list is by far not exhaustive but it shows the wealth of unique research goals which can be successfully addressed by a B factory.

The basic measurements can be accomplished in the first five years of operation of the HELENA storage ring. The broad scope of physics with HELENA will guarantee the continuation of an outstanding research program for many more years.

1 The CKM Matrix

1.1 The Role of the CKM Matrix in Weak Interactions

The central scientific subject of a B factory is a precise determination of the CKM matrix which determines the weak couplings of quarks in the Standard Model.

Any two quarks q of different electric charge can transform into each other by emitting or absorbing a Weak Boson W, see figure 1.

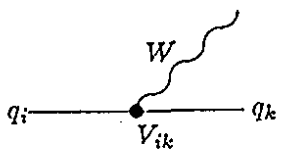

Figure 1: Transformation of quarks by W emission.

Any quark decay amplitude is proportional to a specific CKM matrix element.

All such interactions proceed according to the same formalism with a coupling constant V_{ik} specific to each possible transition between quarks. The constants V_{ik} can be collected in a matrix, namely the CKM matrix:

$$V = \begin{pmatrix} V_{ud} & V_{us} & V_{ub} \\ V_{cd} & V_{cs} & V_{cb} \\ V_{td} & V_{ts} & V_{tb} \end{pmatrix} \quad (1)$$

where the quarks d, s, and b have charge -1/3 and the quarks u, c, and t have charge 2/3.

The CKM matrix can give the explanation of CP violation in the frame of the Standard Model.

The elements of this matrix are complex numbers. Non–vanishing imaginary parts lead automatically to CP violation as observed in K^0 meson decays. The mechanism of CP violation is a key ingredient not only in our understanding of particle physics but possibly also in cosmology and in the creation of matter in the universe.

In the Standard Model the CKM matrix is introduced through the quark mass term in the Lagrangian **L**:

$$\begin{aligned}
\mathbf{L} &= \left\{ (u,c,t) \begin{pmatrix} C_u & 0 & 0 \\ 0 & C_c & 0 \\ 0 & 0 & C_t \end{pmatrix} \begin{pmatrix} u \\ c \\ t \end{pmatrix} \right. \\
&\quad \left. + (d',s',b')\, V \begin{pmatrix} C_d & 0 & 0 \\ 0 & C_s & 0 \\ 0 & 0 & C_b \end{pmatrix} V^\dagger \begin{pmatrix} d' \\ s' \\ b' \end{pmatrix} \right\} \rho^0 \qquad (2) \\
&= (u,c,t) \begin{pmatrix} m_u & 0 & 0 \\ 0 & m_c & 0 \\ 0 & 0 & m_t \end{pmatrix} \begin{pmatrix} u \\ c \\ t \end{pmatrix} \\
&\quad + (d',s',b')\, V \begin{pmatrix} m_d & 0 & 0 \\ 0 & m_s & 0 \\ 0 & 0 & m_b \end{pmatrix} V^\dagger \begin{pmatrix} d' \\ s' \\ b' \end{pmatrix} \qquad (3)
\end{aligned}$$

where primes denote the transformed quark fields:

$$\begin{pmatrix} d \\ s \\ b \end{pmatrix} = V^\dagger \begin{pmatrix} d' \\ s' \\ b' \end{pmatrix} . \qquad (4)$$

Here V is the CKM matrix, (u,c,t) and (d,s,b) are the quark fields, $\rho^0 = 246$ GeV is the field strength of the Higgs field, C_q are the coupling constants by which the quark fields are coupled to the Higgs field, and m_q are the quark masses which are thus generated.

Particle masses are generated by the Higgs field.

In order to give masses to the quarks, the mass matrix must be diagonal. Obviously, the mass generating mechanism does not lead simultaneously to diagonal mass matrices for both kinds of quarks. The two mass matrices are rotated against each other by the CKM matrix. Thus the CKM matrix, though it manifests itself in the Weak Interaction, is actually originating from the mass generation mechanism.

The CKM matrix transforms between mass and weak interaction eigenstates.

A complete determination of the CKM matrix is important for a deeper understanding of this unresolved question at the frontier of our knowledge.

1.2 The Unitarity Triangle

The CKM matrix in the above Lagrangian must be exactly unitary. Any deviation from unitarity would be evidence of the failure of the Standard Model and prove the existence of new physics.

The CKM matrix is parametrized by 4 independent parameters.

With 3 families of quarks, a unitary 3×3 matrix is parametrized by three rotation angles $\theta_1, \theta_2, \theta_3$, and one complex phase δ. Using the abbreviations $c_i = \cos\theta_i$ and $s_i = \sin\theta_i$, Kobayashi and Maskawa originally chose the following parametrization:

$$V = \begin{pmatrix} c_1 & -s_1c_3 & -s_1c_3 \\ s_1c_2 & c_1c_2c_3 - s_2s_3e^{i\delta} & c_1c_2s_3 + s_2c_3e^{i\delta} \\ s_1s_2 & c_1s_2c_3 + c_2s_3e^{i\delta} & c_1s_2s_3 - c_2c_3e^{i\delta} \end{pmatrix} . \quad (5)$$

Unitarity of the CKM matrix

The unitarity condition reads as follows:

$$\sum_{k=d,s,b} V_{ik}^* V_{jk} = \delta_{ij}\,; \quad i,j = u,c,t \quad (6)$$

From these 9 equations one chooses the following one:

$$V_{ud}V_{ub}^* + V_{cd}V_{cb}^* + V_{td}V_{tb}^* = 0. \quad (7)$$

The unitarity triangle

Eq. 7 can be visualized as a triangle in the complex plane, the so called unitarity triangle [1].

Wolfenstein's parametrization of the CKM matrix

A frequently used approximation of the CKM matrix has been suggested by Wolfenstein [2]:

$$V = \begin{pmatrix} V_{ud} & V_{us} & V_{ub} \\ V_{cd} & V_{cs} & V_{cb} \\ V_{td} & V_{ts} & V_{tb} \end{pmatrix} \approx \begin{pmatrix} 1 - \frac{\lambda^2}{2} & \lambda & \lambda^3 A(\rho - i\eta) \\ -\lambda & 1 - \frac{\lambda^2}{2} & \lambda^2 A \\ \lambda^3 A(1 - \rho - i\eta) & -\lambda^2 A & 1 \end{pmatrix} \quad (8)$$

where $\lambda = sin\theta_c$ (θ_c Cabibbo angle). In this particular representation the terms of order higher than λ^3 are neglected. λ, A, ρ and η are related to the three angles θ_i and the phase δ previously mentioned.

The representation of the unitarity triangle in the (ρ, η) plane is shown in fig. 2. Two corners of the triangle are fixed at $(0,0)$ and at $(1,0)$. To fully fix the triangle one has to measure the coordinates (ρ, η) of its apex.

The unitarity triangle checks the Standard Model and tests for new physics

The measurement of two sides and the three angles α, β, γ allows to check the consistency of the CKM ansatz. In contrast, observing an inconsistency between the measured values will reveal the presence of a fourth generation or of new physics. We will now discuss the present knowledge about the unitarity triangle.

1.3 Existing Measurements of the CKM Matrix Elements

The first and second generation CKM matrix elements V_{ud}, V_{cs}, V_{us}, and V_{cd} are essentially given by the well known Cabibbo angle. All other CKM matrix

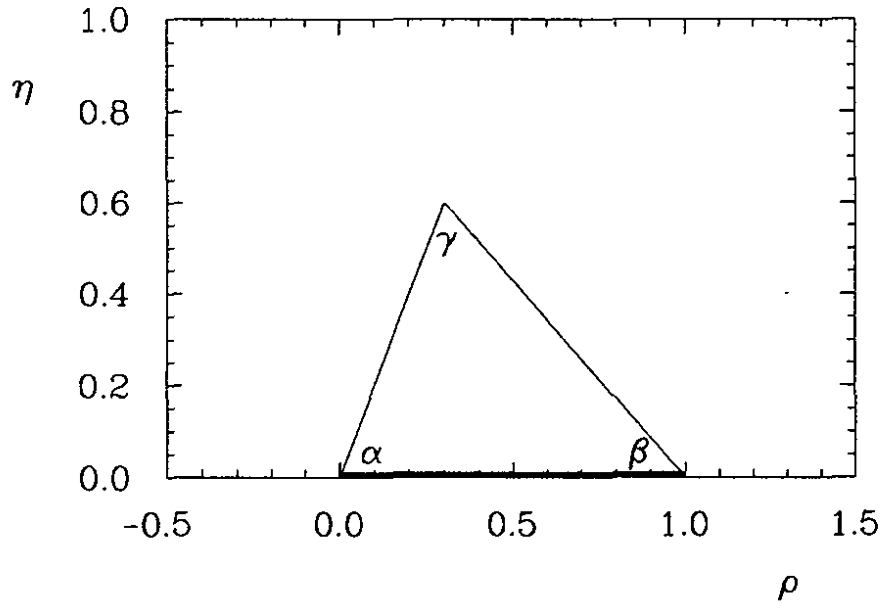

Figure 2: The unitarity triangle in the (ρ, η) plane of the Wolfenstein parametrization. Indicated is the definition of the angles α, β and γ.

elements are accessible in measurements of B meson properties. Two types of transitions can be distinguished with regard to the change in the beauty quantum number B:

1. $|\Delta B| = 1$ transitions are responsible for B meson decays. A representative set of quark diagrams of this type is given in fig. 3. B meson decays allow to determine the CKM matrix elements $|V_{cb}|$ and $|V_{ub}|$.

2. $B\overline{B}$ mixing occurs through $|\Delta B| = 2$ transitions. The corresponding Feynman graphs are the box diagrams shown in fig. 4. From $B^0\overline{B}^0$ mixing one can extract $|V_{td}|$. Similarly, a measurement of $B_s\overline{B}_s$ mixing will yield the value of $|V_{ts}|$.

1.3.1 $|V_{cb}|$ from Semileptonic B decays

The CKM matrix element $|V_{cb}|$ is extracted from inclusive and exclusive measurements of B decays by ARGUS [3,4] and CLEO [5]. The B lifetime τ_b is determined at high energy e^+e^- colliders [6]. The width of the semileptonic decay $\overline{B}^0 \to D^+ l^- \overline{\nu}_l$ is given by

$$\Gamma(\overline{B}^0 \to D^+ l^- \overline{\nu}_l) = \frac{BR(\overline{B}^0 \to D^+ l^- \overline{\nu}_l)}{\tau_{B^0}} = \mid V_{cb} \mid^2 \cdot F \qquad (9)$$

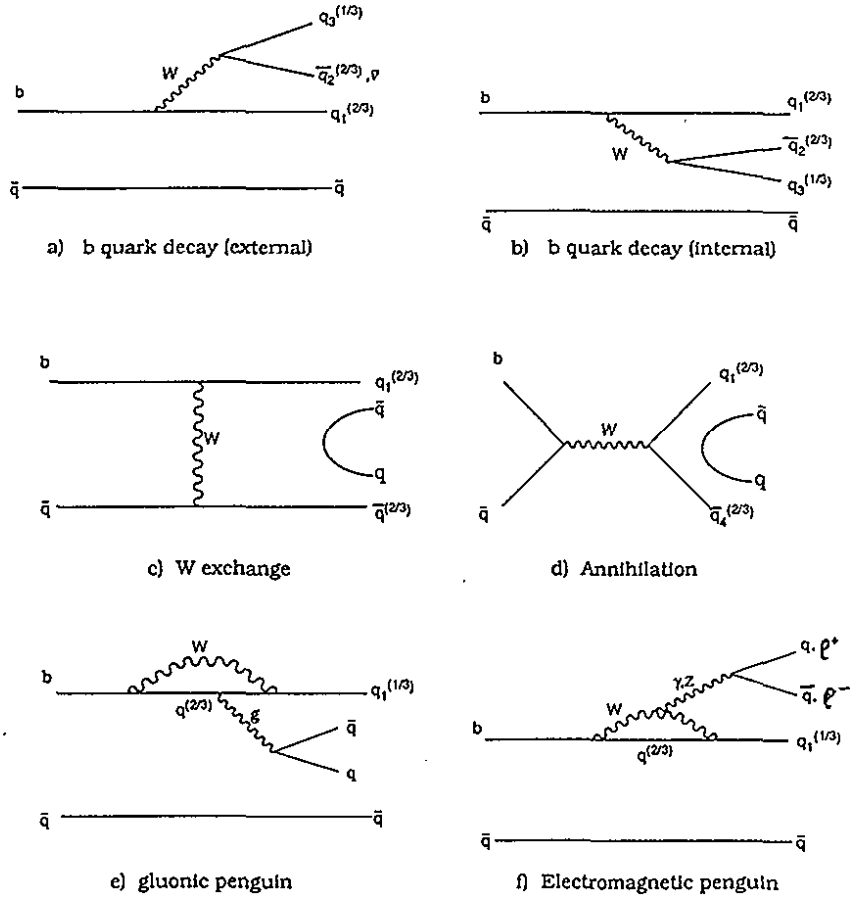

Figure 3: Quark diagrams of B meson decays.

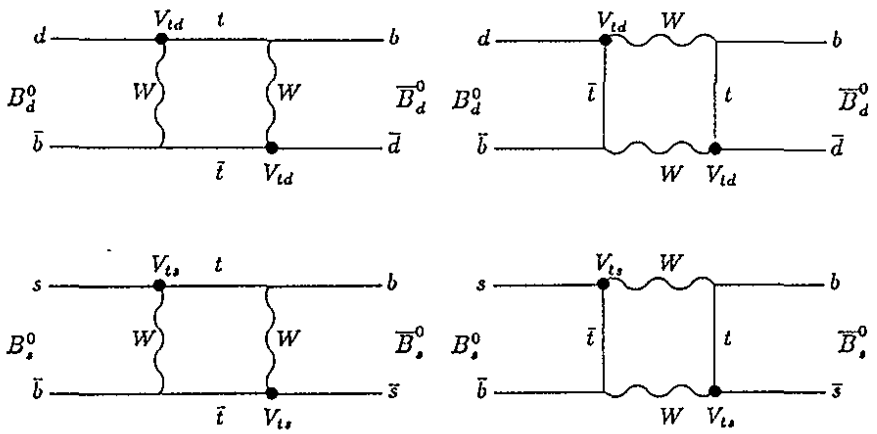

Figure 4: $|\Delta B| = 2$ box diagrams responsible for $B^0\overline{B}^0$ mixing.

A large systematic error on $|V_{cb}|$ is due to charm branching ratios.

where the parameter F is given by a form factor for which the theoretical predictions are quite accurate. Using the measured values together with theoretical calculations one obtains $|V_{cb}| = 0.043 \pm 0.003 \pm 0.004$ where the first error is

due to measurement errors in the B system and the second error is mainly due to imperfect knowledge of charm branching ratios.

1.3.2 $|V_{ub}|$ from Charmless B Decays

Charmless B decays have been studied using B mesons from $\Upsilon(4S)$ decays. Semileptonic B decays with a lepton momentum beyond the kinematical limit for $B \to \overline{D} l^+ \nu_l$ transitions, $p_l > 2.3$ GeV/c, are clear indications for charmless B decays [7,8]. Such leptons have been observed and it has been demonstrated for a few events that these leptons belong indeed to semileptonic $b \to u$ decays such as $\overline{B}^0 \to \pi^+ \mu^- \overline{\nu}_\mu$ and $B^+ \to \omega \mu^+ \nu_\mu$ [9]. Having explicitly shown that $b \to u l^- \overline{\nu}_l$ transitions are responsible for the excess of leptons with momenta above the kinematical limit for $b \to c l^- \overline{\nu}_l$ transitions, the strength of the $b \to u$ coupling can be obtained from the inclusive spectra.

A large systematic error on $|V_{ub}|$ is due to model dependence.

However, the extrapolation from the restricted range $2.3 < p_l < 2.7$ GeV/c to the full range depends on models. This results in a large systematic error for the ratio $|V_{ub}/V_{cb}|$:

$$0.08 < \frac{|V_{ub}|}{|V_{cb}|} = \lambda \sqrt{\rho^2 + \eta^2} < 0.20\,. \qquad (10)$$

1.3.3 $|V_{td}|$ from $B^0\overline{B}^0$ Mixing

$B^0\overline{B}^0$ mixing is mediated by second order weak interactions ($|\Delta B| = 2$) through the box diagrams [10]; see fig. 4. Evaluation of these diagrams in the Standard Model yields the following analytic expression for the measurable parameter $x_d = \Delta m/\Gamma$ [11]:

$$x_d = \frac{G_F^2}{6\pi^2} \cdot \tau_{B^0} \cdot m_{B^0} \cdot B_{B^0} \cdot f_{B^0}^2 \cdot \eta_{QCD} \cdot m_t^2 \cdot F\left(\frac{m_t^2}{m_W^2}\right) \cdot |V_{tb} V_{td}|^2\,, \qquad (11)$$

where

- Δm is the mass difference between the CP eigenstates;
- $\tau_{B^0} = 1/\Gamma$ is the B^0 meson lifetime ($(1.27 \pm 0.06) \cdot 10^{-12}$ sec [12]);
- m_{B^0} is the mass of the B^0 meson (5.2794 ± 0.0015 GeV [6]);
- B_{B^0} is the ratio of the relevant hadronic matrix element to its vacuum expectation value, the so–called bag factor. It is believed to be of order 1;
- f_{B^0} is the B^0 decay constant and is theoretically estimated to be in the range 100 – 300 MeV from QCD sum rules [13] and lattice calculations [14];
- $\eta_{QCD} \approx 0.86$ is a known QCD factor;

- m_t is the mass of the yet undiscovered t quark ($m_t > 89$ GeV [15]);
- m_W is the mass of the W boson (80.6 ± 0.4 GeV [6]);
- $F(m_t^2/m_W^2)$ is a known function which smoothly decreases as m_t gets larger.

$B^0\overline{B}^0$ mixing was experimentally observed by ARGUS [16] through the complete reconstruction of a $\Upsilon(4S) \to B^0\overline{B}^0$ decay where either B meson decays as a B^0. In this event both B^0 mesons decay like $B^0 \to D^{*+}\mu^+\nu_\mu$. The result on x_d, derived from $\Upsilon(4S)$ decays into final states involving $D^{*+}l^-l^-$ and l^-l^- combinations, yielded $x_d = 0.67 \pm 0.11$ [16,17].

A large systematic error on $|V_{td}|$ is due to theoretical uncertainties.

The measurement of x_d provides a handle on the value of $|V_{td}|^2$ if one knows the mass of the t quark and the B^0 decay constant, f_{B^0}. Assuming $m_t = 135$ GeV, $|V_{cb}| = 0.043$, and $f_{B^0} = 150$ MeV, we get:

$$1.0 < \frac{|V_{td}|}{|V_{cd}V_{cb}^*|} \equiv |1 - \rho - i\eta| < 1.35\,. \tag{12}$$

1.3.4 Constraints from $|\epsilon_K|$

If the origin of CP violation is indeed due to the complex phase of the CKM matrix, also $|\epsilon_K|$, the parameter which measures the strength of CP nonconservation due to mass matrix mixing in the $K_L^0 K_S^0$ system, yields constraints on the unitarity triangle. Its value is theoretically predicted to be [18]:

$$|\epsilon_K| = C \cdot B_K \cdot |V_{cb}|^2 |V_{cd}|^2 \eta \times \left\{ y_c \cdot f_1(y_c) + |V_{cb}|^2 \cdot y_t \cdot f_2(y_t)(1-\rho) \right\} \tag{13}$$

The interpretation of $|\epsilon_K|$ is hindered by lack of a theory for the K bag factor.

where C is a constant, B_K is the bag factor of the K^0 and $f_1(y_i)$ and $f_2(y_i)$ are two known functions with $y_i = m_i^2/m_W^2$. Besides the yet unknown value for m_t, large uncertainties exist on B_K. Predictions vary in the range $1/3 < B_K < 1$. The experimentally measured value [6]

$$|\epsilon_K| = (2.27 \pm 0.02) \times 10^{-3} \tag{14}$$

allows nevertheless to further constrain the unitarity triangle.

1.4 Constraints on the Unitarity Triangle

The present experimental values of the quantities relevant for the evaluation of the unitarity triangle can be combined to restrict the coordinates (ρ, η) of its apex: The value of $|V_{ub}|$ yields a circular band around $(\rho, \eta) = (0, 0)$ in which the apex has to lie. The measurement of $|V_{td}|$ defines a circular band around $(1, 0)$. The parameter $|\epsilon_K|$ allows a region bounded by hyperbolae.

Global fits have been performed [19,20,21] in order to obtain the allowed range of the apex. In [19], the input parameters are assumed to be Gaussian distributed around their central values. The following numerical input has been used: $|\epsilon_K| = (2.263 \pm 0.023) \times 10^{-3}$, $x_d = 0.67 \pm 0.15$, $\frac{|V_{ub}|}{|V_{cb}|} = 0.100 \pm 0.008$, $m_t = (137 \pm 39)$ GeV/c^2, and $B_K = 0.8 \pm 0.1$. f_B is varied between 100 MeV and 300 MeV. The measurement of $|\epsilon'/\epsilon| = (2.1 \pm 0.9) \times 10^{-3}$ [22,23] does not add more information. The fit results and the allowed area for the apex are shown in fig. 5. For all values of $f_B\sqrt{B_B}$ taken into account, $|\sin 2\beta|$ is larger than 0.15.

$|\sin 2\beta| > 0.15$

In the following chapters we shall demonstrate that a B factory is the ideal instrument to measure the angles of the unitarity triangle. With an integrated luminosity of $\mathcal{L} = 50 fb^{-1}$ it is possible to fully explore the expected range of the angles α and β. Moreover, $50 fb^{-1}$ allow a precise measurement of the sides of the unitarity triangle so that the triangle can be overdetermined.

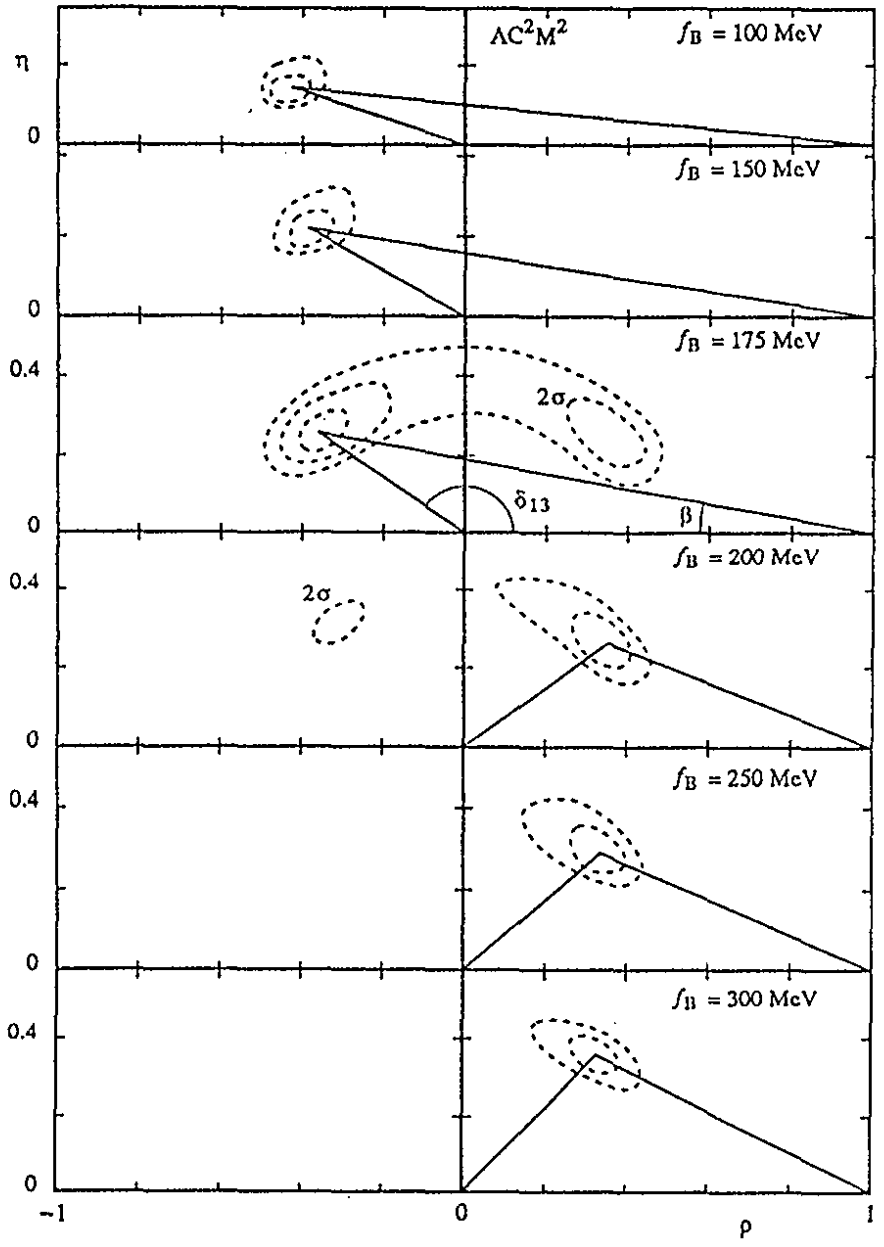

Figure 5: The unitarity triangle in the (ρ, η) plane. The dashed lines show one, two, and three standard deviation contours around the best apex position according to [19], drawn for different values of the B decay constant f_B.

2 CP Violation in B Decays

The measurement of CP violation in the B meson system is the main experimental goal at a B factory and constitutes one of the primary reasons for its construction. A variety of phenomena exists by which CP violation could be detected. We will discuss two different kinds of decays: B meson final states f which are flavor specific and those where f is not flavor specific. The flavor non-specific final states comprise decays where f is a CP eigenstate. These decays show at the same time rather large CP violating effects as well as sizable branching fractions. Because they are the best candidates, they will be discussed in detail in the next chapter.

2.1 General Formalism

Particle-antiparticle mixing

The mixing between the B^0 meson and its antiparticle is a phenomenon that is now experimentally well established [16,17]. This effect is the consequence of a situation where the mass eigenstates are different from the flavor eigenstates which take part in the strong and electroweak interactions. Thus, the mass eigenstates B_1, B_2 can be expressed as linear superpositions of the flavor eigenstates B^0 and $\overline{B}^0$. In the most general case, one can write:

$$\begin{aligned} |B_1\rangle &= \frac{|1+\epsilon|e^{-i\Phi_M}|B^0\rangle + |1-\epsilon|e^{i\Phi_M}|\overline{B}^0\rangle}{\sqrt{2(1+|\epsilon|^2)}} , \\ |B_2\rangle &= \frac{|1+\epsilon|e^{-i\Phi_M}|B^0\rangle - |1-\epsilon|e^{i\Phi_M}|\overline{B}^0\rangle}{\sqrt{2(1+|\epsilon|^2)}} . \end{aligned} \tag{15}$$

The quantity ϵ represents the deviation from the ideal mixing. Φ_M is the relative phase between B^0 and $\overline{B}^0$. This phase can be identified as the phase of V_{td} [11].

If CP is conserved, the mass eigenstates are identical to the CP eigenstates and $\epsilon = \Phi_M = 0$.

The time evolutions of $|B_1\rangle$ and $|B_2\rangle$ are given by

$$\begin{aligned} |B_1(t)\rangle &= e^{-(\frac{\Gamma}{2}+im)t}\, e^{i\frac{\Delta m}{2}t}\, e^{\frac{\Delta\Gamma}{4}t}|B_1\rangle , \\ |B_2(t)\rangle &= e^{-(\frac{\Gamma}{2}+im)t}\, e^{-i\frac{\Delta m}{2}t}\, e^{-\frac{\Delta\Gamma}{4}t}|B_2\rangle \end{aligned} \tag{16}$$

where we have defined

$$m \equiv \frac{m_1+m_2}{2} , \ \Gamma \equiv \frac{\Gamma_1+\Gamma_2}{2} , \ \Delta m \equiv m_2 - m_1 , \ \Delta\Gamma \equiv \Gamma_2 - \Gamma_1 . \tag{17}$$

Here m_i and Γ_i are the respective masses and widths of the neutral B mass eigenstates, B_i. Contrary to the K^0 system, it is expected that $\Delta\Gamma \ll \Gamma$ and $\Delta\Gamma \ll \Delta m$ in the B system [24].

The time-dependent amplitudes for the decay of a neutral B meson created at the time $t_0 = 0$ as a pure $\overline{B}^0$ or as a pure B^0 are, respectively:

$$\begin{aligned} \mathcal{A}\left(\overline{B}^0 \to f\right) &= e^{-\frac{\Gamma t}{2}} e^{-imt} \\ &\quad \left[\cos\frac{\Delta m t}{2}\left\langle f|T|\overline{B}^0\right\rangle + i\,\sin\frac{\Delta m t}{2} e^{-2i\Phi_M}\frac{|1+\epsilon|}{|1-\epsilon|}\left\langle f|T|B^0\right\rangle\right] \\ \text{and} & \qquad (18) \\ \mathcal{A}\left(B^0 \to f\right) &= e^{-\frac{\Gamma t}{2}} e^{-imt} \\ &\quad \left[\cos\frac{\Delta m t}{2}\left\langle f|T|B^0\right\rangle + i\,\sin\frac{\Delta m t}{2} e^{2i\Phi_M}\frac{|1-\epsilon|}{|1+\epsilon|}\left\langle f|T|\overline{B}^0\right\rangle\right] . \end{aligned}$$

Here $\langle f|T|B^0\rangle$ and $\langle f|T|\overline{B}^0\rangle$ represent the overall transition amplitudes of a B^0 and a $\overline{B}^0$ into the final state f.

These amplitudes can be written as:

$$\left\langle f|T|\overline{B}^0\right\rangle = \sum_{j=1}^{n} e^{i\Phi_j}\, e^{i\alpha_j}\, M_j\,, \qquad (19.a)$$

$$\left\langle f|T|B^0\right\rangle = \sum_{j=1}^{n} e^{-i\Phi'_j}\, e^{i\alpha'_j}\, M'_j\,. \qquad (19.b)$$

The phases Φ_j and Φ'_j are those of the CKM matrix elements involved in the decay amplitude while α_j and α'_j are the phases due to the strong Final State Interactions (FSI). Finally, M_j and M'_j are the magnitudes of the decay amplitudes. In eqs. 19.a, 19.b, the terms with different j denote amplitudes with different CKM phases. Thus, distinct Feynman diagrams involving the same CKM phase can be summed into a single amplitude.

One dominating amplitude simplifies the situation.

If only one amplitude dominates in the decay, equations 19.a and 19.b become much simpler. With the conventions $M \equiv M_1$, $M' \equiv M'_1$, $\beta \equiv \Phi_1 + \alpha_1$, and $\beta' \equiv \Phi'_1 - \alpha'_1$ they then read:

$$\left\langle f|T|\overline{B}^0\right\rangle = e^{i\beta}\, M\,, \qquad (20.a)$$

$$\left\langle f|T|B^0\right\rangle = e^{-i\beta'}\, M'\,. \qquad (20.b)$$

Using equations 18 it is straightforward to derive the time–dependent decay probabilities of neutral B mesons created at time $t_0 = 0$ as a pure B^0 (or $\overline{B}^0$).

$$\begin{aligned}
\Gamma\left(\overset{(-)}{B^0} \to f\right) \quad \propto \quad & e^{-\Gamma t}\left(\cos^2\frac{\Delta m t}{2}|\langle f \mid T \mid \overset{(-)}{B^0}\rangle|^2\right. \\
& + \sin^2\frac{\Delta m t}{2}\frac{|1 \overset{(+)}{-} \epsilon|^2}{|1 \overset{(-)}{+} \epsilon|^2}|\langle f|T|\overset{(\ )}{\overline{B}^0}\rangle|^2 \\
\overset{(+)}{-} \quad & \frac{i}{2}\sin\Delta m t\frac{|1 \overset{(+)}{-} \epsilon|}{|1 \overset{(-)}{+} \epsilon|}e^{-2i\Phi_M}\langle f \mid T \mid B^0\rangle\langle f \mid T \mid \overline{B}^0\rangle^* \\
\overset{(-)}{+} \quad & \left.\frac{i}{2}\sin\Delta m t\frac{|1 \overset{(-)}{+} \epsilon|}{|1 \overset{(+)}{-} \epsilon|}e^{2i\Phi_M}\langle f \mid T \mid B^0\rangle^*\ \langle f \mid T \mid \overline{B}^0\rangle\right).
\end{aligned} \tag{21}$$

The same formulae hold if the CP conjugate $\overline{f}$ of the final state f is considered. The time independent decay amplitudes $\langle\overline{f}|T|B^0\rangle$ and $\langle\overline{f}|T|\overline{B}^0\rangle$ are obtained from eqs. 19.a, 19.b by applying a CP transformation under which only the signs in front of Φ_j and Φ'_j change, since CP is conserved in strong interactions.

2.2 The Final State f is Flavor Specific

Flavor specific final states f tag the b flavour of the B meson. This means that

$$|\langle\overline{f} \mid T \mid B\rangle| = |\langle f \mid T \mid \overline{B}\rangle| = 0\ . \tag{22}$$

A CP violating asymmetry can be observed by measuring asymmetries either in decay rates or in mixing rates.

1. *Asymmetry in the decay rates* [25]

Self tagging mode.

An asymmetry in the decay rates can be measured in decays of charged and neutral B mesons (self tagging mode). CP violation occurs if $\Gamma\left(\overline{B} \to \overline{f}\right) \neq \Gamma\left(B \to f\right)$ which results in a non–zero asymmetry $\mathcal{A}$:

$$\mathcal{A} \equiv \frac{\Gamma\left(\overline{B} \to \overline{f}\right) - \Gamma\left(B \to f\right)}{\Gamma\left(\overline{B} \to \overline{f}\right) + \Gamma\left(B \to f\right)} \propto |\langle\overline{f} \mid T \mid \overline{B}\rangle|^2 - |\langle f \mid T \mid B\rangle|^2\ . \tag{23}$$

Direct CP violation.

An asymmetry of these decay amplitudes is called direct CP violation. In the Standard Model, this phenomenon is only possible if several amplitudes with different CKM phases and different strong phases contribute to the decay. This is not the case if f is a semileptonic final state but it may occur in some particular neutral or charged B decays such as *e.g.* $B^\pm \to K^\pm\rho^0$. In the simple example where only two amplitudes contribute in eqs. 19.a, 19.b, one has

$$\mathcal{A} = \frac{2\sin(\Phi_1' - \Phi_2')\sin(\alpha_1' - \alpha_2')M_1'M_2'}{M_1'^2 + M_2'^2 + 2\cos(\Phi_1' - \Phi_2')\cos(\alpha_1' - \alpha_2')M_1'M_2'} \,. \tag{24}$$

It can be seen from this equation that, in order to get large asymmetries, M_1' and M_2' should be of comparable size and the difference between the final state interaction phases should be large. We show in table I different examples of final states for which the CP violating asymmetries are proportional to the angles α, β, and γ in the unitarity triangle.

Table I: Examples of final states with which direct CP violation can be tested. Together with their expected branching fraction [26,27], we give the range of estimated asymmetries and the angle of the unitarity triangle measured.

Modes	Branching fraction	Expected asymmetry	Measured angle
$B^{\pm} \to \pi^{\pm}\rho^0$	$\sim 10^{-6}$	(0.1-1.)%	α
$B^{\pm} \to K^{\pm}\rho^0$	$\sim 10^{-5}$	(1-10)%	β
$B^{\pm} \to K^{\pm}K^{*0}$	$\sim 10^{-6}$	(1-10)%	γ

Direct CP violation shows small asymmetries.

The maximum asymmetry is obtained if $M_1' = M_2'$ and $\alpha_1' - \alpha_2' = \pi/2$. Unfortunately, this is in general not the case, and in practice the expected asymmetries are small ($\sim 10^{-2}$) [28]. Furthermore, even if CP violation is observed (which will be already a great achievement), it will be extremely difficult to extract the value of $\sin(\Phi_1' - \Phi_2')$, the parameter that measures CP violation in this scenario, since $\sin(\alpha_1' - \alpha_2')M_1'M_2'$ is essentially unknown.

2. *An asymmetry in the mixing rates*

Since by assumption the final state f is flavor specific, it can only be reached from either B or $\overline{B}$. If mixing were involved, this statement would no longer hold. Since mixing can only occur in the neutral B sector, one has to work with the $B^0\overline{B}^0$ system. The fact that the mixing rate of $B^0 \to \overline{B}^0$ is different from the mixing rate of $\overline{B}^0 \to B^0$ leads to a CP violating effect. In contrast to the previous case, the semileptonic B decays are now useful. Because $\langle f|T|B^0\rangle = \langle \overline{f}|T|\overline{B}^0\rangle$ for $f \equiv l^-\overline{\nu}_l X$ and $\overline{f} \equiv l^+\nu_l X$, the asymmetry is:

$$\mathcal{A} \equiv \frac{\Gamma\left(\overline{B}^0 \to f\right) - \Gamma\left(B^0 \to \overline{f}\right)}{\Gamma\left(\overline{B}^0 \to f\right) + \Gamma\left(B^0 \to \overline{f}\right)} \simeq \frac{4\mathrm{Re}\,\epsilon}{1 + |\epsilon|^2} \,. \tag{25}$$

If $B^0\overline{B}^0$ pairs are produced, this type of asymmetry could be established by comparing, for example, the number of positive (l^+l^+) and the number of negative like-sign lepton pairs (l^-l^-).

Small asymmetries are expected.

Unfortunately, $\mathrm{Re}\,\epsilon$ is expected to be very small ($\sim 10^{-3}$) [11], making the measurement of the asymmetry extremely difficult. Nevertheless, it is important to

measure this quantity since the observation of a large asymmetry would clearly indicate new physics.

2.3 The Final State f is not Flavor Specific

The final state f is common to B^0 and $\overline{B}^0$.

An asymmetry in the time dependence of the decay rates can be observed [11] if the final state f is common to both B^0 and $\overline{B}^0$. Then two paths are possible to reach the final state f (fig. 6).

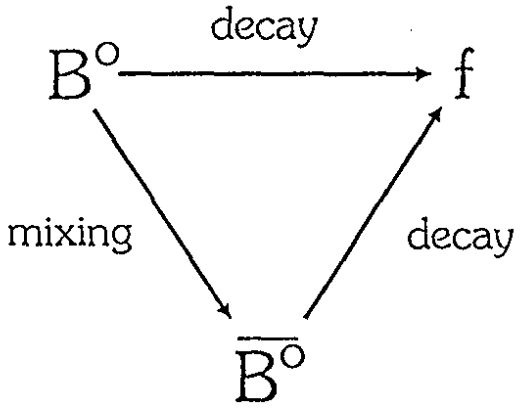

Figure 6: Two decay paths to reach a common final state from a B^0 and from a $\overline{B}^0$.

The flavour of the decaying B^0 meson is tagged by measuring the flavour of the partner $\overline{B}^0$ meson produced simultaneously in the decay of the $\Upsilon(4S) \to B^0\overline{B}^0$. All terms of eq. 21 contribute and, neglecting $|\epsilon|$, the asymmetry reads

$$\mathcal{A} \equiv \frac{\Gamma\left(\overline{B} \to f\right) - \Gamma\left(B \to f\right)}{\Gamma\left(\overline{B} \to f\right) + \Gamma\left(B \to f\right)} = R\cos\Delta mt + D\sin(2\Phi_M + \beta + \beta') \times \sin\Delta mt \tag{26}$$

where $R = (M^2 - M'^2)/(M^2 + M'^2)$ and $D = 2MM'/(M^2 + M'^2)$. In this asymmetry only the term with $\sin\Delta mt$ contains the information on the CKM phase. It is, however, difficult to show that CP is not conserved by simply measuring this asymmetry because the term that contains the CKM phase depends on strong phases as well. To show that CP conservation is indeed violated, one has to either use modes where the strong phases vanish or to measure complementary modes from which the different phases can be sorted out.

Simple situation, if f is a CP eigenstate.

Expression 26 gets particularly simple and interesting if the final state f is a CP eigenstate such as $J/\psi K_S^0$, $\pi^+\pi^-$, or $K_s^0\rho^0$. As a matter of fact, if one amplitude dominates, we have $\Phi_1' = \Phi_1$, $M_1' = M_1$, and $\alpha_1' = \alpha_1$ or $\alpha_1' = \alpha_1 + \pi$ according to the nature of f (CP-even or CP-odd). Equation 26 then simplifies to

$$\mathcal{A} = \eta_{CP} \sin 2\Phi \sin \Delta m t \tag{27}$$

where the CP parity η_{CP} of the final state is ± 1 and $\Phi \equiv \Phi_M + \Phi_1$.

The phase Φ corresponds to one angle in the unitarity triangle.

In the Standard Model, this phase Φ can be written as a well defined combination of the phases of V_{ub} and V_{td} depending on the final state that is studied. In fact, Φ is nothing else than the angle α, β, or γ of the unitarity triangle if f is $\pi^+\pi^-$, $J/\psi K_S^0$, or $K_s^0\rho^0$, respectively. We emphasize the simplicity of equation 27. If a single amplitude dominates the $B \to f$ decays, this expression allows to directly translate the measured value of the asymmetry into a measurement of the phase Φ which is the origin of CP violation, without any uncertainty due to the hadronic sector.

There exist other "near-CP eigenstates", which are also expected to show large asymmetries.

Finally, it should be noted that B decays to CP eigenstates are not the only modes that are interesting to study.

- It has been shown [29] that non-CP eigenstates, such as $\rho^\pm\pi^\mp$ and $D^{*\pm}D^\mp$, can be used efficiently as well. For these modes, in general $M' \neq M$ and $\alpha' \neq \alpha$ but it is still possible to extract the value of $\sin 2\Phi$ using the time dependence of the asymmetry.
- The B decays into two vector particles, such as $J/\psi K^{*0}$, are also useful [30,31]. Here it is important to know the helicity of the particles in the final state. Using these decays without any further information on the overall CP parity might lead to cancellations in the asymmetry. The problem is overcome by analyzing the angular distribution of the decay products of the vector particles.

Most promising for measuring CP violation are the flavour non-specific B decays as far as event rates and the magnitude of the effect is concerned. This case will be considered in more detail in the following section.

3 Measurement of CP Violation at a B Factory

In this section we shall discuss possible measurements of CP violating effects in B meson decays. In the proposed B factory the B mesons originate from $\Upsilon(4S)$ decays. Since the time dependence of the B decays has to be resolved, the B mesons must have sufficient momenta. This is achieved by producing the $\Upsilon(4S)$ at an asymmetric e^+e^- collider.

3.1 Working at the $\Upsilon(4S)$

B meson studies at the $\Upsilon(4S)$ have the following advantages:

- The peak cross section is high ($\sim 1.0\,nb$).
- Only $B\overline{B}$ final states are produced without any extra fragmentation hadrons.
- The energy of the B mesons is known, allowing for an efficient background reduction by using the energy constraint.

A $B^0\overline{B}^0$ pair from a $\Upsilon(4S)$ decay is in a p–wave state. Because of Bose statistics, this pair remains in a coherent $B^0\overline{B}^0$ state as long as neither B has decayed.

The decay probabilities of the $B^0\overline{B}^0$ system depend on the time difference.

Having observed the decay of one of the B mesons into a final state tagging the flavor of a $\overset{(-)}{B}{}^0$ at time t_1, the decay probability at time t_2 of the second B meson into the final state f common to both a B^0 and a $\overline{B}^0$ depends on the time difference $\Delta t \equiv t_2 - t_1$. More precisely, the decay probabilities obtained from eqs. 19.a, 19.b, and 21 are:

$$Pr\left(\overline{B}^0(t_1) \to tag, B^0(t_2) \to f\right) \propto \left(\frac{A^2}{2}\right) e^{-\Gamma|\Delta t|} \times \{1 - R \times \cos\Delta m\Delta t - D\,\sin(2\Phi + \Delta\alpha_{FSI}) \times \sin\Delta m\Delta t\} \quad (28.a)$$

$$Pr\left(B^0(t_1) \to tag, \overline{B}^0(t_2) \to f\right) \propto \left(\frac{A^2}{2}\right) e^{-\Gamma|\Delta t|} \times \{1 + R \times \cos\Delta m\Delta t + D\,\sin(2\Phi + \Delta\alpha_{FSI}) \times \sin\Delta m\Delta t\} \quad (28.b)$$

where $A^2 = M_1^2 + M_1'^2$, $\Delta\alpha_{FSI} = \alpha_1 - \alpha_1'$, and the quantities R and D are defined in eq. 26. We have made the hypothesis that only one amplitude contributes in eqs. 19.a, 19.b. This assumption is in general correct if $b \to c$ quark

decays are involved. For processes where $b \to u$ quark decays are needed, other diagrams (such as penguins or final state rescattering) might contribute [32]. However, there are ways to disentangle the different contributions [29,33,34].

Obviously, the asymmetry given in eq. 27 depends on Δt instead of t, and is an odd function of Δt. This has a very important consequence: No asymmetry due to CP violation can be observed, if one does not know the sign of Δt, namely which B, the tagged one or the other one, has decayed first. A measurement of at least the sign of Δt is necessary to detect CP violation. The time difference Δt is related to the measurable spatial separation Δz of the two B decays by

The decay time difference is calculated from the decay vertex separation

$$\Delta z = \gamma\gamma^*\beta c\Delta t + \gamma\gamma^*\beta^* c\cos\theta_2^*(t_2 + t_1) + \mathcal{O}(\beta^{*2}), \qquad (29)$$

where c is the velocity of light and

- β and γ define the boost which links the $\Upsilon(4S)$ rest frame to the laboratory frame.
- $\beta^* = 0.066$ and $\gamma^* \simeq 1$ define the boost which links the B rest frames to the $\Upsilon(4S)$ rest frame.
- θ_2^* is the polar angle of the B decaying at time t_2 in the $\Upsilon(4S)$ rest frame.

Although the second term in eq. 29 spoils the ideal one-to-one correspondence between Δz and Δt that one would obtain with $\beta^* = 0$, its impact on the $\sin 2\Phi$ measurement turns out to be rather small.

Throughout this study we work with an asymmetric e^+e^- collider operating at a centre–of–mass energy $\sqrt{s} = M_{\Upsilon(4S)}$. The beam energies are $E(e^-) = 9.33$ GeV for the high energy beam and $E(e^+) = 3.0$ GeV for the low energy beam.

The average distance between the B vertices is 210 μm.

This yields $\beta = 0.51$, $\gamma = 1.17$ and an average separation of the B decay vertices of 210 μm. The expected experimental vertex position resolution is $\sigma(\Delta z) = 50$ μm.

Another conceivable possibility to measure CP violation is to use a symmetric e^+e^- collider. It has to run at a centre–of–mass energy slightly above the $\Upsilon(4S)$ mass in order to produce $\overline{B}^0 B^{*0}$ and $B^0\overline{B}^{*0}$pairs. Since the $\overline{B}^{*0}$mesons exclusively decay to $B^0\gamma$, the resulting $B^0\overline{B}^0$ system is in a $C = +1$ state instead of $C = -1$. The decay probability depends then on $\Sigma t = t_1 + t_2$ and no cancellation of the sine term occurs in eqs. 28.a, 28.b when the integration over t_1 and t_2 is performed. In practice, this method needs at least six times the integrated luminosity as compared to the asymmetric solution since the production cross section for a $\overline{B}B^*$ pair is about six times smaller than for the $\Upsilon(4S)$ [35].

3.2 Final States and Expected Event Rates

There are two classes of final states which can be used for CP violation experiments.

Two classes of final states can be used for CP violation measurements: The first class comprises states that are CP eigenstates, the second one consists of "almost" CP eigenstates. For both kinds of final states we expect the CP violating effect to be reasonably large. Furthermore, the branching ratios promise sensible event rates, and the detection efficiencies look encouraging. In the following we will discuss both classes and sketch the CP violation analysis. For the relevant decay channels in each class, we present the expected number of events. The Monte Carlo studies yielding the efficiencies necessary to calculate these numbers are presented in detail in the section hereafter.

3.2.1 B Decays to CP Eigenstates

Several final CP eigenstates provide reasonably large event numbers.

We start discussing the case where the final state f is truly a CP eigenstate f_{CP} with definite CP parity η_{CP}. Here the information on the CKM matrix can be extracted most efficiently from the data, since there are no problems with unknown effects due to strong interaction. The usable decay channels are listed in table II. Monte Carlo studies show that good detection and reconstruction efficiencies are expected for these decay modes in a typical B factory detector. The numbers are summarized in table II together with the total number of events that can be used to measure the angles β and α of the unitarity triangle with an integrated luminosity of $50 fb^{-1}$.

Table II: Expected number N of reconstructed events for measuring β and α. The reconstruction efficiency includes the relevant branching fractions. A 42% tagging efficiency has been used (see section 3.3). The assumed branching fractions are either taken from experiments or from model dependent predictions. The reconstruction efficiencies are obtained from Monte Carlo studies detailed in section 3.3.

Modes	Branching fraction	Reconstruction efficiency	N events ($50 fb^{-1}$)	measured quantity
$B^0 \to J/\psi K_S^0$	4×10^{-4}	7%	~ 590	$\sin 2\beta$
$B^0 \to \chi_{c1} K_S^0$	1×10^{-3}	1.5%	~ 310	$\sin 2\beta$
$B^0 \to \psi' K_S^0$	9×10^{-4}	1.6%	~ 300	$\sin 2\beta$
$B^0 \to D^{\pm} D^{\mp}$	5×10^{-4}	1%	~ 100	$\sin 2\beta$
$B^0 \to \pi^+ \pi^-$	2×10^{-5}	76%	~ 320	$\sin 2\alpha$

Explanation of the measurement procedure.

The procedure how to measure CP violation at an asymmetric B factory when either the B^0 or the $\overline{B}^0$ is tagged and the other one decays to f_{CP} is presented in the following. As "tagging decays" we denote those decays which are specific

to the flavor of the decaying b quark. An example is the semileptonic decay where l^- can only originate from b and l^+ only from $\bar{b}$. We use eqs. 28.a, 28.b with $R = 0$, $D = 1$ and $\Delta\alpha_{FSI} = 0$ or π according to the CP parity (η_{CP}) of f_{CP}. Assuming a non-zero value for $\sin 2\Phi$, the corresponding time dependent decay probabilities are shown in fig. 7.

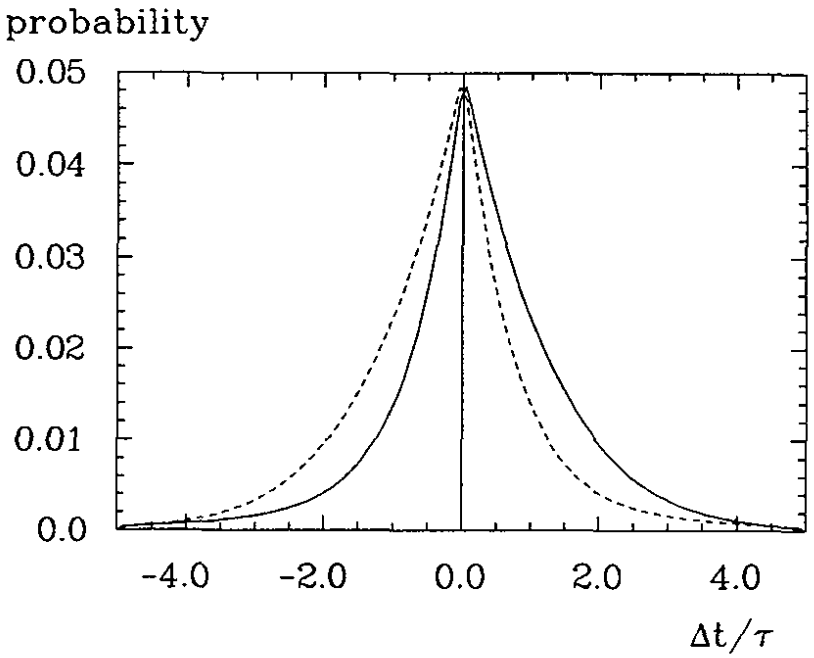

Figure 7: Time difference between the decays of the tagging B ($B^0 \to f_B$) and the tagged B ($\overline{B}^0 \to f_{CP}$) (full line) and its CP conjugate process (dotted line). $\sin 2\Phi = 0.4$ is assumed.

There exist four event categories.

To measure CP violation one classifies the events into four categories (see fig. 7):

- N_1: Events with $\Delta t > 0$ and a tagging B;
- N_2: Events with $\Delta t < 0$ and a tagging B;
- N_3: Events with $\Delta t > 0$ and a tagging $\overline{B}$;
- N_4: Events with $\Delta t < 0$ and a tagging $\overline{B}$.

These categories must be analyzed separately since CP violation produces two different time distributions in $t_2 - t_1$, one for (1) and (4) and another one which characterizes (2) and (3).

Asymmetry as a measure of CP violation.

A measurement of CP violation is then extracted from the asymmetry built from the four event numbers:

$$\mathcal{A} = \frac{N_1 + N_4 - N_2 - N_3}{N_1 + N_4 + N_2 + N_3}. \tag{30}$$

Time dependent event rates.

A calculation (see *e.g.* ref. [36]) leads to the following expressions for the time dependent rates in each decay category:

$$1.\ \frac{dN_1}{d\Delta t} \propto [1 + \eta_{CP} \sin\phi\ \sin(x\frac{|\Delta t|}{\tau})] \exp(-|\Delta t|/\tau), \tag{31.a}$$

$$2.\ \frac{dN_2}{d\Delta t} \propto [1 - \eta_{CP} \sin\phi\ \sin(x\frac{|\Delta t|}{\tau})] \exp(-|\Delta t|/\tau), \tag{31.b}$$

$$3.\ \frac{dN_3}{d\Delta t} \propto [1 - \eta_{CP} \sin\phi\ \sin(x\frac{|\Delta t|}{\tau})] \exp(-|\Delta t|/\tau), \tag{31.c}$$

$$4.\ \frac{dN_4}{d\Delta t} \propto [1 + \eta_{CP} \sin\phi\ \sin(x\frac{|\Delta t|}{\tau})] \exp(-|\Delta t|/\tau). \tag{31.d}$$

Here $\phi = 2\Phi + \Delta\alpha_{FSI}$ according to eqs. 28.a and 28.b. τ denotes the B^0 lifetime and $x = \Delta m/\Gamma$ is the mixing parameter.

Using these expressions, the relation between the asymmetry $\mathcal{A}$ introduced in eq. 30 and the CP violating phase ϕ is given as

$$\mathcal{A}(\frac{t}{\tau}) = \eta_{CP} \sin\phi\ \sin(x\frac{t}{\tau}). \tag{32}$$

Integrating over time yields

$$\mathcal{A} = \eta_{CP} \frac{x}{1+x^2} \sin\phi. \tag{33}$$

3.2.2 B Decays to non-CP Eigenstates

Some classes of non- CP eigenstates can be exploited as well.

We want to emphasize now that decays to CP eigenstates *are not the only* useful ones to measure CP asymmetries. There are two more classes of final states:

1. Near-CP Eigenstates

Final states with self conjugate quark content

If the final states are made out of a collection of self conjugate quarks $(q_1\bar{q}_1 q_2\bar{q}_2)$, the ratio R in eqs. 28.a, 28.b is different from 0 and $D = \sqrt{1-R^2} < 1$. A good example to illustrate this type of events is the decay $B^0 \to \rho^{\pm}\pi^{\mp}$. The ratio R can be measured, *e.g.*, ignoring the time order and integrating eqs. 28.a, 28.b over Δt. As for CP eigenstates, a global fit of the four time-dependent distributions corresponding to $Pr\left(\overline{B}^0(t_1) \to tag, B^0(t_2) \to \rho^+\pi^-\right)$ and $Pr\left(\overline{B}^0(t_1) \to \rho^+\pi^-, B^0(t_2) \to tag\right)$ with $t_1 > t_2$ and with $t_1 < t_2$ allows

to measure $S \equiv \sin(2\Phi + \Delta\alpha_{FSI})$. Since $\Delta\alpha_{FSI}$ is not guaranteed to be 0 (although likely [29]), one is not completely sure to measure $\sin 2\Phi$. The remedy to cure this uncertainty is to also investigate the CP conjugate final state $\overline{f} = \rho^- \pi^+$ in much the same way. The time dependent distributions for $\overline{f}$ are

$$Pr\left(\overline{B}^0(t_1) \rightarrow tag, B^0(t_2) \rightarrow \overline{f}\right) \propto \left(\frac{\overline{A}^2}{2}\right) e^{-\Gamma|\Delta t|} \times \left\{1 + \overline{R} \times \cos\Delta m\Delta t - \overline{D}\, \sin(2\Phi - \Delta\alpha_{FSI}) \times \sin\Delta m\Delta t\right\}, \quad (34.a)$$

$$Pr\left(B^0(t_1) \rightarrow tag, \overline{B}^0(t_2) \rightarrow \overline{f}\right) \propto \left(\frac{\overline{A}^2}{2}\right) e^{-\Gamma|\Delta t|} \times \left\{1 - \overline{R} \times \cos\Delta m\Delta t + \overline{D}\, \sin(2\Phi - \Delta\alpha_{FSI}) \times \sin\Delta m\Delta t\right\}. \quad (34.b)$$

The CP conjugate quantities $\overline{A}^2$, $\overline{R}$ and $\overline{D}$ are defined in the same way as A, R and D using $\overline{M}$ and $\overline{M}'$. The procedure already used for f can be applied here in order to extract $\overline{R}$ and $\overline{S} \equiv \sin(2\Phi - \Delta\alpha_{FSI})$. It is important to note that measuring $R \neq \overline{R}$ is an evidence for direct CP violation and would indicate that more than just one amplitude contributes in that specific decay. In contrast, $R = \overline{R}$ will tend to make the scenario with one dominating amplitude very likely (although not 100% proof [29]). From the measured S and $\overline{S}$ one can evaluate $\sin 2\Phi$ in the following way:

$$\sin^2 2\Phi = \frac{1}{2}\left[1 + S\overline{S} \pm \sqrt{(1 - S^2)(1 - \overline{S}^2)}\right]. \quad (35)$$

The ambiguity of the CP violating phase can be resolved.

Here, one of the signs on the right hand side gives the true $\sin^2 2\Phi$, while the other gives $\cos^2 \Delta\alpha_{FSI}$. A theoretical bias for $\Delta\alpha_{FSI} = 0$ or π exists for some particular final states like $\rho^\pm\pi^\mp$ [37]. Therefore if one solution is measured to be compatible with 1, one could try to resolve the ambiguity in eq. 35 by identifying $\cos^2 \Delta\alpha_{FSI}$ with that solution. In a more rigid approach one can always use other decay modes (*e.g.* the CP eigenstate $\pi^+\pi^-$) to determine first $\sin^2 2\Phi$ unambiguously (but perhaps less precisely) to sort out the solution giving $\Delta\alpha_{FSI}$.

Other final states besides $\rho^\pm\pi^\mp$ are available with the same property of self conjugate quark content. Significant numbers of events in some of them are expected in a typical B factory detector. Table III lists the most significant ones together with the expected event rates and the angle in the unitarity triangle they measure.

Table III: Expected number N of reconstructed events for near - CP eigenstates (final states with self conjugate quark content). The reconstruction efficiency includes the relevant branching fractions when needed. The signal to background ratio is shown in the column S/B. A 42% tagging efficiency has been used (see section 3.3).

Modes	Branching fraction	Reconstruction efficiency	S/B	N events $(50 fb^{-1})$	measured quantity
$B^0 \to \rho^{\pm}\pi^{\mp}$	6×10^{-5}	46%	3	~ 580	$\sin 2\alpha$
$B^0 \to a_1^{\pm}\pi^{\mp}$	6×10^{-5}	21%	2	~ 260	$\sin 2\alpha$
$B^0 \to D^{*\pm}D^{\mp}$	2×10^{-3}	5×10^{-3}	3	~ 210	$\sin 2\beta$

2. Final States with Relative Angular Momentum

Relative angular momentum between the final state particles may wash out the asymmetry. One can isolate the different contributions.

A second category of useful B^0 decays to non - CP eigenstates comprises those modes where different partial waves contribute with different CP parity η_{CP} [30, 31]. The decay of a B^0 meson to two vector particles belongs to this category. A typical example for this class of events is the decay $B^0 \to J/\psi K^{*0}$. In such a final state, both CP parities $\eta_{CP} = +1$ and -1 are possible according to the relative angular momentum ℓ between J/ψ and K^{*0}. Therefore the possibility exists that the asymmetry in eq. 30 vanishes if no additional information is used to discriminate between ℓ-odd and ℓ-even contributions. In the following, we sketch a method that could provide this discrimination. In the example, the K^{*0} meson decays to two spinless particles K_S^0 and π^0. A transverse axis is defined as the normal to the plane containing the three particles $J/\psi K_S^0\pi^0$. The CP parity eigenstates of the final state can be determined using the spin projection τ_i of the particles along this transverse axis.

$$CP|J/\psi K_S^0\pi^0; J=0\rangle = (CP)_{int}(-1)^{\tau}|J/\psi K_S^0\pi^0; J=0\rangle \qquad (36)$$

where $(CP)_{int}$ denotes the intrinsic CP parity of the particles. In the example, $\tau = \tau_{J/\psi}$ since only the J/ψ has spin. The different helicity contributions (0 or 1) are sorted out using the angular distribution of the decay products of the J/ψ (*i.e.* a lepton pair) in its rest frame with respect to the transverse axis. The price that has to be payed for such an analysis is an increase of the error on $\sin 2\Phi$ as is shown in ref. [31]. In the worst case where helicity 0 and 1 contribute equally, the error $\sigma(\sin 2\Phi)$ could be larger by a factor of 2 compared to the situation where only one single helicity contributes. Obviously this type of analysis is not needed if one helicity state largely dominates. A study of the decay $B^{\pm} \to J/\psi K^{*\pm}$ can clarify the situation.

Decays $B^0 \to VF$ are useful and promise substantial rates.

It is possible to generalize this type of analysis to $B^0 \to VF$ decay modes where F denotes a set of particles and V is a vector meson [31]. In table IV we list the three classes of final states that can be used the way indicated. Table V shows

specific final states of this kind which will contribute significant event numbers to the measurement of CP violation.

Table IV: The CP parity of the final state in decays of the type $B^0 \to VF$. V denotes a vector particle, F an intermediate state of spin 0 or 1 and P a pseudoscalar particle. The spins of the particles P_1 and P_2 are denoted by s_{P_1} and s_{P_2}, respectively.

Event class	Examples	CP parity
$V = \overline{V}$ $F = P_1 + P_2$ $P_1 = \overline{P_1}$, $P_2 = \overline{P_2}$	$J/\psi(K_S^0\pi^0)_{nonres}$	$(CP)_{int} \times (-1)^{\tau}$
$V = \overline{V}$, $F = \overline{F}$ $F \to P_1 + P_2$ $P_1 = \overline{P_2}$, $s_{P_1} = s_{P_2} = 0$	$J/\psi(\pi^+\pi^-)_\rho$ [37]	$(CP)_{int} \times (-1)^{s_F+\tau}$
$V = \overline{F}$ $F \to P_1 + P_2$ $s_{P_1} = s_{P_2} = 0$	$D^{*+}D^{*-}$ $\rho^+\rho^-$	$(-1)^{s_F+\tau}$

Table V: Expected number N of reconstructed events for final states with relative angular momentum. The reconstruction efficiency includes the relevant branching fractions where necessary. A 42% tagging efficiency has been used (see section 3.3).

Modes	Branching fraction	Reconstruction efficiency	N events ($50 fb^{-1}$)	measured quantity
$B^0 \to J/\psi K_S^0\pi^0$	4×10^{-4}	3%	~ 250	$\sin 2\beta$
$B^0 \to \psi' K_S^0\pi^0$	2×10^{-4}	0.7%	~ 30	$\sin 2\beta$
$B^0 \to D^{*\pm}D^{*\mp}$	2×10^{-3}	5×10^{-3}	~ 210	$\sin 2\beta$
$B^0 \to \rho^+\rho^-$	5×10^{-5}	20%	~ 210	$\sin 2\alpha$

3.3 Results of Monte Carlo Simulations

In the previous section we gave the event rates which can be expected operating a detector at a B factory. To calculate these numbers several efficiencies have to be known, such as geometrical acceptance, reconstruction and tagging efficiency. Their values are the result of Monte Carlo simulations described on the following pages. We investigated the reactions: $B^0 \to J/\psi K_S^0$, $B^0 \to \chi_{c1} K_S^0$, $B^0 \to \psi' K_S^0$ (measuring $\sin(2\beta)$) and $B^0 \to \pi^+\pi^-$ (measuring $\sin(2\alpha)$). They belong to the group of final states which are CP eigenstates. Out of the group with relative angular momentum between the final state particles we present the decay

$B^0 \to J/\psi K^{*0}$ (measuring $\sin(2\beta)$). The first subsection on $B^0 \to J/\psi K^0_S$ explains the analysis procedure. Technical details on the event generator and the detector simulation can be found in the appendix.

3.3.1 CP Violation in the decay $B^0 \to J/\psi K^0_S$

Reconstruction of one B and both vertices

Generated data samples.

In order to investigate the possibility of measuring CP violation in the decay $B \to J/\psi K^0_S$, we have generated several data sets of 40000 $B^0\overline{B}^0$ events each for studying various aspects of the analysis as well as of the proposed detector. These data samples were processed through a simulation of the detector, including full particle identification. One B decayed to $J/\psi K^0_S$, the other one to a variety of possible final states. For the J/ψ only leptonic decays were taken into account. These data samples are larger than expected for an integrated luminosity of 50 fb^{-1}. The finally expected sensitivities for the reference luminosity of 50 fb^{-1} will be discussed in chapter 3.5.

Reconstruction of $J/\psi K^0_S$.

To reconstruct the J/ψ we demand two leptons to have an invariant mass within ± 100 MeV of the J/ψ nominal mass and to form a single vertex with $\chi^2 < 9$. 73% of the J/ψ meet these criteria. The vertex coordinates of the J/ψ serve as the one B vertex. The K^0_S is reconstructed in both the $\pi^+\pi^-$ and $\pi^0\pi^0$ decay modes where we only take well identified decay products and apply loose selection cuts. We reconstruct 67% of K^0_S in neutral and charged decay modes. We then calculate the invariant mass of $J/\psi K^0_S$ shown as the distribution with error bars in fig. 8.

Reconstruction of the second B vertex.

Since the B mesons have essentially no transverse momentum, we reconstruct the vertex of the tagging B as follows: We search for vertices amongst all tracks excluding the decay products of the J/ψ and the K^0_S, and use the constraint that these vertices have to lie on the z axis. The vertex with the lowest z value is finally accepted. Because other particles usually decay downstream of the B due to the boost, this choice is rather reliable and correct in 99% of all cases.

Tagging

Two tagging methods are used. The tagging efficiency is 42%.

In order to identify the tagging B, two methods have been used: lepton tagging exploits semileptonic B meson decays, and kaon tagging uses charged K mesons from the cascade $b \to c \to s$. In both cases positively charged particles tag a B^0, negative ones a $\overline{B}^0$.

Lepton tagging: To exclude wrong tags from charm semileptonic decays we demand the tagging lepton to have a momentum $p^* > 1.5$ GeV/c in the $\Upsilon(4S)$ rest frame which, to a good approximation, corresponds to the B rest frame. Demanding one lepton with $p^* > 1.5$ GeV/c we tag by this method 7.4% of the accepted events, 92% of the tags being correct.

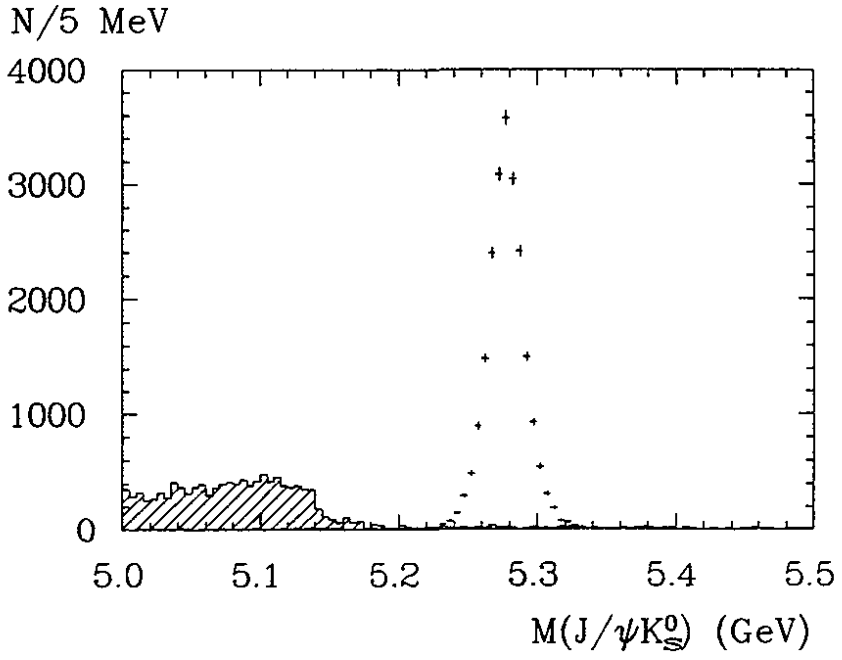

Figure 8: Invariant $J/\psi K_S^0$ mass. Data points with error bars are from the reaction $B \to J/\psi K_S^0$, the hatched histogram constitutes the properly scaled background from the decay $B \to J/\psi K^{*0}$.

Kaon tagging: We accept charged kaons as a tag for the B flavour in two cases: (1) If there is only one charged K and no K_S^0 other than from $B^0 \to J/\psi K_S^0$, its charge is taken. (2) If there are two same-charge kaons out of at most three, this charge is used for tagging. This procedure tags 31% of the accepted events being correct in 91% of the cases.

Combined tagging: In 3.7% of the accepted cases both tags are present. In 91% of these cases the tags agree. Events with contradictory tags are treated as untagged. Combined tagging is then correct to more than 99%.

The overall efficiency is 21%.

In total we tag 42% of the events, 92% of which are correct. The efficiency for tagging one B and reconstructing the other one in the decay $B \to J/\psi K_s^0$ is 21%.

Analyzing the time distributions

Δz to Δt translation.

From the measured z difference of the two B vertices, the time difference is calculated by means of eq. 29 where only the first term is retained since $\beta^* = 0.066$ and $\gamma^* = 1.002$:

$$\frac{t_2 - t_1}{\tau} \approx \frac{\Delta z}{\beta\gamma c\tau}. \tag{37}$$

With $\beta\gamma = 0.6$ one gets $\beta\gamma c\tau \approx 210\mu m$. This has to be compared to the resolution we reach with the proposed vertex detector of $\sigma(\Delta z) = 50\mu m$.

Two ways to extract the CP asymmetry.

As an example for the analysis we show the results based on a data set of 40000 events generated with $\sin(2\beta) = 0.3$. We group the events according to the four classes introduced earlier and extract $\sin(2\beta)$ in two different ways:

1. Asymmetry determination from event counting:
   Inserting the number of events N_i found in the 4 categories into eq. 30 yields a raw asymmetry of $\mathcal{A}' = 0.102 \pm 0.011$, which can be converted to $\sin(2\beta') = 0.217 \pm 0.023$.

2. Determination of the raw $\sin(2\beta')$ by fitting:
   By simultaneously fitting the sum of the distributions (1) + (4) and (2) + (3) to the expressions of eqs. 31.a - 31.d, one gets a raw value $\sin(2\beta') = 0.228 \pm 0.020$. The distributions along with the fit result are displayed in fig. 9.

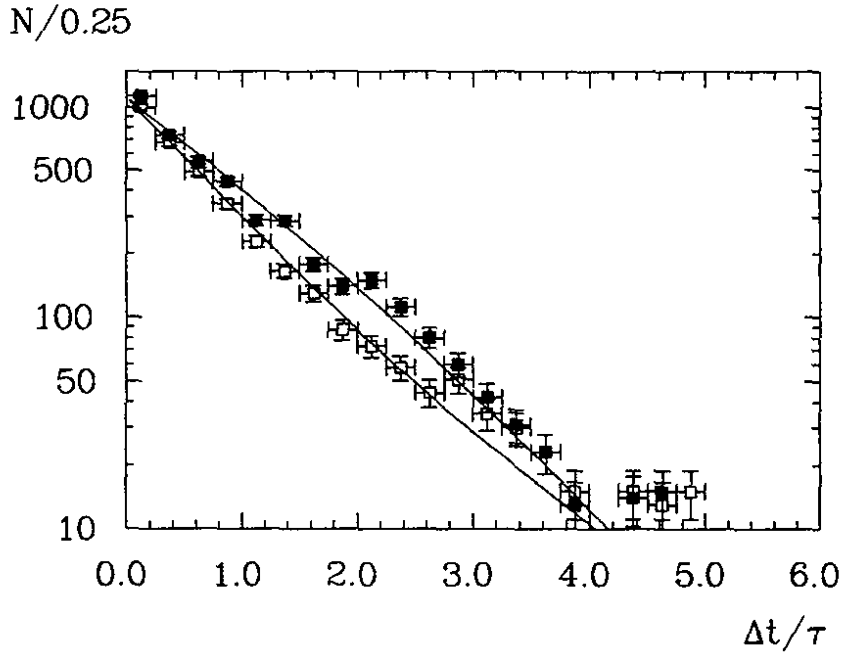

Figure 9: Time distributions of events of categories (1)+(4), open squares, and of (2)+(3), full squares. The lines represent the result of a simultaneous fit.

Corrections to the raw values.

Both results have to be corrected for two different kinds of errors. The first correction is due to wrong tagging, shuffling events between catagories (1) and (3) and between (2) and (4). The second one takes into account wrongly reconstructed vertex sequences, redistributing events between (1) and (2) and

between (3) and (4). Both effects can be corrected for by a migration coefficient formalism. After these corrections one arrives at the final numbers:

1. $\sin(2\beta) = 0.283 \pm 0.032$ and
2. $\sin(2\beta) = 0.298 \pm 0.026$.

They are both in perfect agreement with the input value of $\sin(2\beta) = 0.3$.

Moreover, one notices that performing a simultaneous fit to the time distributions increases the statistical accuracy by about 20%, the origin of this gain being due to more information contained in the functional dependence of the distributions.

At the end of this chapter (section 3.5) we shall discuss the sensitivity of the measurement of the angle β.

Investigation of other detector options

The CP violation measurement is still possible with a modified detector and with another boost value.

Technical or financial pressures may require modifications in the detector. Two designs will be described later in this document. Even with a less optimized detector, the CP violation measurement is still feasible. To demonstrate this we have, at the same level of detail as the analysis presented before, performed analogue studies with different detector set-ups and investigated also the effect of different boost values. We studied the following changes:

1. Perform the particle identification with a TOF system instead of the proposed RICH counter.
2. Replace the silicon vertex detection system by a vertex drift chamber.
3. Change the radius of the beam pipe and therefore the distance between decay vertices and the first layer of silicon.
4. Use $\beta\gamma$ values other than 0.6.

The results are presented in turn.

1. As particle identification, in particular for charged kaons, is crucial for the tagging procedure, we must be able to keep up the tagging efficiency also in case a TOF counter will be used for particle identification. We assume a TOF resolution of $\sigma(\mathrm{TOF}) = 80$ psec. This does not change the overall tagging efficiency of 42% and only marginally reduces the fraction of correct tags from 92% to 90%. This decrease can be totally attributed to changes in the kaon tagging sector. Use of such a TOF system would not increase the luminosity needed to measure CP violation compared to the proposed standard set–up.

2. If unexpectedly bad background conditions prevent us from operating a silicon vertex detector, we may have to use a gaseous vertex drift chamber of the ARGUS type [38]. If we operated such a vertex device at the same beam pipe radius of $r_{Be} = 2.5$ cm, this would not influence the precision of the CP violation measurement.

3. Changing the radius of the Be beam pipe has an impact on the resolution and, in turn, on the integrated luminosity required to perform this measurement. As mentioned above, in the standard set-up with $r_{Be} = 2.5$ cm we get a resolution $\sigma(\Delta z) = 50\mu$m. At $r_{Be} = 1.0$ cm it improves to $\sigma(\Delta z) = 28\mu m$, while at $r_{Be} = 4.5$ cm it degrades to $\sigma(\Delta z) = 80\mu m$. The quantitative consequences in terms of integrated luminosity are illustrated in fig. 10. If one has to increase the beam pipe radius to $r_{Be} = 4.5$ cm, one needs 30% more integrated luminosity.

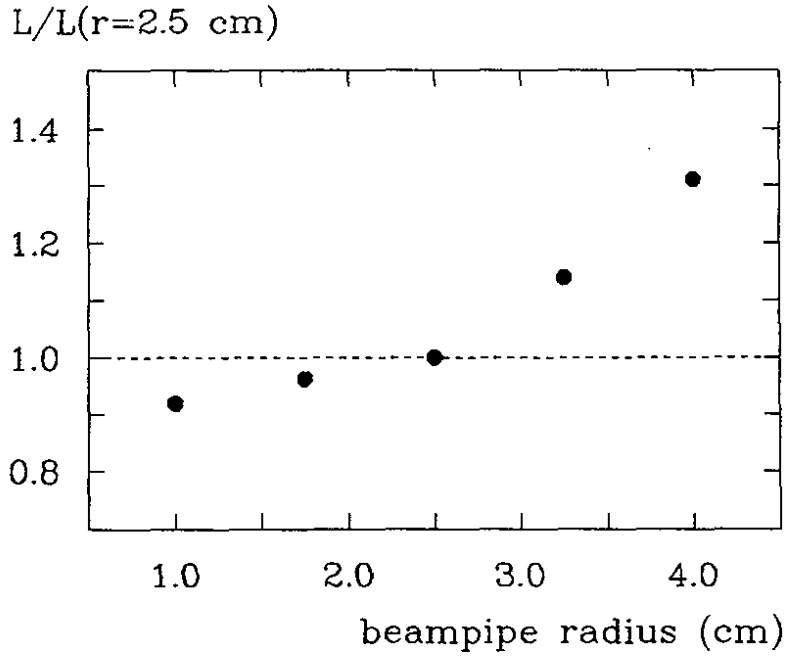

Figure 10: Dependence of the required integrated luminosity on the radius of the beam pipe. The value of the standard set-up with $r_{Be} = 2.5$ cm is normalized to 1.

4. We also studied the effect of boost values different from the proposed one of $\beta\gamma = 0.6$. For this investigation we took exactly the same detector as optimized for the adopted value and performed similar analyses with changed beam energies. We demand a measurement of $\sin(2\beta)$ to the same statistical accuracy as for the case where $\beta\gamma = 0.6$ and show the

integrated luminosity $\mathcal{L}$ needed in excess over $\mathcal{L}(\beta\gamma = 0.6)$ in fig. 11. One notices that $\mathcal{L}$ does not change between a boost value of $\beta\gamma = 0.45$ and $\beta\gamma = 0.6$.

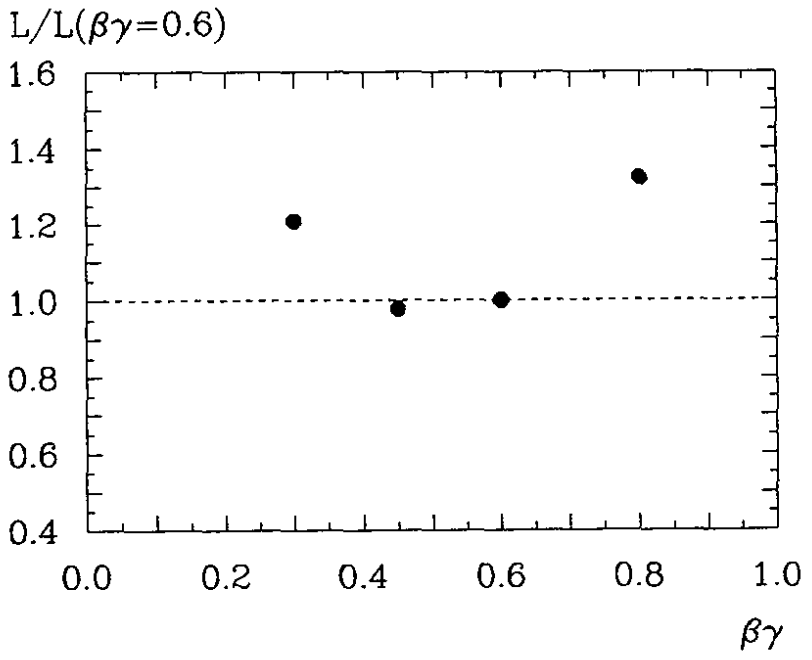

Figure 11: Relative integrated luminosity needed to measure $\sin(2\beta)$ to the same statistical accuracy as function of the boost value $\beta\gamma$. The luminosity at $\beta\gamma = 0.6$ is normalized to 1.

3.3.2 CP violation in the decay $B^0 \to \chi_{c1} K^0_S$

$B^0 \to \chi_{c1} K^0_S$ has a rather high branching ratio.

A second decay channel which contributes significantly to the measurement of the angle β in the unitarity triangle is $B^0 \to \chi_{c1} K^0_S$ with a subsequent radiative decay $\chi_{c1} \to \gamma J/\psi$. A recent ARGUS analysis [39] shows a rather large branching fraction for the analogous decay of the charged B^+: $BR(B^+ \to \chi_{c1} K^+) = 0.19 \pm 0.14\%$. One can expect a similar decay rate for $B^0 \to \chi_{c1} K^0_S$.

The overall efficiency is 16%.

We performed an analysis of this decay channel. The reconstruction of the J/ψ again uses only the leptonic modes. As overall efficiency (including geometry, reconstruction, and tagging) we find 16%. With a branching ratio $BR(B^0 \to \chi_{c1} K^0_S) = 1 \times 10^{-3}$, one finds that this channel adds $\sim 55\%$ of statistics to the CP violation measurement compared to the $B^0 \to J/\psi K^0_S$ events.

3.3.3 CP violation in the decay $B^0 \to \psi' K^0_S$

The branching ration of the decay $B^0 \to \psi' K^0_S$ is expected to be of the order of 1×10^{-3}. We analyzed this reaction, considering only the decay into charged pions $\psi' \to \pi^+\pi^- J/\psi$. As before, the J/ψ was reconstructed in the leptonic decay modes. The product of tagging efficiency, geometrical acceptance, and reconstruction efficiency is 13%. This channel adds $\sim$ 50% of statistics to the CP violation measurement compared to the $B^0 \to J/\psi K^0_S$ events.

For the decay $B^0 \to \psi' K^0_S$ we find an efficiency of 13%.

3.3.4 The Decay $B^0 \to \pi^+\pi^-$

The decay $B^0 \to \pi^+\pi^-$ is one reaction which allows, via measurement of CP violation, to determine the angle α in the unitarity triangle.

The model of Bauer, Stech and Wirbel [40] predicts the branching ratio for the decay $B^0 \to \pi^+\pi^-$ to be $2.1 \cdot 10^{-3} \times |V_{ub}/V_{cb}|^2$. Recent ARGUS [7] and CLEO [8] measurements on semileptonic B decays show that $|V_{ub}/V_{cb}|$ is of order 0.1. This converts to $BR(B^0 \to \pi^+\pi^-) \approx 2 \times 10^{-5}$. The detection efficiency for this channel including geometry and reconstruction is 76%.

$BR(B^0 \to \pi^+\pi^-) = 2 \times 10^{-5}$ is expected.

Background sources are decays where the B disintegrates to very few low mass particles some of which may be lost or misidentified. One candidate decay investigated is $B^0 \to \pi^+\pi^-\pi^0$ with a predicted branching ratio ten times as high as $B^0 \to \pi^+\pi^-$ [41]. Due to the good mass resolution and photon detection this decay does not cause any problem.

Reflections from the decay $B^0 \to K^+\pi^-$ where the K^+ is misinterpreted as a π^+ do not spoil the signal. Particle identification provides a 3.5 standard deviation $\pi - K$ separation in the RICH detector and 2 standard deviations in the dE/dx measurement. Furthermore, the reconstructed energy of these B candidates is more than 2 standard deviations away from the nominal energy.

3.3.5 CP violation in the decay $B^0 \to J/\psi K^{*0}$

The decay $B \to J/\psi K^{*0}$, $K^{*0} \to K^0_S \pi^0$ belongs to the class where the relative angular momentum between the final state particles determines the CP phase.

In these decays one has a mixture of longitudinally and transversely polarized K^{*0}s. Both components have to be separated by a decay angular analysis because they contribute to opposite CP parities as discussed earlier. The basic idea how to do such a separation has been introduced in subsection 3.2.2. A recent ARGUS analysis [42] gives evidence for a large longitudinal polarization of the K^{*0}. In this case all reconstructed and tagged $J/\psi K^{*0}$ final states can be used without any dilution and the intricacies of a decay angular analysis.

As for the $J/\psi K^0_S$ final state we have performed an analysis of this decay chain assuming the K^{*0} to be fully polarized. We find an overall efficiency of 9% including geometry, reconstruction and tagging.

The overall efficiency is 9%.

3.4 Measurement of the Angle γ

The problems to measure the angle γ.

We have, so far, discussed measurements of the angles α and β in the unitarity triangle. Measuring the angle γ with one of the techniques presented above requires to operate the collider at a slightly higher energy where B_s mesons are produced. Their decays provide the best opportunity to measure $\sin 2\gamma$, in particular the decay $B_s^0 \to K_S^0 \rho^0$.

The same technique as explained for $J/\psi K_S^0$ can be applied. This analysis will suffer from the smaller B_s production cross section compared to the B cross section on the $\Upsilon(4S)$. The relative background contribution from events not containing B_s mesons increases. Furthermore, another complication arises because $B_s^0\ \overline{B}_s^0$ can produced in a mixture of CP parities $\eta_{CP} = +1$ and $\eta_{CP} = -1$.

At least $300 fb^{-1}$ are needed to measure γ in the $K_S^0\rho^0$ channel.

In reference [43] the decay $B_s^0 \to K_S^0\rho^0$ has been studied. There the conclusion is that at least 300 fb^{-1} of integrated luminosity is needed, assuming the branching fraction for this decay to be 5×10^{-4}. Unless this branching ratio is significantly larger or other modes can be used, the direct measurement of the angle γ will be very difficult. We do not consider this measurement part of the initial programme of the B factory.

3.5 Achievable Accuracy and Luminosity Requirements

We shall now discuss how well the angles β and α can be measured for a given integrated luminosity.

The value of $\sin 2\Phi$ (where $\Phi \equiv \alpha, \beta$) can be determined from the shape of the time-dependent distributions. The expected variance of such a measurement is:

Error on the angle measurement.

$$\sigma^2[\sin 2\Phi] \simeq \frac{C_2}{d^2(1-2f)^2} \frac{1+\eta_z/(S/B)}{N} \times [1 + \mathcal{O}(\sin^2 2\Phi)] \qquad (38)$$

where

- $C_2 = \frac{1+4x^2}{2x^2}$ with the mixing parameter $x \equiv x_d$ or x_s according to the parent B_d^0 or B_s^0. For the B_d^0 system we take $C_2 = 3$.
- d is a dilution factor. It is unity, if the final state is a CP eigenstate. If the final state is not a CP eigenstate, one encounters the following two cases: (1) Near-CP eigenstates (such as $\rho^\pm\pi^\mp$ type decays) have $d = \sqrt{1-R^2}\cos\Delta\alpha_{FSI}$. Here the notations of section 3.2 are used. (2) For decays to two vector particles (like $B^0 \to J/\psi K^{*0}$) one finds d in the

range 0.4 - 1 depending on the fraction of decays with relative angular momentum $\ell = 0$ or 1 of the decay products [31].

- f represents the fraction of reconstructed $B^0\overline{B}^0$ events assigned to the wrong one out of the 4 possible classes (see the discussion on pp. 43 and the introduction of migration coefficients there). It receives contributions from events with either wrongly tagged flavor or incorrectly reconstructed sequence of the B decay vertices. An average over migration coefficients yields $f = 0.125$.

- η_z is an effective rejection factor resulting from the shape differences between the Δz distributions of background and signal events. The η_z value depends on the resolution $\sigma[\Delta z]$. For example, with $\sigma[\Delta z] = 55\ \mu m$, one has $\eta_z \simeq 0.20$ for the continuum $q\bar{q}$ background. The conservative value $\eta_z = 0.5$ is used in the following.

- S/B is the ratio of the number of selected signal events over the number of selected background events.

- N is the total number of selected $B^0\overline{B}^0$ events.

In tables VI and VII we give the expected errors on $\sin 2\beta$ and $\sin 2\alpha$ for an integrated luminosity of $50 fb^{-1}$ at an asymmetric collider.

Table VI: Expected error on $\sin 2\beta$ using the sum of all events.

Modes	$J/\psi K^0_S$ $\psi' K^0_S$ $D^{\pm}D^{\mp}$ $\chi_{c1}K^0_S$	$D^{*\pm}D^{\mp}$	$J/\psi K^{*0}$ $\psi' K^{*0}$ $D^{*\pm}D^{*\mp}$	All
d	1	1	0.7	
N_{eff}/fb^{-1}	26.0	3.6	4.8	34.4
$\sigma[\sin 2\beta]$ $50 fb^{-1}$	0.064	0.172	0.149	0.056

Table VII: Expected error on $\sin 2\alpha$ using the sum of all events.

Modes	$\pi^+\pi^-$	$\rho^{\pm}\pi^{\mp}$ $a_1^{\pm}\pi^{\mp}$	$\rho^+\rho^-$	All
d	1	1	0.7	
N_{eff}/fb^{-1}	6.4	14.1	2.1	22.6
$\sigma[\sin 2\alpha]$ $50 fb^{-1}$	0.129	0.087	0.228	0.069

Figure 12 shows the accuracy in the determination of the angles α and β. The accuracy of an angle $\Phi > 90°$ is the same as for an angle $180° - \Phi$.

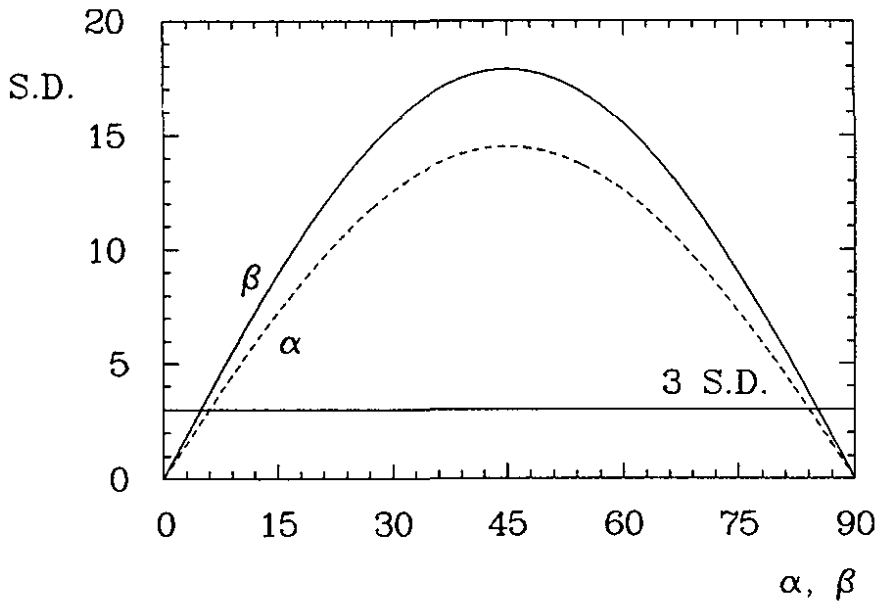

Figure 12: Accuracy in the measurement of the angles α (dash-dotted line) and β (full line), expressed in numbers of standard deviations (S.D.). The horizontal line corresponds to 3 S.D.

At least a 3 S.D. measurement is possible.

From present constraints on the unitarity triangle (see section 1.4), $\sin 2\beta$ is expected to be greater than 0.15. In this case, a positive effect of CP violation will be measured which is at least three standard deviations apart from zero.

However, we would rather take a more conservative attitude and fix $\sin 2\Phi = 0.1$ ($\Phi = \alpha, \beta$) as the goal to be achieved. To ease comparison of event numbers in different decay channels we introduce an effective event number N_{eff} defining

$$N_{eff} = N \frac{d^2}{1 + \eta_z/(S/B)}, \tag{39}$$

which allows simple additive operations of the N_{eff} numbers. In the tables we also give the sensitivity per luminosity unit N_{eff}/fb^{-1}. These numbers are used to determine the luminosity needed to measure the CP violation angle Φ to a given precision:

$$\mathcal{L}(fb^{-1}) = \frac{C_2}{(1-2f)^2} \frac{1}{N_{eff}/fb^{-1}} \frac{1}{\sigma^2[\sin 2\Phi]}. \tag{40}$$

To fully explore the range of $\sin 2\alpha$ and $\sin 2\beta$ down to a value of 0.1 with a significance greater than 3 standard deviations will require $140 fb^{-1}$ for $\sin 2\beta$ and $210 fb^{-1}$ for $\sin 2\alpha$.

4 Measurement of CKM Matrix Elements

In this chapter we are going to demonstrate the improvements in the measurements of CKM matrix elements one can expect from a data set of $50 fb^{-1}$ collected with a B factory. We shall address the determination of $|V_{cb}|$ and $|V_{ub}|$ from semileptonic decays of B mesons, the prospects to measure f_B (the decay constant of the B meson) in the decay $B^- \to \tau^- \overline{\nu}_\tau$, and the expected accuracy on the mixing parameter x_d which measures $|V_{td}|$.

4.1 $|V_{cb}|$ from Exclusive Semileptonic B Decays

The heavy quark effective theory simplifies calculations of heavy mesons.

Exclusive measurements of semileptonic decays of B mesons can be used to determine the CKM matrix elements $|V_{cb}|$ and $|V_{ub}|$ in decays to mesons containing a charm quark or only light quarks, respectively. Over the last years, considerable progress has been achieved in the understanding of these decays. The decay $\mathrm{B}^0 \to \mathrm{D}^{*-} l^+ \nu$ has been observed and analyzed in detail [3]. Following this experimental observation the heavy quark effective theory (HQET) was developed [44]: In the limit of infinitely large masses of the heavy quarks two additional symmetries arise, namely a flavor symmetry where all heavy quarks are treated in the same way, and a spin symmetry which predicts that the pseudoscalar meson made of a heavy quark and a light antiquark and the corresponding vector meson should degenerate. This symmetry allows to express all the hadronic form factors by one single universal function, the so called Isgur-Wise function $\xi(v \cdot v')$ where $v \cdot v'$ is the product of the four-velocities of the heavy particles involved in the decay, *e.g.* for the decay $\mathrm{B}^0 \to \mathrm{D}^{*-} l^+ \nu$:

$$y = v \cdot v' = \frac{m_{B^0}^2 + m_{D^{*-}}^2 - q^2}{2 m_{B^0} m_{D^{*-}}} \,. \tag{41}$$

HQET allows a model independent determination of $|V_{ub}|$ and $|V_{cb}|$.

The Isgur-Wise function is normalized at maximum momentum transfer $q^2_{max} = (m_{B^0} - m_{D^{*-}})^2$ to $\xi(1) = 1$.

The framework of HQET provides the basis for a model independent determination of the CKM matrix elements $|V_{ub}|$ and $|V_{cb}|$. It is exact in the infinite quark mass limit, and corrections can be studied systematically. For $b \to c$ transitions these corrections are of order $\mu^2/m_Q^2 \approx 5\%$ where μ is the characteristic momentum of quarks in the meson. Comparing the theoretical prediction for the differential decay rate $d\Gamma/dy$ of the decay $B^0 \to \mathrm{D}^{*-} l^+ \nu$ with data allows an essentially model independent extraction of $|V_{cb}|$ at $\xi(1) = 1$ and the determina-

tion of the functional form of the Isgur-Wise function $\xi(y)$. Once $\xi(y)$ is known, one can calculate any of the hadronic form factors and their q^2 dependences by means of consistency relations. This allows to compute other semileptonic decay rates, *e.g.* for semileptonic decays into transversely or longitudinally polarized D^* mesons or D mesons. Already with the existent data the theory works well and represents an improvement over various other models.

One can determine $|V_{cb}|$ to better than 1%.

At the B factory we will be able to reconstruct 60000 decays $B^0 \rightarrow D^{*-} l^+ \nu$ by use of the missing mass method [3]. A possible $v \cdot v'$ distribution is shown in fig. 13. From such a measurement we can determine $|V_{cb}|$ at $y = 1$ with an accuracy of better than 1% provided the branching ratios for charmed mesons are known precisely. Also the functional form of $\xi(y)$ can be determined. Similar results can be obtained for the decay $B^+ \rightarrow D^{*0} l^+ \nu$ [45].

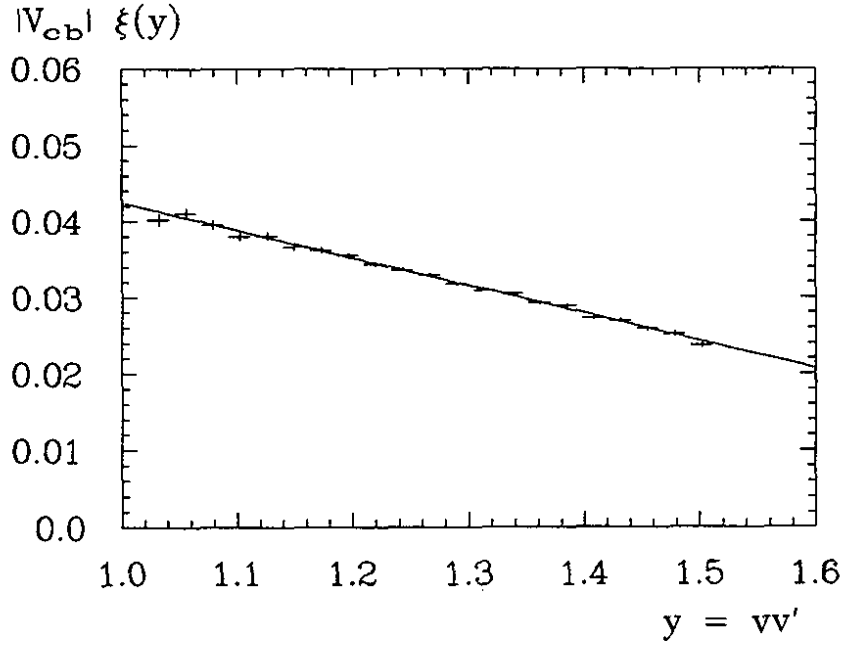

Figure 13: $|V_{cb}|\,\xi(y)$ distribution for 60000 reconstructed decays $B^0 \rightarrow D^{*-} l^+ \nu$.

4.2 The Semileptonic Decay $B^- \rightarrow \rho^0 l^- \overline{\nu}_l$ and $|V_{ub}|$

The HQET provides relations between the branching ratios for semileptonic B decays and the corresponding D decays. These relations can be used to determine the CKM matrix element $|V_{ub}|$ precisely. The relation is particularly

simple for decays of heavy 0^- mesons into light 0^- mesons like $B^0 \to \pi^- e^+ \nu$:

$$BR(B^0 \to \pi^- e^+ \nu) = \frac{\tau_{B^0}}{\tau_{D^0}} \frac{|V_{ub}|^2}{|V_{cd}|^2} \frac{m_{B^0}^5}{m_{D^0}^5} BR(D^0 \to \pi^+ e^- \nu)\,. \qquad (42)$$

Large branching ratios are expected for the decay $B \to \rho l^- \overline{\nu}_l$. The relationship between this decay and the corresponding one of D mesons is more complicated since in the heavy quark limit the longitudinal rate vanishes. Accurate data on these decays including differential distributions like lepton spectra, q^2 behaviour and polarization measurements which will be obtained e.g. for the decay $B^+ \to \rho^0 l^+ \nu$ will improve our understanding.

We have investigated the decay $B \to \rho l^- \overline{\nu}_l$, concentrating on the case where a charged B ends up in a neutral $\rho^0 (\to \pi^+ \pi^-)$. The branching ratio for this decay is predicted to be $BR(B \to \rho l^- \overline{\nu}_l) \approx 3$ to 10×10^{-4} for one specific lepton flavor [40,46,47,48] if one takes $|V_{ub}| = 0.005$ as indicated by recent ARGUS [7] and CLEO [8] measurements. A preliminary result from ARGUS [49] indicates a branching ratio $BR(B \to \rho l^- \overline{\nu}_l) \approx 1 \times 10^{-3}$.

Analysis of the missing mass distribution.

In order to analyze this decay, we searched for a signal in the distribution of the missing mass squared:

$$MM^2 = M_B^2 + M_{\rho l}^2 - 2(E_B E_{\rho l} - \vec{p}_B \vec{p}_{\rho l})\,. \qquad (43)$$

Here we approximate $\vec{p}_B \approx (0, 0, \beta\gamma M_B)$ exploiting the fact that the B meson is essentially at rest in the overall c.m. system and therefore acquires only longitudinal momentum because of the boost. In the case of the $B^- \to \rho^0 l^- \overline{\nu}_l$ decay one expects $MM^2 = m_\nu^2 = 0$.

We applied the following cuts: All $\pi^+\pi^-$ combinations in an event with an invariant mass within ± 150 MeV of the nominal ρ mass were taken. We cut rather sharply on the c.m. momenta of both the ρ candidate and the lepton, demanding for both particles the same minimal value of $p^* = 1.5$ GeV. The next two cuts take advantage of the fact that we can separate the B vertex from the rest of the event. The $\pi^+\pi^- l^-$ system must have a common origin with $\chi^2 < 9$ and none of the three tracks should be attachable to any other vertex in the event.

The resulting MM^2 distribution (fig. 14) shows a peak at $MM^2 = 0$ as expected and can be fitted by a Gaussian of width $\sigma = 0.57$ GeV^2. $\Upsilon(4S)$ decays show an enhancement around 1.9 GeV^2 while continuum events are uniformly distributed. Even with a branching ratio being ten times smaller, the decay can be measured and the form factors analyzed.

In order to extract the CKM matrix element $|V_{ub}|$ the measured branching ratio has to be converted into a decay width: $\mathrm{BR}(B^- \to \rho^0 l^- \overline{\nu}) = \Gamma(B^- \to \rho^0 l^- \overline{\nu}) \times \tau_{B^-}$. The lifetime τ_B of charged and neutral B mesons can be measured at the B factory with an accuracy of better than 1% by using the large number of tagged B mesons (see section 7.1).

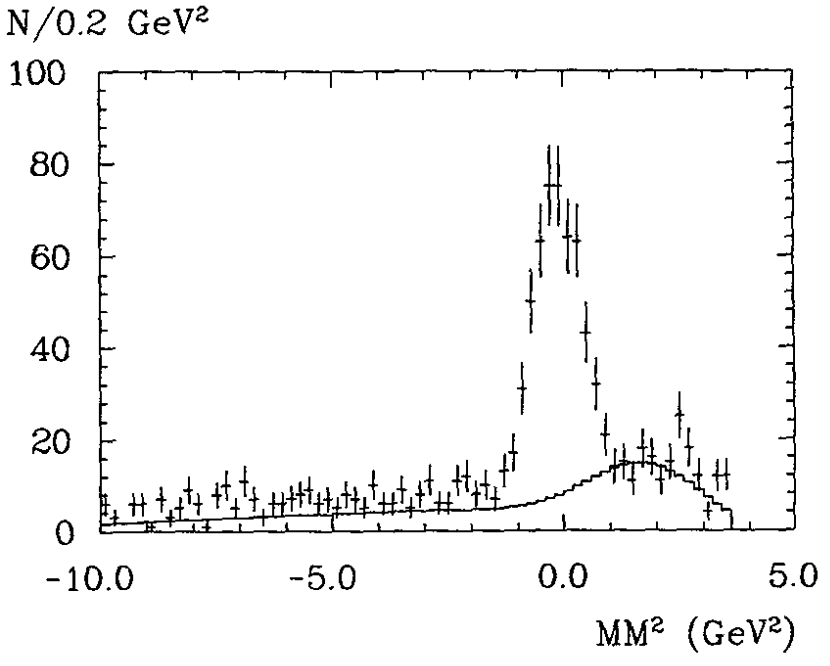

Figure 14: Missing mass squared of $\pi^+\pi^- l$ combinations, only one specific lepton flavor (data with error bars). The histogram shows the contribution from usual $\Upsilon(4S)$ decays. Inputs to this plot are $BR(B^- \to \rho^0 l^- \overline{\nu}_l) = 2 \times 10^{-4}$ and a data set of $50 fb^{-1}$.

Using HQET, $|V_{ub}|$ can be determined to better than 5%.

The accuracy in the determination of $|V_{ub}|$ is then limited by our understanding of semileptonic decays of heavy mesons into light ones. Here the HQET will allow us to determine $|V_{ub}|$ reliably and we conclude that the measurement of semileptonic B decays into light mesons will result in a value for $|V_{ub}|$ with an accuracy of better than 5%.

4.3 Search for the Decay $B^- \to \tau^- \overline{\nu}_\tau$ and f_B

The decay constant f_P of a pseudoscalar meson P is defined as the expectation value of the axial vector current between the vacuum and the meson state: $\langle 0|A_\mu(0)|P(\vec{q})\rangle = i\, f_P\, q_\mu$ where q is the momentum vector of P. For pions and kaons the decay constants are measured to be $f_\pi = 132$ MeV and $f_K = 161$ MeV. For the D mesons there exists an upper limit of $f_D < 310$ MeV. In the case of B decays one expects f_B in the order of 200 MeV from QCD sum rule calculations (see *e.g.* ref. [50]).

The cleanest way to measure f_B is to observe the decay $B^- \to \tau^- \overline{\nu}_\tau$. The decay constant is defined by the width of this decay mode:

$B^- \to \tau^- \overline{\nu}_\tau$ measures f_B and $|V_{ub}|$.

$$\Gamma(B^- \to \tau^- \overline{\nu}_\tau) = \frac{G_F^2}{8\pi} |V_{ub}|^2 f_B^2 m_B m_\tau^2 \left(1 - \frac{m_\tau^2}{m_B^2}\right) . \qquad (44)$$

G_F is the Fermi constant, $|V_{ub}|$ is the CKM matrix element for $b \to u$ transition, m_B and m_τ are the masses of the B and the τ, respectively. Insertion of the B lifetime and the other known quantities leads to the following branching ratio prediction:

$$BR(B^- \to \tau^- \overline{\nu}_\tau) = 9.6 \times 10^{-5} \left(\frac{f_B}{200\text{MeV}}\right)^2 \left(\frac{|V_{ub}/V_{cb}|}{0.1}\right)^2 . \qquad (45)$$

With $f_B = 200$ MeV and $|V_{ub}/V_{cb}| = 0.1$ one expects 4800 $B^- \to \tau^- \overline{\nu}_\tau$ decays in the data set of $50 fb^{-1}$.

From detailed studies of this decay channel we could not find a clean and efficient signature. We conclude that a measurement of f_B from this decay is difficult. A similar conclusion has been drawn in other studies [51,52].

4.4 $|V_{td}|$ from $B^0\overline{B}^0$ Oscillations

From the study of about 400000 $B^0\overline{B}^0$ pairs (the present statistics of ARGUS and CLEO), the mixing parameter x_d is measured to be $x_d = 0.67 \pm 0.11$. With a data sample of 50 fb^{-1} we will in principle be able to determine the CKM matrix element $|V_{td}|$ with an accuracy of better than 2%.

Given m_t and $f_B \cdot \sqrt{B_B}$, $|V_{td}|$ can be measured to a few percent accuracy.

The relation between x_d and $|V_{td}|$ contains the unknown top quark mass m_t and the B decay constant $f_B \cdot \sqrt{B_B}$ (see eq. 11). There is some hope that the top quark will have been discovered by the time a B factory starts running. As we have seen in the previous section, it is difficult to measure f_B. However, there exists some hope that QCD lattice computations could reliably predict this quantity [53]. If this turns out to be true, also $|V_{td}|$ could be measured with an accuracy of a few percent, depending mainly on the precision with which m_t and $f_B \cdot \sqrt{B_B}$ will be known.

4.5 Conclusions

The detection of semileptonic B decays will enable us to measure the CKM matrix elements $|V_{ub}|$ and $|V_{cb}|$ with high accuracy. Together with the corresponding precision measurements in the charm sector, this represents a stringent test on the unitarity of the CKM matrix. The precision in the CKM matrix element $|V_{td}|$ which will be measured through $B^0\overline{B}^0$ oscillations is not limited

by statistics but by the poor knowledge of the mass of the top quark and the B decay constant. The same holds for $|V_{ts}|$ which will be discussed in the next chapter. However, the ratio $|V_{td}|/|V_{ts}|$ does not suffer from unknown quantities. As discussed in chapter 7, this ratio can also be determined from measurements of electromagnetic penguin decays.

5 $B_s\overline{B}_s$ Mixing

A comparison between $B^0\ \overline{B}^0$ mixing and $B_s\overline{B}_s$ mixing allows to measure the ratio of the CKM matrix elements $|V_{ts}|$ and $|V_{td}|$. $B_s\overline{B}_s$ mixing can be observed at centre–of–mass energies above the $\Upsilon(4S)$. The precision of measuring the mixing parameter x_s depends on the integrated luminosity $\mathcal{L}$ of the available data set, on the achievable spatial resolution of the vertex detector, and on the asymmetry of the e^+e^- beams, *i.e.* on the boost value $\beta\gamma$. In the following we will discuss which values of x_s are measurable.

5.1 Definitions and Formalism

Experimental mixing ratio and mixing parameter.

Mixing in the $B^0\ \overline{B}^0$ system is measured by the ratio r:

$$r = \frac{P(B^0 \to \overline{B}^0)}{P(B^0 \to B^0)} \approx \frac{x^2}{2+x^2} \tag{46}$$

where the mixing parameter x is given in equation 11. The same formalism can be applied to $B_s\overline{B}_s$ mixing. For the the ratio x_s/x_d one obtains

$$\frac{x_s}{x_d} \approx \frac{|V_{ts}|^2}{|V_{td}|^2}\,. \tag{47}$$

Probable value of $x_s \approx 10$

In the $B^0\overline{B}^0$ system x_d has been measured by ARGUS and CLEO to be $x_d = 0.67 \pm 0.11$ [54]. The unitarity of the CKM matrix implies that x_s is in the range $3 < x_s < 25$ with a most probable value of x_s around 10.

Such high values of the mixing parameter can no longer be measured with the technique counting like-sign and unlike-sign lepton events because the ratio r is close to unity. In order to measure large values of x one has to determine the time evolution of the mixing.

Time evolution of mixing.

Starting from the time dependent state vectors of B and $\overline{B}$ one uses the Pais-Treiman formalism [55] to construct the states $|B(t_1)\overline{B}(t_2)\rangle$ and $|\overline{B}(t_1)B(t_2)\rangle$, where t_1 and t_2 denote the decay times. These states must be projected onto the specific final states. The rates are integrated over $t_1 + t_2$ and then depend only on the time difference $\Delta t = |t_2 - t_1|$ which can be measured. One finds for the rate of unmixed events

$$N(B^0\overline{B}^0 \to B^0\overline{B}^0) \sim$$

$$\frac{1}{2}\exp(-\frac{\Delta t}{\tau})\begin{cases} \frac{1}{1+x^2}\{2\cos^2(\frac{x}{2}\frac{\Delta t}{\tau}) + x^2 - x\sin(x\frac{\Delta t}{\tau})\}, & \mathrm{C} = +1\,, \\ 2\cos^2(\frac{x}{2}\frac{\Delta t}{\tau}) & \mathrm{C} = -1 \end{cases} \tag{48}$$

and for the rate of mixed events

$$N(B^0\overline{B}^0 \to B^0B^0) + N(B^0\overline{B}^0 \to \overline{B}^0\overline{B}^0) \sim$$
$$\frac{1}{2}\exp(-\frac{\Delta t}{\tau})\begin{cases} \frac{1}{1+x^2}\{2\sin^2(\frac{x}{2}\frac{\Delta t}{\tau}) + x^2 + x\sin(x\frac{\Delta t}{\tau})\}, & \mathrm{C} = +1\,, \\ 2\sin^2(\frac{x}{2}\frac{\Delta t}{\tau}), & \mathrm{C} = -1. \end{cases} \quad (49)$$

For $C = -1$ one simply gets exponentially damped trigonometric dependencies, whereas in the $C = +1$ case additional contributions appear and the oscillations are much less pronounced (see, *e.g.*, ref. [56]).

We have studied the $B_s\overline{B}_s$ mixing on the $\Upsilon(5S)$ where the $B_s\overline{B}_s$ mesons are produced in a mixture of different C parities.

5.2 Determination of x_s

The goal of this study was to find the maximum measurable value of x_s. A Lorentz boost with $\beta\gamma = 1.0$ was used to increase the flight distance of the B_s. This is an essential parameter for the achievable sensitivity of the x_s measurement.

Mixing is analyzed in semileptonic B_s decays.

The analysis of mixing uses events where both B_s mesons are tagged by the leptons of their semileptonical decay. For the leptons, we require a minimum momentum of $p^* > 1.4$ GeV/c. The intercepts of the lepton tracks with the z axis define the z coordinate of the respective B_s decay vertices. From Monte Carlo simulations, we find a resolution in the z distance of the two vertices of $\sigma(\Delta z) = 38$ μm for leptons in the range $30° < \theta < 150°$. This corresponds to a time resolution ($\sigma(\frac{\Delta t}{\tau}) = 0.1$) according to eq. 29. Table VIII shows the masses we used in the simulation.

Table VIII: Masses used in the $B_s\overline{B}_s$ mixing simulation.

particle	mass (GeV)
$\Upsilon(5S)$	10.860
B_s^*	5.427
B_s	5.377

Generation of time dependent mixing distributions.

For a cross section $\sigma(e^+e^- \to \Upsilon(5S)) = 0.27$ nb, we generated the theoretically predicted distributions for mixed and unmixed events following eqs. 48 and 49 for $C = -1$ and $C = +1$ with $x_d = 0.7$ and different values of x_s. The fractions of the various $\Upsilon(5S)$ decays were taken from a potential model of Byers and Hwang [57] and are listed in table IX. For the decay $B_s^* \to \gamma B_s$, a branching ratio of 100 % was assumed. The life time of the B_s was taken to be $\tau(B_s) = 1.13$ psec and its semileptonic branching ratio to be 12 %. The lepton detection efficiency is 20%. For a data set of 20 $fb^{-1}$and a mixing parameter $x_s = 15$ we

expect to observe a time difference distribution for same sign leptons as shown in fig. 15. The spectrum is fitted with a linear combination of the functions 48 and 49. The fit gives $x_s = 14.9 \pm 1.6$.

Table IX: Assumed decay rates of $\Upsilon(5S)$ to neutral B pairs.

decay	fraction	mixing	C parity
$B^{*0}\overline{B}^{*0}$	0.436	x_d	−1
$B_s^*\overline{B}_s^*$	0.292	x_s	−1
$B^0\overline{B}^{*0}$	0.179	x_d	+1
$B_s\overline{B}_s^*$	0.078	x_s	+1
$B^0\overline{B}^0$	0.013	x_d	−1
$B_s\overline{B}_s$	0.002	x_s	−1

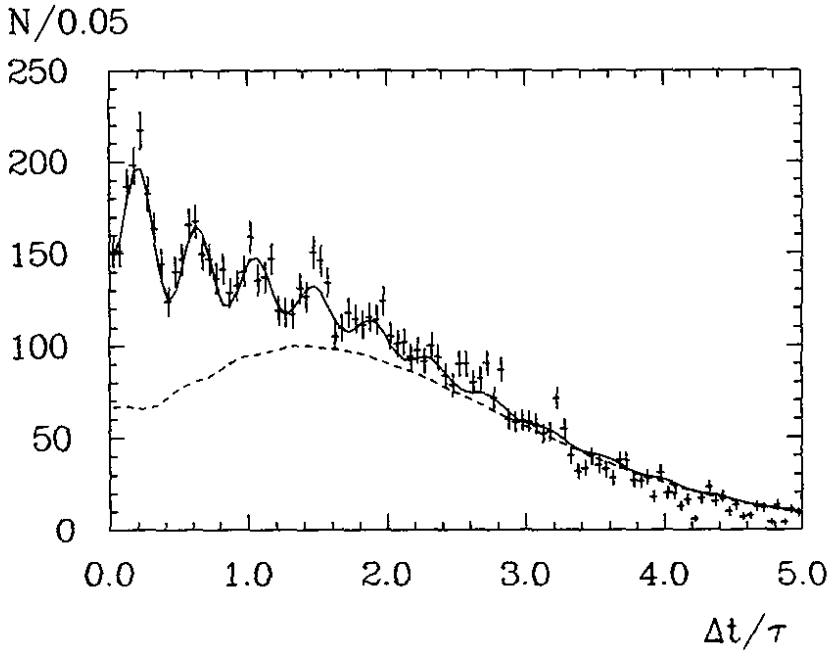

Figure 15: $\Delta t/\tau$ distribution of same sign leptons for $x_s = 15$ and a data set of $20 fb^{-1}$. The full line represents the fit result, whereas the dashed line is the background not coming from $B_s\overline{B}_s$ mixing.

In order to determine the sensitivity of the x_s measurement, data sets with different x_s, luminosities, and boost values were studied. The boost value determines the achievable resolution $\sigma(\Delta t/\tau)$. The maximum reachable value

x_s^{max} denotes the value where the statistics allows to exclude zero with three standard deviations. The results of this study are combined in fig. 16. With a luminosity of 20 fb^{-1}, a spatial resolution of 38 μm, and a boost of $\beta\gamma = 1$ a value x_s^{max} of 20 can be reached.

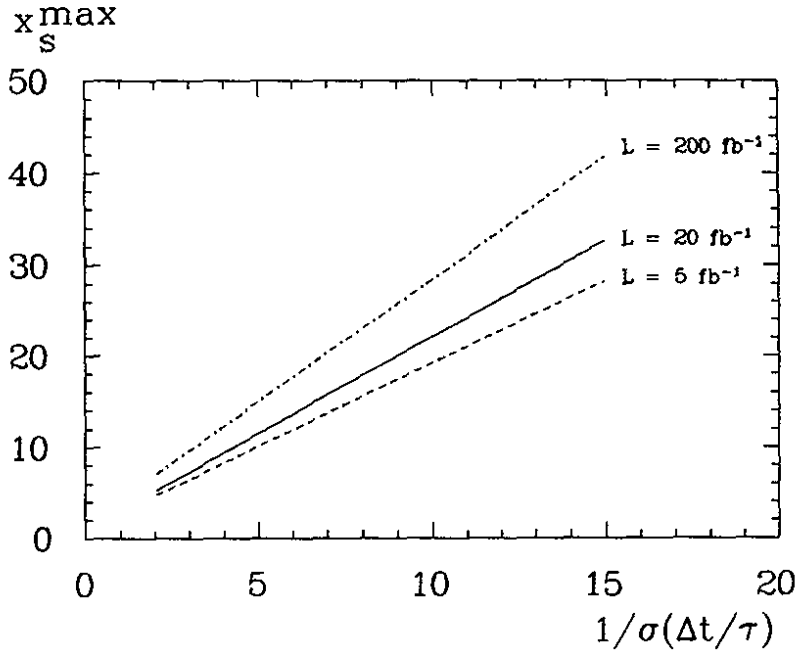

Figure 16: x_s^{max} as a function of $1/\sigma(\Delta t/\tau)$

In conclusion, large values of the mixing parameter x_s in the $B_s\overline{B}_s$ system can be measured. Essential for this measurement is a high boost and a good vertex resolution in order not to have unrealistic luminosity requirements.

6 Achievable Precision in the Unitarity Triangle

In this chapter all results on CKM matrix elements are summarized which a B factory will yield. The great potential to check the consistency of the Standard Model will be demonstrated. For this purpose, we shall discuss the unitarity triangle drawn in the (ρ, η) plane of Wolfenstein's parametrization and show how it will be constrained by the measurements described in the previous chapters. First, the implications of the non–CP violation measurements of $|V_{ub}|$, $|V_{cb}|$ and $|V_{td}|$ are discussed. Then we add the information on the angles β and α which can be extracted from the observation of CP violating effects. Combining these data will overconstrain the unitarity triangle. Inconsistencies lead to the necessity of extending or modifying the Standard Model. In case of consistency, a deeper understanding of the underlying structure will be obtained.

6.1 Non-CP Violation Measurements

The accuracies of the measurements of $|V_{ub}|$, $|V_{cb}|$, and $|V_{td}|$ described in chapter 4 are given in table X. As mentioned before, the value of $|V_{td}|$ depends on the presently unknown mass of the top quark and on the B decay constant.

Table X: Expected accuracies on CKM matrix elements achievable with a data set of $50 fb^{-1}$ and values assumed to constrain the unitarity triangle.

CKM matrix element	relative error (%)	assumed value
$\|V_{cb}\|$	1	0.04500 ± 0.00045
$\|V_{ub}\|$	5	0.00500 ± 0.00025
$\|V_{td}\|$	5	0.01200 ± 0.00060

The measurement of $|V_{cb}|$, $|V_{ub}|$ and $|V_{td}|$ at a B factory constrains the unitarity triangle tightly. This is demonstrated in fig. 17 where we used the values of the three CKM matrix elements as indicated in table X to arrive at the following constraints:

Tight constraints result from the measurement of CKM matrix elements.

$$0.105 < \frac{|V_{ub}|}{|V_{cb}|} = \lambda\sqrt{\rho^2 + \eta^2} < 0.117\,, \tag{50}$$

$$1.143 < \frac{|V_{td}|}{|V_{cd}V_{cb}^*|} \equiv |1 - \rho - i\eta| < 1.271\,. \tag{51}$$

Obviously, there is not much room left for the apex coordinates of the unitarity triangle to vary. Adding the information from CP violation measurements, *i.e.*

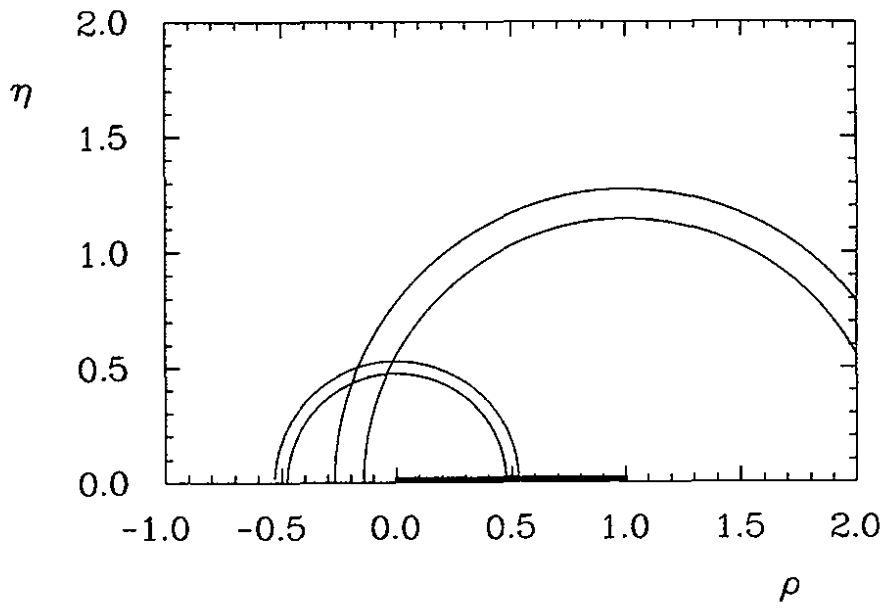

Figure 17: Constraints on the unitarity triangle from measurements of $|V_{cb}|$, $|V_{ub}|$ and $|V_{td}|$ at a B factory.

the values of the angles α and β, will then overconstrain the triangle. This is discussed in the following section.

6.2 Constraints from CP Violation Measurements

The potential of the CP violation measurements is demonstrated in figure 17 where the apex of the unitarity triangle is already tightly constrained without using CP violating measurements. If the Standard Model is correct, the assumed values of $|V_{ub}|$, $|V_{cb}|$, and $|V_{td}|$ given in table X correspond to angles $\alpha = 102°$ and $\beta = 24°$. These angles can be measured with a precision of $\sigma_\alpha = 2.2°$ and $\sigma_\beta = 2.4°$. The measurements are indicated in fig. 18. New physics would be indicated if the four independent measurements do not lead to a common apex.

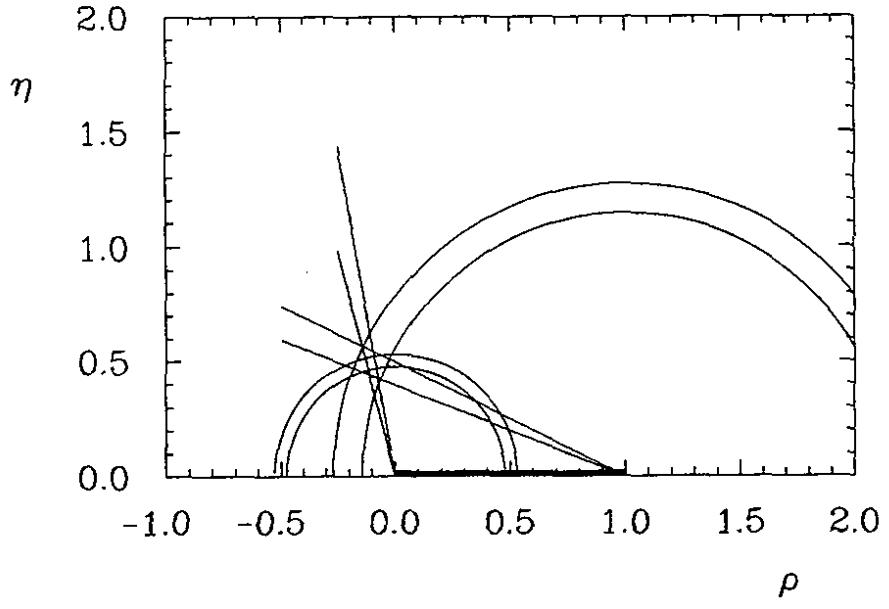

Figure 18: *Constraints on the unitarity triangle from $|V_{cb}|$, $|V_{ub}|$, and $|V_{td}|$ and the angles α and β. The values of the angles are measured via CP violation at a B factory.*

6.3 Implications on the Unitarity Triangle from the x_s Measurement

Up to now we have only used results that will emerge from data taken at the $\Upsilon(4S)$. In addition, the $B_s\overline{B}_s$ mixing parameter x_s can be measured in separate runs at centre-of-mass energies above the $\Upsilon(4S)$.

The theoretical expression for the ratio $x_d/x_s$is given by

$$\frac{x_d}{x_s} \simeq \frac{|V_{td}|^2}{|V_{ts}|^2} \simeq \lambda^2|1-\rho-i\eta|^2(1+\kappa) \qquad (52)$$

where $\kappa \sim -0.1$ takes into account QCD corrections.

A measurement of x_s yields another independent constraint.

The value of x_d will be measured with a data set of $50fb^{-1}$ on the $\Upsilon(4S)$ to much better than 0.5% relative accuracy so that the experimental error on the ratio in eq. 52 will be dominated by the error on x_s. If one assumes $x_d = 0.7$ and $x_s = 15.0 \pm 1.6$ one obtains another independent constraint on the apex of the unitarity triangle. It is concentric with the band originating from the measurement of x_d and is shown as the dashed lines in fig. 19. If $x_s < 15$ this band moves outwards and becomes more narrow, since the measurement will

become more precise. If $x_s > 15$ the radius of the band decreases and its width gets larger.

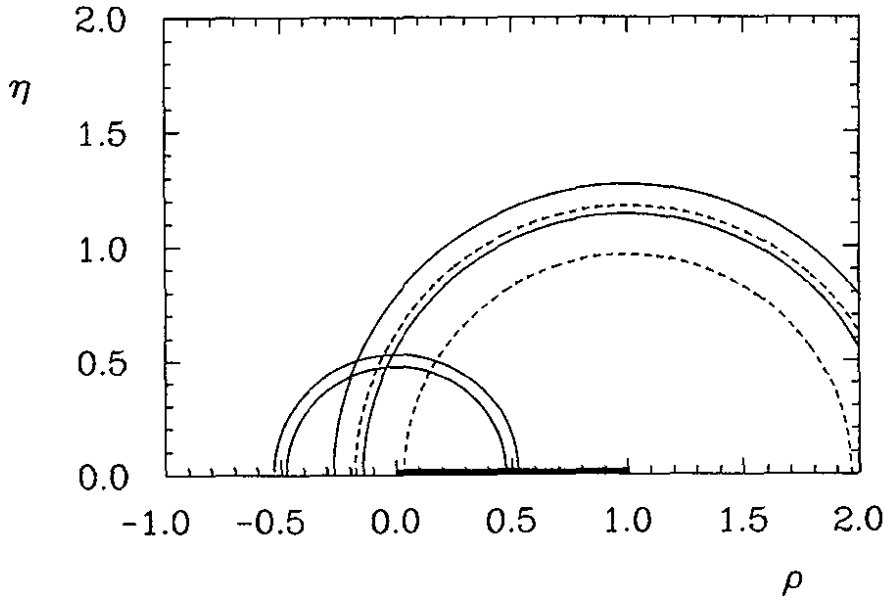

Figure 19: The additional constraint (dashed lines) on the apex of the unitarity triangle which will result from a measurement of $x_s = 15$.

7 Study of Other B Decays

The reconstruction of B mesons is important for many aspects:

- The existence of B mesons was ultimately demonstrated by their full reconstruction [58]. Also $b \to u$ transitions were unambiguously proven to exist only by reconstructing charmless B decays [59]. It is very likely that rare B decays induced by loop diagrams (see below) also will be discovered by reconstructing them completely.
- The reconstruction of B mesons allows to measure precisely their masses and to determine the branching ratios for specific decay channels which is necessary for other experiments and of importance for comparison with theoretical models.
- Another important aspect in reconstructing B mesons is for tagging which provides a unique way to study inclusive and exclusive decays of charged and neutral B mesons separately. Also the fraction of $\Upsilon(4S)$ decays into pairs of charged and neutral B mesons can be determined.

7.1 Reconstruction of Hadronic B Decays

So far, the ability to fully reconstruct B mesons was very limited. The highest reconstruction efficiency was achieved by ARGUS and amounts to less than 0.1%. This ability allowed to measure branching ratios for about 10% of hadronic B decays. Clearly, this situation has to be improved. The main reason for the poor ability to reconstruct B mesons lies in the fact that hadronic B decays involve high multiplicities ($n_{charged} \approx 6$) which causes big combinatorial problems. These problems can be overcome by using kinematical and/or vertex constraints. So far, nearly all reconstructed B decays have D^{*+} mesons in the final state and up to 3 pions. For kinematical reasons D^{*+} mesons can be reconstructed on low background.

The use of a vertex detector will improve the reconstruction efficiency of B mesons substantially.

With the use of vertex detectors one will be able to reconstruct as well B decays into D mesons by exploiting the vertex constraints for the D mesons. The ability to reconstruct B decays will be further enlarged by allowing the D or D^* mesons to be accompanied by more than three pions which originate at the B production vertex. By these arguments, the B reconstruction efficiency will improve by more than a factor of 3. For the envisaged integrated luminosity of 50 fb^{-1} we expect about 200000 fully reconstructed B mesons (together with a comparable amount of reconstructed semileptonic B decays).

One expects a high efficiency to reconstruct both B mesons.

Of particular interest are events where both B mesons are reconstructed. Once one B is reconstructed, one can use kinematical constraints to increase the reconstruction efficiency for the second B meson to about 3%. This would yield about 6000 events with two reconstructed B mesons from which, for example, the branching fraction $\Upsilon(4S) \rightarrow B\overline{B}$ can be determined with better than 2% accuracy:

Reconstruction of both B mesons will allow to measure branching ratios reliably.

$$BR(\Upsilon(4S) \rightarrow B\overline{B}) = \frac{1}{4}\frac{\eta_2}{\eta_1}\frac{N_B^2}{N_{B\overline{B}}}\frac{1}{N_{\Upsilon(4S)}}, \tag{53}$$

where η_1 is the reconstruction efficiency for one single B meson and η_2 that for the second one. The events with double tags can also serve for branching ratio measurements which do not depend on the production rate of charged and neutral B mesons.

Fully reconstructed B mesons allow the determination of τ^+ and τ^0 individually.

About 85 000 of the fully reconstructed B decays will be in clean channels on low combinatorial background which can serve for tagging purposes as well. These tagged B mesons will enable us to measure the individual lifetimes of charged (τ^+) and neutral (τ^0) B mesons with an error of less than 1%. With the same accuracy one will be able to determine the individual semileptonic branching ratios for charged (BR_{sl}^+) and neutral (BR_{sl}^0) B mesons. As for K and D mesons one should get:

$$R_{+0} = \frac{\tau^+}{\tau^0} = \frac{BR_{sl}^+}{BR_{sl}^0}.$$

Contributions of non-spectator diagrams can be measured.

In the B system one expects that the weak decays are dominated by decays through spectator diagrams (fig. 20) which implies R_{+0} close to unity. Deviations from $R_{+0} = 1$ will provide information on the importance of non-spectator diagrams in B decays.

The measured decay width of many hadronic channels can be compared to theoretical predictions. The decay rate for two-body B decays such as $B \rightarrow D\pi$ is predicted in the model of Bauer-Stech-Wirbel [26]. In this model one assumes that the decay amplitudes factorize into products of hadronic matrix elements. The two-body decays are then described by two amplitudes only (fig. 20) which are characterized by two parameters a_1 and a_2. The parameter a_1 is represented by the diagram (a) while the parameter a_2 is represented by the diagram (b). The first diagram is the dominant one while the second one is the so called "color-suppressed" diagram.

Hadronic B decay branching ratios will test the Bauer-Stech-Wirbel model.

A systematic study of many hadronic decays will serve for the determination of the parameters a_1 and a_2. To extract the parameters a_1 and a_2 one depends on the knowledge of the branching ratios of charmed mesons and furthermore on the knowledge of the CKM matrix element $|V_{cb}|$ (see chapter 4). However, relative rates can be compared more precisely with model predictions and prove the consistency of the model.

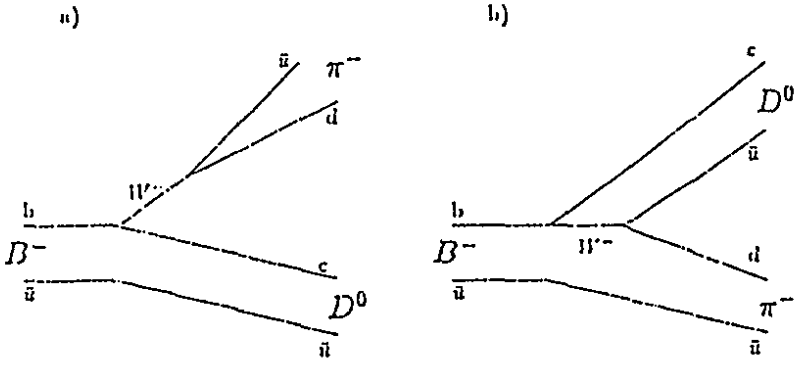

Figure 20: Diagrams contributing to the decays $B^- \to D^0\pi^-$.

7.2 B Decays Induced by Loop Diagrams

So far, B decays other than the ones via $b \to c$ or $b \to u$ tree level diagrams have not been observed. From the observed B decays one can conclude that more exotic B decays contribute only little to the total decay rate of B mesons.

The existence of penguin diagrams may explain some badly understood peculiarities of the Standard Model.

Whereas the tree level diagrams probe simply the classical theory without any quantum corrections, the study of loop-induced B decays allows to look for new physics. The observation of K meson decays proceeding via higher order weak and electromagnetic interactions were useful for the development of the Standard Model. The suppression of flavor changing neutral currents was observed by studying the $K^0 \to \mu^+\mu^-$ decay and explained by the GIM - mechanism. The $\Delta I = 1/2$ rule, an empirical expression of the observed ratio $\frac{\Gamma(K^+ \to \pi^+\pi^0)}{\Gamma(K^0 \to \pi^+\pi^-)} \approx 1/450$, is possibly explained by the introduction of the so called "penguin diagrams" (see fig. 21) involving the presence of strong interaction effects due to gluon exchange. The direct CP violation, resulting in a non-zero value of the parameter ϵ', perhaps could be also explained by these penguin decays. Contributions from penguin diagrams can, in principle, be calculated in the framework of the Standard Model. However, quantitative estimates in the case of the K mesons are not reliable, since strong interaction effects can only be computed in a perturbative framework which is not applicable in this case. Due to the small phase space available, there exist no decays of K mesons which can only occur through penguin type diagrams, and can thus provide a direct proof of their existence and significance.

B decays are especially well suited to study penguin diagram processes.

Decays of the penguin type are more easily studied with B mesons, for the following reasons:

- A larger number of rare B decays than K decays is possible since B mesons are more than ten times as heavy as K mesons.

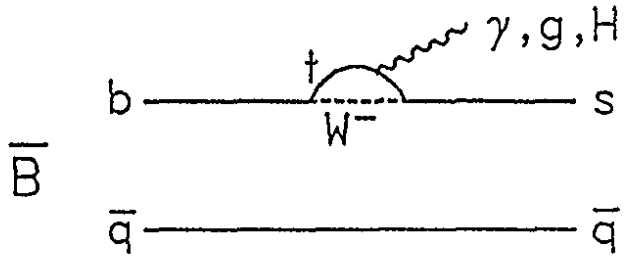

Figure 21: Penguin diagrams for B decays.

- If flavor changing neutral currents are absent, perturbative QCD analysis is expected to be applicable in the case of rare B decays. Thus, Standard Model predictions can be tested.
- Special exclusive B decays, such as the decay $B^0 \rightarrow \phi K^0$ (fig.22), are possible only through the penguin diagram.
- In B decays the penguin diagram involves the CKM matrix elements $|V_{ts}^* V_{tb}|$ which are much larger than their counterparts $|V_{td}^* V_{ts}|$ in the K system [60]. Comparing the relevant couplings one finds for the B system

$$|V_{ts}^* V_{tb}/V_{cb}|^2 \approx 1$$

whereas, for the K system, one obtains

$$|V_{td}^* V_{ts}/V_{us}|^2 \approx 10^{-5}.$$

Penguin-diagrams test for the existence of heavy quarks.

Since the exchanged quarks can couple to gluons, photons, or Higgs bosons, there exist three different types of penguin diagrams which can be studied experimentally. Moreover, the contribution from the heaviest quark dominates the loop amplitude and thus a measurement is potentially sensitive to the existence of a fourth family of quarks.

$|V_{ts}|$ is also measurable in penguin diagram decays.

In the Standard Model with three families the transition amplitudes depend on the mass of the t quark and on the coupling of the t quark to the s quark $|V_{ts}|$ which can be potentially determined.

7.2.1 The Transitions $b \rightarrow s\gamma$

Quark diagrams contributing to the process $b \rightarrow s\gamma$ are shown in fig. 23. The amplitude for this transition depends strongly on QCD corrections [61,62,63] which are expected to give a strong enhancement.

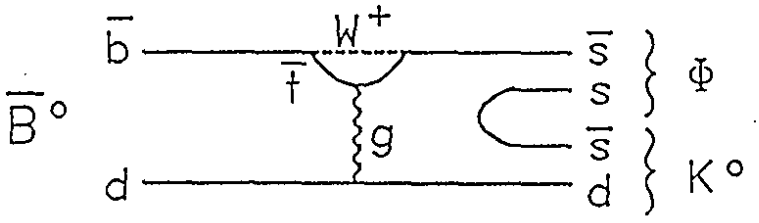

Figure 22: The decay $B^0 \to \phi K^0$.

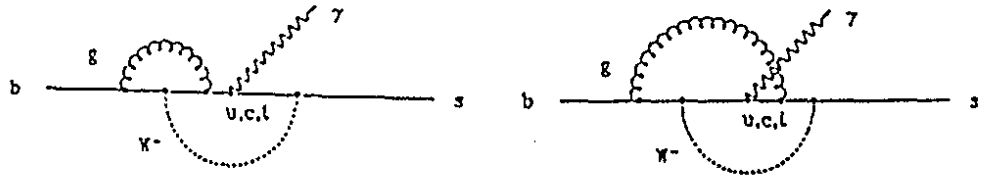

Figure 23: The transitions $b \to s\gamma$.

With three families and the minimal Standard Model with one Higgs doublet, the branching ratio for the process $b \to s\gamma$ can be parametrized by [64]

$$BR(b \to s\gamma) \approx 6 \cdot 10^{-4} \left(\frac{m_t}{135\mathrm{GeV}/c^2}\right)^{1.16} \cdot \frac{|V_{ts}|^2}{0.05^2} \qquad (54)$$

if we neglect $t \to d$ transitions.

The inclusive photon spectrum for this process is hard (fig. 24) [65] and can possibly be measured provided that the continuum contribution is suppressed efficiently.

Measure the γ *spectrum from* $b \to s\gamma$.

More favorable, the process can be detected through the observation of the exclusive decay $B \to K^*(890)\gamma$ which has not been measured so far. The actual probability of this final state to occur as the result of the quark level process, however, is not understood since hadronic calculations cannot be performed reliably. With an estimate of the fraction for the exclusive channel $B \to K^*(890)\gamma$ of about 5% of the $b \to s\gamma$ rate one should be able to detect about 600 of these decays with a reconstruction efficiency of 40%.

$B \to K^*(890)\gamma$ *should be seen.*

The exclusive decay $B \to \rho\gamma$ is suppressed with respect to the decay $B \to K^*(890)\gamma$ in good approximation by a factor $|V_{td}|^2/|V_{ts}|^2$:

$$\frac{BR(B \to \rho\gamma)}{BR(B \to K^*(890)\gamma)} \approx \frac{|V_{td}|^2}{|V_{ts}|^2} \,. \qquad (55)$$

Monte Carlo simulations show that both decays can be disentangled by using the excellent particle identification and energy resolution for charged and neutral

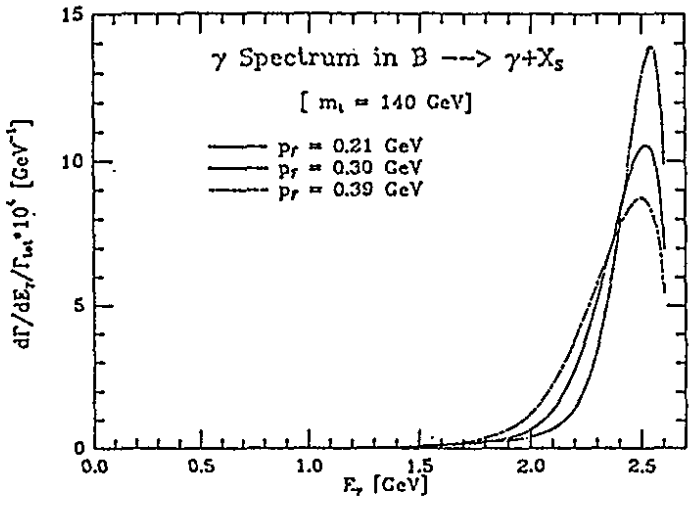

Figure 24: Photon spectrum in $b \to s\gamma$ [65].

particles. The ratio $|V_{td}|^2/|V_{ts}|^2 = 0.1$ could be measured with an accuracy of about 10% with 80 reconstructed $B \to \rho\gamma$. Since

$$\frac{x_d}{x_s} \approx \frac{|V_{td}|^2}{|V_{ts}|^2} , \tag{56}$$

The measurement of $B \to \rho\gamma$ and $B \to K^*\gamma$ allows to determine x_s.

such a measurement is complementary to the determination of x_s from the measurement of $B_s\overline{B}_s$ oscillations (see chapter 5). It should be sensitive up to $|V_{td}|^2/|V_{ts}|^2 = 0.03$ corresponding to $x_s \approx 20$ if the branching ratio for the decay $B \to K^*(890)\gamma$ is in the expected range.

7.2.2 The Transitions $b \to s + l^+l^-$

The process $b \to s + l^+l^-$ can proceed through several amplitudes (fig. 25). The inclusive branching ratio is predicted to be of the order of 10^{-5} (fig. 26). For exclusive decays like $B \to K^{(*)}e^+e^-$ the expected branching ratio is about 1/10 of the inclusive one. Thus, several tens of such inclusive decays can be reconstructed.

7.2.3 The Transitions $b \to s$ + *gluon*

$b \to s$ gluon has a large branching ratio and is sensitive to a fourth generation of quarks.

The largest rate for inclusive penguin type decays is predicted for the transitions $b \to s$ *gluon* (fig. 21) to be

$$BR(b \to s\,gluon) \approx 1 - 2\%$$

in the Standard Model with three families [66,25,67]. The dependence on the mass of the top quark is illustrated in fig. 27. The existence of a fourth family could enhance this rate by an order of magnitude. The calculation of the inclusive rate is affected by QCD corrections. Unfortunately, it is only possible to detect exclusive decays like the decay $B^0 \to \phi K^0$ where the uncertainty is

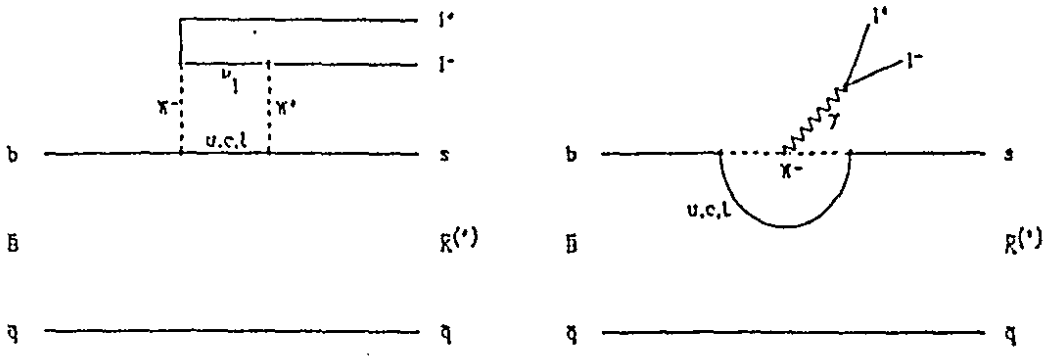

Figure 25: Loop diagram contributing to $b \to s l^+ l^-$.

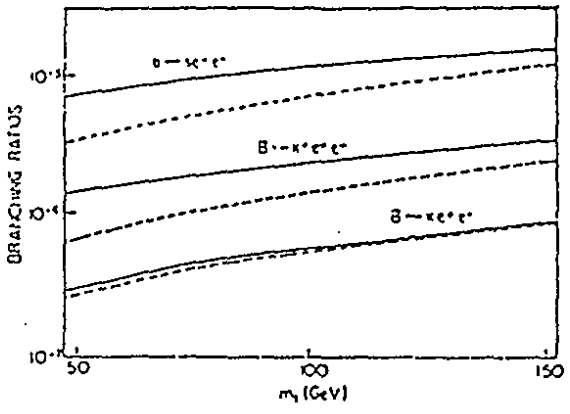

Figure 26: Branching ratio for $b \to s l^+ l^-$.

even larger. As in the case of the usual B decays, high multiplicities dominate the decay $b \to s\,gluon$ (fig. 28) [68]. The largest branching ratio is expected for a decay $B \to K + 5\pi$ which can possibly be discriminated from $b \to c$ decays by rejecting candidates with subsystems of the $Kn\pi$ system close to the D mass or with reconstructed decay vertices which do not coincide with the B decay vertex.

7.2.4 Flavor-changing Neutral Currents in B Decays

Flavor-changing neutral currents in B decays can be detected by observing the decays $B^0 \to \mu^+\mu^-$ or $B^0 \to e^+e^-$. The decay rates can be calculated by evaluating the box diagram (fig. 29) and are expected to be very small. For the decay $B^0 \to \mu^+\mu^-$ one obtains a branching ratio of 10^{-8} which is still too small to be observable with the envisaged sample of B mesons. However, the discovery of such decays would be of tremendous importance since rates much larger than expected would be a hint of new physics at higher energies. The

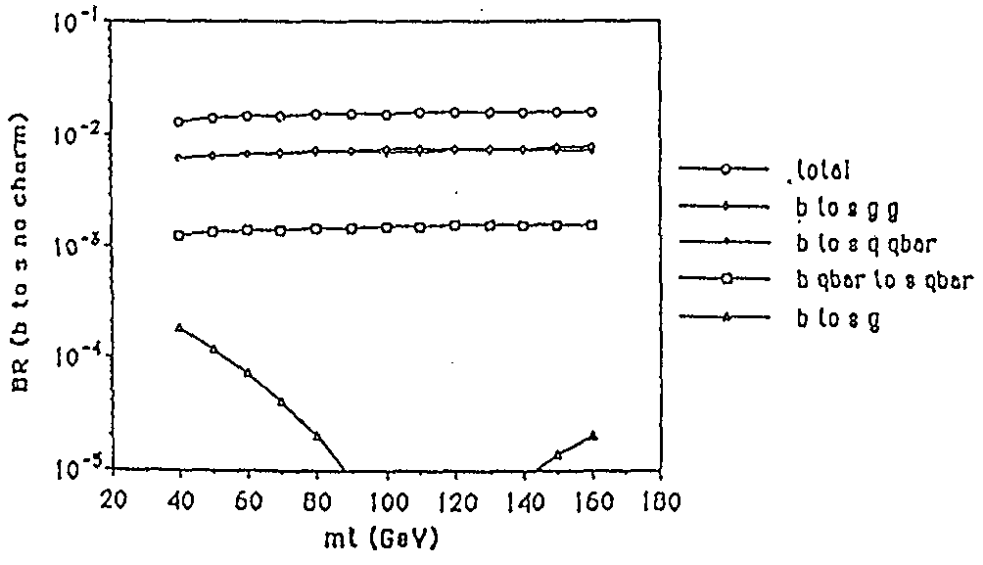

Figure 27: Theoretical prediction for $b \to s$ *gluon* [66].

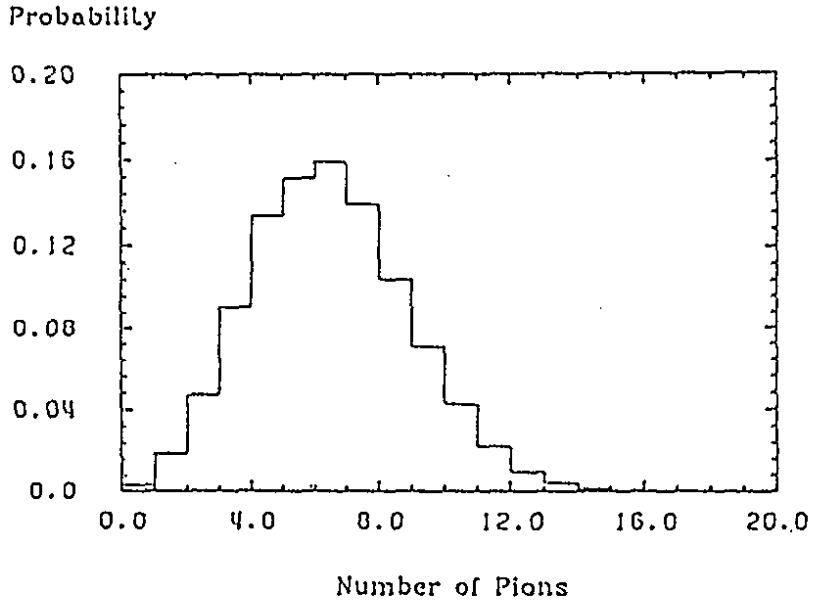

Figure 28: Probability of n-pion final states in B meson decays via $b \to s$ *gluon*.

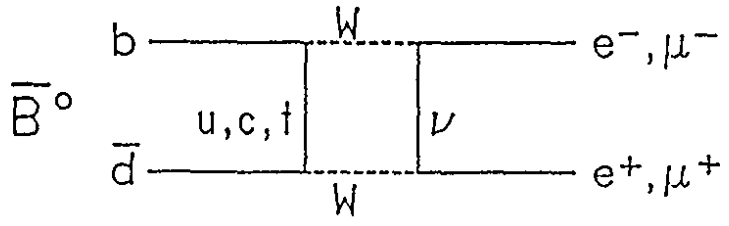

Figure 29: Box diagram for $\Delta B = 1$ transitions.

observation of a decay $B^0 \to \mu^+ e^-$ which is not allowed in the Standard Model would even be the manifestation of a new interaction.

8 Υ–Physics

8.1 General Remarks

$b\bar{b}$-states are the heaviest quarkonium states accessible to experiment

Bound states of heavy quark-antiquark pairs provide an interesting testing ground for many aspects of perturbative and nonperturbative quantum chromodynamics (QCD). The new limits on the top mass [69] and the corresponding large decay width of the toponium [70] exclude the possibility that its rich level structure can be studied experimentally in detail. Therefore, for the time being, bottonium will stay the heaviest quarkonium system to be analyzed. Its spectroscopy is easiest to be interpreted since both higher order perturbative corrections and relativistic effects are less important than for lighter quarkonium systems. Its level structure (Fig. 30) has only partially been verified by experiments. We will show in the following that many of these open physics items can only be clarified with a data volume not achievable at one of the presently available storage rings. On the other hand, running the B-factory a few months at the energy of the 3^3S_1 $|b\bar{b}>$-state – which does not disturb the main physics program at the B-factory – allows to collect $\pi \cdot 10^7$ (3^3S_1)-decays. This data set is large enough to solve many of the presently open problems as follows from branching ratios based on theoretically well founded estimations.

Physics topics

A shopping list of interesting physics topics includes:

- The detection of the $^1S_0$- and $^1P_1$-state which allows a detailed investigation of the properties of the spin-spin interaction of the quarkonium Hamiltonian [71]. While the strength of the spin-spin interaction is reflected in the hyperfine splitting of the $^1S_0$- and $^3S_1$-states, a long range component of the spin-spin force would produce a deviation of the mass of the $^1P_1$ -state from the center of gravity of the ^3P_J-states.

- The observation of the 1^3D_J-states provides a sensitive test of the long range structure of the spin-orbit interaction. While for the ^3P_J-states the short range contribution dominates, for the ^3D_J-states the long and short range contribution are of equal importance [72].

- The investigation of the final hadronic states allows interesting tests of QCD. The measurement of the ratio of branching ratios $Br(\Upsilon(1S) \rightarrow \gamma\, 2\, g)\ /\ Br(\Upsilon(1S) \rightarrow 3\, g)$ has provided one of the most reliable values of α_s [101]. Similarly the measurement of the ratio

$$Br(1^3P_0 \rightarrow 2\, g)\ /\ Br(1^3P_2 \rightarrow 2\, g)\ =\ \frac{15}{4}(1 + 3\,\alpha_s)$$

  might also permit to measure α_s.

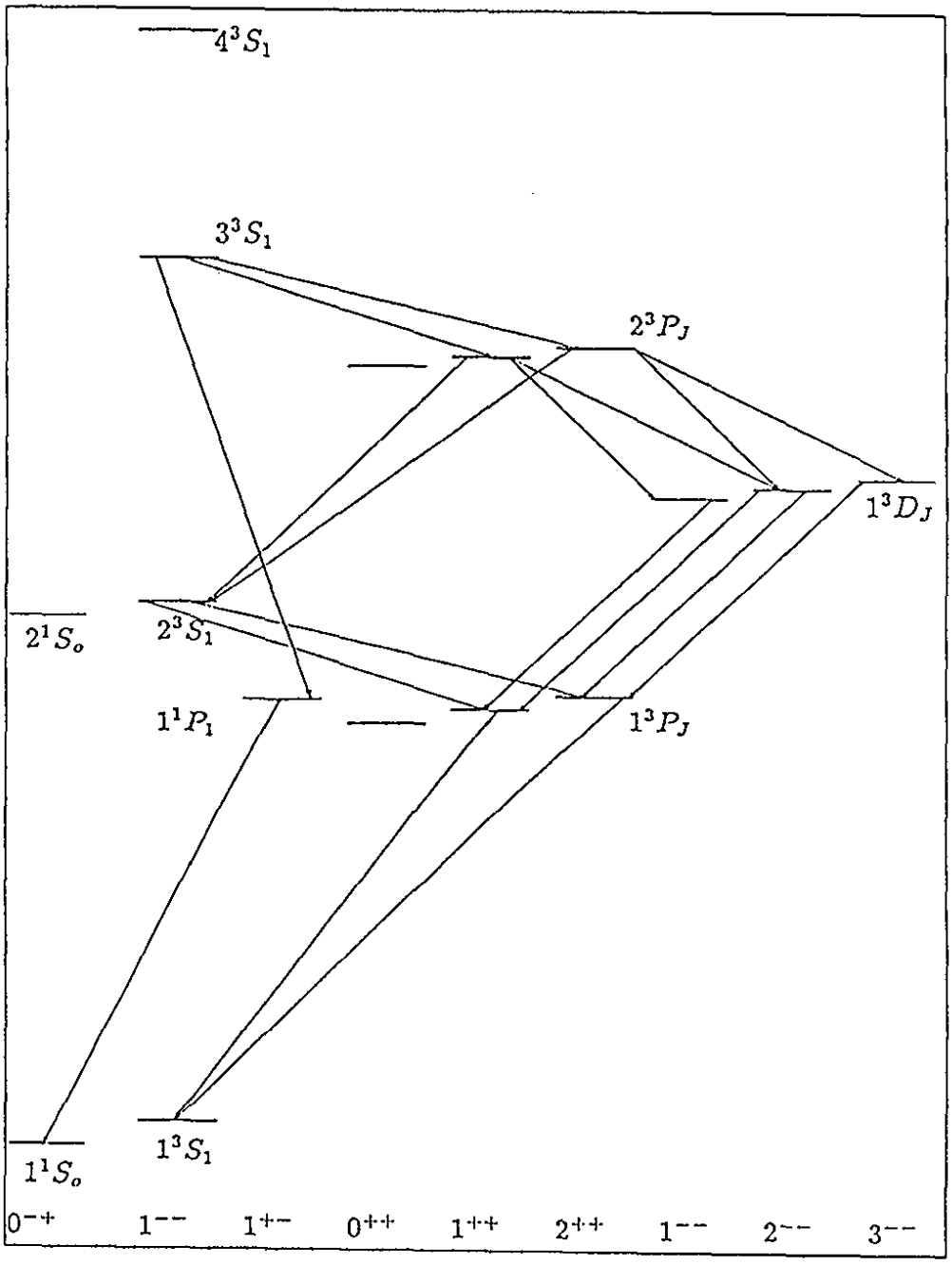

Figure 30: Level scheme of the bottomium system

- Naturally the higher statistics available in such an experiment allows to study with higher prescision states already observed in present experiments. Note that only in one of the 4 first generation experiments the splitting of the 1^3P_J- states was measured precisely enough to fix the Lorentz-structure of the interaction [74].

- Finally the relative long lifetime of the $|b\bar{b}>$ - states combined with their large mass make them an interesting laboratory to search for new particles. Examples are the standard Higgs, the axion, and the search for supersymmetric particles performed up to now [75]. For sure, once a B-factory starts data taking, new theoretical speculations will be around to be confronted with data.

8.2 Hyperfine Splitting

Spin-spin force

One of the basic open questions in quarkonium spectroscopy concerns the nature of the spin-spin force which is assumed to be of short range. Moreover, the hyperfine splitting is expected to be of the order of 30 MeV to 50 MeV [71]. Assuming flavor independence of the interaction one can calculate the branching ratio for the $1^3S_1 \rightarrow 1^1S_0$ M1-transition with the help of the corresponding result for the J/ψ-system to be

$$Br(1^3S_1 \rightarrow 1^1S_0 + \gamma) \approx 1.5 \cdot 10^{-5} \left(\frac{E\gamma}{40\,MeV}\right)^3 .$$

This small branching ratio, combined with the high background from π^0-decays in the energy interval of interest, makes it hopeless to observe the decay in an inclusive study.

Observation of the 1^1S_0-state in a cascade decay

Kuang et al. [76] have proposed to exploit the cascade decay

$$3^3S_1 \rightarrow \pi^+\pi^-\ 1^1P_1 \hookrightarrow \gamma\ 1^1S_0$$

to detect the scalar states. A reliable estimate of the branching ratio for the second decay exists, $Br(1^1P_1 \rightarrow \gamma\ 1^1S_0) \approx 0.5$, while the theoretical predictions for the hadronic decay $3^3S_1 \rightarrow \pi^+\pi^-\ 1^1P_1$ are contradictory. Kuang et al. [76] start from a multipole expansion of the gluon field of the decay which they assume to convert with probability 1 into a $\pi\pi$-system. They predict a branching ratio of 10^{-2} for this decay. A more sophisticated treatment of this conversion using QCD low energy theorems [77,78] arrives at $Br(3^3S_1 \rightarrow \pi^+\pi^-\ 1^1P_1) \simeq 10^{-4}$.

A Monte Carlo simulation has been performed to study the suppression of background from $q\bar{q}$ and gg events exploiting the good resolution of the proposed

detector for charged and neutral particles. A cut on the recoil mass and the energy of the photon allows to reduce the background by a factor of ~ 200. Combining this result with the recent measurement of the inclusive $\gamma-$ spectrum for $\Upsilon(3S)$ decays [79] shows that for a sample of 10^7 (3^3S_1) decays the (1^1S_0) state should be detectable, if the product branching ratio is $\geq 3 \cdot 10^{-4}$.

8.3 D-States

Observation of ^3D_J-states

The strength of the long range spin forces influences strongly the splitting of the ^3D_J-states, therefore, it has been proposed as an independent test of present ideas of scalar confinement [72]. Two strategies have been advocated to study the splitting. Kuang et al. [76] propose to search for the cascade decay

$$3^3S_1 \rightarrow \gamma\ 2^3P_J \hookrightarrow \gamma\ 1^3D_J \hookrightarrow \pi^+\pi^-\ 1^3S_1$$

with an estimated product branching ratio of $3 \cdot 10^{-4}$. Again the main uncertainty is due to the hadronic decay in this chain, which according to a study of Moxhay [77] is strongly suppressed. He predicts a product branching ratio of $< 10^{-6}$. Clearly in the latter case the chance to observe the decay chain even at a B-factory is small.

On the other side the estimations of the branching ratio for the cascade decay

$$3^3S_1 \rightarrow \gamma\ 2^3P_J \hookrightarrow \gamma\ 1^3D_J \hookrightarrow \gamma\ 1^3P_J \hookrightarrow \gamma\ 1^3S_1$$

are reliable, since the branching ratios are either measured or can be calculated reliably [80]. The product branching ratio amounts to $O(3 \cdot 10^{-4})$. In this case even the exclusive decay chain involving the decay $1^3S_1 \rightarrow e^+e^-, \mu^+\mu^-$ should provide $O(100)$ events. With the electromagnetic calorimeter described in this proposal the different components of the decay $2^3P_J \rightarrow 1^3D_J$ can be disentangled (Fig. 31). This is demonstrated in Fig. 32, where the different cascade decays are tagged by the photon from the $3^3S_1 \rightarrow 2^3P_2$ and $3^3S_1 \rightarrow 2^3P_1$ transition, respectively. Note, however, that there exist competing decay channels which might simulate the cascade decay:

$$3^3S_1 \rightarrow \pi^0 \hookrightarrow \gamma\gamma \quad \pi^0 \hookrightarrow \gamma\gamma \quad 1^3S_1$$

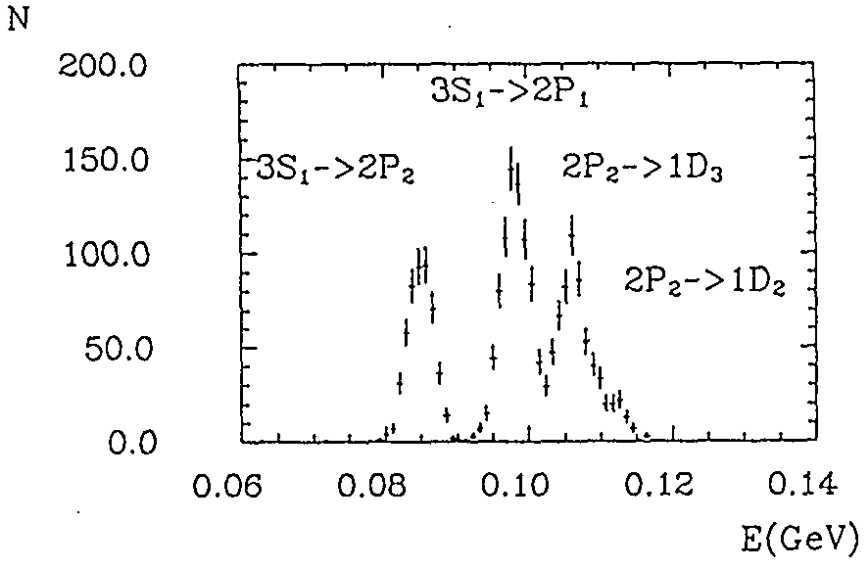

Figure 31: Low energy spectrum for the decay chain $3^3S_1 \rightarrow 2^3P_J \rightarrow 1^3D_{J'}$. The expected energy and angular resolution of the electromagnetic calorimeter described in chapter III.7.7 has been taken into account.

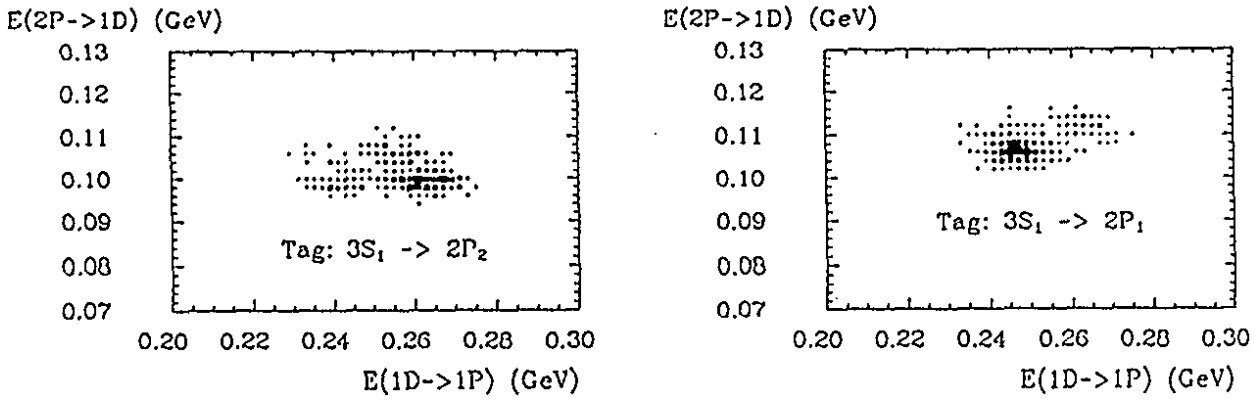

Figure 32: Observed photon lines for the decay $2^3P_J \rightarrow 1^3D_J \rightarrow 1^3P_J$ tagged with a) the $3^3S_1 \rightarrow 2^3P_2$ and b) the $3^3S_1 \rightarrow 2^3P_1$ transition.

A Monte Carlo simulation shows that with the resolution of the proposed electromagnetic calorimeter this decay can be separated. This is not as easy for background due to the decay cascade (Fig. 33)

$$
\begin{aligned}
3^3S_1 &\rightarrow 2^3P_J + \gamma \\
&\quad \hookrightarrow 2^3S_1 + \gamma \\
&\quad\quad \hookrightarrow 1^3P_J + \gamma \\
&\quad\quad\quad \hookrightarrow 1^3S_1 + \gamma
\end{aligned}
$$

The product branching ratios are comparable to those of the channels investigated, moreover, the transition energies of the channels of interest differ only slightly (Table XI). The $2^3P_2 \rightarrow 1^3D_3 + \gamma \rightarrow 1^3P_2 + 2\gamma$ and the

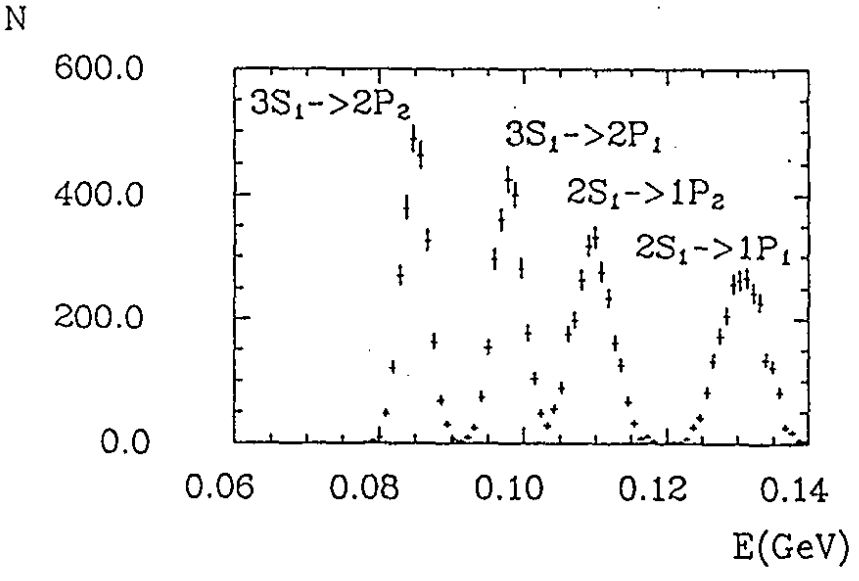

Figure 33: Low energy photon spectrum for the decay chain $3^3S_1 \rightarrow 2^3P_J \rightarrow 2^3S_1$

$2^3P_2 \rightarrow 2^3S_1 + \gamma \rightarrow 1^3P_2 + 2\gamma$ decays cannot be separated, if the 1^3D_3-mass has the predicted value [80]. This follows from Table XI and a comparison of Fig. 34, where the cascade gammas for the decays $2^3P_2 \rightarrow 2^3S_1 \rightarrow 1^3P_J$ are plotted, with Fig. 31.

In summary the excellent energy and angular resolution of the electromagnetic calorimeter combined with the large statistics achievable allows to resolve the (1^3D_1) and (1^3D_2) states of bottomium.

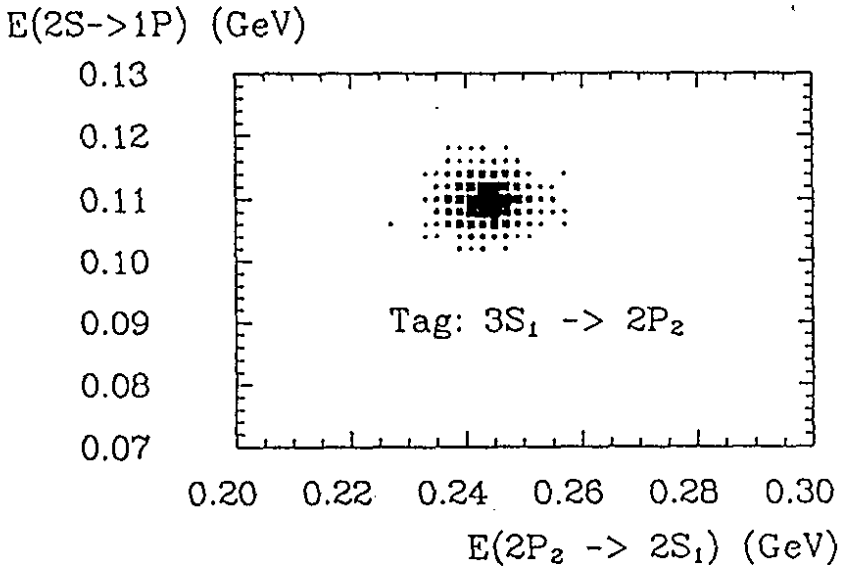

Figure 34: Observed photon lines for the cascade decay $2^3P_J \to 2^3S_1 \to 1^3P_J$ tagged with the transition $3^3S_1 \to 2^3P_2$

Table XI: Cascade decays with the largest branching ratios via the 1^3D_J-states, the competing decays via the 2^3S_1-state are also given.

Cascade via 1^3D_J-state	Competing cascade via 2^3S_1-state	resolved
$2^3P_1 \overset{99}{\to} 1^3D_2 \overset{261}{\to} 1^3P_1$	$2^3P_1 \overset{229}{\to} 2^3S_1 \overset{131}{\to} 1^3P_1$	+
$2^3P_1 \overset{99}{\to} 1^3D_2 \overset{240}{\to} 1^3P_2$	$2^3P_1 \overset{229}{\to} 2^3S_1 \overset{110}{\to} 1^3P_2$	+
$2^3P_1 \overset{106}{\to} 1^3D_1 \overset{254}{\to} 1^3P_1$	$2^3P_1 \overset{229}{\to} 2^3S_1 \overset{131}{\to} 1^3P_1$	+
$2^3P_2 \overset{107}{\to} 1^3D_3 \overset{245}{\to} 1^3P_2$	$2^3P_2 \overset{243}{\to} 2^3S_1 \overset{110}{\to} 1^3P_2$	-
$2^3P_2 \overset{112}{\to} 1^3D_2 \overset{261}{\to} 1^3P_1$	$2^3P_2 \overset{243}{\to} 2^3S_1 \overset{131}{\to} 1^3P_1$	+

8.4 Hadronic Decays

Test of perturbative QCD

A test of perturbative QCD predictions follows from the study of gluons produced in the decays $1^3S_1 \to 3g, \gamma\, 2g, 1^3P_0 \to 2g, 1^3P_2 \to 2g$. The ratio

$$\Gamma(1^3S_1 \to \gamma 2g)/\Gamma(1^3S_1 \to 3g) = \frac{4}{5}\frac{\alpha}{\alpha_s}(1 + 0.7\ \alpha_s); \quad (\overline{MS}\text{ scheme})$$

allows to derive α_s with a mild theoretical model dependence. The main uncertainty is due to the extrapolation of the measured γ-spectrum to low energies which depends sensitively on the spectrum shape, which at present has not been measured precisely enough (Fig. 35). The high granularity and good en-

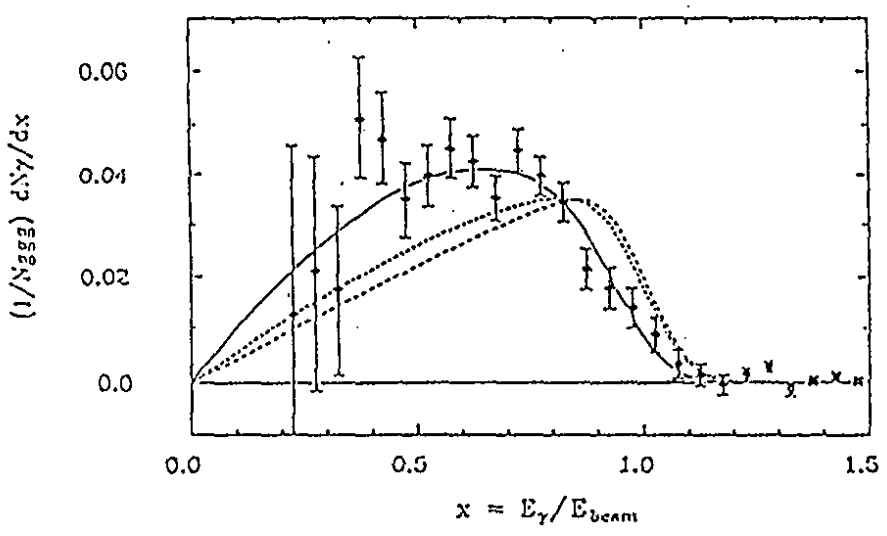

Figure 35: Measured photon spectrum for the decay $\Upsilon \rightarrow \gamma\ 2g$ [101].

ergy resolution of the proposed electromagnetic calorimeter allows to improve the measurement. Besides the study of inclusive radiative decays also the study of exclusive channels in the decay $\Upsilon(1S) \rightarrow \gamma\ 2g$ is of interest, since definite predictions for the branching ratios exist [72]. An improvement of the present limits by a factor of 10, which easily can be achieved at the B-factory with one month running, allows to verify or disprove these calculations.

Also the measurement of the ratio

$$Br(1^3P_2 \rightarrow 2\,g)\ /\ Br(1^3P_0 \rightarrow 2\,g)\ =\ \frac{15}{4}(1+3\,\alpha_s)$$

allows to determine α_s [71]. The good energy resolution of the electromagnetic calorimeter again is essential to achieve the necessary precision.

Fragmentation of gluons

Note that an enhanced sample of monochromatic 2 gluon jets with $E(2g) \approx 10\,\mathrm{GeV}$ can be selected from the data. ARGUS has shown [74] that a signal/background ratio of 1 : 2 can be achieved, if one tags the $^3P_{0,2}$-states with the photons of the transition $2^3S_1 \rightarrow \gamma\, 1^3P_{0,2}$ by detecting the photons which convert [81] (see Fig. 36). These data will allow to study the fragmentation of kinematically well defined gluons in an energy regime where jet structure already exists.

Search for fundamental scalars

Finally, it has already been mentioned (see 8.1) that radiative decays of the $\Upsilon(1S)$ meson open the window for searches of fundamental scalars [71,75]. The necessary experimental requirements have been discussed in detail in ref. [43].

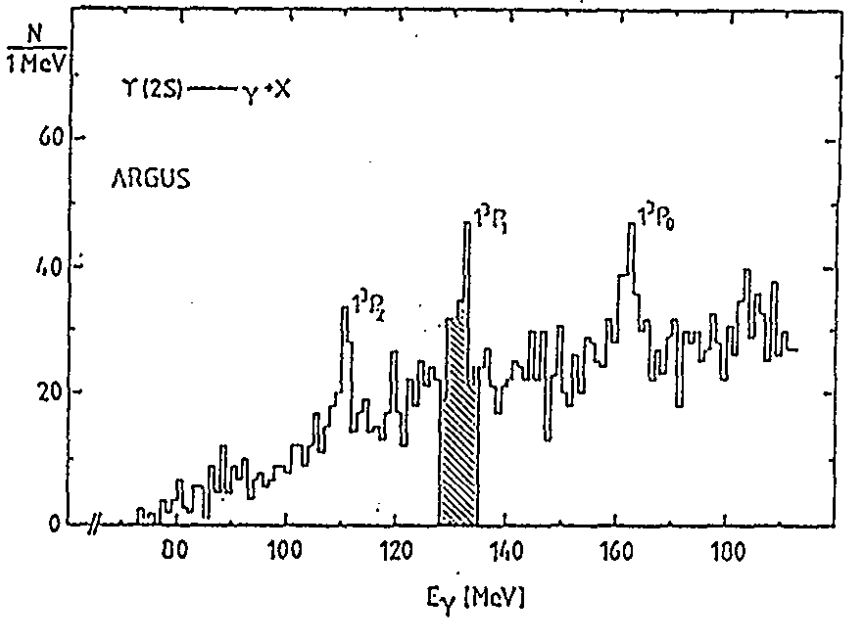

Figure 36: Photon spectrum for the decay $2^3S_1 \rightarrow 1^3P_J$ measured with a pair spectrometer.

9 Beauty Baryons

Spectroscopy of hadrons containing b quarks

The physics scope of the beauty factory may be extended by raising the center-of-mass energy above the $\Upsilon(4S)$ regime in order to successively pass the production thresholds of more and more heavy beauty hadrons. In this way it will be possible to tackle a wealth of spectroscopical investigations with growing physical richness. As an example for possible investigations we shall discuss production, masses and decays of beauty baryons which offers the possibility to study long range QCD in an essentially new context most similiar to atomic physics. We will consider here only baryonic states with one beauty quark and two light quarks u, d, and s, so that the heavy quark resembles the atomic nucleus. This leads - in the spirit of the HQET (see page 51) - to additional symmetries concerning flavour and spin of the heavy quark.

9.1 Production of Beauty Baryons

Let us develop two successively more interesting scenarios, taking into account the fact that they are also of successively decreasing probability to be realized.

Beauty baryon production well above thresholds

The first possibility is the production of beauty baryons at energies well above the respective thresholds. The process here consists of the fragmentation of a b-quark into a (leading) b-baryon by picking up a diquark from the sea. A measurement of the rates will check fragmentation models which predict a suppression of b-baryon production by about one order of magnitude with respect to b-meson production.

Pair production of beauty baryons

The second and more rewarding possibility which we take into account is the pair production of beauty baryons. Just at the threshold (which is unknown until now for any of the states considered here) we expect the production of a baryon-antibaryon pair with the quantum numbers of the photon, being (nearly) at rest in the CMS. This gives us strong handles for the suppression of background and identification of initial states by "tagging" which is necessary for the measurement of absolute branching fractions. In addition, the Lorentz boost of the CMS with respect to the laboratory, $\gamma\beta = 0.6$, being necessary for the observation of CP-violation and of $B_s\overline{B_s}$ mixing, procures us with measurable vertex separations that help to beat down the combinatorial background and make lifetime measurements possible.

Production cross sections

The question of the production cross sections is completely open. They are described by electric and magnetic form factors G_E, $G_M(s)$ according to

$$\frac{d\sigma}{d\Omega} = \frac{\beta\alpha^2}{4s}\left[|G_E|^2\frac{4M^2}{s}\sin^2\theta + |G_M|^2(1+\cos^2\theta)\right]$$

where β is the CMS-velocity and M the mass of the produced baryons, leading to steep maxima closely above threshold, since the form factors are expected to drop fast with rising s; however, no theoretical prediction for their behaviour in the time-like region at the Υ-scale is known.

From $p\bar{p}$- and $\Lambda\overline{\Lambda}$- production data in their respective threshold regions [82] we may derive in a very simple way a probability P for picking up (anti)diquarks of the right colour by the primarily produced $q\bar{q}$ pair. From

$$\sigma_{p\bar{p}} = (2Q_u^2 + Q_d^2)\sigma_{\mu\bar{\mu}} \cdot P \ , \ \sigma_{\Lambda\overline{\Lambda}} = Q_s^2\sigma_{\mu\bar{\mu}} \cdot P$$

probabilities of $P = (5.7 \pm 2.2)\%$ and $(5.9^{+3.5}_{-2.0})\%$ are obtained in the first and second case, respectively. Extrapolating this to $\Lambda_b\overline{\Lambda_b}$ production at $\sqrt{s} = 11.5$ GeV, a cross-section of

$$\sigma_{\Lambda_b\overline{\Lambda_b}} = 4.2 \pm 1.2\, pb$$

is obtained, which corresponds to about 0.16% of the (continuum) hadronic cross section at this energy.*

With the design luminosity of $3 \cdot 10^{33} cm^{-2} s^{-1}$, we would expect production rates of about $10^3 \Lambda_b\overline{\Lambda_b}/day$. The reconstruction efficiency could be estimated on the basis of running experience in the $\Upsilon(4S)$ region before a decision to modify the energy would be taken. But even with an efficiency of the order of only 1%, the rate of useful events would not be prohibitively low.

9.2 Masses of Beauty Baryons

Classification of states

The states to be considered here may be classified according to the flavor group of the light quark pair into a sextet and an antitriplet

$$\{3\} \times \{3\} = \{6\} + \{\bar{3}\}$$

containing the diquark configurations as shown in Table XII. Together with the b quark spin we have $J = 1/2$ for the antitriplet states and $J = 1/2, 3/2$ for the sextet states, the latter usually distinguished by a star. The Ξ_b states of the sextet and the antitriplet are not distinguished here: In fact they may be mixed, depending on the details of the interaction. (This is not the case for the Λ_b^0 and Σ_b^0 states because the isospin invariance should be violated only weakly).

*The MARK II collaboration has estimated the cross section for $\Lambda_c\overline{\Lambda_c}$ pair production at $\sqrt{s} = 5.2$ GeV to be $0.85 \pm 0.2nb$ [83]. Extrapolation to the beauty baryon threshold region would accordingly lead to cross sections higher than estimated above, by about one order of magnitude. So the above estimate has to be considered as a pessimistic one.

Table XII: Diquark configurations. (The squared and figured brackets mean (anti-) symmetrization in flavour and spin.)

I_3					I	S	name	charge
-1	-1/2	0	1/2	1				
dd		$\{du\}$		uu	1	0	$\Sigma_b^{(*)}$	$-\ 0\ +$
	{ds}		$\{us\}$		1/2	-1	$\Xi_b^{(*)}$	$-\ 0$
		ss			0	-2	$\Omega_b^{(*)}$	$-$
		[du]			0	0	Λ_b	0
	[ds]		[us]		1/2	-1	Ξ_b	$-\ 0$

Mass estimates

To get a first orientation about the energy range required for the production of these states, one may use mass formulas fitted to charm and strange baryons [84, 85], an experimental hint [6] of a beauty baryon (Λ_b^0 or Ξ_b^0 at 5.75 GeV/c^2) and a recent measurement of UA1 [86] giving $M(\Lambda_b^0) = 5.64 \pm 0.05 \pm 0.03$ GeV/c^2. We take 5.70 GeV/c^2 as an experimental upper limit. From potential models, an upper limit of 5.66 GeV/c^2 for $M(\Lambda_b^0)$ has been derived [85]. The strangeness splitting $M(\Xi_b^0) - M(\Lambda_b^0)$ may, to a first approximation, be taken from charm data [6] to be equal to $M(\Xi_c^0) - M(\Lambda_c^+) = 188\,\mathrm{MeV}/c^2$. A further information from the charm sector concerns the $\Omega_c^0 - \Xi_c^+$ mass difference to be $280\,\mathrm{MeV}/c^2$ ($M(\Omega_c^0)$ is derived from 3 events and not yet confirmed). This rather large splitting is not unreasonable, since here the sextet-antitriplet splitting is also involved, whereas for the $\Xi_{b,c} - \Lambda_{b,c}$ case the mixing of sextet-antitriplet Ξ states should lower this value.

There is no experimental information from the charm sector concerning the hyperfine splitting of the 1/2 and 3/2 baryon sextets. From the general trend observed for strange and charm vector and pseudoscalar mesons, it should decrease from charm to beauty baryons. Theoretical estimates [85] range from near degeneration to $\sim 50\,\mathrm{MeV}/c^2$ for $M(\Sigma_b^*) - M(\Sigma_b)$, much less than $M(\Sigma^*) - M(\Sigma) \sim 192\,\mathrm{MeV}/c^2$.

Putting everything together, the highest mass $M(\Omega_b^*)$ to be considered here should be less than 6.18 GeV/c^2 or 6.22 GeV/c^2, if we base our estimate on $M(\Lambda_b^0) = 5.66$ GeV/c^2 or the experimental value of 5.70 GeV/c^2, respectively. To be on the safe side HELENA should be able to increase the CMS energy to 12.6 GeV. Apart from higher power consumption, such an increase of the design energy by 20% poses no serious problems to the accelerator rings. A

redesign of the crossing area is eventually required. The discussion of related questions is left to a later stage of the design procedure.

9.3 Decay Modes

$\Sigma_b \to \pi\Lambda_b$ expected to be strong

Although the hyperfine splitting is expected to be small, most theoretical estimates predict a sextet-antitriplet splitting just larger than 140 MeV [85], so we expect strong decays $\Sigma_b \to \pi\Lambda_b$, in analogy to $\Sigma_c \to \pi\Lambda_c$. The mass difference $M(\Sigma_b) - M(\Lambda_b)$ can then be measured with the same resolution as in the charm case (compare [87]). To detect the hyperfine splitting is a priori not excluded.

Electromagnetic transitions are expected between Ω_b^* and Ω_b and perhaps between some of the nearly degenerate $\Xi_b^{(*)}$ states. Their detection may be possible with high resolution electromagnetic calorimetry as proposed in chapter III.7. Λ_b, Ξ_b and Ω_b can only have weak decays, leading to measurable vertex separations.

Semileptonic decays

Semileptonic weak decays of beauty baryons should be well described by the spectator model. For the dominating quark transition

$$b \to c\, l\, \overline{\nu}_l, \qquad l = e^-, \mu^-, \tau^-$$

the charm quark energy (in the rest system of the b quark)

$$E_c = \frac{m_b^2 + m_c^2 - q^2}{2m_b}$$

is less than 2.8 GeV (for $m_b = 5\ GeV/c^2$, $m_c = 1.7\ GeV/c^2$, $q^2 = 0$). The invariant mass of the secondary hadronic system can be calculated in the rest system of the spectator diquark as

$$m_{c(qq)}^2 = m_c^2 + m_{qq}^2 + 2E_c' m_{qq} < 8\ GeV^2$$

if we approximately set ($E_c' \approx E_c$) and take $m_{qq} = 0.7$ GeV. The excitation energy of the hadronic system is then

$$T = m_{c(qq)} - m_c - m_{qq} < 0.4\ GeV\,,$$

rather small compared to charmed baryon masses; that means charmed baryons are expected to be produced singly in most of the semileptonic decays of beauty baryons (in analogy to the $\overline{B} \to Dl\overline{\nu}$ dominance in semileptonic meson decays), very much simplifying the identification of decay chains. Of course, this source of charmed baryons is of interest in itself (see chapter 10).

As far as beauty baryons are produced at threshold, they have opposite helicities. This is helpful for the study of decay asymmetries, (e.g. in the chain $\Lambda_b \to \Lambda_c \to \Lambda$) in order to gain information on the structure of weak baryonic currents.

Nonleptonic decays

Turning to nonleptonic decay modes, important questions concern the role of stimulated decays of baryons – as opposed to spectator decays – where the b quark decay proceeds via weak scattering with other quarks, and last not least the role of penguin diagrams in baryon decays[†]. In the case of beauty mesons, the contribution of annihilation diagrams complicates the separation of these processes. While it will be difficult to identify exclusive channels in this case, important information is expected from lifetime measurements making possible the comparison between total and semileptonic decay width.

[†]The possibility of observing measurable CP-violating asymmetries of the order of 2 to 20% in connection with penguin graphs has been discussed by Bjorken [88].

10 Charm Physics

Advantages of the B-factory in charm physics

The present knowledge of charmed particle spectroscopy and decay is largely due to experiments performed at e^+e^- storage rings. They have the advantage of a signal to background ratio at the production level which exceeds that of other charmed particle sources by one to two orders of magnitude. This is demonstrated by Table XIII, where typical production cross sections of the Λ_c^+ particle in different experiments are compared with the corresponding total cross section.

Table XIII: Ratio of Λ_c^+ production cross section to the total cross section for different experiments.

	$\sigma(\Lambda_c^+)/\sigma_{tot}$	reference
$e^+e^- \rightarrow \Lambda_c^+ + x$	$6.2 \cdot 10^{-2}$	[89]
$\gamma\, p \rightarrow \Lambda_c^+ + x$	$5 \cdot 10^{-4}$	[90]
$p\, p \rightarrow \Lambda_c^+ + x$	$10^{-3}...10^{-4}$	[91]

Moreover, the relatively low multiplicity environment of charm production at a B-factory in comparison to a high luminosity hadron collider run at high energies provides a further advantage, since the combinatorial background is appreciably smaller in the case of a B-factory. The disadvantage of a hadron collider cannot be fully compensated by precise vertex measurements, since multi-vertex reconstruction is far from being trivial. Note that no demonstration of successful secondary vertex reconstruction exists in case of more than one interaction per bunch crossing. Hence the expected increase of the statistics by a factor 100 ... 1000 compared to present experiments and the possibility of precise vertex measurements provide the chance for e^+e^--experiments to compete favorably with experiments on hadron colliders also in the future.

Physics topics

A rich charm physics program is possible which one gets for free, while running on the $\Upsilon(4S)$, from the copiously produced $c\bar{c}$-background. Note that as many $c\bar{c}$ as $b\bar{b}$ pairs are produced by the virtual photon at this energy. Major contributions to the field are expected from the investigation of the following topics:

- Precise measurements of weak decays of charmed mesons and baryons including polarization studies. The analysis of the resulting pattern can lead to unique conclusions on strong interaction physics at the borderline of soft and hard QCD [92,93]. The recent development of the effective heavy quark theory [94] allows to make predictions which are a systematic limit of QCD.
- Studies of semileptonic D-meson decays;
- Spectroscopy of charmed baryons and mesons;
- $D^0 - \overline{D}^0$ mixing;

- Rare charmed meson decays.

In the following the feasibility of such studies is discussed for a few examples.

10.1 Semileptonic D-Decays

Results on semileptonic D-decays are easy to interpret

Semileptonic D-decays have the great advantage that the results can be interpreted easily. They are of particular interest since the Kobayashi-Maskawa matrix elements V_{cd} and V_{cs} can be derived from the measured branching ratio with relatively small theoretical uncertainty. Moreover, the hadronic information factorizes and can be parametrized in a compact way by decay constants whose interpretation is accessible both to analytical and lattice techniques. Their interpretation provides important constraints to QCD [93].

Data volume will be orders of magnitude larger than available up to now

The present analysis of semileptonic D-meson decays is based on an event sample of ≈ 300 events [91]. Starting from $3 \cdot 10^7$ charm events per year available at a B-factory one expects to observe $\mathcal{O}(10^6)$ ($D^+ \to \overline{K^{*0}} l^+ \nu_l$) decays. Because of the long lifetime a clean data sample can be selected with a stringent vertex cut. With this data sample an analysis of the four-momentum dependence of the formfactor is possible allowing to check in detail theoretical predictions and to extract a reliable value for V_{cs}.

Study of (c→d) transitions

Even more interesting is the study of semileptonic (c→d) transitions, since besides the determination of V_{cd} they provide a testing ground for models developed to describe the transition between a heavy and a light quark [44,95]. These studies are of special importance in view of the derivation of V_{bu} from (b→u) transitions which should show a similar sensitivity to models. The decay $D^+ \to \rho^0 l^+ \nu_l$ and $D^0 \to \pi^- l^+ \nu_l$ may serve as typical examples for such studies. One expects to observe $\mathcal{O}(5 \cdot 10^4)$ decays in each channel [26]. They are suppressed in comparison to the Cabibbo allowed transition mentioned above and therefore suffer more strongly from background. A Monte Carlo study shows that besides the cut on the secondary vertex a further signal/background enhancement by a factor of 2 seems to be possible, if one exploits the directional information from the secondary vertex.

10.2 Spectroscopy of Charmed Hadrons

The system of a light and a heavy quark is the 'hydrogen atom' in quark physics

In recent years important contributions to charmed meson and baryon spectroscopy came from the ARGUS and CLEO experiments. Their results were typically based on event samples of $\mathcal{O}(100)$ events [96,97]. Already from this observation follows that the field is still in its infancy and major improvements can be expected from the high statistic data sample available at the B-factory. The theoretical interest in detailed investigation has been stressed [98,99]; the

analogy to the hydrogen atom of such a system consisting of a light and heavy quark is obvious. As in the case of quarkonium the level splitting of the ^3P and ^3D states is of special interest since it provides a means to study the properties of the long range spin dependent confinement potential.

Also for this study the signal/background ratio can be improved by a cut on the secondary decay vertex of the stable D meson produced in the decay chain, while the detection efficiency does not suffer too much. Again the increase of statistics by a factor of 100 and more, possible at a B-factory, is of special importance in view of the small data samples of $\sim$ 100 events presently available.

10.3 $D^0 - \overline{D}^0$ Oscillations

Search for mixing of D^0 *mesons*

$D^0 - \overline{D}^0$ oscillations are expected to be small in the framework of the standard model. The predicted mixing rate is of the order of $r_D \approx 10^{-7}$ [100]. A measurement of this small mixing seems to be out of range of present experimental possibilities, but the observation of a larger value would be a clear signal for new physics. Hence the measurement of $D^0 - \overline{D}^0$ mixing is a sensitive tool to search for physics beyond the standard model at a low energy machine.

Presently, experiments tag the produced D^0-meson via the $D^{*+} \rightarrow D^0\pi^+$ decay which allows [101] to obtain a clean signal. At a certain level the fake of $D^0 - \overline{D}^0$ oscillations by doubly Cabibbo forbidden charm decays $D^0 \rightarrow K^+\pi^-$ cannot be avoided in time integrated measurements. Extensive Monte Carlo studies [43] have shown that high precision vertex measurements allow to separate doubly Cabibbo suppressed decays (DCSD) from $D^0 - \overline{D}^0$ oscillations since the two processes develop differently in time [102]. In case of small mixing one finds

$$N(D^0 \rightarrow K^-\pi^+)_{osc} \sim t^2 e^{-\Gamma t}$$

$$N(D^0 \rightarrow K^-\pi^+)_{DCSD} \sim e^{-\Gamma t}$$

From the study follows that $D^0 - \overline{D}^0$ oscillations are observable with the statistics collected at a B-factory, if $r_D \geq 5 \cdot 10^{-5}$ and the power of the high resolution vertex detector is used. Note that this analysis provides a means to study also doubly Cabibbo forbidden charm decays which has an interest in itself [100].

10.4 Rare Charm Decays

Since the Kobayashi-Maskawa matrix elements for Cabibbo favored charm decays are large, the branching ratios of rare charm decays are expected to be small. This disadvantage is compensated by the fact that the observation of a signal beyond the expectation will present strong evidence for new physics.

One loop decays and doubly Cabibbo suppressed decays will be discussed as benchmarks.

One loop decays: $D^0 \to \gamma\gamma$

The decay $D^0 \to \gamma\gamma$ serves as an example for the one loop decays. The treatment as a two-step process $D^0 \to \pi, \eta, \pi\pi, ... \to \gamma\gamma$ should lead to reliable results as in the case of $K_L^0 \to 2\gamma$. Since the first step is Cabibbo and the second one electromagnetically suppressed, the branching ratio is estimated [100] to be $Br(D^0 \to 2\gamma) \leq 0(tg^2\theta_c \cdot \alpha^2) = 3 \cdot 10^{-6}$. With an integrated luminosity of 50 fb^{-1} and $\sigma(e^+e^- \to D^0 + x) = 1.18\, nb$ [103] this corresponds to 150 events. The signal to background ratio can be improved appreciably, if only D^0–mesons produced in the cascade decay $D^* \to D^0\pi$, $D^0 \to 2\gamma$ are considered. In this case $\sim$ 100 events are expected with strongly suppressed background. Note, however, that a sizeable cancellation of the different amplitudes contributing to $D^0 \to 2\gamma$ may exist, hence the chances to observe this decay channel at an early stage of the experiment are marginal.

$D^0 \to l^+l^-$, μ^+e^-

The sensitivity of the experiment for other one loop decays as $D^0 \to l^+l^-$, μ^+e^- is of the same order as for the $D^0 \to 2\gamma$ decay, i.e. one can observe a $Br \geq \mathcal{O}(10^{-6})$.

Also in this case the narrow $m(D^*) - m(D^0)$ signal can be exploited to improve the signal/background ratio appreciably. Moreover, the reconstruction of the secondary vertex provides a further means of improvement. In the standard model these decays are either forbidden or strongly suppressed due to different mechanisms (helicity–, wave function–, Cabibbo suppression), hence the branching ratios are unmeasurably small. On the other side they are an extremely sensitive indicator of new physics, since e.g. in the case of SU(5) type leptoquarks, it has been shown that no helicity suppression exists [104] and the branching ratio could therefore be much larger than in the standard model.

Doubly Cabibbo suppressed decays

Doubly Cabibbo suppressed decays are another class of rare decays. They should be observable with the statistics corresponding to 50 fb^{-1}. The expected ratios of branching ratios are given in Table XIV [105,100]. The coefficients reflect details of QCD corrections and wave functions, hence interesting information on QCD follows from this analysis. The expected rates are included in Table XIV. A comfortable statistics is available allowing to apply further cuts to improve the signal to background ratio. Examples are the reconstruction of the decay chain $D^* \to D\pi$, $D \to K^+\pi^-, ...$ and/or the selection of decays with a well reconstructed secondary vertex. The rates expected for these subsamples are still of the order of $\sim$ 1000 events/ channel.

Sensitivity to New Physics

Bigi [100] has argued that doubly Cabibbo suppressed decays should have a higher sensitivity to new physics than Cabibbo allowed D-decays. A charged Higgs e.g. induces the $c \to s(u\bar{d})$ as well as the $c \to u(u\bar{s})$ transition. Since the strength of the Higgs coupling depends on the mass of the particle produced [106] one expects a strong enhancement of the Higgs induced decay in

Table XIV: Predicted ratios of branching ratios [105,100] for doubly Cabibbo suppressed decays and rates expected for an integrated luminosity of 50 fb^{-1}. N_{tag} corresponds to events tagged by the decay $D^{*+} \to D^0\pi^+$ or $D^{*+} \to D^+\pi^0$.

	N	N_{tag}
$\frac{Br(D^0\to K^+\pi^-)}{Br(D^0\to K^-\pi^+)} = 2\cdot tg^4\theta_c$	5660	1000
$\frac{Br(D^0\to K^+\rho^-)}{Br(D^0\to K^-\rho^+)} = 0.5\cdot tg^4\theta_c$	11800	2000
$\frac{Br(D^0\to K^{*+}\pi^-)}{Br(D^0\to K^{*-}\pi^+)} = 3\cdot tg^4\theta_c$	2300	400
$\frac{Br(D^+\to K^+\pi^0)}{Br(D^+\to \overline{K^0}\pi^+)} = 3\cdot tg^4\theta_c$	7260	1100
$\frac{Br(D^+\to K^{0*}\pi^+)}{Br(D^+\to \overline{K^{0*}}\pi^+)} = (5...11)\cdot tg^4\theta_c$	11550	2800
$\frac{Br(D^+\to K^{*+}\pi^0)}{Br(D^+\to \overline{K^{*0}}\pi^+)} = (12...25)\cdot tg^4\theta_c$	26400	6400
$\frac{Br(D^+\to K^+\rho^0)}{Br(D^+\to \overline{K^0}\rho^+)} = 0.35\cdot tg^4\theta_c$	1970	500

the doubly Cabibbo suppressed decay channel:

$$\frac{N(c \xrightarrow{H} d(u\bar{s}))/N(c \xrightarrow{W} d(u\bar{s}))}{N(c \xrightarrow{H} s(u\bar{d}))/N(c \xrightarrow{W} s(u\bar{d}))} = \left(\frac{m_s}{m_d}\right)^2 \frac{1}{tg^4\theta_c} \sim 4\cdot 10^4 .$$

The prospects to observe new physics in the suppressed channel are therefore strongly enhanced.

11 Tau Physics

11.1 Introduction

$e^+e^- \to \tau\overline{\tau}$

Since its discovery in 1975 the τ-lepton has been extensively studied. Most of these analyses have been performed at the e^+e^- storage rings SPEAR, DORIS, PEP, and PETRA. Recently the LEP experiments started to contribute to this field of physics. The available data samples of $\tau\overline{\tau}$ pair events from the DORIS II and CESR experiments (e.g. $\approx 5 \times 10^5$ events from ARGUS) are much larger than those of PEP/PETRA experiments, but the latter, operating at higher centre-of-mass energies, have the advantage of less background.

Vertex detection

The new generation of detectors, taking data in the E_{CMS} region of the Υ resonances, will have high precision vertex detectors. With such devices one will be able to use the long lifetime of τ leptons to identify τ-pairs by observing their decay vertices separated in space if at least one τ decays into 3 or 5 charged particles, or by measuring the distance of closest approach if both τ's decay into 1 charged particle.

B-factory = τ-factory

Tau physics at the B-factory will benefit from the huge number of τ-pairs which will be produced. In fact, the B-factory is at the same time also a τ-factory. For an integrated luminosity of 50 fb^{-1} approximately 5×10^7 τ-pairs will be available for the analysis, about two orders of magnitude more than there are at present.

Lorentz boost

The Lorentz boost of the B factory's CMS system, $\beta\gamma = 0.6$, is of minor importance in τ physics, since it is small compared to the $\beta\gamma \geq 2.5$ which τ leptons acquire in the pair production process relative to the CMS system. It is desirable to perform some of the analyses, e.g. measurement of correlations between τ decay products, by boosting the particles back into the centre-of-mass system. An excellent particle identification capability is necessary in order to determine the 4-vectors of the particles, which is available at the proposed detector. The energy spread of the collider has almost no influence on the results.

In the following we present some important topics in τ physics that are within the scope of a B-factory.

11.2 Properties of the τ neutrino

11.2.1 Coupling Constants

Coupling constants

The properties of the ν_τ can only be measured indirectly by analyzing the observable decay products of τ-lepton decays. Recently the ARGUS collaboration presented the first measurement of the ν_τ-helicity from a parity vi-

olating asymmetry in the τ decay into three charged pions, proving the ν_τ to be lefthanded [107]. For both charge states of the τ, the asymmetry appears at the level of three standard deviations. From the measured asymmetry, the normalized product of the axial and vector coupling constants $\gamma_{AV} = 2g_A g_V/(g_A^2 + g_V^2) = 1.25 \pm 0.23 \pm^{0.15}_{0.08}$ has been derived which is in good agreement with the standard model prediction. The result has been obtained from a selected data sample of 5888 events, with $\approx$ 20% background contribution. Due to the vertex detection and particle identification capabilities of HELENA a much cleaner data sample can be selected which is also larger by orders of magnitude. Consequently, the precision of the measurement can be improved by a factor of > 10.

11.2.2 Limits on the ν_τ mass

ν_τ mass

In the framework of the standard model, neutrinos are considered to be massless. However, the Standard Model is not based on the mass of the neutrinos. In fact, many extensions of the standard model predict non-vanishing neutrino masses. Massive neutrinos could contribute to the solution of some problems in cosmology and astrophysics, as to neutrino oscillations and dark matter. Compared to the present limits on the masses of ν_e and ν_μ, $m(\nu_e) < 18$ eV/c^2 at 95% CL [108] and $m(\nu_\mu) < 250$ keV/c^2 at 90% CL [109], the upper bound on the mass of the ν_τ is quite large: $m(\nu_\tau) < 35$ MeV/c^2 at 95% CL [110]. To make considerable progress in the solution of cosmological problems, a sensitivity in measuring $m(\nu_\tau)$ of the order of $\mathcal{O}(1\,\mathrm{MeV/c^2})$ is desirable [111].

Sensitivity

The most sensitive technique to determine the ν_τ mass is to measure the endpoint of the mass spectrum of hadrons from τ decays. The best existing limit on $m(\nu_\tau)$ has been obtained by ARGUS by analyzing the (5π)-mass spectrum in the decay $\tau^- \rightarrow 5\pi^-\nu_\tau$. 12 events have been selected from a data sample of about 200 000 τ-pair events, leading to limit of $m(\nu_\tau) < 35$ MeV/c^2 at 95% CL [110]. Recently ARGUS repeated the analysis including new data. The same result has been obtained with 20 selected events. This demonstrates that the method is very powerful even with only a small number of observed events. However, the power of this method is clearly limited by the precision with which the mass of the τ lepton itself is known: $m_\tau = 1.7841^{+0.0027}_{-0.0036}$ GeV/c^2. Therefore a limit considerably below 10 MeV/c^2 cannot be achieved by this method without new measurements of the mass of the τ. Such measurements can be performed with the new e^+e^- storage ring in Beijing (BEPC) or with the proposed τ/charm-factory, where precisions of $\sigma(\mathrm{m}_\tau) < 1$ MeV/c^2 and $\sigma(\mathrm{m}_\tau) \approx 0.1$ MeV/c^2 [112], respectively, can be reached. This would enable a determination of the ν_τ-mass down to a limit of 2 MeV/c^2.

Data volume

The feasible limit depends strongly on the resolution function and the number of events found with hadronic masses close to the mass of the τ, say $m_{had} >$ 1.7 GeV/c^2. In Fig. 37 the hadronic mass spectrum for the latest ARGUS data

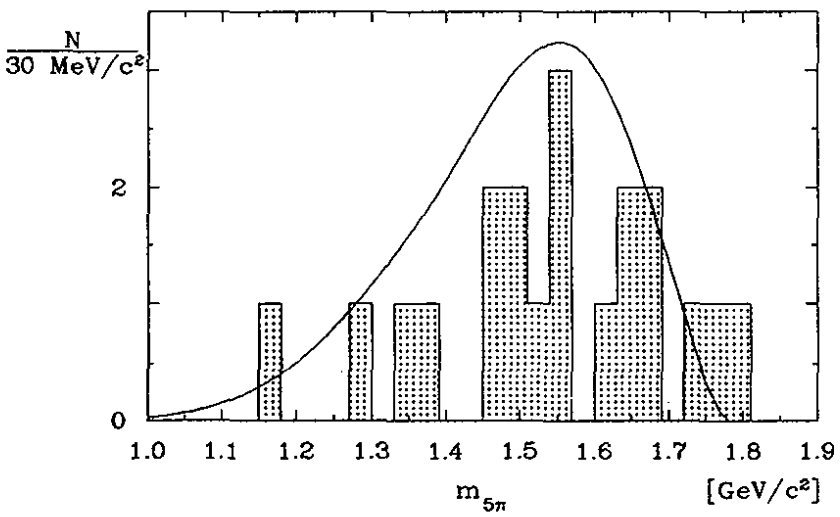

Figure 37: (5π)-mass spectrum of 20 events from the decay $\tau^- \rightarrow 5\pi^-\nu_\tau$ as measured by ARGUS. The curve corresponds to the shape of a phase-space decay weighted with the weak matrix element ($m(\nu_\tau) = 0$ MeV/c^2).

is shown together with the expectation of a phase space decay weighted by the weak matrix element. It appears that the data can be described by such model. Using this model, we expect to find 5% of the events to have (5π)-masses above 1.7 MeV/c^2. Note that other attempts have been made to describe the invariant mass spectrum by a $\rho\rho\pi$ final state (e.g. [113,51]) which shows a considerably larger fraction of events in the sensitive region. Making use of the high precision vertex detector of HELENA to detect the 5-pion vertex and cutting on the distance of closest approach to the single prong side, it seems to be possible to obtain a detection efficiency 2 times the corresponding ARGUS value. Thus the B-factory, with an integrated luminosity of 50 fb^{-1}, will deliver about 500 ± 250 detected events of the type $\tau^- \rightarrow 5\pi^-\nu_\tau$ in the sensitive m(5π) region above 1.7 GeV/c^2.

Mass resolution

A precise measurement of the ν_τ mass requires not only good statistics in the sensitive region, but also an excellent mass resolution. In addition to a good momentum resolution, the contribution of multiple scattering to the mass resolution has to be small. The track parameters at the vertex are known with high precision due to the vertex detector, thereby minimizing the influence of multiple scattering. A mass resolution of $\sigma(\mathrm{m}(5\pi)) < 10$ MeV/c^2 can be reached which is again a factor of > 2 improvement as compared to the ARGUS experiment.

$\tau^- \rightarrow \mathrm{K^+K^-}\pi^-\nu_\tau$

Another decay channel, the decay $\tau^- \rightarrow \mathrm{K^+K^-}\pi^-\nu_\tau$, is also an interesting candidate in terms of measuring the ν_τ mass. It can be shown that the number of selected events from this channel is of the same order of magnitude as from

the (5π)-decay. The experimental boundary conditions have been discussed in detail in [51]. The same procedure as for the (5π)-decay can be applied, yielding a comparable sensitivity for the mass of the ν_τ. Using both decay channels and taking into account an error of the τ-mass of $\sigma(m(\tau)) = 1$ MeV/c^2 we estimate from Monte Carlo calculations that an upper limit of (95% CL)

$$m(\nu_\tau) < 3.5 \text{ MeV/c}^2$$

can be achieved which is close to the value defined by the uncertainty in the knowledge of the τ mass. Note that this limit is comparable to the limit of about 3 MeV/c^2 which is expected from a τ/charm-factory [113].

11.3 τ Lifetime

τ lifetime

The knowledge of the τ lifetime τ_τ is not only of interest as one of the fundamental properties of the particle but is also needed to understand the present consistency problem in τ decays. Since the partial width of the leptonic decays can be calculated, predictions on the leptonic branching ratios can be made by using the τ lifetime. With $\Gamma(\tau^- \to e^- \bar{\nu}_e \nu_\tau) = (1.595 \times 10^{-12} \text{ s})^{-1}$, and using the measured lifetime of $\tau_\tau = (3.03 \pm 0.08)^{-13}$ s [6], the predicted branching ratio for $\tau^- \to e^- \bar{\nu}_e \nu_\tau$ is $(19.0 \pm 0.5)\%$. This value has to be compared to the world average of direct measurements which is $(17.7 \pm 0.4)\%$. The apparent discrepancy demonstrates the need of better measurements of the τ lifetime and the leptonic branching ratios.

Measuring techniques

All present measurements of the lifetime either determine the distance of closest approach of each track of the τ decay to the interaction point, calculated in the plane transverse to the beam direction, or measure the transverse decay length distribution for 3-prong tau decays. These methods contain some intrinsic uncertainties: The flight direction of the τ with respect to the beamline is not known. When measuring the decay length, the direction of the measured tracks has to be taken as the direction of the τ, causing additional systematic uncertainties. In addition, the interaction point is not precisely known due to the beam widths. The r.m.s. beam widths at DORIS II *e.g.* are 800 μm in horizontal direction and 25 μm in vertical direction, respectively, comparable to the mean decay length of ≈ 250 μm.

The high precision vertex detector of HELENA allows a direct measurement of the impact parameter as well as the decay length in all coordinates. In order to be independent of the beam widths and the underlying physics in the τ decay, the B-factory offers three additional methods to measure the τ-lifetime which have been investigated by means of Monte Carlo calculations:

1. Measurement of the distance between the decay vertices of both τ's decaying into a 3-prong. Monte Carlo calculations for events, with both τ's

decaying into 3 charged particles via the a_1-meson, showed that a selection efficiency of 25% without applying any sophisticated cuts is realistic, with a background level of the order of 10%. Therefore we expect ≈ 60000 τ events of this type for a collected integrated luminosity of 50 pb^{-1}. With this data sample we estimate that the lifetime can be determined with an error smaller than 1%.

2. Measurement of the distance of closest approach of the two tracks from both τ's decaying into one prong. A very clean event sample with a background contamination of only $\approx 1\%$ can be selected by using the event types $\tau^- \to e^-\nu\overline{\nu}$ and $\tau^- \to \mu^-\nu\overline{\nu}$. We expect to select more than 5×10^5 events.

3. Measurement of the distance of closest approach of the track from a single prong τ decay to a 3-prong τ vertex. Again a very clean selection is possible when one requires the single prong to be a lepton. Assuming the other τ to decay to be an a_1, we expect to select $\approx 5 \times 10^5$ events. The background level is estimated to be of the order of 1%.

In addition, the conventional technique can be applied. This method has been extensively studied in [51].

Accuracy

By applying all these methods, an accuracy of $\sigma(\tau_\tau)/\tau_\tau < 1\%$ for the τ-lifetime measurement is feasible. Recent results from LEP experiments on the τ lifetime [114] indicate that a precision in the order of about 1% can possibly be achieved. Note that a measurement of the τ-lifetime is hardly possible for a τ/charm-factory where τ-leptons are produced almost at rest.

11.4 τ Decay Branching Ratios

Tagging technique

To make full use of the large number of produced τ-pairs, we want to measure the decay branching ratios without being dependent on theoretical calculations of $\sigma_{\tau\tau}$ and the luminosity monitoring which are only accurate to 1% and $\approx 1\%$, respectively. Most of the τ branching ratios can be measured relative to a "tagging" decay. The leptonic decays of the τ or the decay $\tau^- \to \pi^+\pi^-\pi^-\nu_\tau$ seem to be a good choice as a tag since these events can be easily selected with only a small background contribution [115,107]. The τ branching ratios follow from the measured fractions of the decays of the non-tagged τ. In addition, measurements of τ events, with both τ decaying to the same final state, e.g. $\tau^- \to \rho^-\nu_\tau$ and $\tau^+ \to \rho^+\overline{\nu}_\tau$, will provide extra information. Therefore, enough data are available to determine the τ branching ratios without knowing the number of produced τ-pairs.

Decays with neutral pions

CLEO has shown that it is possible to reconstruct final states containing $3\pi^0$'s [116], using a CsI electromagnetic calorimeter. The measurement of decays with π^0's in the final state is very important to solve the so-called τ-decay problem, referring to the discrepancy between measured inclusive and exclusive branching ratios, since the branching ratios of these decay channels are known only with large errors. More information about "missing" single prong decays can be obtained from inclusive photon counting in those decays. The fraction of photons which do not originate from π^0 decays can be determined from such an analysis, giving information on possible new exclusive final states.
The particle identification capabilities of HELENA allow to measure with high precision branching ratios of τ decays into final states containing kaons, e.g. $\tau^- \to K^-\nu_\tau$, $\tau^- \to K^-\pi^-\pi^+\nu_\tau$. These branching ratios are known only with large errors [6]. With today's experiments major significant improvements are hardly possible to achieve, due to limitations in the data volume and in the capabilities to identify particles. The large sample of τ events can also be used to search for decays which are forbidden in the Standard Model.

11.5 Rare τ Decays

Neutrinoless τ decays

The search for neutrinoless τ decays might lead to the opening of a window to new physics beyond the standard model. Radiative τ-decays (e.g. $\tau^- \to \mu^-\gamma$) can be caused by supersymmetry; lepton flavour changing Higgs couplings can lead to final states such as $\mu^-\mu^-\mu^+$; other channels can be mediated by leptoquarks, e.g. $\tau^- \to \pi^0 e^-$. Upper limits for a variety of decay channels are available up to now which are ranging from $\approx 10^{-5}$ to $\approx 10^{-3}$ [117], but an improvement of the present sensitivity is highly desirable.

Lepton flavour violation

In μ decays, lepton flavour violating channels have been searched for, too. For example, $\mathrm{Br}(\mu^- \to e^-\gamma) < 4.9 \times 10^{-11}$ and
$\mathrm{Br}(\mu^- \to e^-e^-e^+) < 1.0 \times 10^{-12}$, whereas
$\mathrm{Br}(\tau^- \to e^-\gamma) < 1.2 \times 10^{-4}$,
$\mathrm{Br}(\tau^- \to e^-e^-e^+) < 1.3 \times 10^{-5}$, and
$\mathrm{Br}(\tau^- \to \mu^-\mu^-\mu^+) < 1.7 \times 10^{-5}$; all limits at 90% CL [6,118,119],
Although the limits on the muon decays are much more stringent, the sensitivity in τ decays to new physics can be higher due the larger mass of the τ, assuming the same physical mechanism being involved. Supposing the neutrinoless leptonic decays are caused by a Higgs boson, one estimates [120]:

$$\frac{\mathrm{Br}(\tau^- \to \mu^-\mu^-\mu^+)}{\mathrm{Br}(\mu^- \to e^-e^-e^+)} \simeq \left(\frac{m(\tau)}{m(e)}\right)^2 \simeq 10^7,$$

demonstrating that some present limits on τ-decays are already competitive with those on μ-decays. Up to now, limits on lepton and baryon-number vio-

lating decays are available only for 3 decay channels, $\tau^- \to \bar{p}\,\gamma$, $\tau^- \to \bar{p}\,\pi^0$ and $\tau^- \to \bar{p}\,\eta$. These limits are are not very stringent and are well above 2×10^{-4} [118]. An improvement of the sensitivity is highly welcome. With a data sample of 5×10^7 τ-pair events, obtainable at the B factory, the sensitivity for rare decays can be increased by a factor of $\mathcal{O}(200)$. Branching ratios of $\leq 10^{-5}$ can possibly be measured, a region where presently only upper limits exist, whereas upper limits for rare decay channels of $\approx 10^{-7}$ will be reached.

Hadronic decays

The search for hadronic decays, conserving lepton number and lepton flavour, is another point of interest. The only possible combinations of spin, parity and G-parity quantum numbers predicted by the standard $V-A$ theory for isovector hadronic finals states in τ-decays are: $J^{PG} = 1^{-+}$, 0^{--} or 1^{+-}. The observation of final states with different J^{PG} would indicate the existence of second class currents, G-parity violation in the hadronization process, or another non-standard decay mechanism.

$\tau^- \to \eta\pi^-\nu_\tau$, $(J^{PG} = 0^{+-})$

The most extensive search up to now has been made for the decay $\tau^- \to \eta\pi^-\nu_\tau$ $(J^{PG} = 0^{+-})$, yielding an upper limit for the branching ratio of $< 0.9\%$ at 95% CL [121]. Also the search for $J^{PG} = 1^{++}$ contributions in the decay $\tau^- \to \omega\pi^-\nu_\tau$ showed no positive result. However, due to limited statistics, only contributions larger then 50% (95% CL) could be excluded [122]. With the increased statistics and the better detector performance of the proposed B factory branching ratios of less than 10^{-4} can be measured for the decay $\tau^- \to \eta\pi^-\nu_\tau$. For this decay, predictions are available assuming isospin violating effects. The predicted branching ratio amounts to $\mathrm{Br}(\tau^- \to \eta\pi^-\nu_\tau) = 1.5 \times 10^{-5}$ [123] and is thus within reach of the experiment. It is likely that this final state is produced via the a_0^- which also decays into $\mathrm{K}^-\mathrm{K}^0$. Therefore, the search for $J^{PG} = 0^{+-}$ final states is not limited to the search for $\tau^- \to \eta\pi^-\nu_\tau$ alone. In summary, the B-factory offers a wide area in the search for new and exotic phenomena.

11.6 $V-A$ Tests

Lorentz structure of the leptonic τ decay

Contrary to the decays of muons, in τ-decays the parameters which describe the interaction are very poorly known. Presently known is the sign of the ν_τ helicity. Measured values are $\gamma_{AV} = 1.25 \pm 0.23 \pm^{0.15}_{0.08}$ and the Michel parameter ρ. The latter has been measured by several experiments. The most precise value is $\rho = 0.742 \pm 0.035 \pm 0.020$ and has been obtained by the ARGUS collaboration [124]. However, these measurements, although in agreement with the $V-A$ value $\rho = 3/4$, do not uniquely determine the interaction since a most general ansatz also allows other combinations of scalar, tensor and vector couplings to yield the same value [125]. The complete Lorentz structure of leptonic τ decays can be fixed by the measurement of six parameters [125].

- ν_τ helicity;
- τ lifetime;
- Polarization ξ' of the daughter lepton (μ or e);
- Decay asymmetry of the daughter lepton relative to the spin of the τ which is described by the two parameters ξ and δ;
- Total cross section for the inverse decay $\nu_\tau e^- \rightarrow \tau^- \nu_e$ with ν_τ of known helicity.

Apart from the measurement of the total cross section of the inverse τ decay, in principle all these parameters can be measured at a B-factory. To measure ξ' a special polarimeter is required which is not included in the proposed experimental setup. However, such a device might be added. The necessary experimental requirements have been discussed in detail in [120,125].

In summary, τ parameters will be measurable at the proposed B-factory with sufficient precision to be sensitive to effects of possibly existing non standard interactions.

12 Two-Photon Physics

12.1 Introduction

What to measure?

Two-photon scattering reactions (Fig. 38) have been extensively studied in recent years at the e^+e^- storage rings PETRA, PEP, SPEAR, DORIS, DCI, VEPP-4 and others [126]. The most important results have been obtained on

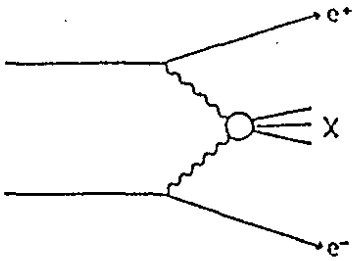

Figure 38: The two-photon scattering process $e^+e^- \to e^+e^-X$.

the two-photon production of hadrons and QCD related topics. Perturbative QCD has been tested at the high-energy machines PETRA and PEP with measurements of the photon structure function and of the production of hadrons at large transverse momenta. While this is the domain of higher energy machines, in the kinematical range accessible to a B-factory the main issues in two-photon physics will be:

- two-photon couplings of resonances,
- two-photon production of non-resonant final states, in particular hadron pair production,
- the total cross section for hadron production by two photons.

Figure 39 shows the expected cross section for the production of a resonance by the two-photon process for different beam energies. The logarithmic increase of the $\gamma\gamma$ flux with the beam energy is partly compensated by a better acceptance at lower energies due to smaller boosts of the $\gamma\gamma$ system (the boost is proportional to the difference in the photon energies). The acceptance for $\gamma\gamma$ events is not affected by asymmetric beam energies due to the asymmetric design of the detector.

The B-factory is a prolific source of η_c's

The B-factory will be competitive with higher energy machines at least up to the η_c region. With an integrated luminosity of 10^5 pb^{-1}, about 1.7 Mio. η_c's will be produced allowing to study rare η_c decays with branching ratios down to 10^{-4} or 10^{-5}. Particularly interesting is the possibility to detect the η_c in the elastic channel, i.e. both production and decay via two photons. The expected

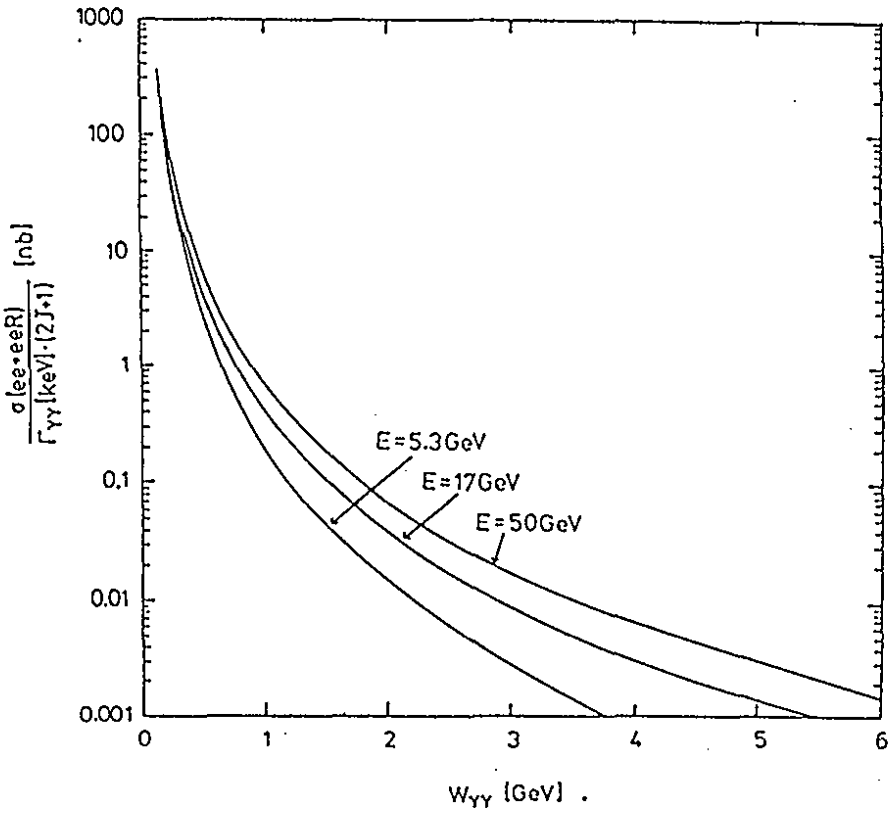

Figure 39: The cross section for the production of a resonance R in the process $e^+e^- \to e^+e^-R$ plotted for different beam energies.

branching ratio of η_c into $\gamma\gamma$ is about 10^{-4}. This decay mode has not yet been seen in radiative J/ψ transitions where most of our knowledge on the η_c comes from. Thus a B-factory would be a prolific source for η_c's or, one may say, an η_c-factory.

By virtue of the expected high luminosity, two-photon experiments at a B-factory will not merely improve the results obtained at the existing machines but almost certainly will provide new physical perceptions. This can be achieved largely with not much additional effort in the construction of a detector, in particular if 'tagging', i.e. the detection of the scattered electrons (Fig. 38), is not required.

12.2 Physics Issues

12.2.1 Two-Photon Couplings to Resonances

Pseudoscalar and tensor mesons

Radiative decays are sensitive to the charge content of particles and thus to their internal structure. The best understood C-even mesons are the pseudoscalar

mesons π^0, η, η' and the tensor mesons a_2, f_2, f_2'. From the completely measured $\gamma\gamma$ widths their quark composition, expressed by the singlet-octet mixing angles, and possible non-$q\bar{q}$ admixtures have been analyzed.

Scalar mesons

For the scalar mesons the situation is much less clear because not even a regular mass pattern of a meson multiplet is observed. The $\gamma\gamma$ widths appear to be suppressed as compared to the tensor mesons which belong to the same P-wave $q\bar{q}$ triplet. Suggestions that the confusion is due to low-mass scalar glueballs and multi-quark states near the $K\overline{K}$ threshold can be scrutinized in a high-statistics analysis of two-photon production of $\pi\pi$ and $K\overline{K}$ pairs at low masses [127].

$J^{PC} = 2^{-+}$-states

Recently, first observations of members of the $J^{PC} = 2^{-+}$ nonet, a neutral π_2 and the hitherto unobserved η_2, have been reported [128]. The spectroscopy of orbitally excited $q\bar{q}$ states is still in its infancy and very few states are established. At high luminosity two-photon reactions offer in many cases particularly clean conditions for filling the empty places in the chart.

Glueballs

A great challenge for two-photon resonance physics is the search for exotic, i.e. non-$q\bar{q}$ states. QCD predicts bound states of gluons, the glueballs. Their discovery would unambiguously prove the non-abelian structure of QCD. Since glueballs contain no electric charge their $\gamma\gamma$ decay width should be OZI suppressed. On the other hand, glueballs are expected to be abundantly produced in radiative J/ψ decays. In this reaction C-even mesons can be formed via the coupling to two gluons rather than to two photons. Thus the comparison of meson spectra obtained in these two reactions seems to be a good method to pin down glueballs. However, until now the $\gamma\gamma$ measurements are statistically not yet comparable to the measurements of radiative J/ψ decays.

Four-Quark states

Another open question in meson spectroscopy concerns the existence of four-quark states, $qq\bar{q}\bar{q}$. Depending on their quark composition, characteristic two-photon widths are expected. Those states which have dominant pseudoscalar-pseudoscalar decompositions should have, via VDM, small $\gamma\gamma$ couplings. Candidate states are the scalars $a_0(980)$ and $f_0(975)$ (formerly δ and S). On the other hand $qq\bar{q}\bar{q}$ states with 'superallowed' decays into vector meson pairs would naturally show up in $\gamma\gamma$ interactions. The experimental investigation of vector meson pair production has been stimulated by the observation of a large threshold enhancement for $\gamma\gamma \rightarrow \rho^0\rho^0$. Similar channels, involving ρ, ω ϕ, and K* mesons, have been investigated. A major contribution comes from the ARGUS experiment exploiting its good particle identification and π^0 reconstruction efficiencies [129]. Crucial tests of the four-quark model are possible with partial wave analyses. However, for most channels the luminosity available today is not sufficient for this purpose.

Resonance formation by virtual photons

Up to this point we were discussing the couplings to real photons. Measurements of the q^2 dependence of $\gamma\gamma$ couplings are much more involved. They require tagging devices and need much more luminosity since the fluxes for

virtual photons are reduced. Resonance formation by virtual photons allows probing the spatial structure of the particles. Definite QCD predictions exist, e.g., for the large-q^2 behaviour of the π^0 form factor. Large-q^2 photons ($q^2 > 1GeV^2$) can be tagged by detecting the scattered electron in the central detector. The π^0 form factor has been measured up to about 2 GeV^2 [128]. At the B-factory one could extend this range to 50 GeV^2 or more, well within the regime where the QCD predictions can stringently be tested.

Axial vector states

Some states are only accessible through virtual photons, *e.g.* axial vectors. Recent measurements of an axial vector state in the E/ι region [130] turned out to have a strong impact on the interpretation of the states observed in this region in radiative J/ψ decays.

Sensitivity: $Br \cdot \Gamma \geq 0.01\ eV$

Experience shows that the classification of resonances is not an easy task. The identification of non-$q\bar{q}$ states can be convincing only if the conventional $q\bar{q}$ states are found and if then extra states remain which do not fit into the scheme. Obviously the situation becomes even more complicated if mixing between the various objects occurs. This problem can only be solved if complementary information from different reaction types can be combined, such as from hadronic reactions, radiative J/ψ decays and $\gamma\gamma$ reactions. The measurements in two-photon physics are not yet on the same statistical level as, e.g., those in radiative J/ψ decays. At a B-factory this situation could be significantly improved. From Fig. 39 one finds that an experimental sensitivity of $Br(R \to X) \cdot \Gamma(R \to \gamma\gamma) \approx 0.01$ to $0.1\ eV$ can be reached in the region up to the charm threshold.

12.2.2 Hadron Pair Production

$\gamma\gamma \to h\bar{h}$ at large p_T

The two-photon production of hadron pairs at large transverse momenta has been calculated in the framework of perturbative QCD. It has been pointed out [131] that a high luminosity B-factory would be well suited for measuring these processes. The accessible kinematical region will probably only allow to study the onset of the perturbative regime. However, for many channels the experiments at higher energy machines have effectively been constrained to a similar kinematical region because of lack of particle identification at higher momenta. With improved particle identification features, a B-factory experiment will be competitive for pion-, kaon- and proton pair production at least up to invariant masses of 3 GeV.

12.2.3 The Total Cross Section for Hadron Production by Two Photons

Total cross section

At the B-factory the total cross section for hadron production by two photons can be measured up to $\gamma\gamma$ invariant masses, $W_{\gamma\gamma}$, of several GeV. Such measurements yield results on

- the $W_{\gamma\gamma}$ dependence of the cross section,
- possible structures, in particular in the resonance region,
- the final state topology,
- the particle composition of the final state,
- the q^2 dependence of the total cross section.

The total cross section depends on the two-photon invariant mass $W_{\gamma\gamma}$ and the momentum transfer q_i^2 of the photons. Measuring the angles and energies of both the scattered electron and positron (double-tag) allows for the determination of these variables. In general, the total cross section has a complicated helicity structure which becomes simple only for quasi-real photons ($q_i^2 \to 0$).

Real-photon cross section

The direct measurement of the total cross section for two real photons requires the detection of both leptons at 0° with good energy resolution. However, 0° tagging may have a major impact on the machine and its compatibility with the high luminosity goal has to be studied. Tagging at larger angles makes a q^2 extrapolation necessary and with no-tag or single-tag measurements the $W_{\gamma\gamma}$ determination becomes model dependent. With its good particle identification features a B-factory experiment could improve the models for the two-photon hadronic final states measuring inclusive particle spectra.

12.3 Detector Requirements

General detector properties

For two-photon physics in the resonance region the detector should have an excellent capability for measuring exclusive final states. This leads to requirements on the apparatus very similar to those for the analysis of B-decays:

- good acceptance for charged and neutral particles with emphasis on the detector coverage in the beam directions;
- efficient triggers for low-momentum particles and low-multiplicity events;
- high reconstruction efficiencies and resolutions for neutral particles (π^0, η,...);
- good charged particle identification;
- good K_S^0 vertex reconstruction down to low momenta (i.e. little material in front of the tracking devices).

Low bias trigger is important

Particularly important for $\gamma\gamma$ physics is the acceptance in beam direction and the trigger requirements.

No-tag measurements

A variety of two-photon experiments can be done without tagging. In particular the reconstruction of exclusive final states produced by quasi-real photons can be well done in the no-tag mode. There is a nice kinematical feature which helps selecting completely detected final states: Since quasi-real photons are emitted with preferentially vanishing transverse momenta the $\gamma\gamma$ final state is characterized by a strong peaking at zero transverse momentum. With a cut on the total transverse momentum of the detected particles, exclusive final states can be extracted with little background.

Tagging

There are different reasons why one may want to tag the photons:

- measurement of the q^2 dependence of a reaction;
- background reduction (important for inclusive measurements);
- complete kinematical reconstruction (total cross section).

For the first two points a single-tag can be sufficient, for the last one a double-tag is required.

Tagging detectors measure the angles and energies of the scattered electrons. For large q^2 values the central detector can serve as a tagger (test of the QCD prediction for the π^0 form factor, see sect. 12.2.1). Small-angle taggers cover forward angles typically from about 20 to 100 mrad, restricting in the single-tag case the two-photon flux to roughly 10% of the no-tag case. At the proposed machine tagging devices can be installed in front of the mini-β quadrupoles starting at about 50 mrad. However, this may not cover sufficiently small angles. Smaller tagging angles can be detected behind the mini-β quadrupoles or even further downstream. Such a scheme allows in principle 0° tagging using the machine magnets near the interaction region to bend the scattered electrons out of the beam. In addition, the magnets serve as momentum analyzers. Such 0° taggers have been operated at DORIS, DCI and VEPP4.

12.4 Summary

- Exploiting the very high luminosity of a B-factory experiments on the formation of resonances by two-photons will provide indispensable information for the classification of light mesons. An issue of fundamental importance is the search for glueballs.
- The experimental program would also include total cross section measurements and inclusive and exclusive studies of the hadronic final states.
- With a rate of about 2 Mio. η_c's per year the B-factory is also a η_c-factory giving access to rare η_c decays.

- A large part of two-photon experiments can be done without specific requirements on the detector which would go beyond the needs for B-physics.
- During the design stage of the detector attention should be paid to the acceptance near the beam directions and the layout of the trigger.
- Small angle or 0° tagging devices will be installed if they are compatible with the high luminosity requirements.

13 Other Sources of B Mesons: A Comparison

13.1 Overview

Other options to do B physics

In recognition of the significant potential of the physics of b quarks, and partly also because of the absence of new exotic phenomena, experiments at high-energy e^+e^- colliders and at hadron machines are turning to the study of B decays. Compared to a threshold B factory, LEP and in particular high-energy hadron accelerators offer a much larger b production cross section (see Fig. 40). In this section, we outline the possibilities and limitations of those other options for B physics. All these approaches differ from a threshold B Factory in that:

- cms energies are well above $B\overline{B}$ threshold; many other particles are produced together with the B's, and all kinds of b-flavored hadrons, such as $B_u, B_d, B_s, B^*, \Lambda_b$, and possibly some B_c can be produced;
- the B's are no longer monochromatic (in the cm frame); they have a wide momentum distribution;
- while a b quark is still produced in association with its antiparticle, their momenta and flavors are (essentially) uncorrelated;
- the b hadron and its antiparticle are no longer in a pure quantum state; for all practical purposes, a B^0 and a $\bar{B}^0$ will e.g. oscillate independently of each other.

Advantages

These features offer some advantages over threshold B factories:

- all flavors of b hadrons, including B_s and Λ_b, can be studied simultaneously in one experiment;
- the momenta of B's and hence of their decay products are usually larger, easing the influence of multiple scattering on the vertex reconstruction, but making particle identification more difficult;
- compared to a 9.3 on 3 GeV B Factory, where the B's are not yet fully relativistic, average impact parameters of B decay tracks are up to 2 times bigger.

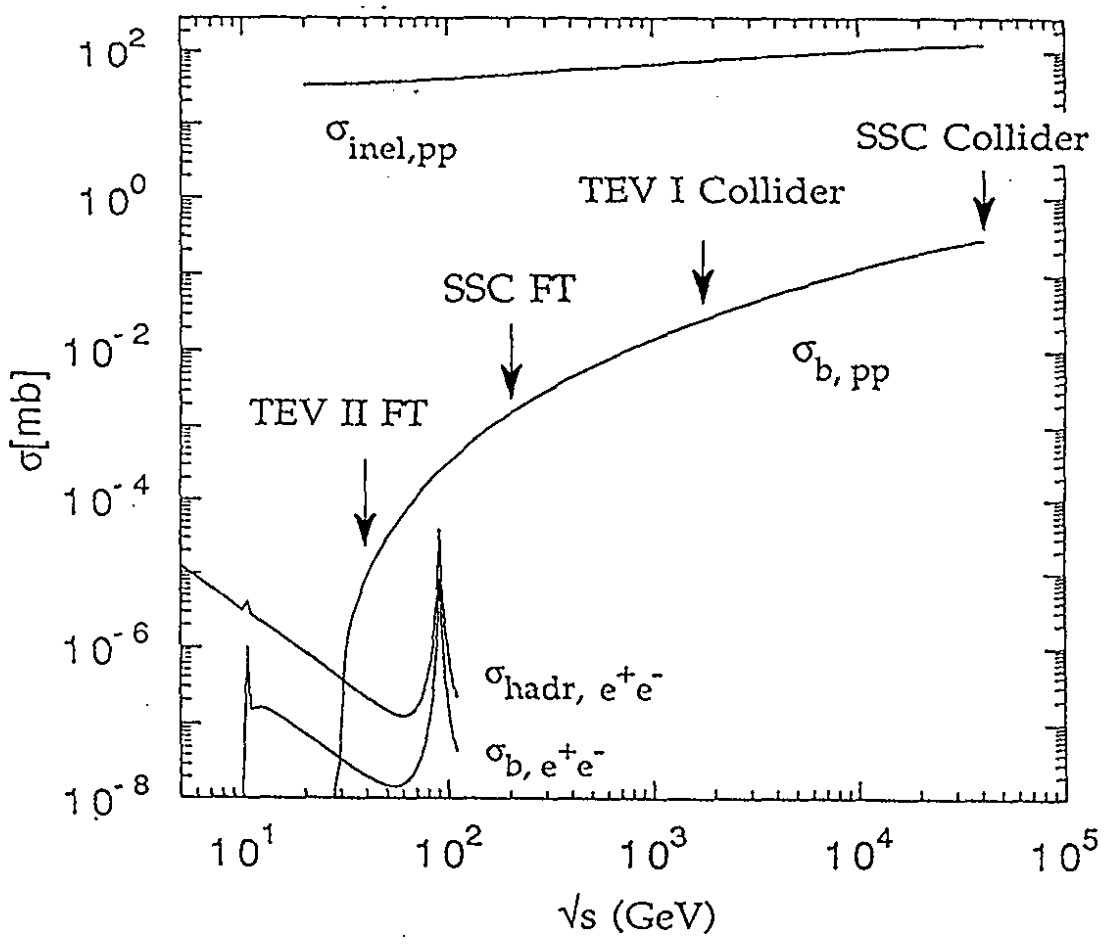

Figure 40: Total inelastic cross sections and $b\bar{b}$ production cross sections (as implemented in the PYTHIA MC) as a function of $\sqrt{s}$, for e^+e^- collisions and for pp interactions (at TEV I energies and above, the difference between pp and $p\bar{p}$ cross sections is negligible). The hadronic $b\bar{b}$ cross sections have significant uncertainties [132].

Disadvantages

There are also significant disadvantages:

- it is no longer possible to tag the flavor and the momentum of one b hadron by reconstructing its partner. However, even at SSC energies, there will rarely be more than one $b\bar{b}$ pair be produced in an event; one can therefore still use a b hadron to tag the anti-b hadron and vice versa;
- due to the incoherent oscillations of neutral B mesons, mistagging will be somewhat more frequent and will dilute asymmetries compared to B's from $\Upsilon(4S)$ decays;
- since one can no longer use energy constraints, the mass resolution worsens from 3-4 MeV (for threshold B factories) to 20-60 MeV, and combinatorial backgrounds rise;
- at hadron machines, the b cross section is a very small fraction of the total inelastic cross section, raising trigger problems.

B factories and other B sources are complementary

This discussion shows already that independently of rates, efficiencies etc., threshold B factories and the other b sources will tend to complement each other, and that most likely both approaches are needed to fully exploit the physics of b quarks and their hadrons. This is evident from past B physics results: high energy e^+e^- colliders have e.g. provided interesting results on average lifetimes, average semileptonic branching ratios or average mixing rates, but have up to now failed to go beyond inclusive measurements and to reconstruct exclusive decay modes. Collider experiments have offered tantalizing glimpses - such as the 35 $J/\psi K$, $J/\psi K^*$ events of *CDF* or their limits on $B^0 \to \mu^+\mu^-$, but could so far not compete on a broad basis with the wealth of results from CESR and DORIS.

For later reference, Tables XV and XVI as well as Fig. 40 summarize the main properties of b sources available now, or coming into operation during the life cycle of the proposed B Factory. Experiments currently running, or in preparation for data taking, include the LEP and SLC general-purpose detectors, the CDF and D0 detectors at the Fermilab Tevatron collider, and several dedicated fixed-target b experiments such as E-687, E-791, E-771 at Fermilab and WA-82 at CERN. With the exception of E-771, these latter experiments use an open geometry and try to enhance b events by triggering on charm; E-771 is a restricted-geometry, special-purpose apparatus to detect two-body B decay modes such as $B^0 \to \pi^+\pi^-$. A significant number of proposals for next-generation B experiments are being discussed at this time, both for the Tevatron collider and for the fixed-target program. Closer to home, the groups working at HERA are actively studying the options for heavy quarks physics in electron-proton collisions. Finally, it appears technically feasible to increase the LEP luminosity to 10^{32} cm^{-2}s^{-1}, with B yields comparable to those of a dedicated

Table XV: Properties of B Sources

	$\sqrt{s}$ (TeV)	$\mathcal{L}$ $(cm^{-2}s^{-1})$	$\int \mathcal{L}\, dt$ $per\ 10^7 s$	σ_{inel} (hadr.)	$\sigma_{b\bar{b}}$ [132]	$\sigma_{b\bar{b}}/\sigma_{inel}$	$b\bar{b}$ $per\ 10^7 sec$
B Factory	0.01	$3 \cdot 10^{33}$	30 fb^{-1}	4 nb	1 nb	0.2	$3 \cdot 10^7$
HERA (a)	0.31	$1.5 \cdot 10^{31}$	150 pb^{-1}	$\approx 5\mu b$	4 nb	$\approx 10^{-3}$	$6 \cdot 10^5$
LEP	0.09	$1.5 \cdot 10^{31}$	150 pb^{-1}	30 nb	5 nb	0.15	$8 \cdot 10^5$
TEV I Collider (before 1995)	1.8	10^{31}	100 pb^{-1}	60 mb	45 μb	$8 \cdot 10^{-4}$	$5 \cdot 10^9$
TEV I Collider (after 1995)	1.8	$5 \cdot 10^{31}$	500 pb^{-1}	60 mb	45 μb	$8 \cdot 10^{-4}$	$2 \cdot 10^{10}$
TEV II fixed target (b,c)	0.04	$(3 \cdot 10^{32})$	3 fb^{-1}	35 mb	15 nb	$5 \cdot 10^{-7}$	$5 \cdot 10^7$
SSC Collider (b,d)	40	10^{32}	1 fb^{-1}	100 mb	500 μb	$5 \cdot 10^{-3}$	$5 \cdot 10^{11}$
SSC fixed target (b,c)	0.2	$(2 \cdot 10^{32})$	2 fb^{-1}	45 mb	900 nb	$2 \cdot 10^{-5}$	$2 \cdot 10^9$

a) The total cross section used here refers to events with tracks in the detector acceptance and should only indicate the order of magnitude; the total photoproduction cross section is significantly larger.

b) Trigger and radiation damage problems are likely to limit interaction rates to 10 MHz.

c) Numbers refer to pN collisions; use of a heavy target (W) is likely to increase the (rate-limited) B yield by a factor 3-5, due to the different A dependence of total and b cross sections.

d) Cross sections given for the SSC are uncertain by factors 2-5. The ratio of b cross sections at the SSC and the LHC is roughly 2:1; the two machines are basically equivalent as far as b physics is concerned.

Table XVI: Properties of b sources: Median momentum P_B of reconstructed B mesons, median momentum p_{hadron} of their charged decay products, median impact parameter δ of charged decay products, and mean number n_{ch} of charged tracks in the detector.The numbers quoted are based on the PYTHIA 5.4 MC; they are approximate and depend somewhat on the detailed selection criteria.

Experiment	Detector coverage	P_B (GeV/c)	p_{hadron} (GeV/c)	$\delta(mm)$	n_{ch}
$\Upsilon(4S)$ B Factory	$\approx 4\ \pi$	3	0.5	0.17	11
LEP	$\approx 4\ \pi$	37	2.6	0.28	21
TEV II Fixed Target	10-200 mrad	120	9.4	0.29	14
TEV I Collider, forward	10-600 mrad	43	3.7	0.28	26
TEV I Collider, central	> 600 mrad	7	0.8	0.21	17
SSC Fixed Target	2-100 mrad	500	37	0.29	22
SSC Collider, forward	2-600 mrad	100	7.9	0.28	46
SSC Collider, central	> 600 mrad	10	1.0	0.21	21

B Factory; however, given the strong push towards LHC, it seems increasingly unlikely that this option will be realized.

The following sections address the b physics potential of HERA, of LEP, of the fixed target experiments and of the hadron colliders. Quoted annual rates refer to one "Snowmass year" (10^7 s at nominal luminosity).

13.2 Heavy Quark Physics at HERA

B meson yield of HERA is not sufficient to measure CP violation in B decays

While HERA will provide a copious source of charmed particles - rates near 10^8 charmed hadrons per year are predicted at design luminosity - the B hadron yield from photon-gluon fusion processes is "only" comparable to already existing e^+e^- facilities [133]. Due to the kinematics of the events and the rather significant backgrounds, both trigger- and reconstruction efficiencies will be smaller than at e^+e^- colliders [134]. We conclude that while HERA will certainly contribute to charm physics, the main goals in B physics, and the detection of CP violation in particular, are well beyond its projected reach.

13.3 B Physics at LEP

CP violation studies are out of reach for LEP I

The performance of LEP as a b-source has been discussed at various occasions [135]. As far as the number of produced $b\bar{b}$ pairs is concerned, LEP is roughly equivalent to a $10^{32}\,\mathrm{cm}^{-2}\mathrm{s}^{-1}$ B-Factory. The mass resolution for exclusive decays is 10-20 times worse. Since, however, decay products of B and $\bar{B}$ are well separated, the rise in combinatorial backgrounds will not fully reflect this factor. Cuts on secondary vertices may ultimately allow similar S/B ratios as for $\Upsilon(4S)$ machines, at the expense of efficiency. Partial reconstruction should be possible for "easy" decay channels such as Dl, D^*l, D_sl. In those partial modes, however, the lack of a good energy determination impairs the measurement of proper decay times and results in a smearing of oscillation signals. Ultimately, LEP experiments may collect samples of $O(10^3)$ fully or partially reconstructed B_u and B_d, and $O(10^2)$ B_s, sufficient for separate lifetime measurements in the 10%, and 20% range, respectively. Efficient flavor tagging in experiments with kaon identification, such as DELPHI, is claimed to allow B_s mixing measurements up to $x_s \approx 10$, or lower limits near $x_s \approx 15$. The limited b yield renders CP violation studies hopeless.

With a 10-fold luminosity upgrade, b rates at LEP are within a factor 3-4 of the proposed B Factory, and CP violation may be marginally within reach. A threshold B Factory is likely to have fewer systematic problems, since e.g. states with opposite CP parity such as $\mathrm{J}/\psi K_s$ and $\mathrm{J}/\psi K_s\pi^0$ are more easily separated. Without question, however, an enhanced LEP would nicely complement an $\Upsilon(4S)$ B Factory.

13.4 B Physics at Hadron Machines

Problems of triggering and radiation damage

As is evident from Table XV, nearly all high-energy hadron machines qualify as B factories in the sense that they produce 10^7 or more B's per year; the problem is mainly one of triggering and radiation damage, caused by the overwhelming rate of "ordinary" events. Throughout this section, we assume that interaction rates need to be limited to 10 MHz, for these reasons.

Rate handling requires orders-of-magnitude speed-up

We would like to emphasize in the very beginning that due to the trigger problems, the questions of backgrounds and radiation damage, and the small b yield (when compared to the total cross sections), present rate estimates for hadron machines have significant uncertainties - often up to one order of magnitude or more - in particular for complex processes such as the reconstruction and tagging of a B decay chain. It is often impossible to run a detailed enough simulation for a large enough sample of events, and trigger strategies will continue to be optimized during the whole lifetime of an experiment. Proposals for new detectors involve daring assumptions concerning data transfer rates and online processing capabilities, and may prove to be too optimistic.

13.4.1 Fixed Target Experiments

TEV II or SpS experiments do not challenge the B-factory

TEV II or SpS fixed target experiments start with a similar number of produced $b\bar{b}$ pairs as do B factories. However, with respect to the fraction of $b\bar{b}$ to all events, they provide by far the most unfavorable environment and require highly selective triggers, with low efficiency. Despite recent proposals for new and interesting triggering schemes [136], we are not aware of any existing or planned fixed-target B experiment, which would seriously and reliably challenge the proposed B factory on a broad basis. While fixed target experiments may ultimately be able to contribute to B spectroscopy and lifetimes, CP violation measurements and probably even B_s mixing studies are most likely beyond their scope [137].

13.4.2 The Fermilab Collider

Unprecedented amounts of processors required

The Tevatron collider (TEV I) will provide luminosities around 10^{31} cm^{-2}s^{-1} in the near future, and $5 \cdot 10^{31}$ cm^{-2}s^{-1} after the main injector upgrade foreseen for 1995. Both CDF [100] and D0 [139] have submitted proposals for major upgrades. CDF needs electronics modifications to cope with shorter bunch spacings and increased trigger rates, and expanded bandwidth into and increased capacity of the online processor farm; also the muon coverage should be improved. Especially for B physics, D0 proposes to add a small superconducting solenoid with silicon and scintillating fiber trackers, in addition to electronics and processor upgrades. Ideas for dedicated B detectors include "mini" and "micro" versions of the BCD apparatus discussed for the SSC [140], and a variant of the P238 detector originally proposed for the CERN-$Sp\bar{p}S$ [141]. The BCD detectors cover the central and forward regions with silicon tracking and Čerenkov particle identification; a "micro"-BCD could replace the CDF or D0 core detectors. The P238 detector is a forward spectrometer with silicon trackers inside the beam pipe, at a few mm from the circulating beams, using a data driven processor for on-line vertexing and triggering. Both the BCD and P238 options require unprecedented (but not impossible) amounts of trigger processors and higher-level online processor farms. In the following, we discuss the expected performance of these detectors for some of the classical B-physics benchmarks. Relevant B rates and expected sample sizes for existing or discussed TEV I and SSC/LHC experiments are summarized in Table XVII.

Exclusive B reconstruction and lifetimes.

Straight forward extrapolation of present CDF results to a sample of $500\,pb^{-1}$ let us expect $O(10^3)$ reconstructed B_u, B_d decays in modes with J/ψ, and some 10-100 events $B_s \to J/\psi\phi$. Lower lepton trigger thresholds and increased muon acceptance are likely to raise these numbers by a factor ≈ 10, sufficient for reasonably precise lifetime measurements and mass determinations (see Table XVII). With dedicated B detectors, B samples may increase by another factor $O(10)$. At CDF, rare decays like $B^0 \to \mu^+\mu^-$ may become accessible at

Table XVII: Expected B Event Samples and related Parameters

Experiment Trigger	CDF @ TEV I lepton	Mini BCD @ TEV I * sec. vtx.,l	P238 @ TEV I sec.vtx	BCD @ SSC sec. vtx.,l	P238 @ SSC sec. vtx.	SM'84 lepton
Luminosity $\#$ of $b\bar{b}$	$5 \cdot 10^{31}$ $2 \cdot 10^{10}$	$5 \cdot 10^{31}$ $2 \cdot 10^{10}$	10^{31} $5 \cdot 10^{9}$	10^{32} $5 \cdot 10^{11}$	10^{31} $5 \cdot 10^{10}$	10^{32} $5 \cdot 10^{11}$
$\#$ of $B \rightarrow J/\Psi K$, detected ΨK, lifetime error tagged ΨK, S/B for ΨK, $\Delta sin(2\beta)$	$2 \cdot 10^{5}$ $5 \cdot 10^{2}$ $5 - 10\%$ a few (l) ≈ 1 ≈ 1	$2 \cdot 10^{5}$ $6 \cdot 10^{3}$ $< 5\%$ $7 \cdot 10^{2}(K)$ $>> 1$ 0.15	$5 \cdot 10^{4}$ $1 \cdot 10^{3}$ 5% $4 \cdot 10^{2}(K)$ $>> 1$ 0.2	$5 \cdot 10^{6}$ $3 \cdot 10^{5}$ *few %* $2 \cdot 10^{4}(Dl)$ $>> 1$ 0.03	$5 \cdot 10^{5}$ $1 \cdot 10^{4}$ *few %* $4 \cdot 10^{3}(K)$ $>> 1$ 0.06	$5 \cdot 10^{6}$ $2 \cdot 10^{4}$ $2 \cdot 10^{3}(Dl)$ $>> 1$ 0.08
$\#$ of $B \rightarrow \pi^+\pi^-$ detected $\pi^+\pi^-$ tagged $\pi^+\pi^-$ S/B $\pi^+\pi^-$ $\Delta sin(2\alpha)$	$3 \cdot 10^{5}$ a few a few (l) $<< 1$ $>> 1$	$3 \cdot 10^{5}$ $3 \cdot 10^{4}$ $4 \cdot 10^{3}(K)$ < 1 > 0.1	$7 \cdot 10^{4}$ $7 \cdot 10^{2}$ $2 \cdot 10^{2}(K)$ ≈ 0.1 ≈ 1	$7 \cdot 10^{6}$ $2 \cdot 10^{6}$ $6 \cdot 10^{4}(Dl)$ ≈ 1 ≈ 0.02	$7 \cdot 10^{5}$	$7 \cdot 10^{6}$

Note: all numbers are based on $10^7 s$ running at the nominal luminosity, which is sometimes detector-limited. Almost all numbers involve some optimistic assumptions, such as a 10 fold increase in trigger efficiency for CDF due to increased coverage and lower lepton thresholds, *100% trigger efficiency in the case of BCD with (not yet* designed) J/ψ, lepton and sec. vertex triggers and almost perfect particle identification for BCD and P238.

branching ratios below 10^{-7}, while the triggering problems for $B^0 \to \pi^+\pi^-$ and many other hadronic modes are likely to require a secondary vertex trigger, as discussed e.g. by P238.

B_s mixing studies

Studies of B_s mixing require the determination of the B_s decay vertex, and a tag to identify the initial state. In the present CDF, only a lepton tag is possible, resulting in less than 100 tagged B_s for $500\,pb^{-1}$, not sufficient for a mixing measurement. A special detector using a kaon tag and a vertex trigger could ultimately allow the reconstruction of $O(10^4)$ tagged B_s; just about the number needed to establish B_s mixing in the expected range of mixing parameters, given present estimates for backgrounds and mistagging.

$x_s \leq 10$ may be measurable

CDF also proposes to study mixing using the distribution in the minimum distance of dileptons with $p_\perp$ above 5 – 10 GeV/c. The main limitation here is the smearing due to the poorly known B_s momentum. Nevertheless, a measurement up to $x_s \sim 10$ with an error of $\pm$ 2 is claimed to be possible with less than 100 pb^{-1}. However, even with more data it seems hard to extend this technique to larger x_s.

CP violation measurements

In the limit of small asymmetries, the error in the measurement of angles of the unitarity triangle (via ψK_s or similar decays to CP eigenstates) is given by

$$\Delta sin2\phi \approx \frac{1}{D(1-2p)}\sqrt{\frac{1+b}{N}}$$

where N is the number of events, b the signal-to-noise ratio, p the mistagging probability, and $D \approx 0.47$ a dilution factor related to the oscillation frequency. Table XVII lists the relevant numbers for CDF and for two special-purpose detectors. CDF will have to rely mainly on a double-lepton trigger and a lepton tag; the BCD- and P238-like detectors propose to use combined secondary-vertex and lepton triggers and to tag with a kaon, exploiting their particle identification.

Little hope to study CP asymmetries

As is evident from the table, CDF has little hope to study CP asymmetries; even for a new state-of-the art detector and large asymmetries, the case is marginal at best (given that *e.g.* the BCD numbers assume a perfect trigger, whereas even the ambitious P238 vertex trigger has at most 20% efficiency).

13.4.3 SSC/LHC

Assuming orders-of-magnitude advances in technology SSC/LHC will challenge B Factories

Much of what has been said for the BCD and P238 detectors for the Fermilab colliders can be carried over to their SSC/LHC incarnations, where usually an additional small-angle spectrometer is required to maintain the good acceptance. Interaction rates and radiation damage limit the luminosity to 10^{32} cm^{-2}s^{-1}, or even lower for P238 with its silicon detector very close to the beam. Mainly due to the larger b production cross sections, $b\bar{b}$ rates rise to $5 \cdot 10^{11}$/year, compared to $2 \cdot 10^{10}$ for the (upgraded) Tevatron. About one

in 200 events contains a b, easing triggering issues somewhat (but requiring readout of up to 10^5 events, or 500 GBytes, per second). Assuming that these problems can be solved, the SSC will contribute significantly to B physics. The projected detectors provide mass resolutions around 10 MeV, sufficient for the unambiguous identification of B final states. Even the (by today's standards) very cautious estimate of the snowmass group (SM 84) [142] puts the SSC/LHC on par with a B Factory, as far as CP violation in ψK_s modes is concerned; *more recent proposals [140][143] claim significantly enhanced sensitivity* (see Table XVII). At SSC/LHC energies, the merits of fixed-target experiments increase due to the larger b cross sections; the SSC fixed target program may indeed provide serious competition for a B factory. A recent, more detailed discussion can be found in [144].

13.5 Summary

CP violation studies have to wait for a B Factory or LHC/SSC

In an optimistic scenario, some of the open questions of B physics will be answered by the time a B Factory could come into operation. Measurements of separate B lifetimes with 10% precision and an observation of B_s mixing (for $x_s < 10...15$) seem feasible. CP violation studies will most likely have to wait for a B Factory or LHC/SSC (where detectors require orders-of-magnitude advances in technology and data handling capability). The study of decay dynamics, $b \rightarrow u$ transitions etc - which is needed for any comparison with SM predictions - is rarely addressed in detail in other proposals, but we feel that there - given similar numbers of events - a B Factory has a significant edge due to the known B momentum.

A Appendix

A.1 Event Generation

For the event generation we use the framework of the LUND Monte Carlo program version 6.3. The events are produced in asymmetric e^+e^- collisions of 9.33 GeV against 3.0 GeV, corresponding to $\beta\gamma = 0.6$. The LUND program has been modified to generate decay vertices of long lived particles such as B's, charmed mesons and τ leptons. The lifetimes used are listed in table XVIII.

Table XVIII: Lifetimes of heavy mesons and the τ lepton used in the event generation.

particle	lifetime (psec)
B_d, B_u	1.13
B_s	1.13
D^+	1.03
D^0	0.44
D_s	0.39
τ^-	0.46

All branching ratios were updated to be in accordance with the latest values from the particle data group [6].

We generated a variety of data sets. The signal events for specific reactions coming from $\Upsilon(4S)$ decays are described in the respective analysis sections. For certain cases we had the option to switch to an extension of the LUND generator which we especially developed to provide particle/antiparticle mixing and to model the proper CP violating time distributions in the case of neutral B decays in full detail. The present value of the mixing parameter in the B_d system is, averaged over the ARGUS and CLEO results, $x_d = 0.67 \pm 0.11$ [54]. Throughout our study we use a value of $x_d = 0.7$. To investigate backgrounds we used data sets of usual $\Upsilon(4S)$ decays with a ratio $\frac{f_0}{f_+} = \frac{BR(\Upsilon(4S) \to B^0\overline{B}^0)}{BR(\Upsilon(4S) \to B^+B^-)} = \frac{0.5}{0.5}$ and events coming from continuum $q\bar{q}$ production. We checked that the parameter setting in the LUND program is compatible with measured distributions such as multiplicities, topological quantities etc.

A.2 Detector Simulation

Having generated the events they were passed through a simulation of the detector as it is presented in part III. Before giving some details how the specific components were treated we like to emphasize two points of interest.

- We accounted for multiple scattering in every detector component and treated all the material exactly at its geometrical position.
- We allowed charged kaons, pions and muons to decay when traversing the detector. Specific energy loss was applied wherever appropriate.

All detector components were simulated with the geometric dimensions and materials as presented in part III. Certain assumptions were made to accomodate the CPU time needs in producing large data sets:

1. In the silicon vertex detector we assumed straight tracks for the charged particles neglecting any deflection due to the magnetic field in that small volume.
2. The momentum resolution of the main drift chamber was inferred by a parametrization. We smeared the transverse momentum p_T, the azimuthal angle ϕ and the polar angle $\cot\theta$. The resolution in p_T was taken as
$$\frac{\sigma(p_T)}{p_T} = \sqrt{0.01^2 + (0.009\, p_T[GeV/c])^2}\,. \tag{57}$$
3. The Ring Image Čerenkov counter was simulated in its geometry, the expression for the photoelectron statistics was taken into account properly.
4. The resolution of the electromagnetic calorimeter was parametrized, too. Energy, azimuthal angle ϕ and polar angle $\cot\theta$ were smeared. We took the following energy resolution:
$$\frac{\sigma(E)}{E} = \sqrt{0.004^2 + \frac{0.012^2}{\sqrt{E[GeV/c^2]}}}\,. \tag{58}$$

In the analyses we adopt for particle identification the strategy which is standard in the ARGUS collaboration and is explained in detail in ref. [38]. In short one calculates likelihoods for all particle hypotheses from the various components capable of any particle identification (*i.e.* main drift chamber via dE/dx, RICH, calorimeter, and μ chambers) by comparing the measured with the theoretically expected values, evaluates normalized likelihood and accepts the hypothesis which exceed a given cut–off value.

Bibliography

[1] L.-L. Chau and W.-Y. Keung, Phys. Rev. Lett. 53 (1984) 1802;
J.D. Bjorken, Fermilab Preprint, 1988 (unpublished);
C. Jarlskog and R. Stora, Phys. Lett. B208 (1988) 268;
J.L. Rosner, A.I. Sanda, and M.P. Schmidt, in Proceedings of the Workshop on High Sensitivity Beauty Physics at Fermilab, Fermilab, Nov. 11-14, 1987, ed. by A.J. Slaughter, N. Lockyer, and M.P. Schmidt, p.165.

[2] L. Wolfenstein, Phys. Rev. Lett. 51 (1983) 1945.

[3] ARGUS collaboration, H. Albrecht et al., Phys. Lett. B 197 (1987) 452, Phys. Lett. B 219 (1989) 121.

[4] ARGUS collaboration, H. Albrecht et al., Phys. Lett. B 229 (1989) 175, Phys. Lett. B 249 (1990) 359.

[5] CLEO collaboration, R. Fulton et al., Phys. Rev. D 43 (1991) 651.

[6] Particle Data Group, Phys. Lett. **239B** (1990).

[7] ARGUS collaboration, H. Albrecht et al., Phys. Lett. B 234 (1990) 409.

[8] CLEO collaboration, R. Fulton et al., Phys. Rev. Lett. 64 (1990) 16

[9] ARGUS collaboration, H. Albrecht et al., Phys. Lett. B 255 (1991) 297.

[10] M.K. Gaillard and B.W. Lee, Phys. Rev. D 10 (1974) 897.

[11] I.I.Y. Bigi, V. Khoze, N.G. Uraltsev, and A.I. Sanda: The question of CP noninvariance - as seen through the eyes of neutral beauty.
In C. Jarlskog (ed.): CP violation; Advanced Series on Directions in High Energy Physics Vol.3 pp. 175; World Scientific, Singapore, 1989

[12] World average using LEP results; see for example F. Dydak, Summary talk of the Moriond Electroweak session, Les Arcs, March 10-17th, 1991.

[13] L.J. Reinders, H. Rubinstein, and S. Yazaki, Phys. Rep. C 127 (1985) 1;
S. Narison, QCD Spectral Sum Rules; World Scientific Lecture Notes in Physics, Vol. 26; World Scientific, Singapore, 1989

[14] C.R. Allton et al., Nucl. Phys. B 349 (1991) 598;
C. Alexandrou et al., PSI-PR 90-28 (1990)

[15] C. Campagnari, CDF collaboration, Top Search in CDF, presented at the 25th Int. Conf. on High Energy Physics, Singapore (1990).

[16] ARGUS collaboration, H. Albrecht et al, Phys. Lett. B 192 (1987) 245.

[17] CLEO collaboration, A. Jawahery, Proccedings of the XXIV International Conference on High Energy Physics, Munich, W.Germany (1988).

[18] T. Inami and C.S. Lim, Prog. Theor. Phys. 65 (1981) 297.

[19] M. Schmidtler and K. R. Schubert, Karlsruhe preprint IEKP–KA/91/4.

[20] Feasibility Study for a B-meson Factory in the ISR Tunnel, CERN 90-02, March 1990, edited by T. Nakada.

[21] C.S. Kim, J.L. Rosner, and C.P. Yuan, Phys. Rev. D 42 (1990) 96.

[22] NA 31 collaboration, H. Burkhardt et al., Phys. Lett. B 206 (1988) 163.

[23] E 731 collaboration, J.R. Patterson et al., Phys. Rev. Lett. 64 (1990) 1491.

[24] I. Dunietz and J.L. Rosner, Phys. Rev. D 34 (1986) 1404.

[25] M. Bander, D. Silverman, and A. Soni, Phys. Rev. 43 (1979) 242.

[26] M. Bauer, B. Stech, M. Wirbel, Z. Phys. **C34** (1987) 103

[27] L.-L. Chau, *B* Mesons, a Beautiful Source of New Physics.
In C. Jarlskog (ed.): CP violation; Advanced Series on Directions in High Energy Physics Vol.3; World Scientific, Singapore, 1989

[28] I.I. Bigi and A.I. Sanda, Nucl. Phys. B 281 (1987) 41.

[29] R. Aleksan, I. Dunietz, B. Kayser, and F. LeDiberder, Saclay preprint DPhPE 90-17, SLAC-373 (1990)

[30] B. Kayser, M. Kuroda, R.D. Peccei, and A.I. Sanda, Phys. Lett. B 237 (1990) 508.

[31] I. Dunietz, H. Quinn, A. Snyder, W. Toky, and H.J. Lipkin, SLAC-PUB-5270, November 1990.

[32] M. Gronau, Phys. Rev. Lett. 63 (1989) 1451.

[33] M. Gronau and D. London, Preprint DESY 90-106, Sept.1990.

[34] M. Gronau, Phys. Lett. B 233 (1989) 479.

[35] CLEO II collaboration, D.S. Akerib et al., Phys. Rev. Lett. 67 (1991) 1692

[36] A. Fridman, CERN-EP/88-123 (1988)

[37] J.D. Bjorken, Nucl. Phys. B (proc. Suppl.) 11 (1989) 325.

[38] ARGUS collaboration, H. Albrecht et al., Nucl. Instr. Meth. A 275 (1989) 1

[39] ARGUS collaboration, H. Albrecht et al., DESY 91-077 (1991), to be published.

[40] M. Wirbel, M. Bauer, and B. Stech, Z. Phys. C 29 (1985) 637

[41] A.V. Dobrovolskaya, A.B. Kaydalov, K.A. Ter-Martirosyan, and V.R. Zoller, Phys. Lett. B 229 (1989) 293.

[42] R. Mundt, private communication; to be published

[43] SLAC-353 (1989)

[44] N. Isgur and M. Wise, Phys. Lett. B 232 (1989) 113, Phys. Lett. B 237 (1990) 527.

[45] ARGUS collaboration, H. Albrecht et al., DESY preprint DESY XXX (1991).

[46] N. Isgur, D. Scora, B. Grinstein, and M.B. Wise, Phys. Rev. D 39 (1989) 799

[47] J.G. Körner and G.A. Schuler, Z. Phys. C 38 (1988) 511

[48] J.M. Cline, W.F. Palmer, and G. Kramer, Phys. Rev. D 40 (1989) 793

[49] ARGUS collaboration, T. Oest et al., International Symposium on Heavy Flavours, Orsay 1991

[50] V.L. Chernyak et al., Sov. J. Nucl. Phys. 38 (1983) 773;
S. Narison, Phys. Lett. B 197 (1987) 405;
C.A. Dominquez and N. Paver, Phys. Lett. B 197 (1987) 423, Phys. Lett. B 199 (1987) 596.

[51] H.Marsiske in "The physics program of a high luminosity asymmetric B-factory at SLAC" ed. D. Hitlin, SLAC-**353**, p. 197

[52] K. Lingel et al., in "Physics rationale for a B-factory" CLNS 91-1043

[53] G. Martinelli, I.N.F.N. Roma preprint n.754 (1990)

[54] H. Schröder, in Physics in Collisions 1990, pp. 300

[55] A. Pais and S.B. Treiman, Phys. Rev. D 12 (1975) 2744

[56] P. Krawczyk, D. London, and H. Steger, Nucl. Phys. B 321 (1989) 1

[57] N. Byers and D.S. Hwang, UCLA preprint UCLA/87/TEP/44 (1987)

[58] ARGUS collaboration, H. Albrecht et al., Phys. Lett. 185 B (1987) 218.

[59] ARGUS collaboration, H. Albrecht et al., Phys. Lett. 255 B (1991) 297.

[60] K. Kleinknecht and B. Renk, Z. Phys. C 34 (1987) 209.

[61] B.A. Campbell and P.J. O'Donnell, Phys. Rev. D 25 (1982) 1989.

[62] N.G. Deshpande et al., Phys. Rev. Lett. 59 (1987) 183.

[63] S. Bertolini et al., Phys. Rev. Lett. 59 (1987) 180.

[64] E. Golowich and S. Pakvasa, Phys. Lett. B 212 (1988) 393.

[65] A. Ali and C. Greub, Phys. Lett. B 259 (1991) 182.

[66] W.-S. Hou et al., Phys. Rev. Lett. 59 (1987) 1521.

[67] B. Guberina et al., Phys. Lett. 90 B (1980) 169;
B. Guberina, Fizika (Zagreb) 16 (1984) 49;
G. Eilam, Phys. Rev. Lett. 49 (1982) 1478.

[68] J.D. Swain, ARGUS collaboration, Ph.D.thesis, University of Toronto, 1988, unpublished.

[69] F. Dydak, Rapp. talk, 25th International Conference on High Energy Physics, Singapore 1990

[70] J.H. Kühn,P.M. Zerwas, Phys. Rev. 167 (1988) 321

[71] W. Buchmüller , S. Cooper, High Energy Electron-Positron Physics, Singapore 1988, p.412

[72] J.H. Kühn, Proc. Intern. Symposium on Production and Decay of Heavy Hadrons, Heidelberg 1986, p.3

[73] H. Albrecht et al. (ARGUS) Phys. Lett. 199B (1987) 291

[74] H. Albrecht et al. (ARGUS) Phys. Lett. 160B (1985) 331

[75] M. Danilov, Proc. Intern. Symposium on Production and Decay of Heavy Hadrons, Heidelberg 1986, p.49

[76] Y.P. Kuang, T.M. Yan, Phys. Rev. D24 (1981) 2874

[77] P. Moxhay, Phys. Rev. **D37** (1988) 2557

[78] M.B. Voloshin, Sov. J. Nucl. Phys. 43 (1986) 1011

[79] R. Morrison et al. (CLEO), Phys. Rev. Lett. 67 (1991) 1696

[80] W. Kwong, J.L. Rosner, Phys. Rev. D38 (1988) 279

[81] H. Albrecht et al. (ARGUS) Phys. Lett. 167B (1986) 360

[82] A.Castro, et al. LAL 88-58, Los Alamos 1988.

[83] G.S.Abrams et al., Phys. Rev. Lett. 44 (1980) 10 .

[84] I.L.Rosner, Fermi-Inst. Preprint EFI 90-63, Chicago 1990.

[85] A.Martin and I.M.Richard, Phys. Lett. **185B** (1987) 246.

[86] C.Albajar et al. (UA1), Phys. Lett. bf 273B (1991) 540.

[87] H.Albrecht et al., Phys. Lett. **211B** (1988) 489.

[88] I.D.Bjorken, Fermilab-Conf-88/134-T.

[89] H. Schröder, Proc. XXIV Intern. Conf. High Energy Physics, Munich 1988, p.73

[90] E.L. Berger, Proc. XXIV Intern. Conference High Energy Physics, Munich 1988, 987

[91] J.C. Anjos et al., Phys. Rev. Lett. **62** (1989) 722

[92] J.M. Gerard, Rheinfels Workshop on Hadron Mass Spectrum (1990) UCL–IPT–90–16

[93] B. Stech, in Proposal for an e^+e^- – Collider, PSI PR-88-09

[94] M. B. Voloshin and M. A. Shifman, Sov. J. Nucl. Phys. **47** (1988) 199

[95] M. Voloshin and M. Shifman, Sov. J. Nucl. Phys. **45** (1987) 292; Sov. J. Nucl. Phys. **47** (1988) 511

[96] H. Albrecht et al., (ARGUS) Phys. Lett. **232B** (1989) 398

[97] T.Bowcock et al. (CLEO), Phys. Rev. **D41** (1990) 774

[98] J.L. Rosner, Comm. Nucl. Part. Phys. **16** (1986) 109

[99] S. Fleck and J.M. Richard, Part. World 1 (1990) 67

[100] I.I. Bigi UND–HEP–88–BIG03 (1988)

[101] H. Albrecht et al., (ARGUS) Phys. Lett. **199B** (1987) 447

[102] R.J. Morrison and M.S. Whitherell, Ann. Rev. Nucl. Sci. **39** (1989) 183

[103] H. Albrecht et al., (ARGUS) DESY 91-023

[104] D. Wyler and W. Buchmüller, Phys. Lett. **177B** (1986) 377

[105] I. Bigi and A.I. Sanda, Phys. Lett. **171B** (1986) 320

[106] J.F. Gunion et al., UCD-89-4

[107] H.Albrecht et al. (ARGUS), Phys. Lett. **250B** (1990) 164

[108] S.Boris et al., Phys. Rev. Lett. **58** (1987) 2019

[109] R.Abela et al., Phys. Lett. **146B** (1984) 431

[110] H.Albrecht et al. (ARGUS), Phys. Lett. **202B** (1988) 149

[111] H.Harari and Y.Nir, Nucl. Phys. **B292** (1987) 251
S.Sarkar and A.M.Cooper, Phys. Lett. **148B** (1984) 347

[112] Nading Qi, Proc. Workshop on tau lepton physics, Orsay, 1990
J.Kirkby, Proc. Workshop on tau lepton physics, Orsay, 1990

[113] J.J.Gomez-Cadenas et al, Phys. Rev. **D41** (1990) 2179

[114] P.Abreu et al. (DELPHI), Phys. Lett. **267B** (1991) 422.
B.Adeva et al. (L3), Phys. Lett. **265B** (1991) 451.

[115] H.Albrecht et al. (ARGUS), DESY preprint **91-084** (1991).

[116] J.Smith (CLEO), Proc. Workshop on tau lepton physics, Orsay, 1990

[117] K.G.Hayes et al. (MARK II), Phys. Rev. **D25** (1982) 2869
R.M.Baltrusadis et al. (MARK III), Phys. Rev. Lett. **55** (1985) 1842
H.Albrecht et al. (ARGUS), Phys. Lett. **185B** (1987) 228
S.Keh et al. (CRYSTAL BALL), Phys. Lett. **212B** (1988) 123
T.Bowcock et al. (CLEO), Phys. Rev. **D41** (1990) 805

[118] H.Albrecht et al. (ARGUS), DESY preprint **92-013** (1992).

[119] T.Bowcock et al. (CLEO), Phys. Rev. **D41** (1990) 805.

[120] "Proposal for an electron positron collider for heavy flavour particle physics and synchrotron radiation", PSI PR-**88-09**

[121] H.Albrecht et al. (ARGUS), Z. Phys. **C41** (1988) 405.

[122] H.Albrecht et al. (ARGUS), Phys. Lett. **185B** (1987) 223

[123] A.Pich, Phys. Lett. **196B** (1987) 561

[124] H.Albrecht et al. (ARGUS), Phys. Lett. **246B** (1990) 278

[125] W.Fetscher, Phys. Rev. **D42** (1990) 1544

[126] H. Kolanoski, Two-Photon Physics at e^+e^- Storage Rings, Springer Tracts in Modern Physics, Vol.105, Springer Verlag, Berlin, 1984;
Ch. Berger and W. Wagner, Phys. Rep. 146 (1987) 1;
H. Kolanoski and P. Zerwas, in 'High Energy Electron-Positron Physics', ed. A. Ali and P. Söding, World Scientific, Singapore.

[127] M.Feindt and J.Harjes, Two-Photon Couplings of Scalar and Tensor Mesons, Proc. of the Workshop on the Hadron Mass Spectrum, St.Goar 1990, eds. E.Klempt and K.Peters.

[128] M.Feindt, Some Snapshots of New CELLO and Crystal Ball Results on $\gamma\gamma$ Reactions, Proc. of the 25. Intern. Conf. on High Energy Physics, Singapore 1990 (DESY 90-128).

[129] A. Nilsson, Proceedings of the 8th Intern. Workshop on Photon-Photon Collisions, Shoresh Israel, April 1988.

[130] TPC/Two-Gamma Coll., H. Aihara et al., Phys. Rev. Lett. 57 (1986) 2500;
Mark II Coll., G. Gidal et al., Phys.Rev.Lett. 59 (1987) 2016.

[131] E. Maina, University of Torino, DFTT 26/87 (1987)

[132] P. Nason et al., Nucl. Phys. B303 (1988) 607, B327 (1989) 49, B 335 (1990) 260;
G. Altarelli et al., Nucl. Phys. B308 (1988) 724;
J.C. Collins, R.K. Ellis, Fermilab-Pub-91/22-T (1991)

[133] A. Ali et al., in Proc. of the HERA Workshop, Hamburg, 1987, p. 395

[134] H1 Collaboration, J. Burger et al., PRC-91-01

[135] J.H. Kuhn, P. Zerwas, CERN 89-08 (1989) p.267;
P. Roudeau, LAL 89-21 (1989), LAL 90-47 (1989);
G. Wormser, 89-29 (1989)

[136] G. Charpak, Y. Giomataris, L. Lederman, CERN-PPE/91-22 (1991)

[137] J.A. Appel, Fermilab-Conf-90/173 (1990)

[138] Proposal for an Upgraded CDF Detector, Proposal to FNAL, CDF Collaboration (1990)

[139] D0 Upgrade proposal, Proposal to FNAL, D0 Collab. (1990)

[140] BCD Collaboration, SSC-EOI0008 (1990);
J.G. Heinrich and K.T. McDonald DOE/ER/3072-61 (1990)

[141] A Brandt et al, CERN-SPSC/88-33 (1989);
J. Ellet et al, Proposal to FNAL, (1991)

[142] J.W. Cronin et al., Proceedings of the 1984 Summer Study, Snowmass, Co.(1984), p. 161

[143] J. Ellett et al., CERN/DRDC 91-18

[144] D. Denegri, CERN-PPE/90-181 (1990)

Part II

Study of an Asymmetric e^+e^- Collider for B-Physics in the PETRA Tunnel at DESY

1 Introduction

How to increase luminosity

The physics program for an asymmetric collider in the 10 GeV center of mass energy range requires a luminosity of $\mathcal{L} \approx 3 \cdot 10^{33} cm^{-2} s^{-1}$. This is one to two orders of magnitude larger than the luminosities which are presently obtained in e^+e^- storage rings. This study shows how such a large improvement can be achieved. The essential factors which determine the luminosity are

- focusing of the beams at the interaction point,
- storage of beam currents,
- control of beam-beam forces.

Strong focusing

As far as the focusing is concerned, there is not much room for improvement with respect to present colliders. The bunch length imposes a limit for the size of the beam envelope functions at the interaction point (IP). The bunch length of stored e^+e^- beams is not a very flexible parameter. It can be reduced on the expense of a large increase in rf voltage and rf power or by reducing the longitudinal focusing by choosing a less dispersive optical lattice. The change of these parameters is limited by the rapidly increasing costs and by the destructive impact on the beam stability. In addition, strong focusing requires strong lenses and large beam envelopes within these lenses. This causes considerable chromatic aberrations and must be compensated by nonlinear sextupole fields in the arcs which in turn introduce nonlinear acceptance limitations. Most existing e^+e^- colliders operate already very close to the chromaticity limit. Moreover, strong lenses have to be placed very close to the IP. This competes with the space requirements of the detector. Very compact quadrupole lenses are needed to overcome this problem. A large improvement with respect to conventional quadrupole design has already been achieved by using rare earth permanent magnets at the CESR collider at CORNELL [1] which allows one to focus the beam very close to the bunch length limit.

Beam-beam interaction

An important performance limitation of e^+e^- storage rings is the beam-beam interaction. The strongly nonlinear forces imposed by the beams upon each other are parameterized by the induced betatron tune shift $\Delta\nu$, which can be calculated from a linearized beam-beam force. Even if one compares very different colliders, the tune shifts achieved for each interaction varies only between $0.015 \leq \Delta\nu \leq 0.07$ (see Table X). Its dependence on machine parameters like circumference, beam energy, damping time, energy spread or number of interaction points is rather weak. As important is the optimization of operating conditions, like closed orbit corrections, choice of tunes, optimization of damping distributions, compensation of optical distortions and corresponding distortions of symmetries, and the suppression of spurious dispersions [2]. Round

beams (horizontal beam size equal to vertical beam size at the IP $\varepsilon_x = \varepsilon_y$, $\beta_x^* = \beta_y^*$) promise higher values of the tune shift according to some simulations [3]. However, they appear to be much more unfavorable from the point of view of focusing and synchrotron radiation background [4]. Therefore, the conventional flat beam scenario is still more attractive.

Large beam currents are essential

From these considerations one has to conclude that the major part of the gain in luminosity has to come from an increase in the beam currents. Since the intensity of a single bunch is limited by the beam-beam interaction and the available aperture, the total current has to be increased by the use of many bunches in each ring. Since additional parasitic bunch crossings must be avoided this implies that the electrons and positrons are stored in different rings which merge only at well defined interaction points.

Energy asymmetry

Crucial for the experiments to be done at the new e^+e^- collider is the ability to accurately measure the distance between the decay points of the two B mesons originating from the reaction $e^+e^- \rightarrow \Upsilon(4S) \rightarrow B^0\overline{B}^0$ (see Chapter I.3). With modern vertex detectors one is able to measure this distance with a resolution of about 50 μm. If the e^+e^- collider is operated with equal beam energies, the $\Upsilon(4S)$ is produced at rest in the laboratory system and the B mesons travel only about 30 μm, a distance too small to be measured with present day's detectors. The solution to this dilemma is to boost the $\Upsilon(4S)$ in the laboratory frame by running the e^+e^- collider with unequal beam energies, hence the name Asymmetric Collider. If one chooses $E^- = 9.33\,GeV$ and $E^+ = 3.0\,GeV$ the $\Upsilon(4S)$ moves in the laboratory frame with a Lorentz boost of $\beta\gamma = 0.6$ and the mean distance between the two B meson decays becomes 210 μm which is well measurable.

As far as accelerator design and performance is concerned, an asymmetric scheme offers certain advantages compared to symmetric high luminosity colliders, but it also implies some problems. The advantage of asymmetric collisions is that the beams can be separated magnetically and can therefore easily be collided head-on. On the other hand, simultaneous focusing of the two beams becomes a problem which can only be solved on the expense of larger chromaticity. There are no known direct disadvantages of unequal beam energies for beam-beam collisions. However the fact that other important parameters such as beam cross sections or β-functions at the IP of the two beams are not necessarily the same and cannot easily be made equal can be disadvantageous. Another problem is, of course, that there is no experience available on asymmetric collisions and one relies completely on theoretical predictions and simulations.

For fixed circumferences of the two machines, it is obvious that the costs of installation and supply of rf power will increase rapidly with the ratio of the two beam energies. Furthermore, the maximum beam currents will be unbalanced due to the different sensitivities with respect to beam-beam forces which makes it more difficult to achieve the beam intensities necessary for high luminosity.

As a consequence, the design of a double ring e^+e^- collider presents an interesting challenge. Main tasks have been identified in the following areas:

Interaction region

- The layout of the interaction region (IR) is rather complex. The two beams need to be separated early after the collision to avoid parasitic beam-beam interactions. The beam envelopes have to stay manageably small and the single bunch currents low. Furthermore the beams have to be focused more or less simultaneously to achieve small cross sections at the IP for both beams (10 μm vertical rms beam size) while the beam envelopes in the quadrupoles of the final focus section have to remain small enough to stay within the aperture and chromaticity limits. This has to be achieved without generating much synchrotron radiation in order to obtain tolerable background conditions for the detector.

Active damping

- The large beam currents to be stored in an asymmetric collider require a large number of rf cavities to restore the energy lost by synchrotron radiation. This implies a large impedance of parasitic resonant cavity modes. They are responsible for a coupling between the particle bunches, causing coherent instabilities. Special rf cavities which are optimized for small impedance of the parasitic modes rather than for high shunt impedance of the fundamental mode are needed. Even with such an rf system, the necessary beam currents cannot be kept stable in the machine without powerful active dampers which control the coherent coupled bunch instability. Since the beam currents have to be distributed over many bunches, such a damper system has to have a broad bandwidth. For the collider described in this study the required bandwidth amounts to 42 MHz. The requirements on strength and bandwidth exceed by far what has been achieved in this field up to now. The feedback system is the most delicate and critical new technical component of an asymmetric collider.

The remaining elements of the collider design are quite conventional and require only state-of-the-art accelerator concepts and technology.

Flexible design

The machine has to be designed to meet the main parameters and boundary conditions such as planned beam currents, an anticipated strength of the beam-beam interaction, requirements on geometry and beam envelope to achieve tolerable background conditions. However, main parameters and necessary conditions can only be predicted from extrapolations with limited reliability. Therefore it is necessary to keep the design flexible. This means especially that the beta functions at the interaction point and the beam emittances must be allowed to vary at least by a factor of two in either direction.

Choice of PETRA

In this study, we demonstrate the feasibility of a high luminosity asymmetric e^+e^- collider with two rings of the same circumference in the PETRA tunnel. The aim of this study is to show how such a facility can be built in principle and how it would fit into the PETRA tunnel. There is no detailed technical layout of standard machine components yet; we reserve this for a later technical

proposal. However, critical areas such as the layout of the interaction region have been carefully investigated. Major components of the collider have been designed in some detail to the extent to allow a first cost estimate.

Two rings of same size

The collider is based on two rings of the same size. The main reasons to abandon the principle of rings of different sizes as described earlier [5,6,7,8] are to improve the interaction region layout especially with respect to synchrotron radiation background, to have the possibility of more than one experiment, to avoid some problems with coherent beam-beam interactions [9], and to decouple the choice of the location of the IP from the location of existing injection channels.

High energy ring (HER) + low energy ring (LER)

In contrast to other projects [10,11,12,13] an asymmetric collider in the PETRA tunnel will have a somewhat large circumference of $C = 2304$ m. We consider this a good size for an asymmetric beauty factory. In the present study, a copy of the existing PETRA storage ring is forseen to store the high energy beam (HEB). The available bending radius matches well the needs of a high intensity 9 GeV machine. The low energy beam (LEB) is stored in a ring of the same circumference but with fewer and stronger bending magnets. The rf power and rf installation needed to store the large beam currents necessary for the high luminosity do not exceed the 10 MW already installed during PETRA 23 GeV e^+e^- operation. The power density of the synchrotron light radiated by the HEB in the interaction region and in the arcs does not impose a heavier load on the vacuum system than the one which has been mastered already during previous PETRA operation. All the single bunch beam parameters of the two equally sized rings can be achieved quite safely. A certain disadvantage of a large circumference and a low revolution frequency is that it is potentially more difficult to achieve large beam currents because the more densely spaced lines of the beam spectrum overlap more likely with parasitic modes of the rf resonators. On the other hand, the impedance of these parasitic modes scales at least linearly with the inverse machine radius. Lack of radiation damping is not expected to be an important issue. There is only a weak dependence of coupled bunch stability and thus total beam intensity on the machine radius which becomes irrelevant in presence of a strong active damper system. We conclude that the optimum circumference of a B-factory, were it to be designed without the constraint of using existing facilities, would be rather close to the PETRA circumference.

2 Choice of Parameters

Beam energies

The choice of the beam energies, *e.g.* the degree of energy asymmetry, is a compromise between optimum machine design and asymmetry requirements from the experiments. As has been pointed out in Part I, there are good arguments to keep the Lorentz boost $\beta\gamma$ of the $\Upsilon(4S)$ near 0.6 . This corresponds to beam energies of $E_1 = 9.3\,GeV$ and $E_2 = 3\,GeV$. The present study is based on this asymmetry of $E_1/E_2 = 3.1$. If one considers the rf power consumption of the high energy beam (HEB) of a double ring collider with equal circumferences and the stability of the low energy beam (LEB), it is obvious that the asymmetry should be as small as possible. At a first look one might conclude that for fixed rf power consumption the luminosity of a symmetric collider would be roughly twice as large as for a collider with an energy asymmetry of $\gamma_1/\gamma_2 = 3.1$. However, for small or zero asymmetry, the advantage of easy magnetic separation would be lost and the optimum luminosity could not be achieved. An energy asymmetry of $\gamma_1/\gamma_2 = 3.1$ is large enough to find satisfactory solutions for the magnetic separation (see section 4.1).

Equal beam cross sections at the interaction point

The design parameters of the machine which are necessary to achieve the desired luminosity of $\mathcal{L} = 3 \cdot 10^{33} cm^{-2} s^{-1}$ may be derived from the luminosity formula

$$\mathcal{L} = \frac{N_1 N_2 f_b}{2\pi \sqrt{\sigma_{x1}^2 + \sigma_{x2}^2}\sqrt{\sigma_{y1}^2 + \sigma_{y2}^2}} \tag{59}$$

where "1" and "2" indicate electrons and positrons, respectively, N is the number of particles per bunch, $\sigma_{x,y}$ are the rms beam width and height at the IP, respectively, x and y indicate the horizontal and the vertical coordinate, and f_b is the bunch frequency. It can be seen from equation (59) that, if the beam cross section of one of the two beams is decreased with respect to the other one, the corresponding increase of the luminosity is limited to a factor of two. However, the emittance blow up of the larger beam due to the nonlinear forces imposed by the smaller beam prevents that this can be achieved. The damage may be parameterized by the tune shift which results from linearizing the beam beam force around the origin

$$\Delta\nu_{y1} = \frac{r_0\, N_2\, \beta_{y1}^*}{2\pi\, \gamma_1\, \sigma_{y2}\, (\sigma_{x2} + \sigma_{y2})}. \tag{60}$$

Here, r_0 is the classical electron radius, β^* the beam envelope function at the IP, and γ the relativistic factor; gaussian spatial distributions are assumed. The tune shift rises quadratically with the decrease in σ of the opposite beam. Moreover, experience on hadron collisions at the SPS [14] indicates that the larger beam suffers additional damage by the increase of nonlinearity due to the smaller size of the opposite beam. This does not mean that the beam cross

sections have to be exactly the same. Tennyson[15] for example demonstrated by a semianalytic treatment that the optimum choice of beam sizes does not necessarily correspond to exactly equal cross sections. However, in general one may safely assume that the difference in cross section of the two beams needs to be small ($|\sigma_1/\sigma_2 - 1| \leq 1$). If one neglects a small difference in cross sections, the luminosity formula can be expressed by the parameters of either beam "1" or "2" as

$$\mathcal{L} = \frac{I_{1,2}\,\gamma_{1,2}\,\Delta\nu_{1,2}\,(1+\kappa)}{2\,e\,r_0\,\beta^*_{y1,2}} \tag{61}$$

(κ is the aspect ratio of the beams, e is the elementary charge and I is the beam current). For flat beams, it is a conservative guess that the horizontal maximum beam-beam tuneshift is limited at the same value as the vertical one, $\Delta\nu_x = \Delta\nu_y$. Hidden behind equation (61) are requirements on the current of the opposing beam

$$I_2 = I_1 \frac{\beta^*_2}{\beta^*_1} \cdot \frac{\Delta\nu_1}{\Delta\nu_2} \cdot \frac{\gamma_1}{\gamma_2} \tag{62}$$

and on the beam emittances

$$\varepsilon_1 = \frac{I_2\,r_0}{2\pi\,e\,f_b\,\gamma_1\,\Delta\nu_1\,(1+\kappa)} \tag{63}$$

$$\varepsilon_2 = \varepsilon_1 \cdot \frac{\beta_1}{\beta_2} \tag{64}$$

The basic parameters of the collider are related by these formulae.

Design luminosity: $3 \cdot 10^{33} cm^{-2} s^{-1}$

In this study, a collider design is presented which provides beam currents, beam-beam tune shifts, β^* values, and beam emittances which correspond to a luminosity of $3 \cdot 10^{33} cm^{-2} s^{-1}$. These main parameters are listed in Table I.

Table I: Main Parameters of an Asymmetric $e^+ - e^-$ Collider in the PETRA tunnel

	High Energy Ring	Low Energy Ring
Particles	electrons	positrons
Beam Energy E/GeV	9.33	3.0
Circumference L/m	2304	2304
Harmonic Number	3840	3840
Beam Current I/A	0.71	1.1
Number of Bunches	640	640
Particles per Bunch	$5.28 \cdot 10^{10}$	$8.21 \cdot 10^{10}$
Hor. Emittance $\varepsilon_x/rad \cdot m$	$0.5 \cdot 10^{-7}$	$1.0 \cdot 10^{-7}$
$\varepsilon_y/\varepsilon_x$	0.05	0.05
β_x^*/m	0.40	0.20
β_y^*/m	0.02	0.01
Beam-Beam Tuneshift $\Delta\nu_x$	0.04	0.04
Beam-Beam Tuneshift $\Delta\nu_y$	0.04	0.04
Luminosity $\mathcal{L} = 3 \cdot 10^{33} cm^{-2} s^{-1}$		

3 The Asymmetric Collider in the PETRA tunnel

The asymmetric collider has to be integrated into the existing accelerator chains at DESY. Especially the possible interference with the operation of the HERA e-p-collider has to be minimized. This means that PETRA has to be left essentially untouched. The two B-factory rings have to be assembled in large well-planned shutdown periods.

Space requirements

The preferred scenario is as follows: The two B-factory rings are situated on top of the existing PETRA ring. The two rings will be supported from the outer tunnel wall and the tunnel roof. Fig. 41 shows a cross section of the

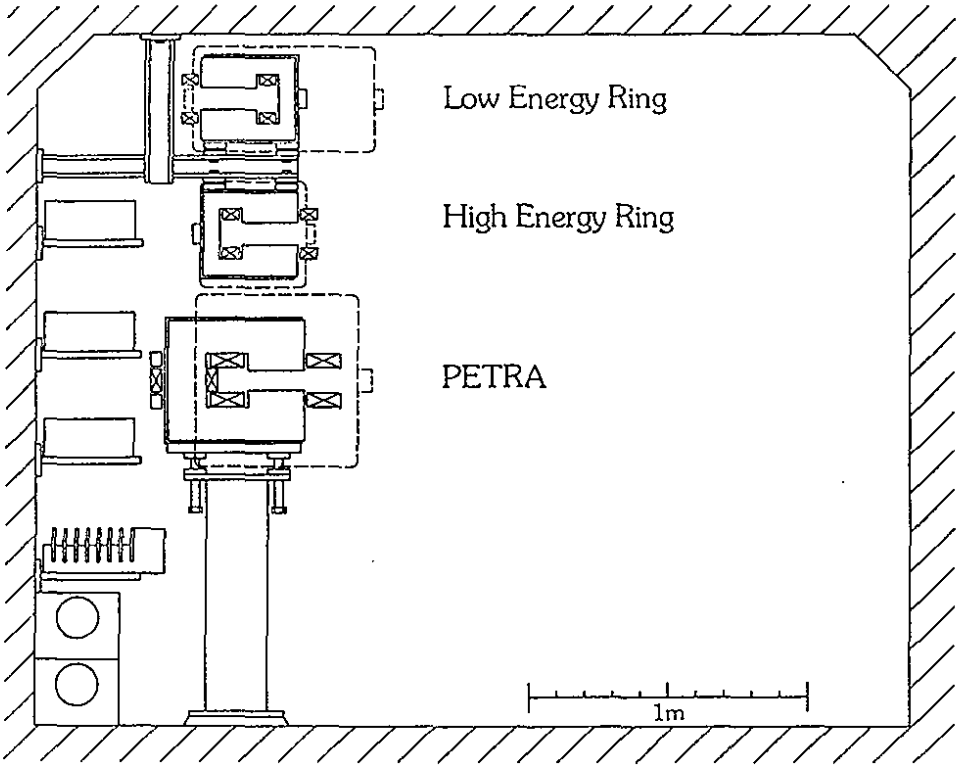

Figure 41: PETRA tunnel cross section in the arcs with HELENA magnets added

PETRA tunnel in the normal arcs. In the rf sections conflicts between the space requirements for waveguides, tuners and couplers of the three machines will occur. This can however be avoided by placing the rf systems in the two remaining former experimental halls of PETRA. An engineering layout of the rf sections still needs to be finalized.

Interaction region in the PETRA NE hall

In the interaction region, the PETRA ring has to be separated horizontally from the asymmetric collider. This is accomplished by inserting a 20 m long straight section into the PETRA arcs about 120 m from the IP. The subsequent ends of the arc are shifted into the straight section. No change in bending radius is necessary. At the IP, the PETRA ring is horizontally separated from the collider by 7 m (see Fig.42). The tunnel cross section has to be enlarged on the outside over a length of ca. 200 m. The use of the PETRA North East Hall as the experimental hall would be favorable, because the tunnel is above ground level in this region and there are no buildings that could hinder the civil engineering.

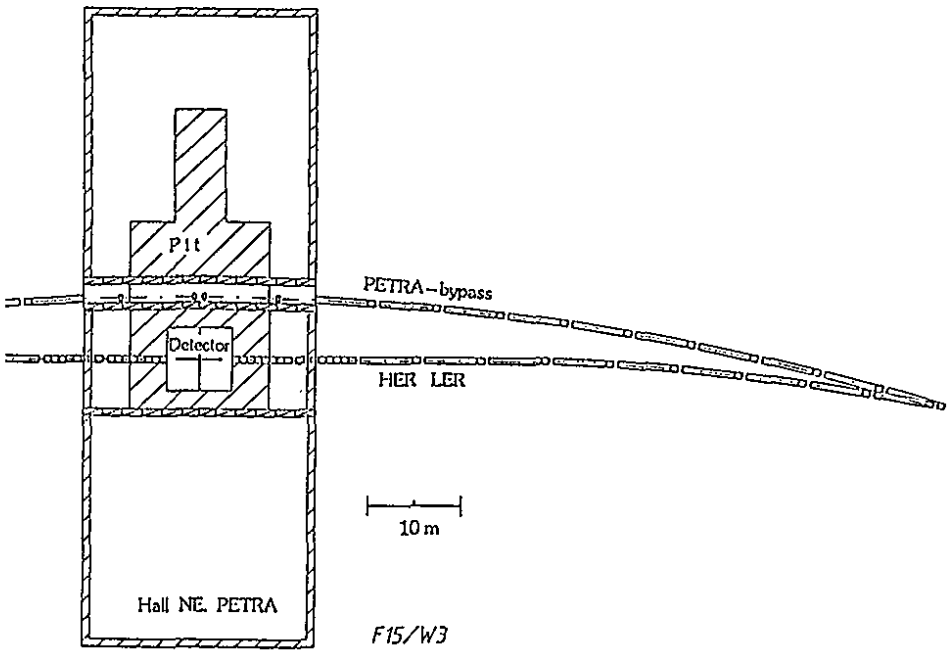

Figure 42: PETRA bypass in the NE interaction zone

Infrastructure

The cooling infrastructure of PETRA has to be upgraded by doubling the present capacity. Additional cable trays at the inside tunnel wall and below the ceiling are also needed.

4 Design of the Asymmetric Collider

4.1 Layout of the Interaction Region

The most difficult part of the lattice design is the layout of the interaction region (IR). Both beams need to be focused strongly to provide the small β-functions which are necessary for high luminosity. They need to be separated immediately after collision. Great care has to be taken to avoid intolerable background conditions for the experiment due to synchrotron radiation reaching the IR.

Beam separation in the vertical plane

In the present design, early separation is provided in the vertical plane by making partial use of the field of the detector solenoid (B = 1 T) which is horizontally tilted by 110 mrad with respect to the beam axis. The orbits of both the HEB and the LEB pass off-center through the low-β quadrupole magnets, where they are deflected further. The displacements of the quadrupole axis with respect to the two orbits are carefully optimized. The displacements are just large enough to preserve the necessary separation all along the low β focusing section. A minimum separation of two times seven vertical standard deviations is obtained for all parasitic bunch crossings near the IP. There is no symmetry in the quadrupole placements between the left and right side of the IP. The offsets of the beam traveling towards the IP are kept as small as possible. Thus the amount of synchrotron radiation generated during the beam separation and directed towards the interaction region is kept at a relatively low level.

Simultaneous focusing of both beams

Small values of the β-functions at the IP (β^*) must be achieved for both beams. This requires that the two beams must be focused more or less simultaneously to avoid large chromatic aberrations and unreasonable large values of the beam envelopes in the high energy beam. The chromaticity of the two beams is balanced by overfocusing the LEB by the inner low β quadrupole triplet (Q1,Q2,Q3). The LEB focus is mapped that way into two additional waists of the envelope function which occur at a distance of 3.2 m from the IP. Outer quadrupole doublets (Q4,Q5) follow which focus the beam more gently to match with the envelopes outside the low-β insertion. Right in the additional envelope waist points, strong additional quadrupoles lenses (Q3) are placed which have an impact mainly on the HEB. This arrangement of six quadrupole lenses on each side of the IP focuses the two beams simultaneously and yields for both beams the same ratio of β^*-values and chromaticity.

After leaving the outer quadrupole, the trajectories of the two beams can be separated completely. This is accomplished by a 10 m long, very soft vertically defocusing quadrupole (combined function separator magnet) which is aligned

along the axis of the HEB. The two beams enter this magnet already pre-separated by the tilted solenoid and the displaced quadrupoles (see Fig. 45). Therefore, the LEB trajectory diverges rapidly from the magnet axis. The high field region is only reached towards the end of the quadrupole which is rather far away from the IP and the detector. This magnet provides the final beam separation in the vertical plane. The synchrotron radiation generated in this beam separation scheme is extremely low. It provides an excellent starting point for further reduction of detector backgrounds by optimized collimators and masks.

There is sufficient space left between the quadrupole doublet and the triplet for dipole correction coils and trim quadrupoles, vacuum pumps and beam position monitors.

The two rings are finally completely separated by two vertical bending magnets. One of such a pair is needed on both sides of the IP in each of the two rings. Due to the limited space in a PETRA interaction straight section, vertical and horizontal bending magnets are interleaved. As a consequence, the two beams are tilted with respect to the main machine plane. This tilt is restricted to the interaction region and has opposite signs for the two beams. Fortunately the relative tilt angle of $\Delta\Theta \simeq 0.01\,\mathrm{mrad}$ is much smaller than the aspect ratio of the beams ($= 50\,\mathrm{mrad}$).

It should be pointed out that this beam separation scheme is also applicable in the horizontal plane. In addition it could be arranged antisymmetrically with respect to the IP in order not to exclude the option of collisions at a crossing angle with and without crab crossing. In this study, only the geometrically most simple case has been worked out.

Beta functions at the IP

The reference solution has for the LEB β-functions at the IP of $\beta_y = 1\,\mathrm{cm}$ and $\beta_x = 20\,\mathrm{cm}$. The natural chromaticities in the low-energy lattice are $\xi_x = -68.5$ and $\xi_y = -88.3$ whereas the lattice without insertion would have $\xi_x = -37$ and $\xi_y = 39.6$. This is close to the limit given by the shrinking of the dynamic aperture due to chromaticity correcting sextupoles.

For the HEB, the parameters are somewhat more relaxed with $\beta_y^* = 2\,\mathrm{cm}$, $\beta_x^* = 40\,\mathrm{cm}$ and chromaticities of $\xi_x = -53$, $\xi_y = -54$ for the lattice with the insertion and $\xi_x = -29$, $\xi_y = -30$ without. Maximum β-functions do not exceed 400 m in the HEB and are below 100 m in the LEB. Fig. 43 and Fig. 44 show the beam envelopes for the HEB and the LEB in the IR.

The innermost low-β quadrupole (Q1) is made from Sm_2Co_17 permanent magnetic material. The other two quadrupoles (Q2,Q3) in the first triplet are superconducting. The magnets including supports fit inside a polar angle of 200 mr. These magnets are partly inside the magnetic field of the detector. The extra HEB quadrupole (Q4) and the quadrupole doublet (Q5,Q6) are conventional quadrupole magnets. The separator magnet is a Panofsky type quadrupole with a large aperture. They are described below.

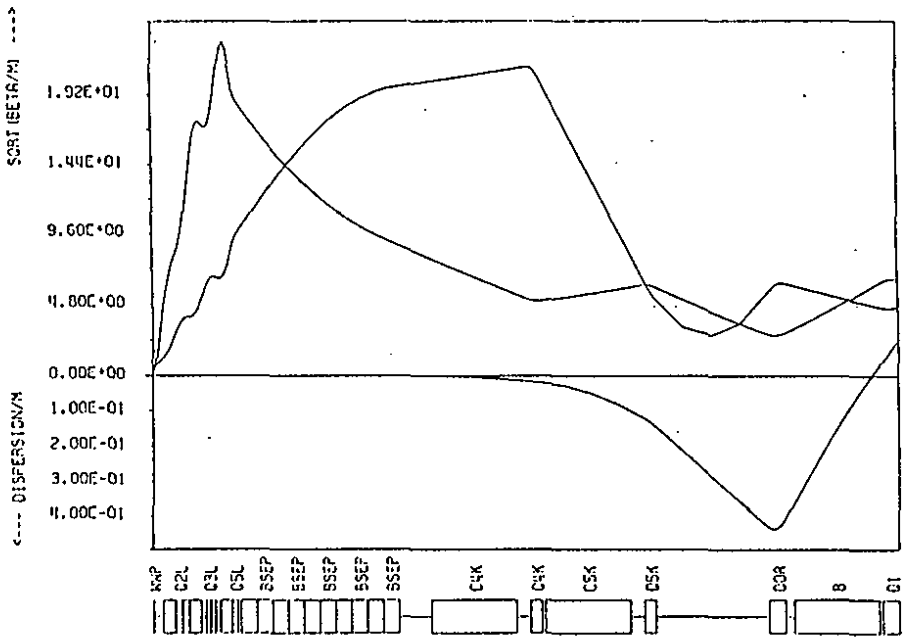

Figure 43: High energy beam optics in the arcs. Plotted are the horizontal and vertical envelope functions $\sqrt{\beta_x}$, $\sqrt{\beta_y}$ and the dispersion function D_x vs. z .

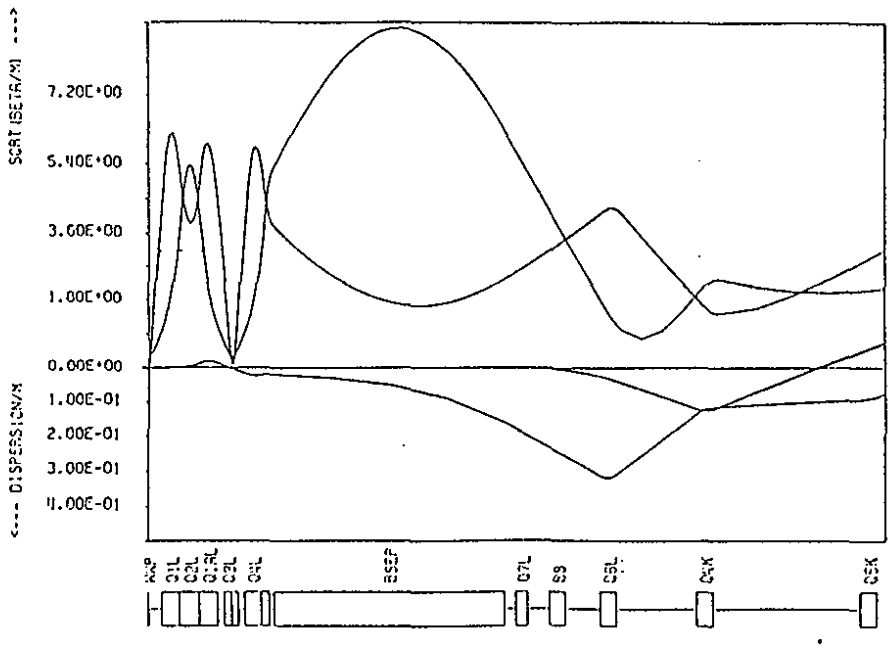

Figure 44: Low energy beam optics in the arcs. Plotted are the horizontal and vertical envelope functions $\sqrt{\beta_x}$, $\sqrt{\beta_y}$ and the dispersion function D_x vs. z .

Beam transport elements in the IR and their properties are listed in Table II. Table III describes the beam separation and beam focusing parameters.

Table II: Parameters of Elements in the IR

Element	type	distance from IP $[m]$	length $[m]$	Gradient $[T/m]$	Apertures h/v $[mm]$
Left-side Elements (l)					
Sol	Solenoid	0.0	1.700	0.0000	25.
Q1a-l	Perman. Quad	0.60	0.270	3.0851	39.
Q1a-l	Perman. Quad	0.87	0.250	3.0851	42.3
Q1b-l	Perman. Quad	1.12	0.250	3.0851	48.5
Q2-l	S.C. Quad	1.37	0.860	3.2174	50.0
Q3-l	S.C. Quad	2.23	0.770	3.0851	50.0
Q4-l	Normal Quad	3.30	0.860	2.7349	50.0
Q5-l	Normal Quad	4.20	0.705	3.2996	50.0
Q6-l	Normal Quad	4.955	0.345	3.2016	50.0
Sep-l	Panofsky Quad	5.50	10.0	0.0294	70.-150.
Right-Side Elements (r)					
Sol	Solenoid	0.0	2.000	0.0000	25.
Q1a-r	Perman. Quad	0.60	0.270	3.0851	39.
Q1a-r	Perman. Quad	0.87	0.250	3.0851	42.3
Q1b-r	Perman. Quad	1.12	0.250	3.0851	48.5
Q2-r	S.C. Quad	1.37	0.860	3.2103	50.0
Q3-r	S.C. Quad	2.23	0.770	3.1072	50.0
Q4-r	Normal Quad	3.30	0.860	2.7369	50.0
Q5-r	Normal Quad	4.20	0.705	3.2992	50.0
Q6-r	Normal Quad	4.955	0.345	3.1983	50.0
Sep-r	Panofsky Quad	5.50	10.0	0.0294	70.-150.

Fig. 45 gives a side view of the interaction region with enlarged vertical scale, showing the apertures of quadrupole lenses and vertical beam envelopes of both beams. Fig. 46 shows the design of the IR magnet supports.

Precision of positioning

The lenses have to be positioned precisely. Without correction, the lenses are allowed to deviate systematically by only $\Delta x = 0.1\,\mathrm{mm}$ from their ideal position. Otherwise the orbit distortions in the interaction region exceed $\Delta x_{c.o.} = 10\,\mathrm{mm}$ which is all the available spare aperture. Uncorrelated displacements of the quadrupoles have to be smaller than $\Delta x \leq 10\,\mu\mathrm{m}$. If one assumes that the positions of quadrupoles within a triplet or doublet are not independent, the requirement is relaxed to $\Delta x \leq 30\,\mu\mathrm{m}$. In order to prevent spontaneous separation of the beams during beam beam interaction by more than 1/10 vertical standard deviation, the mechanical motion of the lenses have to be limited to amplitudes below $0.3\,\mu\mathrm{m}$. This means that the mechanical motion has to be

Table III: Beam Separation Parameters

Element	Offset		10 σ-Beam Envelope				Beam
name	HEB	LEB	HE-Hor	HE-Ver	LE-Hor	LE-Ver	Separ.
	$[mm]$		$[mm]$				$[mm]$
Left Side IR (l) HEB incoming							
IP	0.0	0.0	1.3	0.065	1.3	0.065	0.0
Sol-u	-0.4	-1.8	2.4	1.9	6.5	5.2	1.4
Q1a-l-d	0.1	-2.3	3.2	2.8	6.5	5.2	2.4
Q1b-l-d	0.6	-2.2	4.3	3.4	9.8	5.4	2.6
Q1c-l-d	1.1	-1.8	5.6	3.7	15.2	4.5	2.9
Q2-l-d	0.8	-2.1	5.6	3.7	15.2	4.5	2.9
Q2-l-u	0.8	-4.5	8.1	6.2	15.2	3.4	5.3
Q3-l-d	2.8	-2.5	8.1	6.2	15.2	3.4	5.3
Q3-l-u	2.8	-4.1	10.2	8.1	4.2	3.7	6.9
Q4-l-d	0.0	-5.7	12.1	7.9	2.4	1.8	5.7
Q4-l-u	0.0	-5.9	13.8	8.8	2.4	1.7	5.9
Q5-l-d	5.0	-2.3	13.6	9.9	4.2	3.7	7.3
Q5-l-u	5.0	-2.2	16.7	9.8	14.0	4.5	7.2
Q6-l-d	0.0	-6.9	17.2	9.6	15.3	4.2	6.9
Q6-l-u	0.0	-6.3	19.6	8.8	20.6	3.4	6.3
SEP-l-d	-30.0	-36.7	20.3	8.6	21.6	3.3	6.7
SEP-l-u	-30.0	-114.6	41.0	4.0	24.3	2.1	84.6
Right Side IR (r) LEB incoming							
IP	0.0	0.0	1.3	0.065	1.3	0.065	0.0
Sol-u	0.4	-1.0	2.4	1.9	6.5	5.2	1.4
Q1a-r-d	1.2	-2.3	3.2	2.8	6.5	5.2	3.5
Q1b-r-d	1.9	-2.2	4.3	3.4	9.8	5.4	4.1
Q1c-r-d	2.4	-1.0	5.6	3.7	15.2	4.5	3.4
Q2-r-d	3.4	0.0	5.6	3.7	15.2	4.5	3.4
Q2-r-u	5.4	0.0	8.1	6.2	15.2	3.4	5.4
Q3-r-d	5.4	0.0	8.1	6.2	15.2	3.4	5.4
Q3-r-u	6.9	0.0	10.2	8.1	4.2	3.7	6.9
Q4-r-d	6.7	0.0	12.1	7.9	2.4	1.8	6.7
Q4-r-u	7.4	0.0	13.8	8.8	2.4	1.7	7.4
Q5-r-d	8.7	0.5	13.6	9.9	4.2	3.7	9.2
Q5-r-u	8.9	0.5	16.7	9.8	14.0	4.5	9.4
Q6-r-d	6.8	-1.5	17.2	9.6	15.3	4.2	8.3
Q6-r-u	6.5	-1.5	19.6	8.8	20.6	3.4	8.0
SEP-r-d	-30.0	-38.3	20.3	8.6	21.6	3.3	8.3
SEP-r-u	-30.0	-110.7	41.0	4.0	24.3	2.1	80.7
-u = upstream end, -d = downstream end							

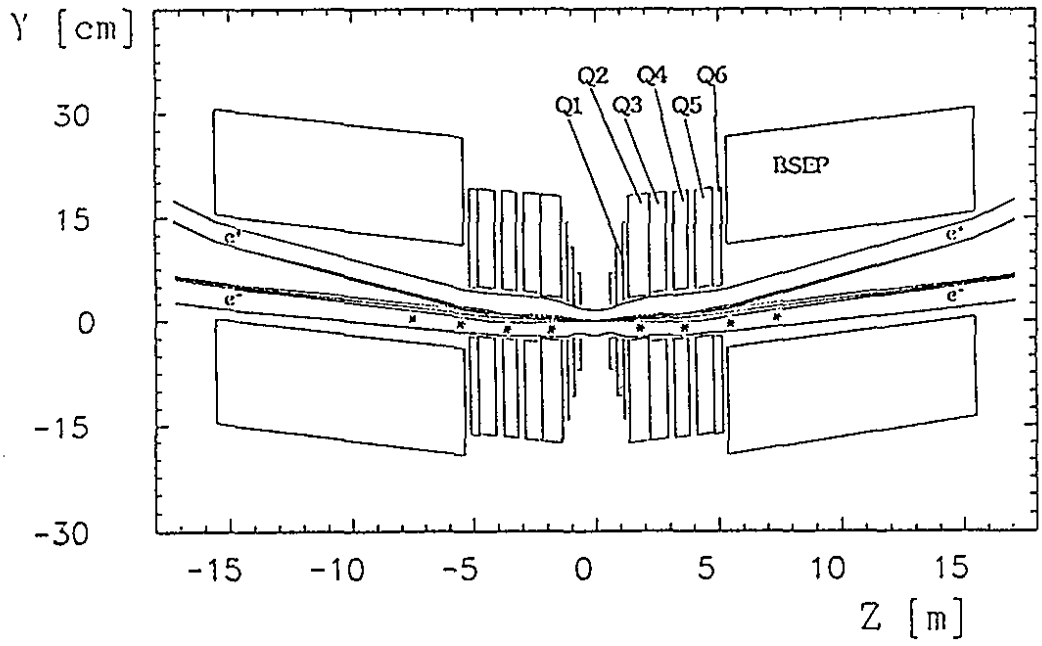

Figure 45: Side view of the IR with enlarged vertical scale, showing the apertures of quadrupole lenses and vertical beam envelopes of both beams.

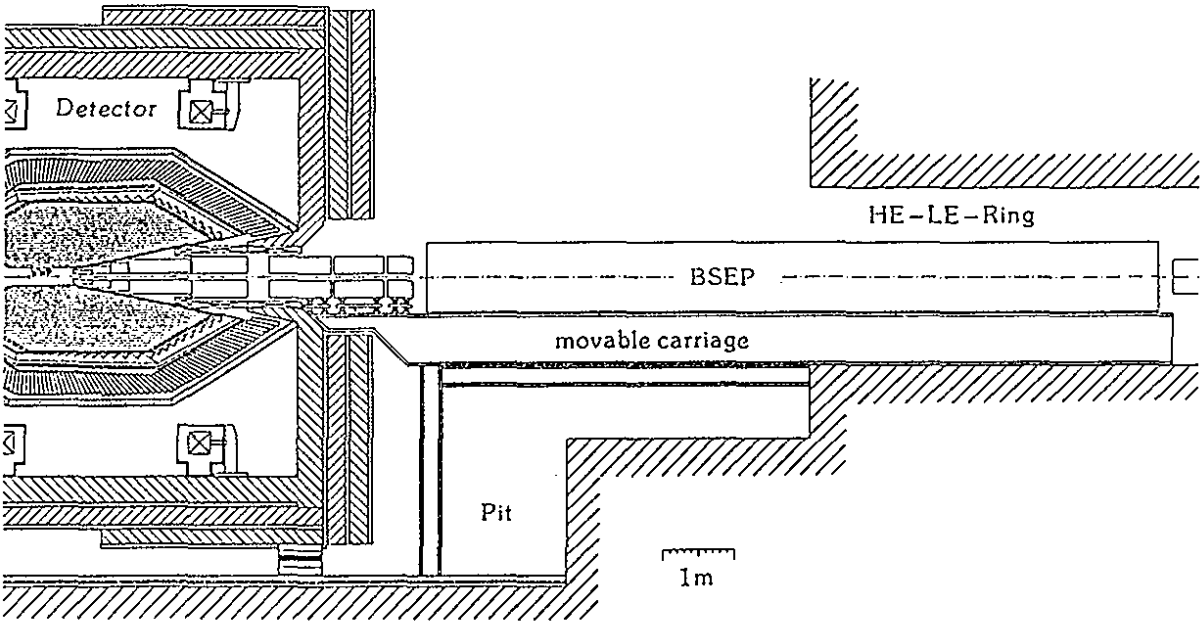

Figure 46: Design of the IR magnet supports

stabilized very well and temperatures of the magnets and the supports during operation have to be well controlled. Continuous monitoring of slow drifts in the quadrupole positions appears to be necessary. Local dipole correction coils have to be placed close to the low β-triplet. The permanent magnetic quadrupole magnets must be movable within a few tenths of a millimeter. The longitudinal component of the detector field causes a coupling of the vertical orbit into the horizontal plane. This can be compensated by a vertical tilt of the solenoid of about 1 mrad.

The quadrupole gradients must be very precise. The systematic gradient error should be as small as $\Delta G/G \leq 10^{-3}$ to limit the β-beat to 10%. The rms value of uncorrelated quadrupole errors has to be as small as $(\Delta G/G)_{rms} \leq 5 \cdot 10^{-4}$. This makes local quadrupole trims unavoidable since permanent magnetic quadrupole magnets cannot be kept stable to such a precision. Measurement of the beam spot at the IP appears to be necessary to correct for unavoidable gradients errors.

4.2 Low Energy Lattice

Radiation damping in the LER

The main issue of the low energy lattice design is to improve the weak radiation damping which would be obtained for a low beam energy of E = 3.0 GeV in a large machine with an average machine radius of $\bar{R}$ = 367 m.

In a realistic design, the lattices of the high energy ring and of the low energy ring should not differ very much from the lattice of the existing PETRA ring such that a common support structure and infrastructure can be used for the three rings in the same tunnel. Thus the basic cells of the two lattices should have the same length. This is an important constraint. The low energy ring (LER) cell structure is therefore a copy of the PETRA FODO lattice. It is composed of eight octants which are separated by four short straight sections (the former interaction regions) and the four long straight sections. The IR of the asymmetric collider is located in the North-East short straight section. However, for sufficient radiation damping, the bending field which corresponds to the nominal PETRA bending radius of ρ = 192 m is too weak. To obtain strong magnetic fields, the 5.378 m long dipole magnets are placed only into every 4th half cell. This reduces the bending radius to ρ = 48 m. It also reduces the magnet costs for the LER since the same dipole magnets can be used for HER and LER. Another advantage is that the strong magnetic field B = 0.21 T is favorable for effective pumping with integrated ion getter pumps. The center of the LER-dipole magnets has to be shifted radially outwards by 20 cm with respect to the PETRA dipole in order to preserve the circumference of 2304 m. At each end of the arc a special dipole magnet is needed to match the design trajectory along the course of the tunnel in the straight section.

The two rings of the collider are arranged on top of each other. The vertical distance between the two orbits in the arc is 50 cm. Two vertical bending magnets at each side of the IR are necessary to match the low energy orbit to the IR orbit.

Wigglers

The reduction of the bending radius is still not sufficient for satisfactory radiation damping and large beam emittance. The lattice includes therefore six superconducting wiggler magnets with an effective integrated magnetic field of $\int ds|B_{wiggler}| = 1.8\,T \times 6\,m$. With these magnets, the energy spread $\Delta E/E$ of the LEB is increased to 10^{-3}, which is a limit given by the width of the $\Upsilon(4S)$ resonance. The damping times are reduced by a factor of about five (from $\tau_x = 300\,\text{ms}$ to $\tau_x = 65\,\text{ms}$). The required beam emittance of $\epsilon_x = 10^{-7}\,rad \cdot m$ can be easily obtained by choosing the appropriate value of the emittance of the dispersion trajectory $D_x^2\gamma_x + 2\alpha_x D_x D_x' + D_x'^2\beta_x$ inside the wiggler magnets. This is accomplished by adjustment of six matching quadrupoles in the arcs. The wiggler magnets are situated in the centre of the SE, SW and NW short straight sections. They consist of eight short 25 cm long superferric magnets separated by 1 m long drift sections where the synchrotron radiation of 30 kW per magnet is absorbed.

Lattice in the arcs

The beam optics in the arc is determined by alternating focusing (QF) and defocusing (QD) quadrupoles. The periodic cell which consists of two FODO cells with one bending magnet has the structure
$QF - BEND - QD - DRIFT - QF - DRIFT - QD - DRIFT - ....$
With a 120° betatron phase advance per cell (which corresponds to a 60° FODO lattice) one obtains a rather periodic course of the dispersion function in the arc (see Fig. 47) which is necessary for an effective chromatic correction. Increasing the phase advance to 180° between dipoles leads to an isochronous lattice. Thus the momentum compaction factor which is $\alpha_{comp} = 1.1 \cdot 10^{-3}$ in the nominal 120°-structure can be varied easily over a wide range which provides a large flexibility in the longitudinal focusing and in the bunch length. The nominal bunch length amounts to $\sigma_s = 1\,\text{cm}$ and requires an rf voltage of $U_{rf} = 9.5\,\text{MV}$ peak value. The parameters of the low energy ring are summarized in Table IV.

Due to the small β-functions at the interaction point of $\beta_y^* = 1\,\text{cm}$ and $\beta_x^* = 20\,\text{cm}$ and corresponding strong focusing in the interaction region, an elaborate chromaticity correction system has to be installed. The natural chromaticities amount to $\xi_x = -68.5$ and $\xi_y = -88.3$. This corresponds to values which have been achieved earlier in PETRA e^+e^- operation for optics with vertical β^*-function values of 6 cm and four interaction points.

In order to compensate linear and quadratic tune shift with momentum, four times six sextupole families are necessary (six families in each octant taking into account the mirror symmetry of the lattice). With this effort, the optics has a satisfactory chromatic behaviour (see Fig.48). The dynamic aperture for an optimized adjustment of the sextupole families is sufficient. Stability is provided for a six dimensional phase space volume which includes somewhat

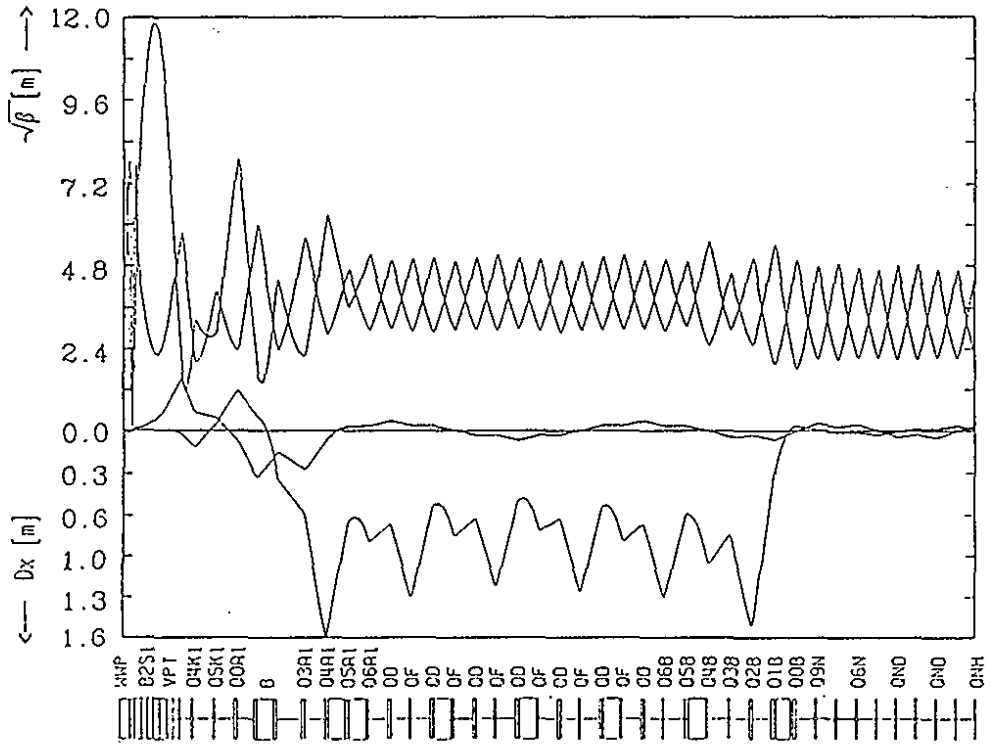

Figure 47: Beta functions and dispersion in one quadrant of the LER.

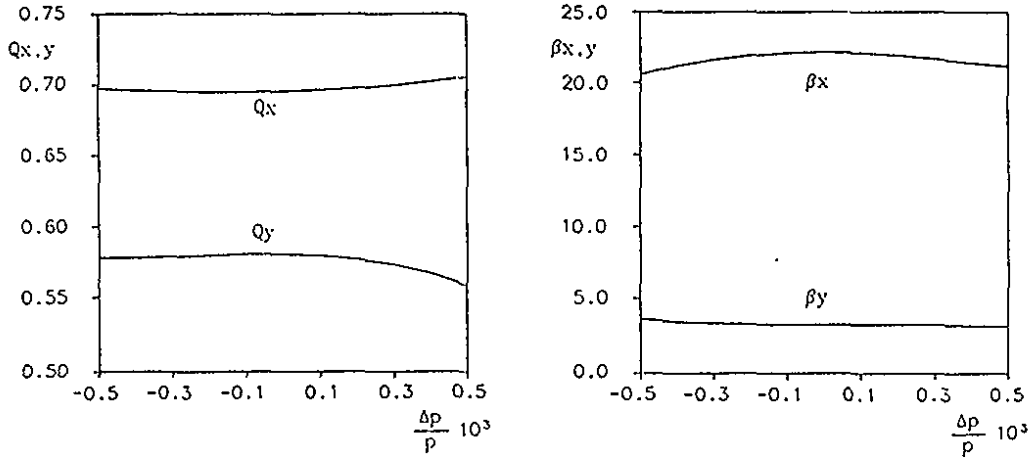

Figure 48: Chromatics of the LER 1 cm Optics. (a) Horizontal and vertical tunes and (b) beta functions in the low energy ring as a function of momentum deviation $\Delta p/p$.

more than 6.5 σ of the transverse and longitudinal beam size (see Fig.49). The blow up of the vertical beam emittance due to the nonlinear sextupole fields is small. Further improvement of the dynamics is desirable and possible. This can be achieved by the addition of eight sextupole circuits in the dispersion-free straight sections in order to minimize first order sextupole driving terms of nonlinear resonances and second order tuneshift terms.

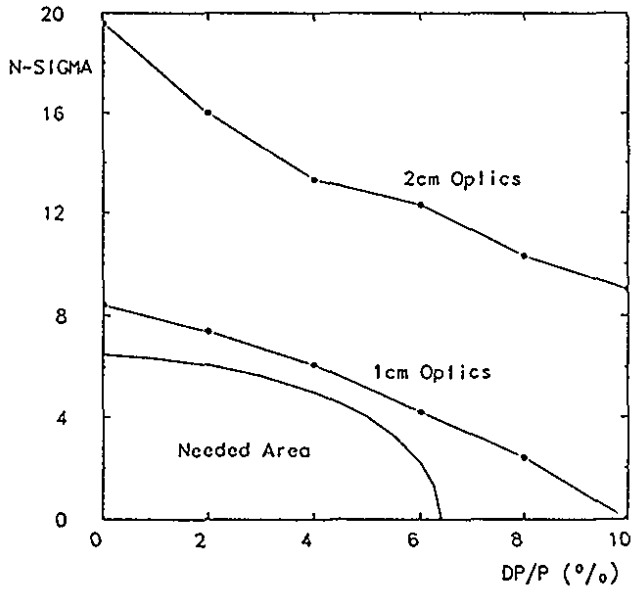

Figure 49: Dynamic aperture in units of rms beam size of the LER

4.3 High Energy Lattice

The high energy lattice is an identical copy of the present PETRA lattice with the exception of the interaction region. Lattice parameters are given in Table V. Only near the IR, small modifications are necessary to match the orbits of the two beams in the interaction region. The arcs consist of FODO cells with a betatron phase advance of 45°. HER and LER use the same type of bending magnet. A considerable part of the available long straight sections is needed to install the 30 single-cell rf resonators. A special optics in the rf sections with very small β-functions of the order of 5 m is possible but has not been worked out in detail. The linear chromaticity which corresponds to the collider optics with $\beta_x^* = 0.4\,\mathrm{m}$ and $\beta_y^* = 2\,\mathrm{cm}$ is with $\xi_x = -45$ and $\xi_y = -66$ not particularly large. Two sextupole families are sufficient to provide a satisfactory chromatics which preserves sufficient dynamic aperture.

Table IV: Lattice Parameters of the LER			
Beam energy	$E =$	3.0	GeV
Circumference	$C =$	2304.	m
Bending radius	$\rho =$	48.00	m
Dipole length	$l_D =$	5.378	m
Relative power loss per turn	$\Delta E/E =$	0.000221	
Momentum compaction factor	$\alpha =$	0.0013	
Energy spread	$\sigma_e =$	0.0012	
Damping time (longitudinal)	$\tau_s =$	36.0	ms
Horizontal β-function IP	$\beta_x^* =$	20.0	cm
Vertical β-function IP	$\beta_y^* =$	1.0	cm
Horizontal tune	$Q_x =$	35.20	
Vertical tune	$Q_y =$	33.13	
Horizontal chromaticity	$\xi_x =$	$-69.$	
Vertical chromaticity	$\xi_y =$	$-88.$	
Wiggler field	$B =$	1.8	T
Wiggler period	$L =$	4×0.25	m

Table V: Lattice Parameters of the HER			
Beam Energy	$E =$	9.333	GeV
Circumference	$C =$	2304.	m
Bend radius	$\rho =$	192.	m
Dipole length	$l_D =$	5.378	m
Relative Power loss per turn	$\Delta E/E =$	0.000371	
Momentum Compaction Factor	$\alpha =$	0.00235	
Energy Spread	$\sigma_e =$	0.00058	
Damping Time (longitudinal)	$\tau_s =$	20.1	ms
Horizontal β-function IP	$\beta_x^* =$	40.0	cm
Vertical β-function IP	$\beta_y^* =$	2.0	cm
Horizontal Tune	$Q_x =$	26.17	
Vertical Tune	$Q_y =$	22.58	
Horizontal Chromaticity	$\xi_x =$	$-47.$	
Vertical Chromaticity	$\xi_y =$	$-65.$	

5 Radiation Background in the Interaction Region

5.1 Introduction

Sources of background radiation

The requirement of acceptable background conditions is one of the main issues in the layout of the interaction region, concerning the beam optics, the vacuum profile, the collimator geometry and beam pipe cooling. It also forces compromises on the detector layout, in particular on the minimum radius of the beam pipe, which strongly influences the experimental vertex resolution.

The radiation background originates mainly from two processes:

- Synchrotron photons are emitted wherever the beam is bent or focused. The beam separation to prevent parasitic bunch crossings and the necessity to focus the two beams at the IP make synchrotron radiation in the vicinity of the detector unavoidable.
- Interactions with the residual gas cause beam particles to undergo deflections (Coulomb scattering) and radiative energy losses (bremsstrahlung). Particles lost due to either process initiate electromagnetic showers when hitting the beam pipe and may send shower debris into the detector.

Radiation effects

The "acceptable" radiation doses in the detector region are defined by whichever of the following criteria is the most stringent:

- The maximum dose which the detector components can stand without being damaged.
- The maximum occupancy, *i.e.* the highest tolerable probability of background hits overlapping with real hits in the detector.
- The maximum background rate the trigger system can suppress without producing excessive detector dead time.
- The maximum heat load for which adequate cooling can be supplied to the beam pipe near the IP.

Radiation limits

Due to their proximity to the IP, the Silicon Vertex Detector (SVD) and the innermost layers of the Central Track Chamber (CTC) are mostly subject to radiation damage. Present day VLSI electronics associated with the silicon counters survives some hundreds of Grays (see chapter III.3). Consequently, for a minimum lifetime of 10^7 s the energy deposition per time and area in a 200 μm thick silicon layer must not exceed 10^{-9} W/cm^2 or 0.1 Gy/h. For the CTC sense wires, an accumulated charge of $O(1\ \mathrm{C})$ per cm of wire length is considered the limit for proper performance [16]. This corresponds to a deposition of $5 \cdot 10^{-11}$ W/cm^2 during $5 \cdot 10^7$ s, assuming an ionization energy of 25 eV, a gas amplification of 10^4 and a cell size of $O(1$ cm). The corresponding particle fluxes depend on the nature and the energy of the particle. For example, a photon of 8 keV has a 95% chance of being absorbed in a 200 μm silicon layer, and about 10% absorption probability in a CTC cell. The energy loss of a minimum ionizing particle is 60 keV in the silicon layer and 4 keV in the CTC cell.

Occupancy

The maximum occupancy is reached when the probability of false hits overlapping with real ones amounts to a few percent. The occupancy limits are of the same order of magnitude as the values for the maximum doses stated above. A numerical example is given in section III.3.3.3 for the Silicon Vertex Detector.

Detector dead time

The trigger (chapter III.9) is expected to be insensitive to synchrotron radiation within the above limits. Charged particles, *i.e.* lost electrons or shower debris thereof, are relevant when escaping the rejection criteria of the first level trigger. The rate of tracks originating within $\pm$ 5 cm from the nominal IP with transverse momentum larger than 150 MeV/c should be well below 10 kHz.

Heating of beam pipe and collimators

The bulk of generated synchrotron radiation power, if not passing freely through the interaction region, must be absorbed by collimators upstream of the IP. In the present layout of the IR a power density of up to 50 Wcm^{-2} occurs on certain collimators requiring them to be water cooled. The heating of the sensitive Be beam pipe due to radiation however is negligible. It is rather the image current heating and HOM losses which may demand active cooling of the Be beam pipe.

Monte Carlo studies

To determine the amount and spatial distribution of various types of background in the IR, Monte Carlo simulations have been performed, based on the beam optical parameters as given in 4.1 . In the following, methods and results are presented separately for synchrotron radiation and background from lost beam particles.

5.2 Simulation of Synchrotron Radiation in the IR

Method

The amount and spatial distribution of synchrotron radiation (SR) hits in the

IR has been determined by following electron trajectories, randomly chosen in phase space (x, x', y, y'), and sampling the radiation emitted tangentially along the trajectory within each magnet. For a given beam current I and assuming a Gaussian electron density distribution $\rho(x, x', y, y')$, each trajectory represents a number of electrons per second N_e/s. For a given Lorentz factor γ and local radius of curvature r, the critical photon energy E_c, the mean photon energy $\langle E_\gamma \rangle$ and the number of quanta N_γ emitted along an arc of length l are computed. The total power assigned to a photon sample is then given by $\langle E_\gamma \rangle N_\gamma N_e/s$, where [17]

$$\langle E_\gamma \rangle = \frac{8}{15\sqrt{3}} E_c; \quad E_c = \frac{3}{2}\frac{\hbar c \gamma^3}{r}; \quad N_\gamma = \frac{5}{2\sqrt{3}}\frac{\gamma}{137}\frac{l}{r}; \quad N_e/s = \frac{I}{e}\rho(x, x', y, y').$$

The geometry of the beam pipe within the detector and the surrounding three silicon layers of the vertex detector have been modelled in detail. A photon sample that hits the beam pipe is subdivided into portions of different photon energies E_γ, weighted according to the known power spectrum $S(E_\gamma/E_c)$. Each portion is propagated like an individual photon through the different media, using known cross sections [18] for the following processes:

- Rayleigh or Compton scattering with energy dependent characteristics;
- Photo-fluorescence, *i.e.* isotropic emission of a K_α, K_β or L-line photons;
- Non-radiative photoelectric absorption.

The propagation process continues until terminated either by non-radiative absorption or by leaving the IR. For each medium, the spectrum of the deposited power is recorded. The dose received per second is the integral over the spectrum, divided by the mass of the medium. For occupancy considerations, the number of photons per second (= power/E_γ) is the quantity of interest.

Collision optics

The collision optics, resulting from an optimization process that went through several iterations of lattice design and background calculation including the collimator geometry, is presented in chapter 4.1 . However, the following results on SR power distribution are obtained by using emittances twice as large as the design values to provide a safety margin for the case that the desired tune shift of $\Delta\nu \approx 0.04$ cannot be achieved and the emittances have to be enlarged accordingly.

Generated power

As shown in Table VI, most of the radiation generated by the incoming LEB is produced in the low-β-triplet (Q1,Q2,Q3). For the HEB the Q5 magnet, required to keep its β-function sufficiently small, is the main source of radiation. The smooth final separation in the 10 m long BSEP magnet produces only little synchrotron radiation. In total, the incoming LEB and HEB generate 310 W and 5.1 kW, respectively.

Table VI: Synchrotron radiation power generated by the incoming beams assuming twice the design emittance.

Magnet	HEB W	LEB W	Distance to IP m
Detector Field	525	85	0
Q1	118	29	0.60
Q2	99	83	1.37
Q3	649	19.3	2.23
Q4	190	0.4	3.3
Q5	3240	21	4.2
Q6	219	31	4.95
BSEP	49	41	5.5

The critical part of the beam pipe is a 25 cm long Be tube of 25 mm radius and 500 μm thickness, coated inside with 10 μm Cu and centered around the IP. It is highly transparent to photons above a few keV.

Masking

To protect this region from direct SR two elliptical synchrotron masks are foreseen on either side of the IP (Fig. 50). Without these masks, about 310 W would be incident on the Be tube, 40 W of which would be deposited in the detector. The outer masks (about 1 m from the IP) are introduced to absorb the bulk of radiation power, where the heat load can be handled without conflicting with the space requirements of the detector. The inner masks are placed at both ends of the Be tube and shield it from any direct radiation and partly from photons scattered off the outer masks.

On the HE side, the outer mask is made of copper, since the large power deposition requires a good heat conducting material. For the inner masks, where some backscattering into the detector cannot be avoided, titanium has been chosen due to the comparatively low energy of its K_α line (4.5 keV). All masks are designed to stay clear by 2 mm from the 12-σ beam envelope.

The outer HE collimator absorbs 3.1 kW of the radiation fanning out vertically. Due to its inclined surface, no backscattered radiation can enter the detector and photons from forward "tip scattering" are mostly stopped by the inner mask which receives no direct radiation.

In addition to the vertical fan, radiation from the LE beam spreads horizontally due to the rather large horizontal β-function at the low-β-magnets. Thus, the outer mask is narrow in the horizontal plane but has a wide vertical opening as to minimize backscattering of photons from the HE beam, and receives 18 W of direct radiation. Its position is chosen to minimize direct radiation on the inner mask which absorbs only 0.4 W.

Synchrotron radiation reaching the detector

About 3 mW are absorbed in the Cu coating of the Be beam pipe (Fig. 51 and 52). The spectrum of photons leaking through the beam pipe and being

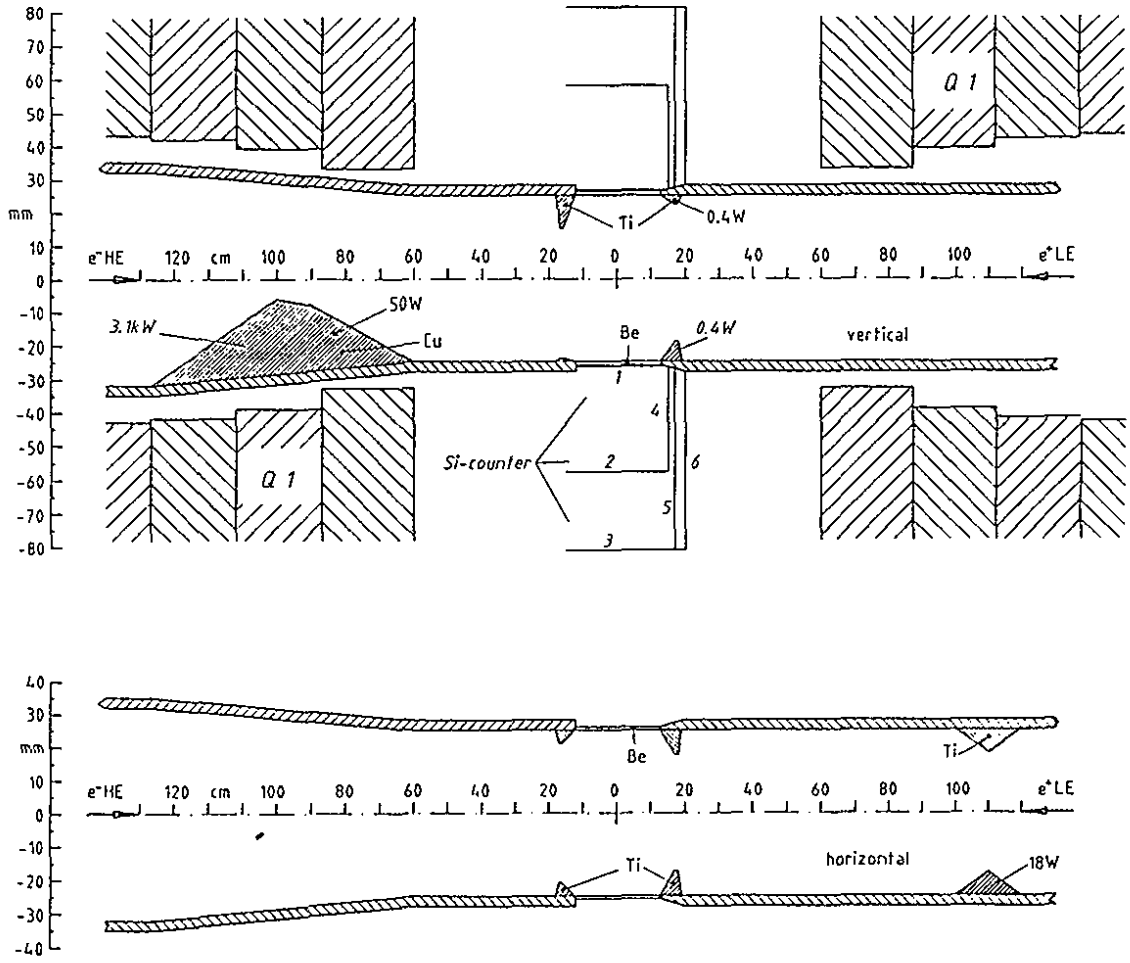

Figure 50: Vertical (above) and horizontal (below) view of the collimator system and detector arrangement used in the background calculations. The labels of the Si counters refer to Table VIII.

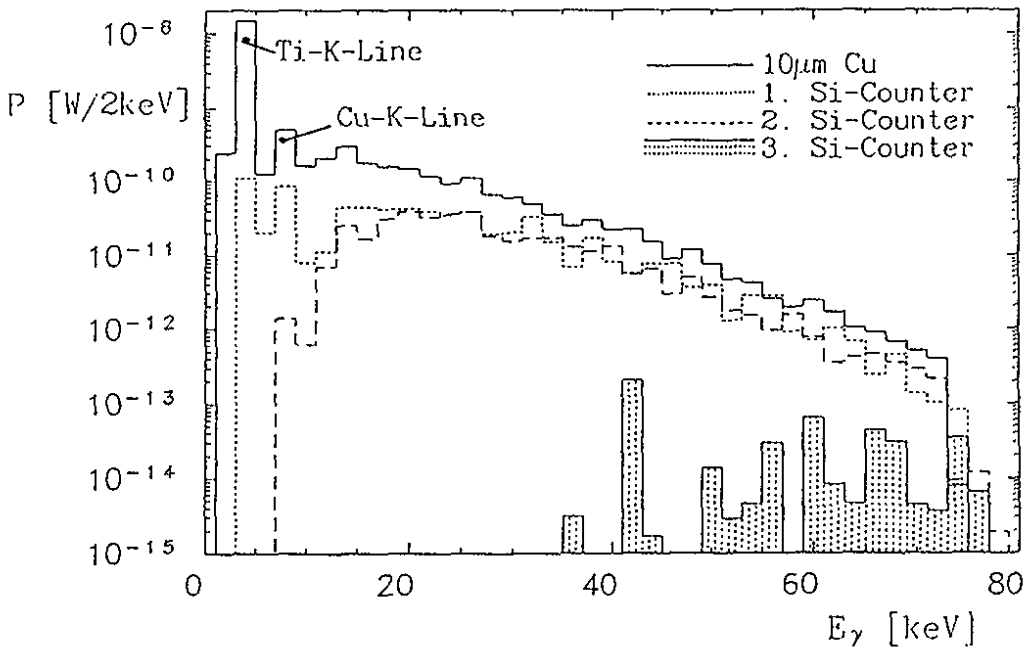

Figure 51: Spectral distribution of synchrotron radiation power generated by the HEB and deposited in the 10 μm thick Cu coating of the beam pipe and in the three layers of silicon detectors.

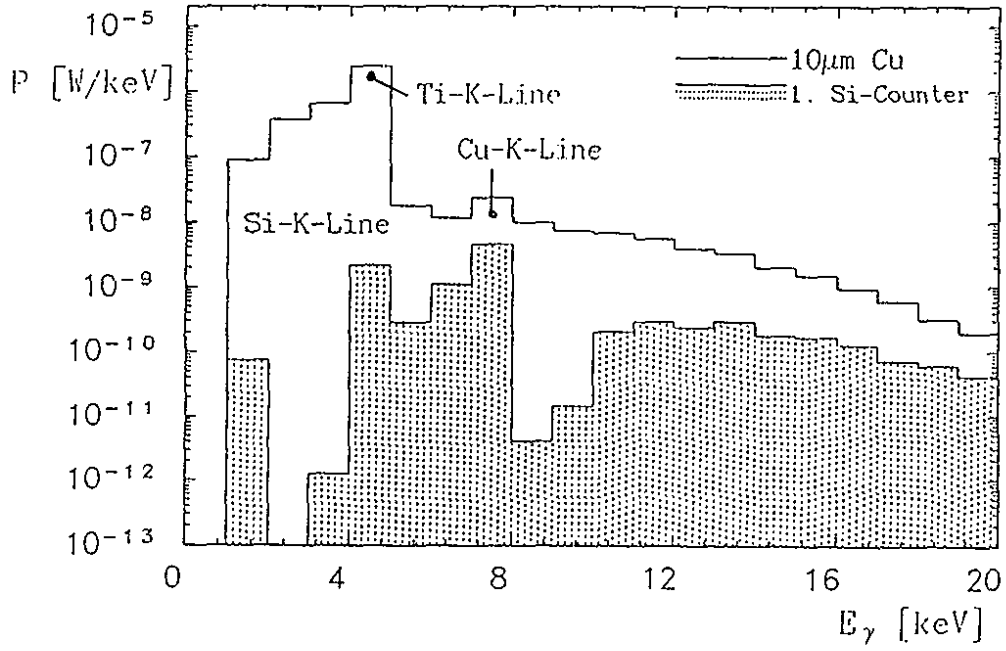

Figure 52: Spectral distribution of synchrotron radiation power generated by the LEB and deposited in the 10 μm thick Cu coating of the beam pipe and in the innermost layer of silicon. There is no significant energy deposition in the outer detector layers.

absorbed by the innermost layer of silicon is dominated by the $K_{\alpha,\beta}$ lines of Cu at 8 keV, and Ti at 4.5 keV (Fig. 51 and 52). On average, $1.8 \cdot 10^{-12}$ W/cm^2 from the HE beam and $2.5 \cdot 10^{-11}$ W/cm^2 from the LE beam are absorbed in this silicon layer, but the distribution is not homogeneous. Close to the inner LE mask, it reaches $1.3 \cdot 10^{-10}$ W/cm^2, mainly due to scattered photons from the LE beam. This value, although obtained by using twice the nominal emittance, is still an order of magnitude below the dose and occupancy limits stated above.

For the outer Si layers, the power spectra are shifted to higher energies with much smaller integral values (Fig. 52). This contribution comes only from the HEB. The photons from the LE are almost completely absorbed by the inner Si layer.

High energetic photons between 40 keV and 80 keV from the HEB also enter the drift chamber, where $1.5 \cdot 10^{-10}$ W or $O(10^4)$ photons/s are absorbed in a large volume which leads to a deposition per cm^2 well below the allowed limit.

5.3 Simulation of Background in the IR from Lost Beam Particles

Beam-gas interactions

The interaction with residual gas molecules causes beam particles to change their flight direction and to lose energy by emitting bremsstrahlung photons. Since the scattering cross section rises steeply in the low energy limit as well as at small angles, each effect can be treated separately while neglecting the other. The computer code DECAY TURTLE [19] simulates both bremsstrahlung and elastic Coulomb scattering for a given vacuum profile and transports off-energy or off-angle particles through the lattice until they hit the beam pipe or a scraper. Shower debris from particles hitting a scraper are also considered. Once the particle flux incident on a specific surface is known, the code EGS4 [20] can be used to model the shower development in detail.

Beam losses

Using DECAY TURTLE, beam-gas interactions have been simulated for the LEB and HEB respectively, with and without introducing scrapers. In all cases, the vacuum was assumed to be 10^{-8} mbar (see chapter 11). The tracking of both electrons and positrons started 288 m away from the IP which is 1/8 of the ring circumference. The energy of radiated photons was limited to 0.01 - 1 of the beam energy. The angular deflection due to Coulomb scattering was restricted to 0.1 - 7 mrad. Scattering events outside of these boundaries do not contribute to the energy deposition in the IR. The beam losses are 18 e^- / turn and 35 e^+ / turn which corresponds to a lifetime of 6.3 h for the HEB and 5 h for the LEB.

Scraper

Scrapers to remove particles which have lost energy due to Bremsstrahlung should be placed at positions of large dispersion where the transverse displace-

ment of these particles is large. After having undergone Coulomb scattering, beam particles perform betatron oscillations of an increased amplitude. Therefore, scrapers against off-angle particles are most effective at positions that are multiples of half the oscillation wavelength away from the IP. It is not always possible to find places where both conditions are fulfilled. There are three scrapers used in the LE ring to reduce the number of hits by more than an order of magnitude, while seven scrapers were required to produce a substantial effect in the HE ring. The scrapers closest to the IP in either ring are effective against Coulomb scattered particles but not against off-momentum particles, because the dispersion is too low at these positions.

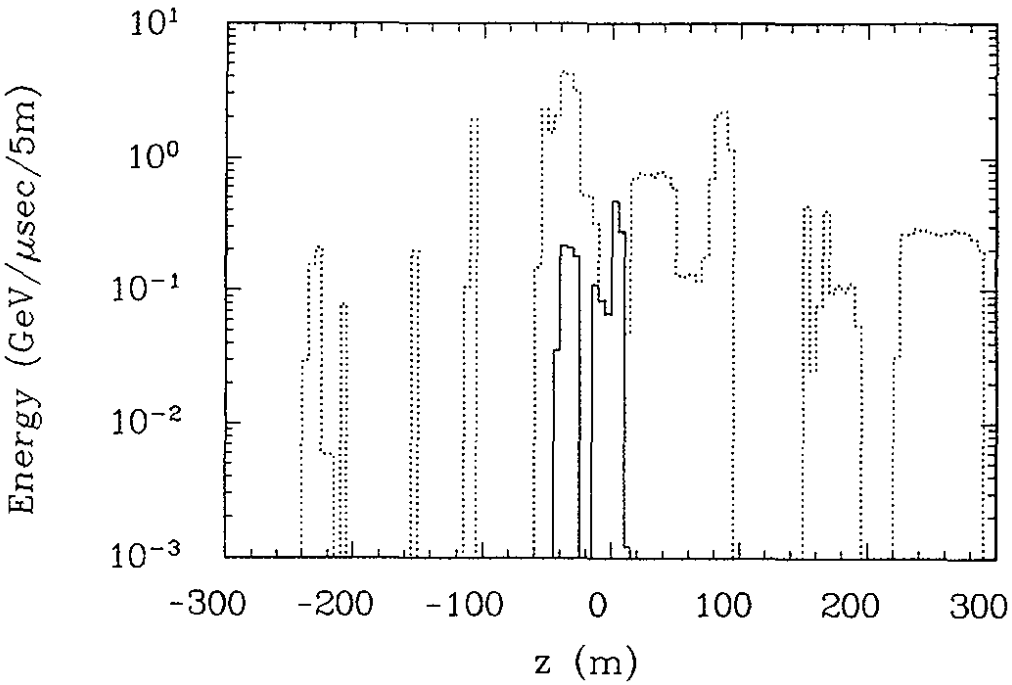

Figure 53: Flux of bremsstrahlung-scattered electrons and positrons as a function of the scattering point without (dotted histogram) and with scrapers (full histogram).

To demonstrate the influence of the scrapers, the scattering point (either bremsstrahlung or Coulomb scattering) of those electrons and positrons which strike the sensitive part of the beam tube around the IP (within the Q2 quadrupoles = ±1.37m) is displayed in Fig. 53. The number and energy of these tracks is given in Table VII for an interval of 1 μs, which is a typical integration time for various detector components (CTC, ECAL). Particles hitting the beam tube outside this sensitive region do not deposit any energy in the detector. Only the particles scattering within ± 50 m around the IP cannot be eliminated completely. Thus it would be sufficient to improve the vacuum

system around the IP, in order to further reduce the background of beam-gas interactions. Fig. 54 shows where the scattered electrons and positrons hit the beam pipe. The various peaks can be assigned to the synchrotron masks. Due to the large distance of the scrapers from the IP, they cannot reduce the flux of bremsstrahlung photons (Fig. 55). Photons from the HEB are completely absorbed (-z = 100 - 137 cm) by the HE synchrotron mask (Fig. 50).

Table VII: Number and energy (GeV) of beam particles striking the beam pipe around the IP per μs

HEB	e^- brems.	γ brems.	e^- Coul.
Hits no scraper	3.	7.	7.
Hits with scrapers	0.2	7.	0.03
Energy no scraper	22.	9.	62.
Energy with scrapers	0.9	9.	0.3
LEB	e^+ brems.	γ brems.	e^+ Coul.
Hits no scraper	6.5	3.	26.
Hits with scrapers	0.6	3.	0.06
Energy no scraper	17.	0.9	77.
Energy with scrapers	0.8	0.9	0.2

Electromagnetic showers

As already mentioned, it is essential to study the effect of electromagnetic cascades on the different detector components. Tracks striking the beam pipe or one of the masks initiate an electromagnetic shower, swamping the detector with many particles. Therefore all rays striking the beam pipe were passed to an EGS4 simulation program. The geometry of the beam pipe including the elliptical synchrotron masks has been included. All shower particles were traced through the detector until they were either absorbed in the calorimeter or their energy fell below a cutoff value. The total energy cutoffs were 0.6 MeV for electrons and 0.01 MeV for photons. The interaction of the background particles with the Silicon Vertex Detector, the Central Track Chamber and the calorimeter was determined.

The SVD was approximated by three cylinders around the beam tube and three planes perpendicular to the beam (Fig. 50). The CTC walls were included with their proper thickness. CO_2 has been used as chamber gas in which electrons deposit about 4 keV per cm of path length. The magnetic fields of the quadrupole Q1 and of the tilted Helmholtz coils was also taken into account. Low momentum charged tracks curl up in the magnetic field and can cross the detector layers many times.

Background in Si detector

The discussion of the results starts with the most sensitive component, the Si vertex detector. The radiation damage in the Si layers is proportional to the flux and not to the energy of the incident tracks. The number of hits and the energy deposited per μs are summarized in Table VIII. Photons passing the Si layers without any energy loss were not included. To calculate the absorbed

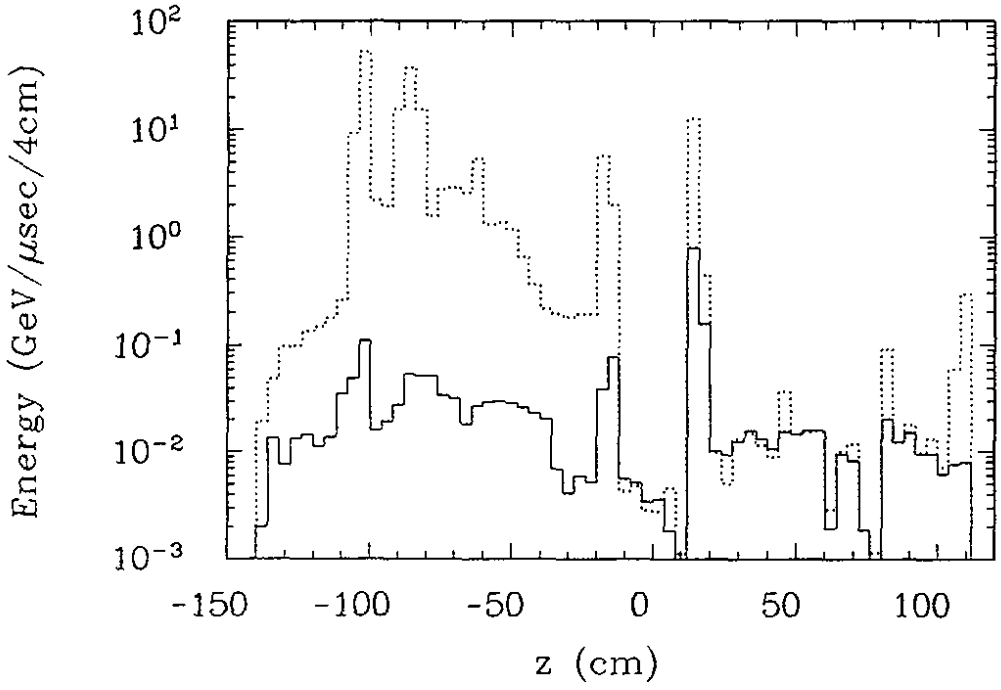

Figure 54: Flux of electrons and positrons striking the beam pipe without (dotted histogram) and with scrapers (full histogram).

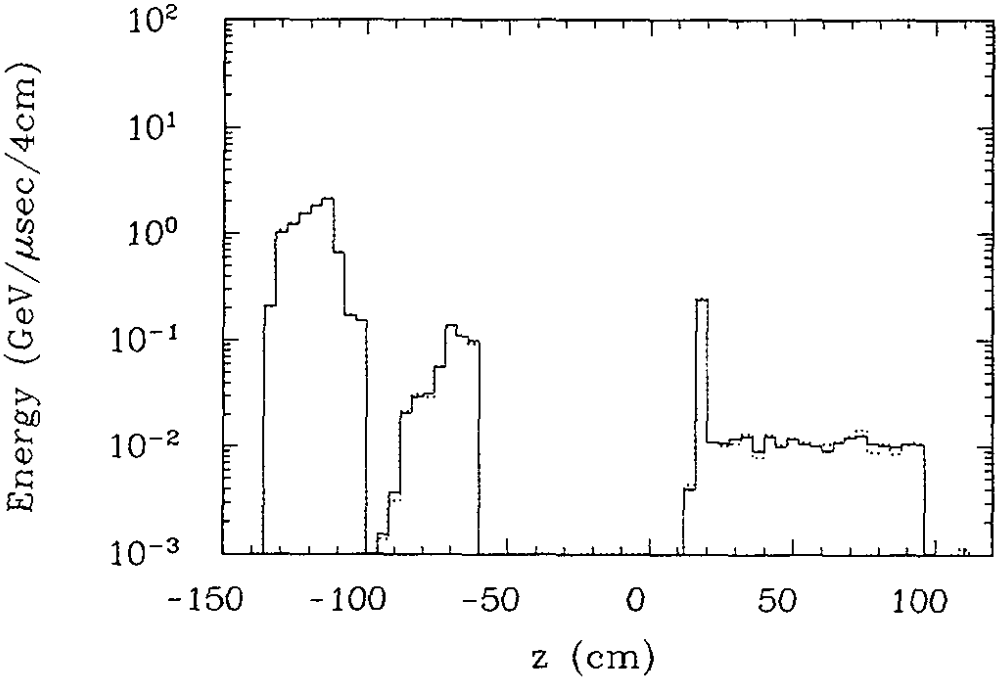

Figure 55: Flux of photons striking the beam pipe without (dotted histogram) and with scrapers (full histogram).

dose, a uniform energy deposition has been assumed which is, however, not quite true. Off-momentum charged tracks are deflected in the arcs and thus strike the beam pipe around the azimuthal angle $\Phi = \pi$. The resulting asymmetry is obvious from Fig. 56 where the deposited energy is plotted as a function of this angle for the three Si layers. The innermost layer shows an additional contribution coming from bremsstrahlung photons of the positron beam. Fig. 57 shows the radial distribution for the Si planes in forward direction. Except for the innermost part, the incident flux falls off slowly with increasing radius. The radiation load can be further reduced by filling the space around the Si-vertex detector with a tungsten absorber.

Table VIII: Number of hits / μs and energy deposition (MeV/μs) in the Si layers.

Hits/μs	HEB	LEB	SUM
Si layer 1	0.4	3.1	3.5
Si layer 2	0.3	2.6	2.9
Si layer 3	0.4	2.0	2.4
Si plane 4	0.1	0.8	0.9
Si plane 5	0.2	0.6	0.8
Si plane 6	0.2	0.5	0.7
Energy (MeV/μs)	HEB	LEB	SUM
Si layer 1	0.1	1.0	1.1
Si layer 2	0.1	0.8	0.9
Si layer 3	0.1	0.6	0.7
Si plane 4	0.01	0.08	0.09
Si plane 5	0.03	0.11	0.14
Si plane 6	0.04	0.09	0.13
Dose (Rad/h)	HEB	LEB	SUM
Si layer 1	0.4	3.3	3.7
Si layer 2	0.1	0.7	0.8
Si layer 3	0.05	0.3	0.3
Si plane 4	0.2	1.2	1.4
Si plane 5	0.2	0.5	0.7
Si plane 6	0.2	0.4	0.6

Background in CTC

The backgrounds in the drift chamber and in the electromagnetic calorimeter are characterized by the numbers collected in Table IX. The energy release in the CTC falls off steeply in the inner region, because low momentum tracks are curling in the magnetic field (Fig. 58). The calculated energy deposition in the innermost layer is a factor 2 below the corresponding radiation limit of 0.03 MeV/μs whereas for larger radii (layer 5) this factor is at least 10.

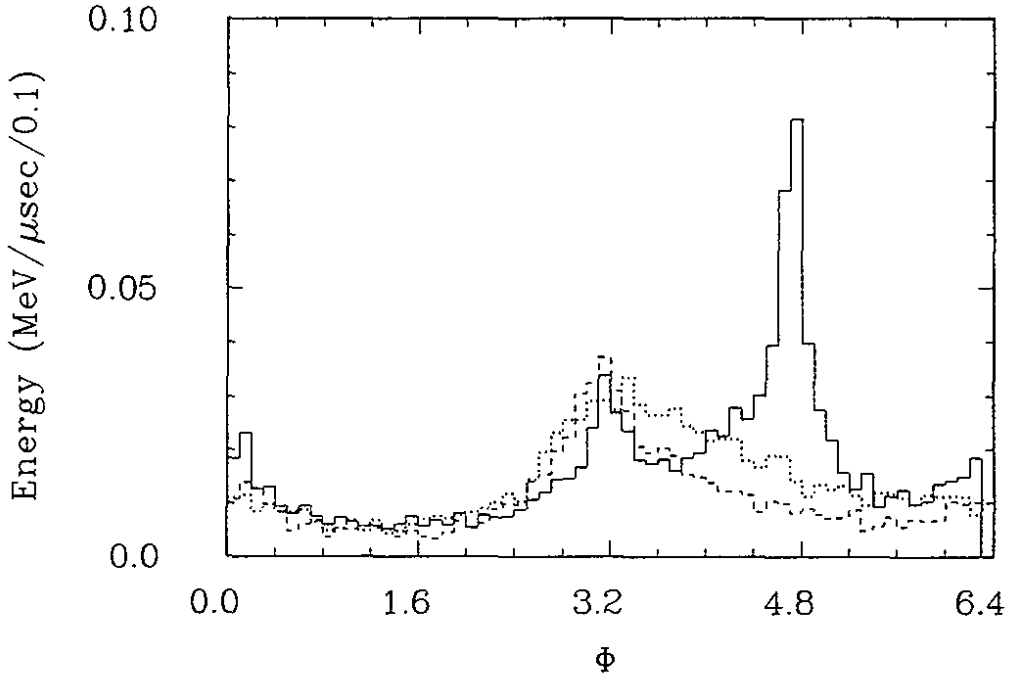

Figure 56: Azimuthal energy distribution in the 3 Si layers. (1 = full, 2 = dotted, 3 = dashed).

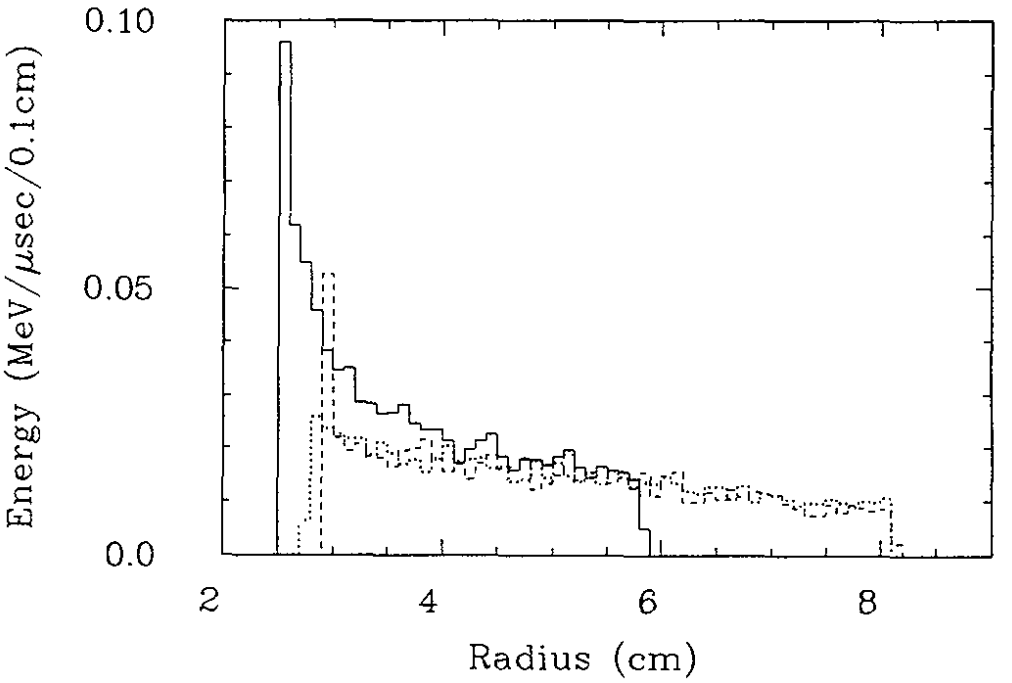

Figure 57: Radial energy distribution in the 3 Si planes. (4 = full, 5 = dotted, 6 = dashed).

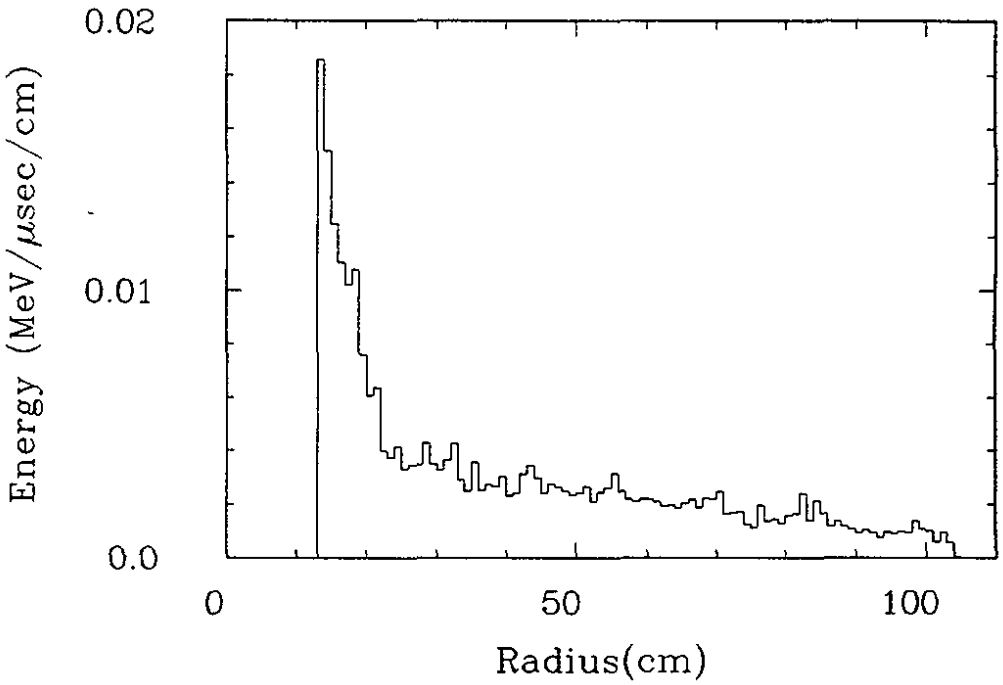

Figure 58: Energy deposition in the drift chamber as a function of the radius.

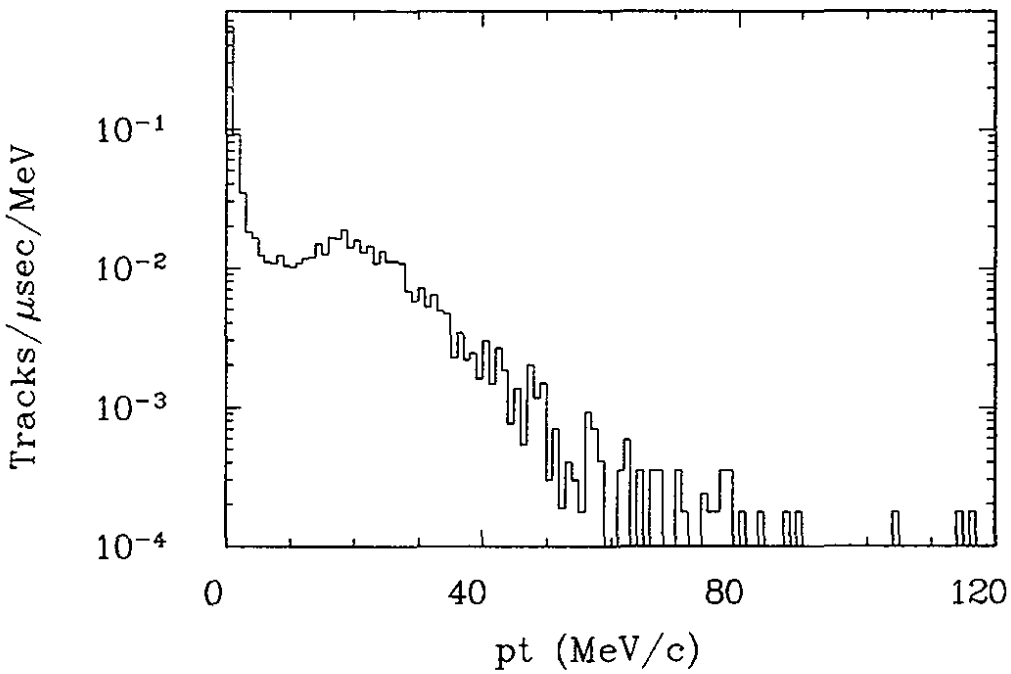

Figure 59: Transverse momentum distribution in the CTC.

The amount of fake triggers can be estimated from the transverse momentum distribution which is plotted in Fig. 59. With a trigger threshold of 100 MeV/c, the trigger rate due to beam gas interactions will be below 1 kHz.

Background in ECAL

No background problems are expected in the calorimeter (Table IX). Most of the energy is due to low energetic photons. With a readout threshold of 0.2 MeV per crystal about 30 hits/μs are to be expected, but only 0.2 faked photons/μs with an energy above 20 MeV will be produced.

Table IX: Number of hits / μs and energy deposition (MeV/μs)

Energy (MeV/μs)	HEB	LEB	SUM
Beam pipe -z	590.	510.	1100.
Beam pipe Be	0.4	3.4	3.8
Beam pipe +z	260.	200.	460.
Sync. mask -z	7000.	400.	7400.
Sync. mask +z	240.	14.	254.
CTC $e^{\pm}$	0.08	0.2	0.28
ECAL $e^{\pm}$	0.24	0.42	0.66
ECAL γ	21.	45.	66.
Hits / μs	HEB	LEB	SUM
CTC $e^{\pm}$	0.3	0.8	1.1
ECAL $e^{\pm}$	0.04	0.07	0.11
ECAL $e^{\pm}$ > 20MeV	0.0005	0.0001	0.0006
ECAL γ	17.	60.	77.
ECAL γ > 20MeV	0.1	0.1	0.2

5.4 Conclusion

It has been demonstrated that the chosen beam optics and the design of the interaction region allow to run the detector with tolerable background at the design luminosity. The synchrotron radiation absorbed in the innermost Si-layer is an order of magnitude below the dose and occupancy limits despite the fact that the calculations were performed using twice the nominal emittances. The proper placing of scrapers reduces the flux of scattered beam particles hitting the sensitive part of the beam pipe to a level which is acceptable for all detector components. In addition, there is still room for improvements like better vacuum around the IP and further optimization of the scraper positions.

6 Beam Beam Interaction

Beam beam effects

The luminosity of the asymmetric e^+e^- collider will be limited by the beam-beam interaction. A charged particle beam which collides with an oppositely charged beam will suffer from the strong nonlinearity of the beam-beam force. As a consequence of the nonlinearity, particles with different amplitudes will have different tunes and the beam will cover an extended area in the tune plane which must be free of strong resonance lines. The effective strength of the beam-beam interaction is enhanced by increasing the density of the opposite beam or, alternatively, by increasing the sensitivity of the beam under consideration by enlarging the value of the envelope function or the IP β^*. On the transition from weak to strong beam-beam interaction, one observes first a widening of the tails in the amplitude distribution of the beam. If the tolerable limit is exceeded, the amplitudes of the particles in the beam will grow until they become larger than the size of the opposite beam. This is the blowup phenomenon which has been observed experimentally in all e^+e^- colliders.

In colliding beam operation, both beams are usually close to the blowup limit. In a symmetric e^+e^- collider, the forces which act on each of the two beams are very close to be identical and the beam-beam limit is reached almost simultaneously which gives rise to the so called flip-flop effect where the two beams are alternatively blowing up.

Consequences of asymmetric beams

In an asymmetric collider this natural balance is not given automatically and unless special care is taken, one of the two beams may reach the limit earlier than the other one. Therefore the parameters of the two beams must be chosen to end up in a quasi balanced situation in order to achieve the maximum luminosity. The forces which the two beams experience may be very different. Not only the linear lattices and lattice nonlinearities are different, the motion may be influenced in addition by ion effects which are different for electrons and positrons, which differ not only in charge but also in intensity and in beam energy. To solve this problem, we follow the HERA principle by assuming that there exists an individual beam-beam limit for each beam below which the beam sizes are controllable. Approaching this limit from below with both beams, we expect that the two beams can be operated simultaneously at their individual limits. We do not expect a large advantage in making some of the parameters like damping increments or linear beam-beam tuneshifts exactly the same, since the remaining differences in the beam dynamics will still require balancing. As far as the beam sizes at the interaction point are concerned it is well known from $p\bar{p}$ colliders [14] that the optimum has to be close to equal values. Since the beta function values at the IP have to be pushed close to the limits – which means that they become comparable to the bunch length – unbalanced β^*-values are unfortunate since particles in the tails of the longitudinal distribution of the beam which has the smaller β^* value experience an

additional enhancement of the beam-beam tuneshift by the square of the ratio of β^* values. These considerations motivated the choice of parameters for the asymmetric colliders with equal σ^* in both rings and β^* values which differ by not more than a factor of 2.

Limits to the tune shift

The strength of the beam-beam interaction is usually parametrized by the linear beam-beam tuneshift parameter

$$\Delta\nu_{y1} = \frac{r_0 N_2 \beta^*_{y1}}{2\pi\gamma_1\sigma^*_{y2}(\sigma^*_{y2} + \sigma^*_{x2})} \tag{65}$$

where $\sigma_1 = \sigma_2 = \sqrt{\epsilon\beta}$ $\Delta\nu_{y1} = \frac{r_0 N_2}{2\pi\gamma_1\epsilon_{x1}(1+\sigma_y/\sigma_x)}$. $\Delta\nu$ contains the beam brightness N/ϵ and enters directly into the expression for the luminosity

$$\mathcal{L} \approx \frac{\Delta\nu_1 \Delta\nu_2 \gamma_1 \gamma_2}{\beta_1 \beta_2}. \tag{66}$$

Experimental values for this important parameter are found in a surprisingly narrow range which extends from $\Delta\nu_y \geq 0.015$ to $\Delta\nu_y \leq 0.08$ even if one compares very different machines. Table X shows a collection of data ranging from VEPP-2M to LEP as an illustration of this fact. On the other hand, inside this range, the maximum achievable or tolerable tuneshift is hard to predict. In particular, there are no simple scaling laws which would allow an extrapolation of the experimental data from one machine to another one. If a particular machine is considered the situation is somewhat better. In many machines the tuneshift values scale well with the number of interactions points $\Delta\nu \sim \frac{1}{\sqrt{k}}$ and with energy $\Delta\nu \sim E^\alpha$, $1 < \alpha < 3$, as suggested by [32]. Similar conclusions have been obtained in a recent review on experimental results on beam-beam interaction [24]. This in particular is true for PETRA. It has been operated in colliding beam mode at different beam energies, among others at 7 GeV, 11 GeV and 17 GeV. At all three energies the machine was well tuned and delivered luminosity to the experiments. In all three cases, the machine has been operated close to the beam-beam limit. For the high beam energy of 17 GeV, the limit has not quite been reached [2]. The three data points lie on a straight line in a double logarithmic plot of tuneshift versus damping decrement, as it can be seen in Fig. 60.

Tune shift in the HER

The high energy ring of the asymmetric collider will be almost identical to PETRA being operated at 9.33 GeV with only one interaction point. We feel quite confident to interpolate between the existing data to estimate a tolerable tuneshift limit for the high energy ring of $\Delta\nu \approx 0.035$.

Tune shift in the LER

The low energy ring is a different machine. A considerable amount of the damping of the machine comes from wigglers. The energy spread which is associated with achieving a certain damping tune is enhanced by a factor of $\sqrt{\frac{B_{Magnet}}{B_{Wiggler}}}$ which amounts to roughly 3. There is no scaling law which can be applied with confidence to describe the transition between PETRA and the LER of

Table X: Vertical Beam-Beam Strength Parameter $\Delta\nu_y$ in Various $\epsilon^+ - \epsilon^-$ Colliders

Collider	circumference [m]	Energy [GeV]	Number of IP's	$\Delta\nu_y$	ref.
LEP	26659	46.5	4	0.018	ref[21]
TRISTAN	3018	30.70	4	0.023	ref[22]
PETRA	2304	17	4	$\geq$0.040	ref[2]
PETRA	2304	11	4	0.024	ref[2]
PETRA	2304	7	4	0.014	ref[2]
PEP	2200	14.5	1	0.050	ref[23]
PEP	2200	14.5	2	0.065	ref[23]
PEP	2200	13.7	6	0.045	ref[23]
CESR	768	5.5	2	0.028	ref[24]
CESR	768	5.4	2	0.020	ref[24]
CESR	768	5.3	2	0.026	ref[24]
CESR	768	5.0	2	0.022	ref[24]
CESR	768	4.7	2	0.018	ref[24]
KEK-AR	375	5.0	1	0.045	ref[25]
KEK-AR	375	5.0	2	0.030	ref[25]
VEPP-4	365	5.0	1	0.060	ref[26]
DORIS-2	316	5.3	2	0.026	ref[27]
BEPC	240	1.6	2	0.035	ref[28]
SPEAR	234	2.1	2	0.055	ref[29]
SPEAR	234	1.9	2	0.056	ref[24]
SPEAR	234	1.2	2	0.018	ref[29]
ADONE	105	1.5	6	0.070	ref[30]
DCI	95	0.8	2	0.041	ref[31]
VEPP-2	18	0.5	2	0.050	ref[26]

the asymmetric collider. Due to limited resources, no simulation of beam-beam behaviour has been performed for this study. However, extensive simulations have been performed elsewhere [33] for a very similar machine which do indicate that tuneshift values of $\Delta\nu = 0.040$ are within reach of an asymmetric collider. We have therefore based the choice of the main collider parameters on tune shift values of $\Delta\nu = 0.040$ in both rings.

Effect of parasitic crossings

The two beams of the asymmetric collider are exposed to long range beam-beam forces due to parasitic crossings. There are four parasitic crossings on each side of the IP. For the LEB, only the first parasitic crossing which occurs at a distance of 1.8 m from the IP has a noticeable impact. It causes a horizontal long range beam-beam tune shift of $\Delta\nu_{lr}^{x} = 2 \times 0.0095$ and a vertical one of $\Delta\nu_{lr}^{y} = 2 \times 0.0045$. The horizontal long range tune shift of the HEB is small. All eight parasitic crossings contribute almost equally to the tune shift of $\Delta\nu = 0.0094$. More critical is the vertical tuneshift of the HEB. It amounts

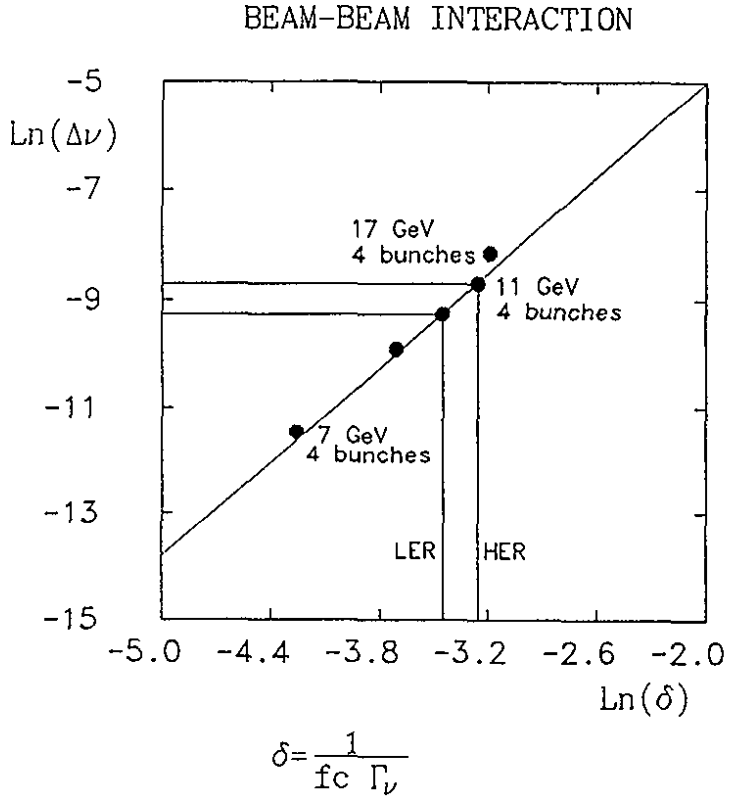

Figure 60: Summary of PETRA performance

to $\Delta\nu \approx -0.042$ and is composed of contributions from all 8 crossings. Table XI contains a summary of the parasitic beam-beam tune shift.

Experience from PETRA

How important are these effects for the stability of the two beams? There is experience available from the PETRA e^+e^- operation. The two beams have been separated at the IP by electrostatic separators. At the injection energy of 7 GeV, the ratio of head-on tune shift and parasitic tune shift for the separators switched on and off, respectively, was measured as $\Delta\nu^y_{parasitic}/\Delta\nu^y_{head-on} \approx 0.11$ [34]. Since the long range tune shift for constant separator voltage scales linearly with energy this ratio was increased to 0.27 for the 17 GeV operation, where tune shifts of 0.04 per interaction region have been achieved. The conclusion is that PETRA has been operated routinely with a parasitic tune shift of $\Delta\nu Q^y_{PETRA} = 4 \times 0.0106$ *without any serious performance limitations.*

Table XI: Parasitic Beam-Beam Interactions in the Asymmetric Collider

Parasitic Crossing #	Distance from IP m	Separation mm	Low Energy Beam β_x m	β_y m	σ_x mm	σ_y mm	$\Delta\nu_x$	$\Delta\nu_y$
1 left	1.8	4.4	51.6	26.5	2.1	0.34	0.0095	-0.0049
2 left	3.6	10.0	0.16	0.013	1.2	0.07	0.00005	10^{-6}
3 left	5.4	11.3	50.0	25.9	2.1	0.33	0.0018	-0.007
4 left	7.2	17.7	99.4	12.2	2.9	0.23	0.0014	-0.0014
1 right	-1.8	4.4	51.6	26.5	2.1	0.34	0.0095	-0.0049
2 right	-3.6	10.0	0.16	0.013	1.2	0.07	0.0005	-10^{-6}
3 right	-5.4	11.3	50.0	25.9	2.1	0.33	0.0018	-0.0007
4 right	-7.2	17.3	99.4	12.2	2.9	0.23	0.0014	-0.0014
						$\sum \Delta\nu_{\text{parasitic}}$	0.026	-0.014
						$\Delta\nu_{\text{head-on}}$	0.040	0.040
						$\sum \Delta\nu$	0.066	0.026

Parasitic Crossing #	Distance from IP m	Separation mm	High Energy Beam β_x m	β_y m	σ_x mm	σ_y mm	$\Delta\nu_x$	$\Delta\nu_y$
1 left	1.8	4.4	13.4	94.5	0.76	0.46	0.0013	-0.0090
2 left	3.6	10.0	42.3	297.7	1.35	0.81	0.0008	-0.0053
3 left	5.4	11.3	90.0	356.8	1.97	0.89	0.0016	-0.0052
4 left	7.2	17.7	160.0	242.1	2.62	0.73	0.0010	-0.0015
1 right	-1.8	4.4	13.4	94.5	0.76	0.46	0.0013	-0.0090
2 right	-3.6	10.0	42.3	297.7	1.35	0.81	0.0008	-0.0053
3 right	-5.4	11.3	90.0	356.8	1.97	0.89	0.0016	-0.0052
4 right	-7.2	17.3	160.0	242.1	2.62	0.73	0.0010	-0.0015
						$\sum \Delta\nu_{\text{parasitic}}$	0.026	-0.014
						$\Delta\nu_{\text{head-on}}$	0.040	0.040
						$\sum \Delta\nu$	0.066	0.026

7 Beam Intensity Limitations in an Asymmetric Collider

Bunch instabilities

In the following we investigate possible current limitations caused by single- and multi-bunch instabilities. Instabilities are caused by the action of the beam on itself through the metallic environment. This effect is usually described in terms of wakefields or impedances. Short range wakes and their corresponding broad band impedance affect the single bunch stability whereas long range wakes (narrow band impedance) couple the motion of subsequent bunches and determine the multibunch stability. Since the bunch spacing is short and the total current is very high, multibunch instabilities are almost unavoidable. Therefore means are necessary to reduce the narrow band impedance and probably to stabilize the beam by an active damper. In comparison to that, the single bunch currents are relatively moderate and single bunch instabilities should not limit the luminosity.

7.1 Single Bunch Instabilities

Impedance

Cavities, the vacuum system (bellows, flanges, etc.) and the complicated masking scheme to suppress the synchrotron radiation background in the interaction region form the major part of the broad band impedance.

The impedance of the cavity has been calculated using TBCI [35]. The contribution of the masking scheme has been estimated by considering a simplified geometry which served as an input for TBCI. Since the design of the vacuum system is not fixed we take the PETRA vacuum system instead. The impedance of the PETRA vacuum system has been estimated by using results of measurements [36] and calculations. Comparison of calculations of the longitudinal impedance of PETRA and HERA indicates that the vacuum impedance of HERA is three times smaller than the broadband impedance of PETRA. Therefore we assume that the impedance of the B-factory can be reduced to one third of the PETRA vacuum impedance.

In Table XII we give the longitudinal loss parameter $k_{||}$ and the transverse kick parameter $k_{\perp}$ for the objects mentioned above.

Longitudinal instabilities

The bunch length has to be kept constant in order not to lose luminosity. Therefore longitudinal instabilities have to be avoided. The broad band impedance is inductive because it is dominated by the vacuum system. Thus even potential well distortion may lead to bunch lengthening. A good measure of the strength of these two effects is the shift of the incoherent synchrotron tune, since it is of the same order as the coherent shift of the internal bunch modes and describes the distortion of the potential well. If the incoherent shift is much smaller than

Table XII: Impedance Related Parameters

	HER		LER	
object	$k_{\parallel}$ (V/pC)	$k_{\perp}$ (V/pC/m)	$k_{\parallel}$ (V/pC)	$k_{\perp}$ (V/pC/m)
cavities	6.35	16.2	3.76	9.66
vacuum system	0.87	331	0.87	331
masking scheme	0.12	25.0	0.12	25.0

the synchrotron tune no instability and only a tolerable potential well distortion will occur. The limit of the relative shift of the incoherent shift is set to be 5% so a potential well bunch lengthening of 5% is permitted. Using the value of the impedance the shift of the incoherent tune in the HER ring is much smaller than 5%. In the LER ring the shift is smaller but close to 5%. Therefore it seems possible to keep the bunch lengthening below a 5% limit but the LER ring needs a very careful design of the vacuum chamber.

Transverse instabilities

The transverse mode coupling [37] instability is dangerous because it leads to current loss. This instability occurs if the frequency of two head tail modes (usually the rigid dipol mode and the first head tail mode) merge. Since the frequency difference of two neighboring modes is the synchrotron frequency, the instability does not occur for coherent frequency shifts which are much smaller than the synchrotron tune. The calculated coherent betatron shift is only a few percent of the synchrotron tune for both rings, and therefore the transverse mode coupling instability should not impose a limit on the single bunch current. On the other hand the frequency shift is bigger than the expected betatron tune spread so one could only rely on radiation damping to suppress coupled bunch instabilities.

7.2 Coupled Bunch Instabilities

The high luminosity can only be achieved by distributing a large average current over a large number of bunches. Therefore coupled bunch instabilities are likely to be a severe problem. Multi-bunch instabilities can be counteracted in principle in two ways, (a) by passive damping and (b) by active damping.

Passive damping of parasitic cavity modes

Passive damping denotes the reduction of the narrow band impedance which is equivalent to decreasing the Q-values of all parasitic cavity modes. The Q-values required to store the design current can be determined as follows. The geometric shunt impedance R_s/Q of the parasitic modes of a 500 MHz copper cavity are around 20 Ω. Applying analytic formulae to determine the effective shunt impedance [38] gives an upper limit for the Q-values of around 20-50. Therefore the parasitic modes of a copper cavity have to be damped by four orders of magnitude since the Q-value is usually a few ten thousand.

Some investigations show that it may be possible to reduce the Q-values by such a significant factor [39]. Experiments indicate that it is possible to reduce the Q-values by a factor of one hundred to values of around 400 [40]. Compared to the required values of 20 the instability threshold will then be 5% of the design current.

Active damping by feedback systems

Therefore, the second way of fighting multi bunch instabilities is necessary, namely powerful feedback systems. It should be pointed out that a strong feedback system does not mean that one can use conventional copper cavities. A feedback system will be able to increase the threshold current of the lowest order internal bunch modes – longitudinal dipole mode and transverse rigid dipole mode – but for short electron bunches it seems impossible to increase the threshold current for instabilities of higher internal bunch modes as for example head-tail modes by applying feedback. Since the threshold current of instabilities of higher internal bunch modes is usually by a factor of 20 - 50 bigger than the threshold of the dipole modes, the Q-values have to be around 600 - 1000. Therefore, cavities with highly suppressed parasitic modes and a powerful feedback system are necessary.

8 Rf System

8.1 General Considerations

The two B-factory rings carry very large beam currents. The total power loss of the beam due to synchrotron radiation is in the order of several MW. However, the voltage required to restore the energy loss of a single particle and to provide the necessary longitudinal focusing is quite moderate as compared to the previous PETRA operation.

Main issue is the parasitic impedance of the Rf system

The needed rf cavities produce a large impedance for the beam. The parasitic cavity modes drive coupled bunch instabilities which are believed to be the most important performance limitation for a high luminosity two ring collider. To minimize these impedances when delivering the necessary power and longitudinal focusing to the beam is the main issue for the layout and design of the rf system. There are several ways of reducing the impedance of parasitic cavity modes.

- Reduction of the geometrical impedance R/Q by using single cell cavities and by choosing a smooth geometry. The impedance of the parasitic modes is reduced in this case together with the impedance of the fundamental acceleration mode.
- Passive damping of selected modes by damping antennas.
- Active damping of the modes by an rf feedback

Normal versus superconducting cavities

All these methods can be applied to reduce the parasitic impedances in normal conducting cavities or superconducting cavities. Since the voltage required for the asymmetric collider is quite moderate and since it is generally believed that selected higher order mode damping will be much more easy to accomplish for normal conducting cavities at room temperature, we have based our study on normal conducting cavities.

Normal conducting single cell cavities

The parasitic impedance of the rf system can be limited by the choice of the impedance of the fundamental accelerating mode. The reduced impedance has to be paid by an increased rf power need to produce the necessary voltage. This is tolerable and reasonable as long as the power which has to be fed to the beam exceeds the power dissipated in the cavities. The total impedance of the rf system can be expressed by the following formula:

$$R_{HOML} \sim R = \frac{1}{2}\, n_c \cdot R_c \frac{I \cdot U \cdot \sin\phi}{(P_w - P_h)} \left(1 + \sqrt{1 + \frac{2(P_w - P_h)}{n_c \cdot R_c I^2 \sin^2\phi}}\right) \qquad (67)$$

Here R_c is the shunt impedance of the fundamental mode per cavity cell, n_c is the number of cells per cavity, I is the total beam current, U is the circumferential voltage, ϕ is the synchronous phase, P_w is the power which can be coupled into the cavity, and P_h is the power dissipated in the parasitic modes of the cavities. The impedance is reduced if the accelerating structure will be composed of single cell cavities each equipped with a high power input coupler. The cell geometry is optimized for minimum impedance of the parasitic modes rather than for large impedance of the fundamental mode. The impedance of the higher order modes scales down at least linearly with the shunt impedance of the fundamental mode. Some of the parasitic modes even disappear completely or are reduced much stronger than the fundamental mode. A suitable cavity geometry is shown in Fig. 61. This shape has originally been optimized for the

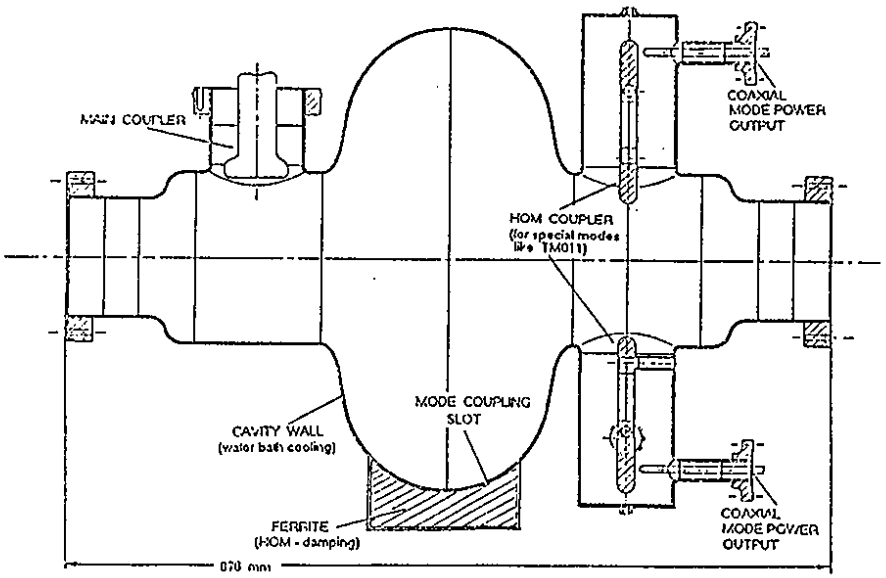

Figure 61: Shape of a single cell 500 MHz resonator for the Asymmetric Collider

DESY superconducting cavity. For a given cavity geometry, the total parasitic impedance is minimized for the maximum power P_w which can be coupled into the cavity. This power may be limited by the input coupler capacity or by the amount of power P_c which can be dissipated in the cavity. The cell impedance, the input power, and the dissipated power are in this case related by

$$R_c = \frac{1}{2}\frac{(P_w - P_c)^2}{I^2 \sin^2\phi P_c} \,. \tag{68}$$

Effective cooling of the cavity is essential.

The most important argument for the choice of the rf frequency is the availability of the equipment and the available experience. The other arguments

Rf frequency is 500 MHz for both HER and LER

for a particular frequency are much weaker. A larger frequency would be advantageous to obtain the small bunch length more easily, and in addition the longitudinal Landau damping would be enhanced. On the other hand, a lower frequency cavity is more favorable from the point of view of cooling because of the larger cavity surface. Furthermore the transient power losses and the broadband impedance are reduced. If the coupled bunch instability thresholds for rf systems with different frequencies are compared, one finds only marginal differences. The rf frequency will therefore be 500 MHz for both HER and LER which allows to use standard DESY rf equipment.

These considerations led to the concept of rf systems based on 500 MHz copper rf resonators. Its geometry has been derived from the superconducting rf resonators of the HERA rf system [41]. The shunt impedance of this resonator amounts to $R_c = 2.5\,M\Omega$ (20°C). Standard rf window techniques allow to couple more than 200 kW into this resonator.

8.2 Low Energy Ring RF Parameters

Energy loss per turn

The beam energy of the low energy ring is nominally 3 GeV. If the damping wigglers are turned on, the energy loss per turn due to synchrotron radiation is 664 keV (the power which is radiated in the bending magnets is only 150 keV). Since the vertical β-function at the IP should be as small as 1 cm, the bunch length must be limited to 1 cm as well. The momentum compaction factor is $\alpha_{comp} = 0.0011$, the rms energy spread of $\sigma(E)/E = 0.0012$ is close to the upper limit which can be tolerated by the experiment, and the longitudinal damping time is $\tau_s = 35$ ms. A 500 MHz accelerating structure has been chosen. An rf voltage of U = 9.5 MV (peak value) is needed to achieve the required bunch length of 1 cm. The synchronous phase is 4.2° in this case.

Rf power

The power which can be dissipated in the cavity is 80 kW (see below). This is matched by choosing the input power of the cavity to be $P_w = 128$ kW. Assuming these parameters, 16 single-cell 500 MHz-resonators are needed. The 30 cm long cavities have a shunt impedance of $R_c = 2.5\,M\Omega$ each. The accelerating gradient is $E_{acc} = 2.11$ MV/m. A total rf-power of P = 1.95 MW has to be made available. The total shunt impedance is $R = 40\,M\Omega$. The rf power will be delivered by two standard PETRA 500 MHz klystrons (see [42]). Table XIII summarizes the rf parameters of the low energy ring. Fig. 62 shows the block diagram of the rf system.

8.3 High Energy Ring RF Parameters

Energy loss per turn

The beam energy of the high energy ring is 9.33 GeV. The energy loss per turn due to synchrotron radiation in the bending magnets is 3.61 MeV, and the

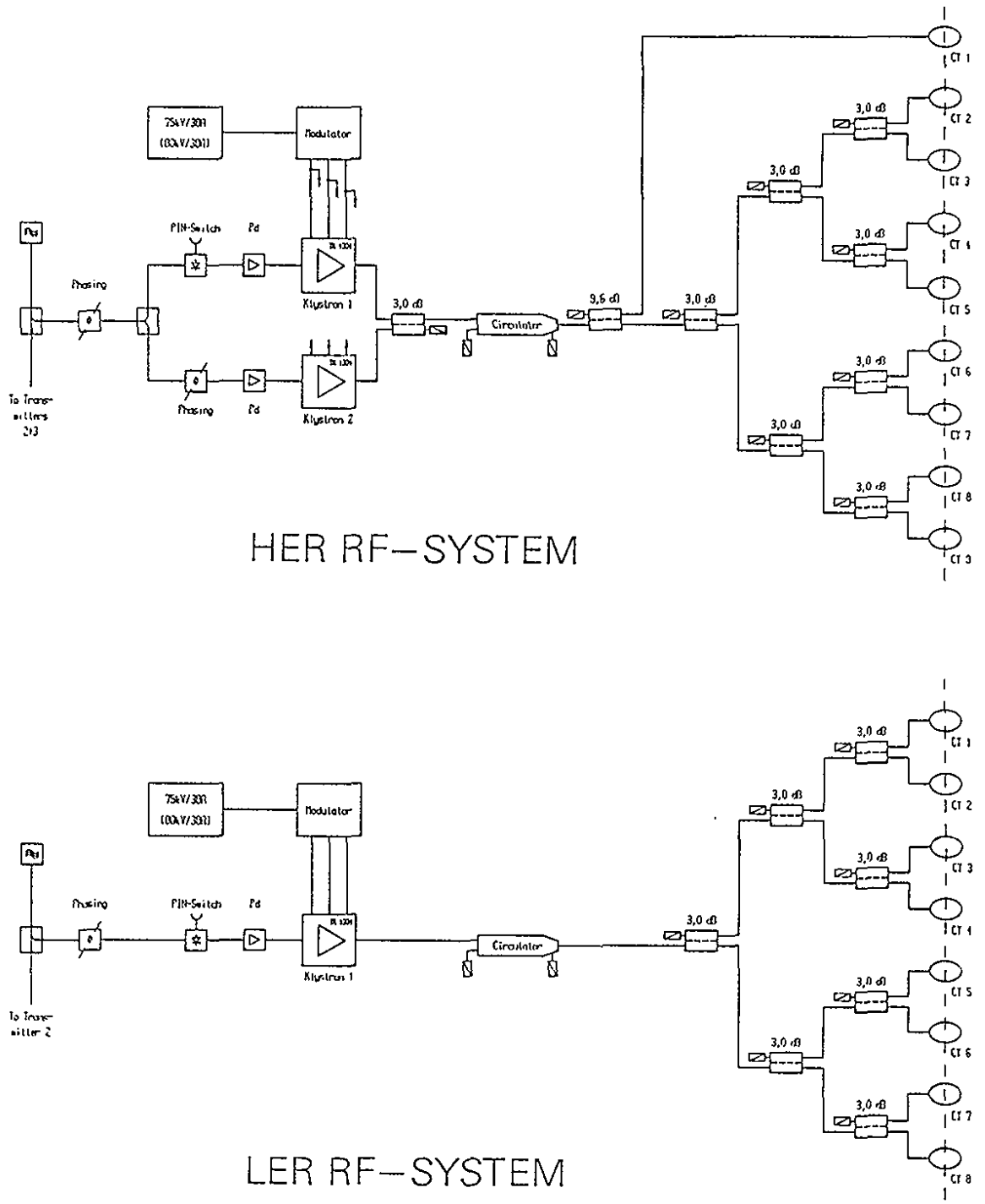

Figure 62: Block diagram of the rf systems of the two collider rings.

Table XIII: Rf-Parameters of the Low Energy Ring			
Beam Energy	E =	3.0	GeV
Beam Current	I =	1.1	A
Energy Loss per Turn	ΔE =	664	keV
Beam Power Loss	P_b =	730	kW
Momentum Compaction Factor	α =	0.0011	
Energy Spread	$\sigma(E)/E$ =	0.0012	
Damping Time (longitudinal)	τ_s =	36.0	ms
Circumferential Voltage (peak)	U =	9.5	MV
Synchronuous Phase	ϕ_s =	8.5	degree
Synchrotron frequency	f_s =	8.57	kHz
Bunch Length	σ_s =	1.01	cm
Rf-Frequency	f_{rf} =	500	MHz
Harmonic number	h =	3840	
Cavity Input Power	P_w =	128	kW
Dissipated Power per Cavity	P_c =	80	kW
HOML Power per Cavity	P_h =	10	kW
Shunt Impedance per cavity	R_c =	2.5	$M\Omega$
Number of Cavities	N_c =	16	
Total Rf Power	P =	1.95	MW
Total Shunt Impedance	R =	40	$M\Omega$
Accelerating Gradient	E_{acc} =	2.11	MV/m

total energy loss of the beam due to synchrotron radiation in the arcs is 2.57 MW. The bunch length requirement is with σ_s = 1 cm the same as for the low energy ring. The momentum compaction factor is α_{comp} = 0.00236, the rms energy spread is only $\sigma(E)/E$ = 0.000575. The longitudinal damping time is τ_s = 20.7 ms. In the HER we also use a 500 MHz rf structure and need a rf (peak)-voltage of U = 16.5 MV to achieve the required bunch length of 1 cm. The synchronuous phase is 12.6° in this case.

Rf power

The power which can be dissipated in the 500 MHz-cavity is 80 kW (see below). The input power of the cavity then has to be P_w = 175 kW. With these parameters, 27 single-cell 500 MHz-resonators are needed. The 30 cm long cavities have a shunt impedance of R_c = 2.5 $M\Omega$ each. The HOM losses are estimated to be $P_h \simeq$ 10 kW per cell. The accelerating gradient is E_{acc} = 2.11 MV/m. A total rf-power of P = 4.6 MW has to be made available. The total shunt impedance is R = 67.5 $M\Omega$. The rf power will be delivered by standard DESY 500 MHz rf equipment. Table XIV summarizes the rf parameters of the high energy ring.

Table XIV: Rf-Parameters of the High Energy Ring			
Beam Energy	E =	9.333	GeV
Beam Current	I =	0.710	A
Energy Loss per Turn	ΔE =	3.61	MeV
Beam Power Loss	P_b =	2.57	MW
Momentum Compaction Factor	α =	0.00236	
Energy Spread	$\sigma_(E)/E$ =	0.00057	
Damping Time (longitudinal)	τ_s =	20.7	ms
Circumferential Voltage (peak)	U =	16.5	MV
Synchronous Phase	ϕ_s =	11.75	degree
Synchrotron Frequency	f_s =	6.5	kHz
Rf-Frequency	f_{rf} =	500	MHz
Harmonic Number	h =	3840	
Bunch Length	σ_s =	0.98	cm
Cavity Input Power	P_w =	175.	kW
Dissipated Power per Cavity	P_c =	80.0	kW
HOML Power per Cavity	P_h =	10.0	kW
Shunt Impedance per cavity	R_c =	2.5	$M\Omega$
Number of Cavities	N_c =	27	
Total Rf Power	P =	4.6	MW
Total Shunt Impedance	R =	67.5	$M\Omega$
Accelerating Gradient	E_{acc} =	2.11	MV/m

8.4 Cavity Cooling

Pipe cooling

In order to limit the number of cells and to minimize the impedance, the power dissipated in each cavity is quite large. We are aiming at 100 kW to be dissipated in a 500 MHz resonator. This can be achieved by cooling the cavities by 50 parallel cooling pipes with 4 mm inner diameter. These pipes are arranged laterally. This way the areas near the irises which carry the largest wall current density are cooled effectively. There is a common ring shaped feeder at the upstream end and a corresponding collector at the downstream end of the cavity. A pressure gradient of 0.51 bar is necessary to push 172 l of cooling water per hour through each cooling pipe. The flow velocity is 3.8 m/s. The temperature gradient in the cooling system is limited to 10°C. This is considered necessary to keep the frequencies of the cavity modes sufficiently stable. The temperature difference at the transition between the walls of the cooling pipe and the water has been calculated to be ΔT = 20.2°C. The heat load per unit area in the cavity is with 16.7 Wcm^{-2} quite large. The temperature gradient between the cooling pipes peaks at the equator where it reaches 14.2°C. Assuming an inlet temperature of 20°C, the cavity inner surface temperature does not exceed 69.4°C. The total rf system of the asymmetric collider requires a water cooling

capacity of 350 m^3/h. The cavities have to be protected against loss of cooling by an appropriate temperature monitoring and interlock system. This is not expected to be a problem.

Bath cooling

Higher power losses can be tolerated if bath cooling is used instead of pipe cooling. The manufacturing technique for a bath cooled cavity is expected to be even less complicated. On the other hand, there is an enhanced hazard for the vacuum system. The final decision about the cooling system will depend on a detailed cavity design study.

8.5 Damping of Parasitic Cavity Modes

In order to be able to control the coupled bunch instabilities by a feedback system which damps the oscillations in the beam, the impedances of the parasitic modes of the rf cavities have to be reduced by a large factor by selective higher order mode damping. This means that the power which is deposited by a single bunch in the higher order modes has to be coupled out before the next bunch arrives at the cavity. Standing wave accelerating cavities ($\beta = 1$) have been developed at different laboratories. Usually the transfer of generator power to accelerating voltage has been optimized. The figure of merit is the shunt impedance Z which is given by $Z = U^2/P = (R/Q) \cdot Q$ where U is the accelerating voltage, R/Q is the geometry constant, Q is the quality factor of the cavity, and P is the power dissipated in cavity wall. The conductivity of the metal wall determines the value of Q whereas the geometry of the cavity enters via the geometry constant R/Q. Usually the factor R/Q is optimized by computer cavity modelling (SUPERFISH, URMEL, etc.) with respect to the fundamental mode frequency. As long as the excited HOM spectrum does not influence the beam quality itself (i.e. at low beam currents) this procedure is valid. With increasing beam current the HOM fields might deteriorate the beam quality and finally lead to a complete loss of the beam. The most effective passive remedy is to couple out all single bunch deposited HOM power before the next bunch arrives at the cavity. This can be achieved by strong selective damping at the frequencies of the most dangerous HOM resonances. The necessary strong damping requires couplers at a location with high HOM fields.

In order to damp the strong TM011 line mode, a capacitive beam pipe HOM coupler will be used. This requires further development of the HOM couplers of the DESY superconducting cavities, which is described elsewhere [43].

Because of the variety of HOM field patterns it is difficult to reach sufficient coupling by only a few dedicated couplers. Furthermore, these couplers need an effective rejection of the fundamental mode power.

Slotted cavities

A complementary method which leads to broadband damping of parasitic modes

was investigated and developed [44]. Properly placed slots in the cavity wall cause radiation of HOM power and thus reduction of their impedances seen by the beam. The damping effectiveness of one slot vs. width, length and position of the slot has been measured and the obtained results have been applied to a single cell "slotted" cavity.

Test results for slotted cavities

Test measurements on 1 GHz copper cavity models have been performed. In a first step, the computer code URMEL [45] has been used to calculate frequencies and R/Q values in the range of 1-3 GHz. For first measurements modes with significant values of R/Q (monopole, dipole and some quadrupole modes) have been selected. The HOM spectrum of the unperturbed cavity was measured (frequencies, mode patterns, polarizations, and Q values) before adding one or more slots. As a first step, one slot was milled at the equator parallel to the beam axis (Fig. 63a). This orientation of the slot has the least influence on

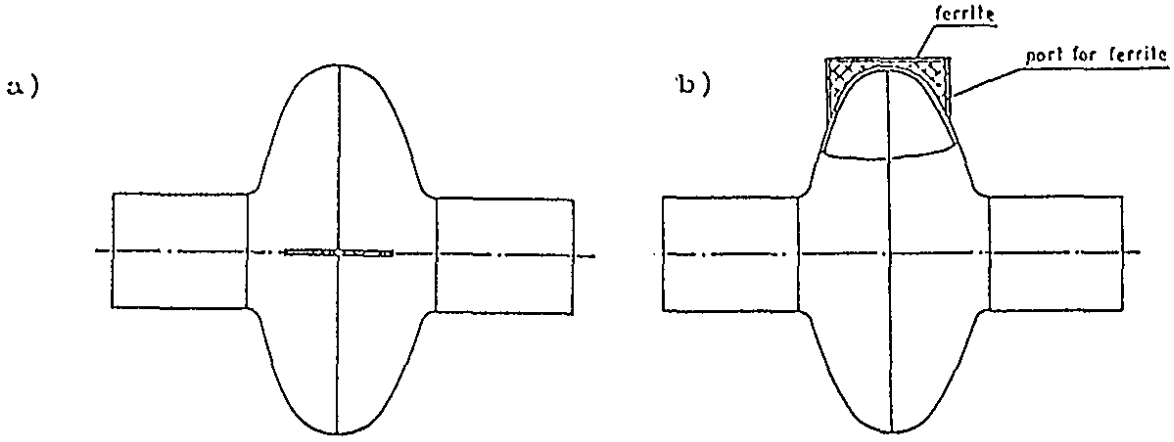

Figure 63: Slotted Cavity to reduce the Impedance for HOM.
(a) Location of the slot. (b) Slot covered with the ferrite.

the surface current of the fundamental mode. In early measurements the slots radiated into the free space. Later a surrounding cavity, filled with absorbing material, was added to dissipate the HOM radiated power. In another set of tests, absorbing material (ferrite) was placed outside the cavity to cover the slot area (Fig. 63b). With proper size and location of the ferrite material this results in the same damping as free space radiation. Once the optimum parameters (location, length, width) were found for one slot, cavities with increasing number of slots were measured. Finally the influence of the slots to the low R/Q HOM resonances were measured to prove the broadband character of this damping scheme.

Fig. 64a shows the damping of the most important HOM vs. increasing length (L) of a 2 mm wide (W) slot. Fig. 64b shows the damping of a 90 mm long slot with increasing width. Two polarizations of non-monopole modes are affected

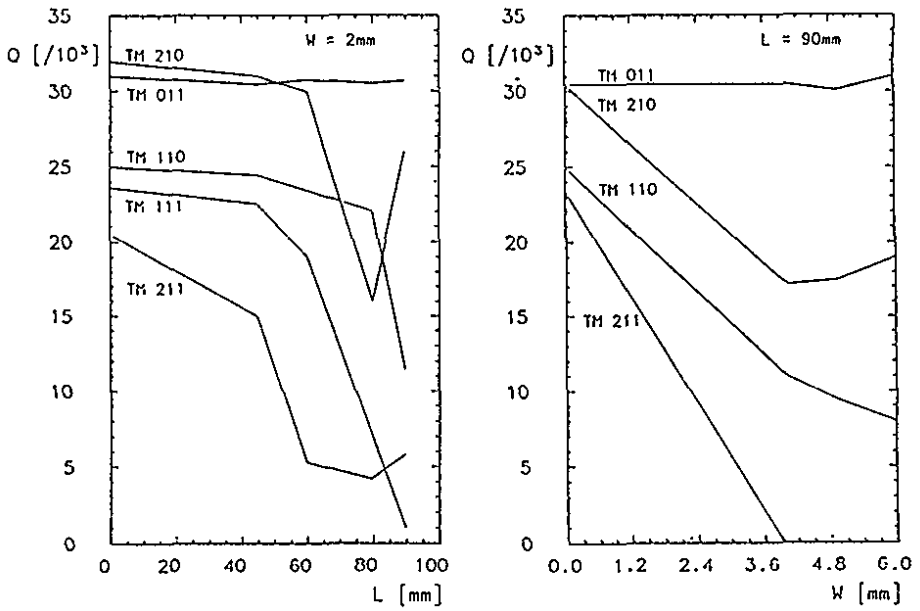

Figure 64: Damping of HOM in a slotted cavity. (L,W = length, width of slot) (a) Q vs. L, W = 2 mm; (b) Q vs. W, L = 90 mm

differently by only one slot. It means that more than one slot is needed to damp polarized field patterns. The polarization of TM_{210}, plotted in Fig. 64, shows less damping for a slot longer than 80 mm. This is due to a rotation of this polarization caused by the slot.

Based on the single slot data, single cell cavities with 2, 4, 8 and 12 slots have been measured. It turned out that a cavity with 8 equally spaced slots, each 100 mm long and 3 mm wide, is a good compromise between high damping of HOM resonances and only moderate effect to the fundamental mode.

Table XV shows the properties of all modes in the frequency range 1-3 GHz of a single cell resonator without slots and with 8 slots (L = 100 mm, W = 3 mm). With the exception of the two modes TM_{011} (high R/Q) and TM_{020} (low R/Q), all other HOM resonances are strongly damped. This demonstrates that slots of proper width and length provide a broadband damping device.

Other damping devices

One general problem with damping by slots is the fact that all HOM resonances with only longitudinal surface currents (as in the case of the fundamental mode) are less affected by longitudinal slots. To reduce the impedance of TM_{011} we used one dedicated electrical antenna coupler located at the equator. With this coupler a quality of Q = 400 was reached. The vanishing electric field of the fundamental mode at this location results in an only very weak (due to asymmetry effect) coupling to this mode so that only a moderate rejection filter in needed. The strong electric field of the TM_{011} mode, however, produces a

Table XV: HOM spectrum of the 1-cell cavity with no slots and with 8 slots

	Computed URMEL-T[45]		Measured					
			No slot on Cavity			Eight Slots on Cavity		
Mode	f(MHz)	R/Q(Ω)	f(MHz)	Q	Z($k\Omega$)	f(MHz)	Q	Z($k\Omega$)
TM_{010}	999.36	111.646	987.9	29400	3286.0	986.0	26520	2960.9
TE_{111}	1359.64	19.540	987.9	23600	461.1	–	< 50.	< 1.
			987.9	23500	458.8	–	< 50.	< 1.
TM_{110}	1411.26	44.094	987.9	24700	1088.6	1403.2	2200	97.0
			987.9	25100	1107.7	1486.0	2700	117.4
TM_{210}	1873.01	3.800	987.9	31900	121.1	1859.8	1000	3.9
			987.9	32600	123.9	1860.4	900	3.5
TM_{011}	1971.05	33.932	987.9	31200	1058.8	1958.8	400	13.6
TM_{020}	2025.07	0.030	987.9	32600	1.0	2015.3	29600	0.9
TM_{120}	2148.15	2.652	987.9	18000	47.7	2123.3	1100	3.0
			987.9	18000	47.7	2123.9	1300	3.9
TM_{310}	2235.40	0.656	987.9	33100	21.7	2232.8	1900	1.2
			987.9	37700	24.7	2236.1	1700	1.1
TE_{311}	2300.27	0.112	987.9	27600	3.1	2281.0	400	0.1
			987.9	27600	3.0	2288.4	500	0.0
1 TM_{211}	2654.06	10.802	987.9	21000	226.8	2634.9	500	5.5
			987.9	22500	243.0	–	< 20	< 0.2
TE_{411}	2707.86	0.0026	2719.1	25400	0.1	2701.7	1200	0.0
			2719.5	36700	0.1	2721.9	400	0.0
TM_{212}	2761.04	15.89	2787.4	28300	450.0	2781.0	3100	49.9
			2789.0	25000	397.6	2783.6	3700	59.5
TE_{124}	2935.96	1.900	2939.1	38700	73.6	2946.0	400	0.7
			2939.2	36200	68.9	2957.8	600	1.1

strong coupling and thus a strong damping of this mode. In another solution this single mode remains undamped and is tuned between machine lines.

Threshold currents

Beam instabilities were simulated in the LER of the proposed asymmetric B-factory using single cell cavities with an HOM spectrum as given in Table XV. The calculated threshold current of multibunch instabilities is 2.7 A. In comparison, the beam would be limited at about 2.0 mA if the standard 7-cell cavities of the PETRA ring would be used. For the given example of 8 slots the fundamental mode impedance Z is slightly reduced from 3.3 MΩ to 3 MΩ as compared to the cavity without any slots. If one accepts further reduction of this value, even more damping can be gained. On the other hand, the dissipated fundamental mode power warms the ferrite absorbers. For the presented cavity geometry (scaled to 500 MHz) we expect about 1.3 kW fundamental

mode power dissipation in each absorber if the cavity operates at an accelerating voltage of U = 0.61 MV (2.1 MV/m). At this field level the power dissipated in the cavity wall is 80 kW.

9 Multibunch Feedback System

Band width

Passive damping of parasitic modes is not sufficient to provide stable conditions for the large beam currents necessary in the asymmetric collider. An active damper system is needed. Due to the high number of bunches (640), the bandwidth of the feedback system necessary to cure the instabilities has to be around 40 MHz. According to calculations of the threshold of instabilities for the two machines it turns out that the natural damping times of about 12 msec (transverse) and 20 msec (longitudinal) must be reduced down to 500 μsec in order to reach the design currents. This means that the machines have to be operated at a factor of 20 above threshold currents. That this is indeed possible has recently been shown [46] by operating the PETRA e^- machine successfully in such a regime with a feedback system of 5 MHz bandwidth adapted to PETRA's operation mode.

The feedback gain necessary to damp the transverse and longitudinal oscillations in the injection process determines the maximum feedback cavity voltages in the longitudinal direction and the kicker strength in the transverse direction respectively. The difference between the proposed system and the existing PETRA/HERA broadband feedback system is the bandwidth of the deflecting and accelerating devices. For the PETRA/HERA system, the deflecting kicker was built up as a ferrite-capacitor loaded delay line together with a strip chamber, to protect the ferrite material against beam induced currents. The advantage of such a device is its high field at relative low input power. Its disadvantage is the limited bandwidth. For the proposed system the kicker magnets will not contain any ferrite and will therefore have a lower field strength but will have a sufficiently broadband frequency response. A series of kicker-amplifiers provide the necessary deflection.

Design of the feedback system

In order to damp dipole oscillations in the longitudinal direction an overlapping cascade of five 750 MHz-klystrons will be used. They are operated in single sideband amplitude modulation mode and have a bandwidth of $\Delta f = 8$ MHz each. Each transmitter drives a single rf resonator of the HERA/PETRA feedback type which has a bandwidth of 5 MHz.

The pick up of the PETRA/HERA feedback detection system has a bandwidth of about 40 MHz. After the pick up the signal will be split in eight parallel channels. For the digitization of each channel a 5 MHz ADC will be available. Eight detectors and digital filters in parallel will provide the proper delay and independently the required phase shift by using a three turn deep memory. After recombination the processed digital signals enter a DAC. The analog signals drive five feedback transmitters after passing the corresponding bandpass filters. A pre-equalizing network will be used to provide a sufficiently flat frequency response.

Most parts are existing

All the components except the gated splitter and the equalizer are already available and tested. They can be carried over from the PETRA/HERA system. Fig. 65 shows the blockdiagram of the proposed system.

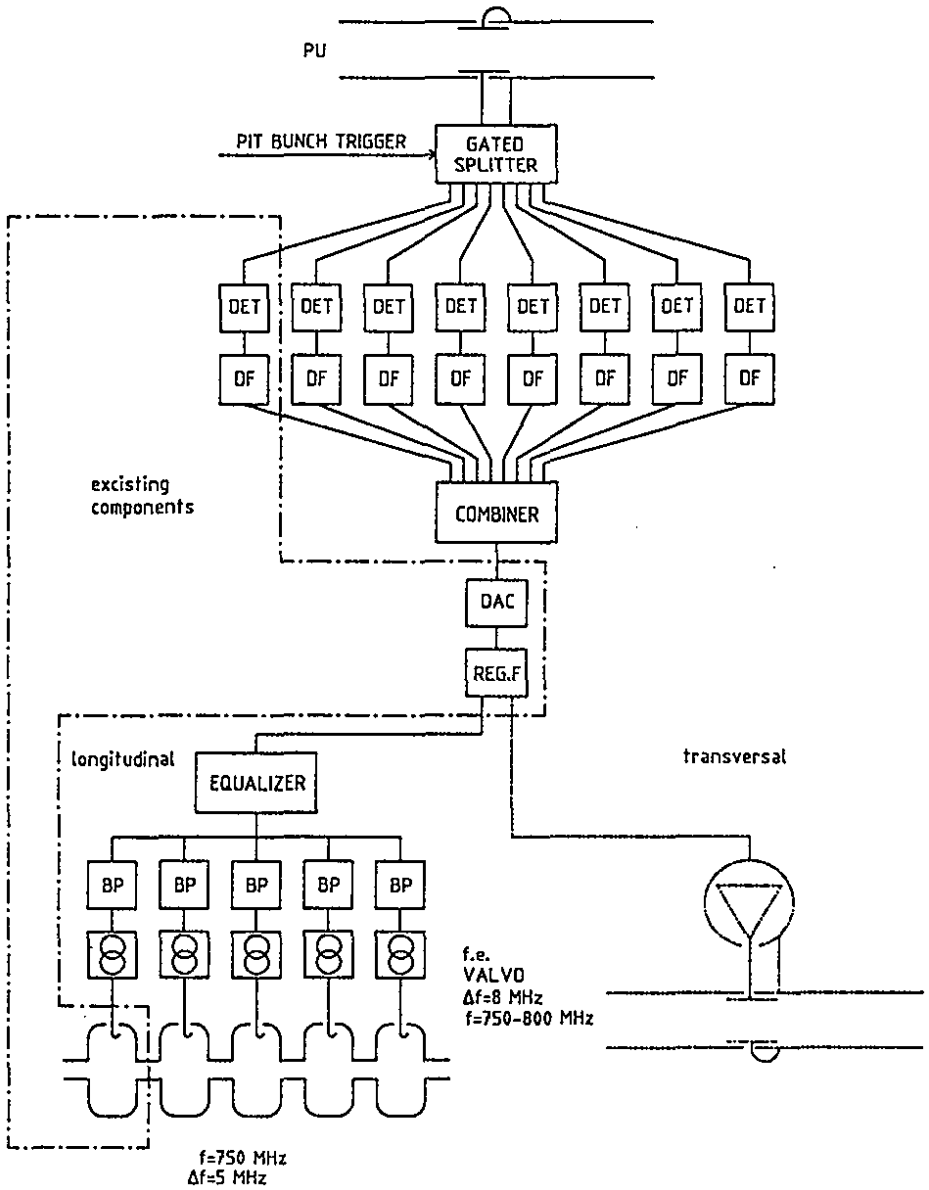

Figure 65: Blockdiagram of the fast feedback system

10 Magnets

Most magnets are standard

The magnets of the asymmetric collider require only standard accelerator technology. Bending and focusing magnets outside the interaction region are conventional magnets. They will be sketched below in order to allow a cost estimate. In the interaction region permanent magnetic quadrupoles and superconducting quadrupoles will be used. The aim of their study is to make sure that there exist technical solutions fitting into the limited space available near the IP. A special magnet is the large aperture Panofsky-type separator quadrupole. Interesting are also the short superconducting wiggler magnets in the LER.

10.1 Magnets in the Interaction Region

Permanent magnetic quadrupoles

The first low beta quadrupole is placed only 60 cm from the IP inside the detector field. The limited space available inside the 200 mrad polar angle cone requires a very compact quadrupole design. A permanent magnetic quadrupole is a good solution. A disadvantage of these quadrupoles could be their fixed gradient which does not allow to vary the machine energy. This is not considered an important constraint, however, since it concerns only the LER. Small scans of the center of mass energy can be accomplished by varying the energy of the HER.

There are several choices of permanent magnetic material for quadrupoles. Although Sm_2Co_{17} does not provide the same magnetization as other materials, it nevertheless appears to be the optimum choice for its small dependence of the magnetization on temperature, its resistivity against external magnetic fields and its good mechanical stability.

The first low beta quadrupole is divided into three sections of 25.7 cm length each, with rising inner and outer radii. They provide radial apertures of 33, 39 and 42 cm, respectively, for the beam and fit into the 200 mrad polar angle limit of the detector. A poletip field of $G \times r = 32.3\ T/m \times 28\ mm$ is achieved in a 16 segment quadrupole. Inbetween the 16 blocks a spacing of 0.6 mm is left which is necessary for tuning the quadrupole [47]. The ratio of the inner free aperture and the outer diameter with shielding is 4.8. This includes 5 cm for the beam pipe and an outer supporting cylinder, as well as fixtures for the Sm_2Co_{17} blocks. An integrated gradient of 23.57 T is provided. The relative nonlinear distortion of the quadrupole field at a radius of $10\,\sigma$ from the LEB is 3.8×10^{-4}. Fig. 66a shows a cross section of the permanent magnetic quadrupole, Fig. 66b the magnetic field lines as calculated by the PANDIRA magnet code [48].

Superconducting quadrupoles

For the other two quadrupoles in the low beta triplet, a superconducting design was chosen. Possible solutions are the magnets considered in the PETRA

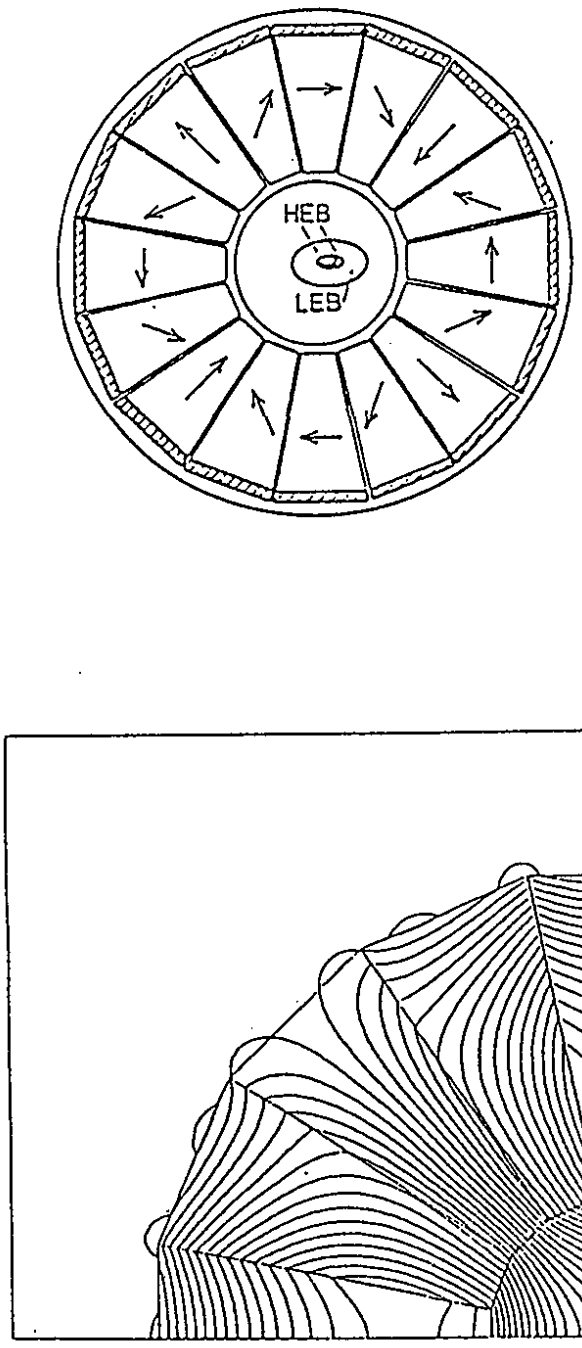

Figure 66: Permanent magnetic low beta quadrupoles for HELENA: (a) Schematic cross section and (b) Magnetic field lines as calculated by the PANDIRA magnet code [48].

microbeta study [49] or the TRISTAN superconducting low beta quadrupole [50].

Combined function separator magnet

The 10 m long combined function separator magnet is a hybrid between Panofsky quadrupole and window frame dipole. An aperture of 70 mm horizontal and 150 mm vertical is needed. The required quadrupole gradient of 0.29 Tm^{-1} is very low. The maximum field inside this magnet does not exceed 400 Gauss. Good field qualities are achieved with a simple design as shown in Fig. 67. No technical problems are expected for the layout of this magnet.

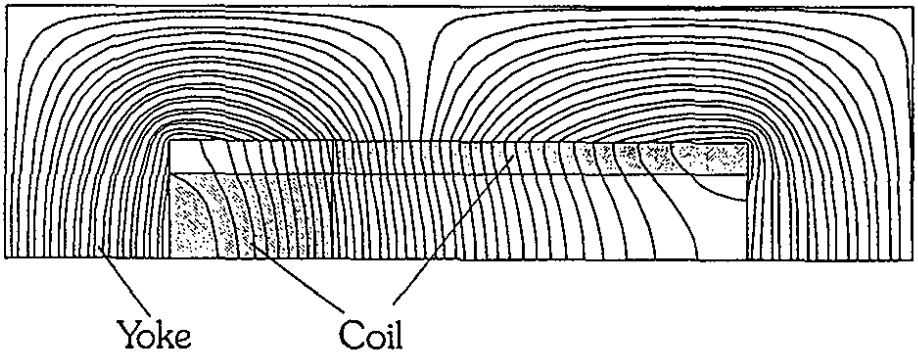

Figure 67: Schematic cross section of the separator magnet with magnetic field lines.

10.2 Conventional Magnets in the Arcs

Standard design

Fig. 68 and Fig. 69 show schematic cross sections of the LER magnets. Technical parameters are listed in Table XVI and XVII. Fig. 70 shows the field distribution in the bending magnets. Although a detailed engineering design still needs to be done for these magnets, no severe problems are expected. The same magnet profile will be used for the dipole magnets of both the HER and the LER. The two dipole types will only differ by their curvature.

The standard quadrupole magnet for the LER has been designed on the basis of the HERA QR-type quadrupole magnet [51]. Its cross section is shown in Fig. 68. For the HER the same design will be used with somewhat increased cross sections of the conductors and the return yoke.

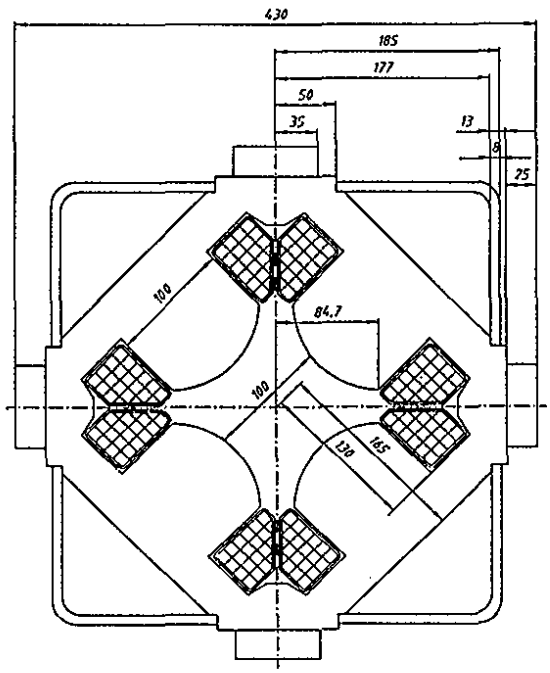

Figure 68: Schematic cross section of the LER quadrupoles.

Table XVI: Technical parameters of LER quadrupoles		
Quadrupole strength K_{max}	0.45	m^{-2}
Field Gradient	5.4	T/m
Pole distance	100	mm
Effective magnetic length	700	mm
Turns per pole	18	
Mean winding length	1.75	m
Copper cross section	$9 \times 9; 5\phi$	mm
Resistance (50°C)	~ 42	mΩ
Current	~300	A
Current density	~5	A/mm^2
Voltage	13	V
Power	~4	kW
Number of cooling circuits per magnet	1	
Cooling water flow	1.4	l/min
Cooling water velocity	1.15	m/sec
Cooling water pressure drop	6.6	bar
Magnet length	800	mm
Magnet cross section (height $\times$ width)	$\sim 430 \times 430$	mm
Iron weight	400	kg
Copper weight	70	kg
Total weight	~500	kg
Number of magnets	328	

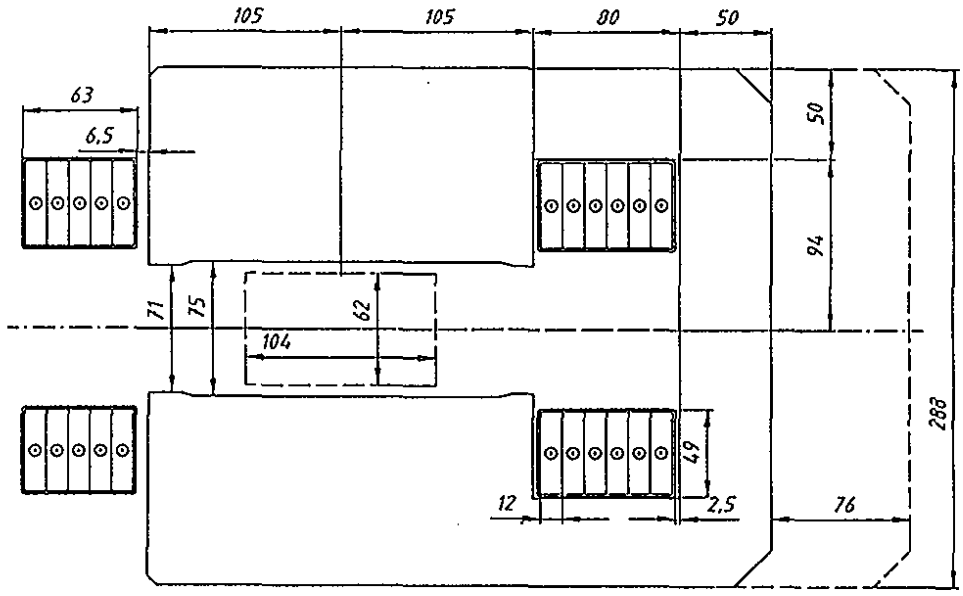

Figure 69: Schematic cross section of the LER bending magnets.

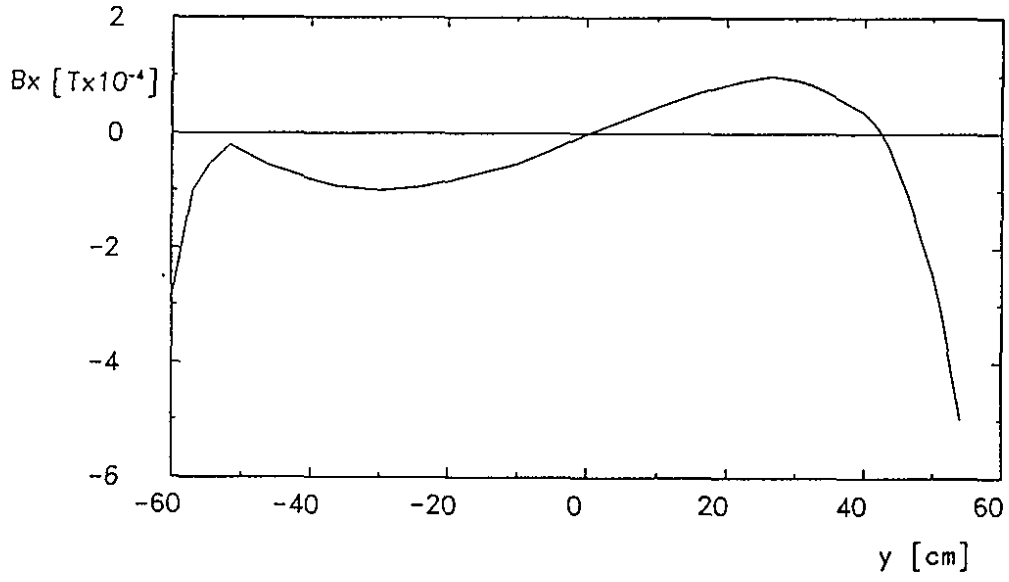

Figure 70: Field homogeneity of the LER bending magnets.

Table XVII: Technical parameters of LER bending magnets

Conductor material	Cu | Al	m^{-2}
Bending angle	6.4286	Grad
Bending radius	48	m
Sagitta	76	mm
Effective magnetic length	5.378	m
Pole distance	75	mm
Magnetic field	0.25	T
Ampere windings (no loss)	14920	A
Number of coils	2	
Turns per coil	6	
Conductor cross section	$11 \times 45; 65°$	mm
Mean winding length	11.5	m
Resistance	5.5 | 8.7	mΩ
Current (with 1.8% loss)	1267	A
Current density	2.75	A/mm^2
Voltage	7 | 11	V
Power	8.8 | 14	kW
Number of cooling circuits per magnet	1 | 2	
Cooling water flow	3.15 | 5	l/min
Cooling water velocity	1.6 | 1.5	m/sec
Cooling water pressure drop	8.5 | 4.2	bar
Iron body length	$\sim$ 5310	mm
Iron weight	3	t
Conductor weight	0.53 | 0.16	t
Total weight	4 | 3.6	t
Number of magnets	56	
Number of current circuits	1	

11 Vacuum System

Lifetime

For maximum average luminosity a beam-gas bremsstrahlung lifetime of better than 10 h is needed in the asymmetric collider. The average vacuum pressure in the two rings should therefore be better than 10^{-8} mbar.

Synchrotron radiation power load

At the operating conditions of the asymmetric collider with beam currents of I = 1.1 A for the LER and I = 0.71 A for the HER a large gas desorption rate is produced by the synchrotron radiation (SR) in the arcs. The linear power density in the bending magnets peaks at 20 W/cm in the HER. In the LER the power density reaches 5.4 W/cm. Outside the bending magnets the power load falls off quickly, and in the largest part of the 23 m long straight sections between bending magnets the load is negligibly small (see Fig. 71).

Synchrotron radiation power load

The critical energies of the SR photons are 9.77 keV for the HER and 1.3 keV for the LER. For nominal operational parameters one calculates the rates of photons per unit length to be $N_\gamma = 4.25 \cdot 10^{18}\,s^{-1}m^{-1}$ (HER) and $N_\gamma = 8.8 \cdot 10^{18}\,s^{-1}m^{-1}$ for the LER. Following [52] we estimate the production of nitrogen equivalent gas molecules with an effectivity of $\eta \approx 10^{-5}$. This leads to gas desorption rates of $Q \approx 1.21 \cdot 10^{-6}$ mbar l/s/m for the HER and $Q \approx 2.12 \cdot 10^{-6}$ mbar $l/s/m$ for the LER. Table XVIII summarizes the vacuum parameters for both rings.

Table XVIII: Parameters of the Vacuum System

	HER	LER
Beam Energy E/GeV	9.33	3.0
Beam Current I/A	0.71	1.1
Bending Radius /m	192	48
Linear Power Density W/cm	20.5	5.44
Power Density W/mm^{-2}	1.68	0.31
Critical Energy keV	9.77	1.30
Linear Photon Flux Density $s^{-1}cm^{-1}$	$4.25 \cdot 10^{18}$	$8.48 \cdot 10^{18}$
Photon Dose Density $cm^{-1}h^{-1}A^{-1}$	$2.15 \cdot 10^{22}$	$2.77 \cdot 10^{22}$
Gas Production Efficiency	10^{-5}	10^{-5}
Gas Desorption Rate	$1.21 \cdot 10^{-6}$	$3.12 \cdot 10^{-6}$
Pumping Speed l/s/m	120	670
Pumps	integr. Ion Getter Pumps	integr. Ion Getter + distr. NEG
Average Pressure mbar	10^{-8}	10^{-8}

Ion sputter pumps for the LER

In case of the HER the vacuum requirements can be met using conventional ion sputter pumps which will be integrated in the bending magnets. An optimized ion sputter pump integrated into a HERA-type vacuum chamber made of Cu-Sn-alloy provides an average pumping speed of S = 120 l/m/s which yields

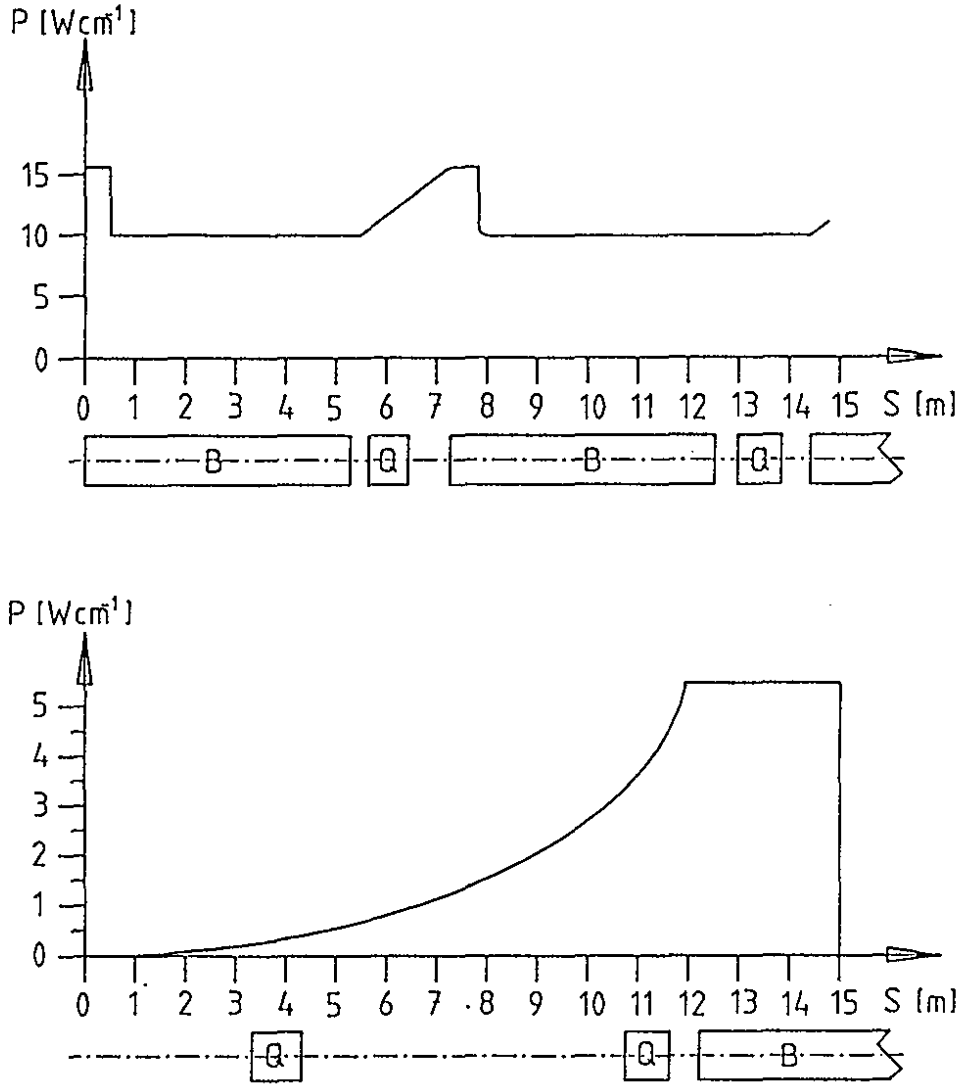

Figure 71: Linear Power Density on the Beam Pipe from Synchrotron Radiation .

an average pressure of 10^{-8} mbar. Fig.72 shows the profile of the proposed HER chamber. Copper, enforced by tin additions, appears to be the optimum material not only because of its superior thermal properties but also because of the highly developed production techniques available at DESY [53].

Ti sublimation pumps for the HER

In case of the LER, conventional integrated ion pumps do not perform well enough to provide the required vacuum. It is possible to reinforce the integrated ion sputter pumps by NEG material in which case it should be easy to achieve the required 300 l/s/m effective pumping speed. Due to the long straight sections of 23 m between bending magnets, distributed pumps are needed in addition. Six distributed Ti sublimation pumps provide additional 50 l/s/m needed to maintain the vacuum in the straight sections.

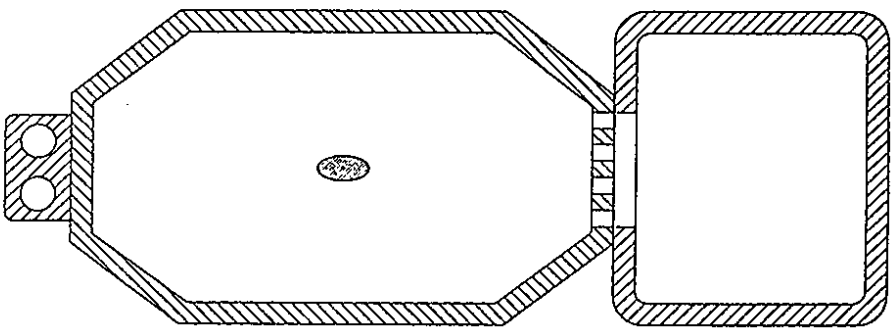

Figure 72: Cross Section of the HERA Copper Vacuum Chamber.

12 Injection into the Asymmetric Collider

Injection into the LER

The injection scheme for the preferred scenario is considered. The positrons for the LER come from the existing LINAC II. They are accumulated at 400 MeV and are then accelerated by the DESY II synchrotron up to 3 GeV and injected into the LER of the asymmetric collider (see Fig. 73). The existing positron transfer channel between DESY II and PETRA-SOUTH EAST needs to be

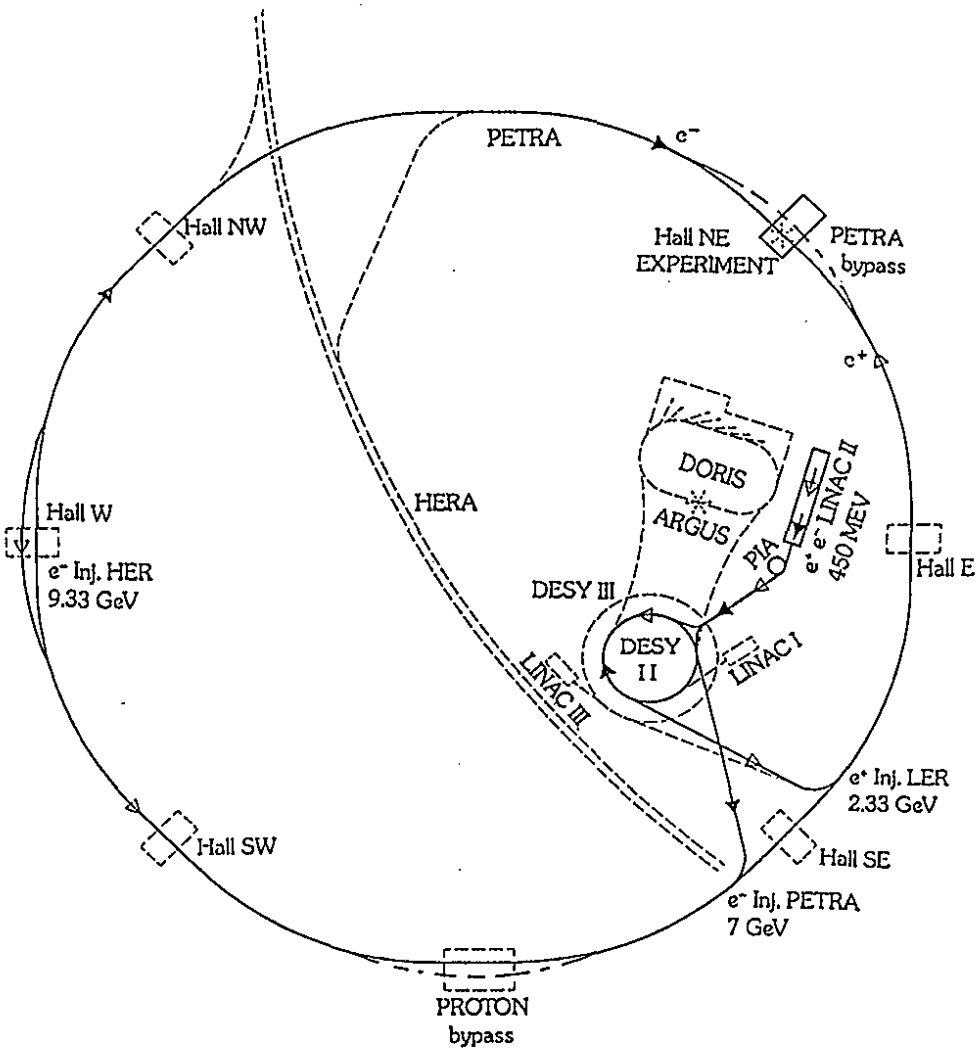

Figure 73: Injection Chain into the Asymmetric Collider.

modified. The existing positron injection in PETRA II will be maintained. A switchyard is needed in the straight section of the line which bends the 3 GeV positrons for the LER upwards. In the arc of the line the 7 GeV and the 3 GeV lines run in parallel on top of each other. There is sufficient space in the transfer tunnel.

The positrons need to be accumulated in the LER. The present performance of the positron source and acceleration chain is already sufficient. Every 160 ms which is the cycle time of the synchrotron, 10^{10} positrons are delivered. Nine shots are needed to fill the bucket with $8.3 \cdot 10^{10}$ positrons. To fill the LER will take 16 minutes. This is just satisfactory.

Injection is accomplished in the standard way with a thin active septum (d = 3 mm) and a kicker bump with 3 kicker magnets. The emittance of the injected beam is π mrad·mm. The available aperture for the injected beam amounts to 10 standard deviations of the circulating beam. The circulating beam has to be kicked from a $10\,\sigma_x$ distance to a $3.4\,\sigma_x$ distance from the septum. The necessary strength of the kicker amounts to 0.4 mrad corresponding to 40 Gauss·m. For a rectangular kicker pulse of 100 ns length, $1.1 \cdot 10^8$ particles from the circulating beam are lost at the septum. It is expected that a fraction of at most 10^{-3} or 10^5 particles will be lost in the detector region at each injection process which is considered tolerable. This should allow a quasi continuous injection mode to top-off the beam intensity which is important for high average luminosity.

Injection into the HER

The electrons of the HER are injected at top energy. This allows to top-off the intensity and is also favorable with respect to instabilities. The existing PETRA ring will be used as a 9.3 GeV injector. It has to be ramped between its injection energy of 7 GeV to the 9.3 GeV transfer energy. Injection into the HER is accomplished by a 20 m long straight transfer channel in the WEST straight section. Two 1 m long 1 T magnets are needed to bend the beam by 20 mr. Ejection and injection is in the horizontal plane. The bunch distance in PETRA is 100 ns. Bunches are extracted from the axis using the same elements as for the extraction towards HERA [54].

Particles could in principle be injected on the axis of the HER circulating beam. However since the bunch distance of 12 ns is too short for the kicker to rise, the beam has to be injected in quasi accumulation mode. A kicker strength of 0.27 mrad is needed which corresponds to 84 Gauss·m. The bunch spacing in PETRA is 100 ns. $3 \cdot 10^{10}$ particles in 70 bunches can be accelerated and transfered at one time. Two bunches from PETRA have to be accumulated in the HER to obtain the desired intensity of $5.3 \cdot 10^{10}$ electrons per bunch. This means that PETRA has to be ramped 18 times. Each ramp cycle from 7 to 9.3 GeV takes about 2 minutes. This is large compared to the filling time of PETRA. The present electron injection system via LINAC II and the PIA accumulator ring is able to deliver $3 \cdot 10^{10}$ electrons every 160 ms. To fill the HER takes about 20 minutes. Topping off the intensity appears to be very desirable.

13 Cost Estimate

Table XIX: Cost Estimate of the Asymmetric Collider

	LER	HER	
	[MDM]	[MDM]	
Magnets	10.9	20.9	
Vacuum	8.0	7.5	
Stands	$\approx$ 1.0	$\approx$ 1.0	
Rf	16.4	29.3	
Power Supplies	7.3	8.1	
Cabling	2.1	2.1	
Diagnostics	2.0	2.0	
Controls	9.0	9.0	
Cooling	3.5	3.5	
Mounting	3.0	3.0	
Interaction Zone	3.4	0.5	
Cryogenics	4.3	—	
Wiggler	2.4	—	
Feedback	2.0	2.0	
Total	$\approx$ 76.0	$\approx$ 89.0	
	Civil Engineering	$\approx$ 10.0	
	Grand Total	$\approx$ 175.0	MDM

Bibliography

[1] D. Rubin, Proc. of the XIVth Interntl. Conf. on High Energy Accelerators, Tsukuba (1989), Part I, p 64.

[2] A. Piwinski, "Review of Mini Beta Luminosities in PETRA at Different Energies", DESY 81-066 (1981)

[3] S. Krishnagopal, "Beam-Beam Dynamics with Round Beam Profiles", Thesis, Cornell University, Jan.1991.

[4] A. Hutton, Proceedings of the Workshop on Beam Dynamics Issues of High Luminosity Asymmetric Colliders, Berkeley (1990), p. 284

[5] H. Nesemann, W. Schmidt-Parzefal and F. Willeke, "The Use of PETRA as a B-Factory", Proceedings of the European Particle Acc. Conf., Rome 1988, p. 439 (1988)

[6] H. Nesemann, W. Schmidt-Parzefal and F. Willeke, "The Use of PETRA as a B-Factory", Proceedings of the European Particle Acc. Conf., Rome 1988, p. 439 (1988)

[7] F. Willeke et al, Proc. of the XIVth Interntl. Conf. on High Energy Accelerators, Tsukuba (1989), p 1355

[8] F. Willeke et al, Proceedings of the Workshop on Beam Dynamics Issues of High Luminosity Asymmetric Colliders, Berkeley (1990), p. 565

[9] K. Hirata and E. Keil, CERN/LEP-TH/89-76 (1989)

[10] S.Kurokawa, K.Satoh, E.Kikutani (editors), "Accelerator Design of the KEK B-Factory", KEK Report 90-24 (1991), Part A.

[11] CESR B-Factory, Cornell University, CLNS 91-1050 (1991).

[12] T. Nakada (editor), "Feasibility study for a B-Meson Factory in the CERN ISR Tunnel"

[13] A. Zholents, Proceedings of the Workshop on Beam Dynamics Issues of High Luminosity Asymmetric Colliders, Berkeley (1990), p. 592

[14] L.R.Evans, J.Gareyte, "Beam-Beam Effects", CERN SPS 86-8 (DI-MST), 1986.

[15] J. Tennyson, Proceedings of the Workshop on Beam Dynamics Issues of High Luminosity Asymmetric Colliders, Berkeley (1990), p. 130

[16] Th.Browder, M.Witherell, CLNS 90-1019

[17] D.C.Carey 'The Optics of Charged Particle Beams' (1987) Harwood Academic Publishers, and references therein

[18] E.Storm, H.I.Israel Nucl.Data Tables A7 (1970) 565

[19] D.C.Carey et al., DECAY TURTLE (1982) SLAC-246

[20] W.R.Nelson, H.Hirayama, D.W.O.Rogers, The EGS4 Code System, SLAC-Report 265 (1985)

[21] S. Myers, Proceedings of the EPAC, Nice (1989), p 13ff

[22] Y. Kimura, Proc. of the XIVth Interntl. Conf. on High Energy Accelerators, Tsukuba (1989), p 87

[23] J. Seeman, Proc. of the XIIth Interntl. Conf. on High Energy Accelerators, Batavia (1983), p 212

[24] D. Rice, Proceedings of the Workshop on Beam Dynamics Issues of High Luminosity Asymmetric Colliders, Berkeley (1990), p. 219

[25] E. Kikutani et al., Proc. of the XIVth Interntl. Conf. on High Energy Accelerators, Tsukuba (1989)

[26] G.M.Tumaikin, A.R.Temnykh, XIIIth Internatl. Conf. on High Energy Accelerators, Nowosibirsk (1986), p. 88

[27] H.Nesemann, B.Sarau, IEEE Trans. Nucl. Scie. NS-32 (1985) p. 1655 High Energy Accelerators, Nowosibirsk (1986), p. 88.

[28] calculated from Fang Shouxian and Chen Senyu, Proc. of the XIVth Interntl. Conf. on High Energy Accelerators, Tsukuba (1989), p. 51

[29] H.Wiedemann, SLAC Pub 2320 (1979)

[30] E.Amanan et al., Proc. of the VIIIth Interntl. Conf. on High Energy Accelerators, (1971), p. 132

[31] R.Chehab et al., Proc. of the VIIIth Interntl. Conf. on High Energy Accelerators, Geneva, (1980), p. 702

[32] E. Keil and R. Talman, CERN-ISR-TH/81-33 (1981)

[33] "An Asymmetric B-Factory based on PEP", Conceptual Design Report, SLAC-372 (1991)

[34] A. Piwinski, "Observation of Beam-beam effects in PETRA" DESY 79-11 (1979)

[35] T. Weiland, Nucl. Instr. Methods, 212 (1983) 13-34.

[36] Basetti,Gerke,Huebner,Kohaupt, DESY 79/07, 1979
T. Weiland DESY M-81/23, 1981
Klatt, Kohaupt, Weiland, Particle Accelerator Conference, Vancouver 1985.

[37] R.D. Kohaupt, DESY 80/22, 1980.

[38] K. Balewski, R.D. Kohaupt, DESY 90-122, 1990.

[39] KEK Report 90-24, 1991, (KEK Proposal)
CLNS 91-1050 (Cornell Proposal).

[40] Yinghua, Proch, Sekutowicz, Particle Accelerators, 1990, Vol.29,p 41-46.
Massarotti et al., Particle Accelerator Conference, San Francisco 1991.

[41] H.Vogel, DESY M-85-09 (1985)

[42] H.Musfeldt et al., " PETRA 500 MHz Klystrons", DESY M-81-15 (1981).

[43] E.Haebel and J.Sekutowicz, "Higher Order Mode Coupler Studies at DESY", DESY M-86-06 (1986).

[44] C. Yinghua, D. Proch, J. Sekutowicz, "The Slotted Cavity-A Method of Broadband HOM Damping" Internat. Conf on High Energy Accelerators, Tsukuba (1989)

[45] U.Laurströer, U.Van Rienen, T.Weiland, "URMEL and URMEL-T User Guide", DESY M-87-03 (1987).

[46] D.Heins et al., "Wide Band Multibunch Feedback Systems for PETRA", DESY 89-197 (1989).

[47] S.Herb, "Field Quality and Stability of Permanent Magnetic Quadrupoles", PAC 1985, Vancouver, IEEE Trans. on Nucl. Science, Vol. NS-32, No.5 (1985).

[48] A.M.Winslow, Journal of Computational Physics, 2 (1967) 149.

[49] E.Daskowski (editor), "PETRA Micro Beta Study", DESY M-82-11 (1982).

[50] S.Ito, J.Nazhazawa, S.Bonsai, M.Hirana, "On the Construction of a Superconducting low beta Quadrupole Magnet",
Proc. Workshop Superc. Magn. and Cryogenics, Brookhaven, May 1986, BNL 52006, UC-28 (1986).

[51] M. Leenen, private communication

[52] C.Benvenuti, VACUUM 37 (8) 699.

[53] R.Balliou et al., "The Vacuum System of High Energy Storage Rings", Proc. of the XIVth Interntl. Conf. on High Energy Accelerators, Tsukuba (1989), p. 847

[54] J.Rümmler, private communication.

Part III

Design of a Detector for a High Luminosity Asymmetric B Factory

1 General Layout

Layout of a universal detector

We propose to construct a universal detector. It is optimized for the observation of CP-violation, but also allows for an extremely wide additional physics programme.

It consists of the following active detector components:

Abbreviation	Component
SVD	Vertex detector
CTC	Central track chamber
RICH	Ring imaging Čerenkov counter
TOF	Time of flight system
ECAL	Calorimeter
MUCH	Muon detector

A r,z-section through the detector is shown in Fig. 74, a cross section in r,ϕ is given in Fig. 75.

The detector of an asymmetric B-factory has a similar structure as a classical detector at a symmetric storage ring. The main difference is that is has to be extended in the direction into which the high energy beam points, in order to cover the same solid angle as for the symmetric case.

Lorentz boost

The shape of the detector is dictated by the Lorentz boost $\beta\gamma$ of the centre of mass system of the beams in the storage ring. It is given by the beam energies $E_1 = 9.33$ GeV and $E_2 = 3.0$ GeV

$$\beta\gamma = \frac{E_1 - E_2}{2\sqrt{E_1 E_2}} = 0.6$$

Due to this Lorentz boost the average flight path of a B-meson originating from $\Upsilon(4S)$ resonance will be

$$x = \beta\gamma c\tau = 0.21 \; mm$$

Distances of this order can be resolved by the vertex detection system of the proposed detector.

The Lorentz transformation induced by this boost is illustrated in Fig. 76.

A fast particle emitted at an angle of $\theta^* = 90°$ relative to the beam axis in the *CM* frame will appear at a polar angle

$$\theta_\perp = \arctan\frac{1}{\beta\gamma} = 59°$$

in the detector. A forward moving low mass particle with *CM* momentum p^* will have its momentum transformed into the laboratory frame given by

$$p_+ = (\gamma + \beta\gamma)\, p^* = 1.76\, p^*.$$

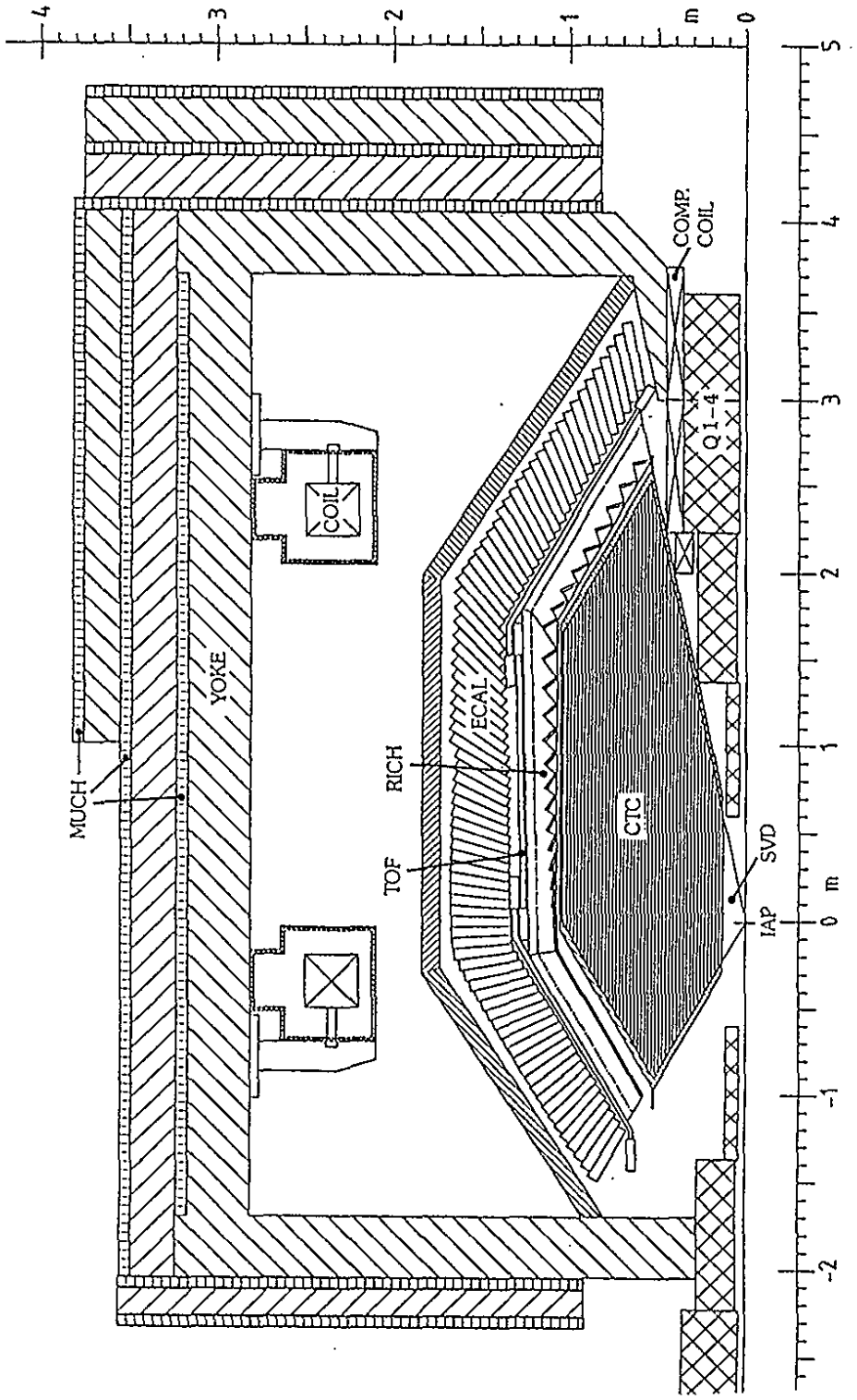

Figure 74: Cross Section of the Colliding Beam Detector (r,z view).

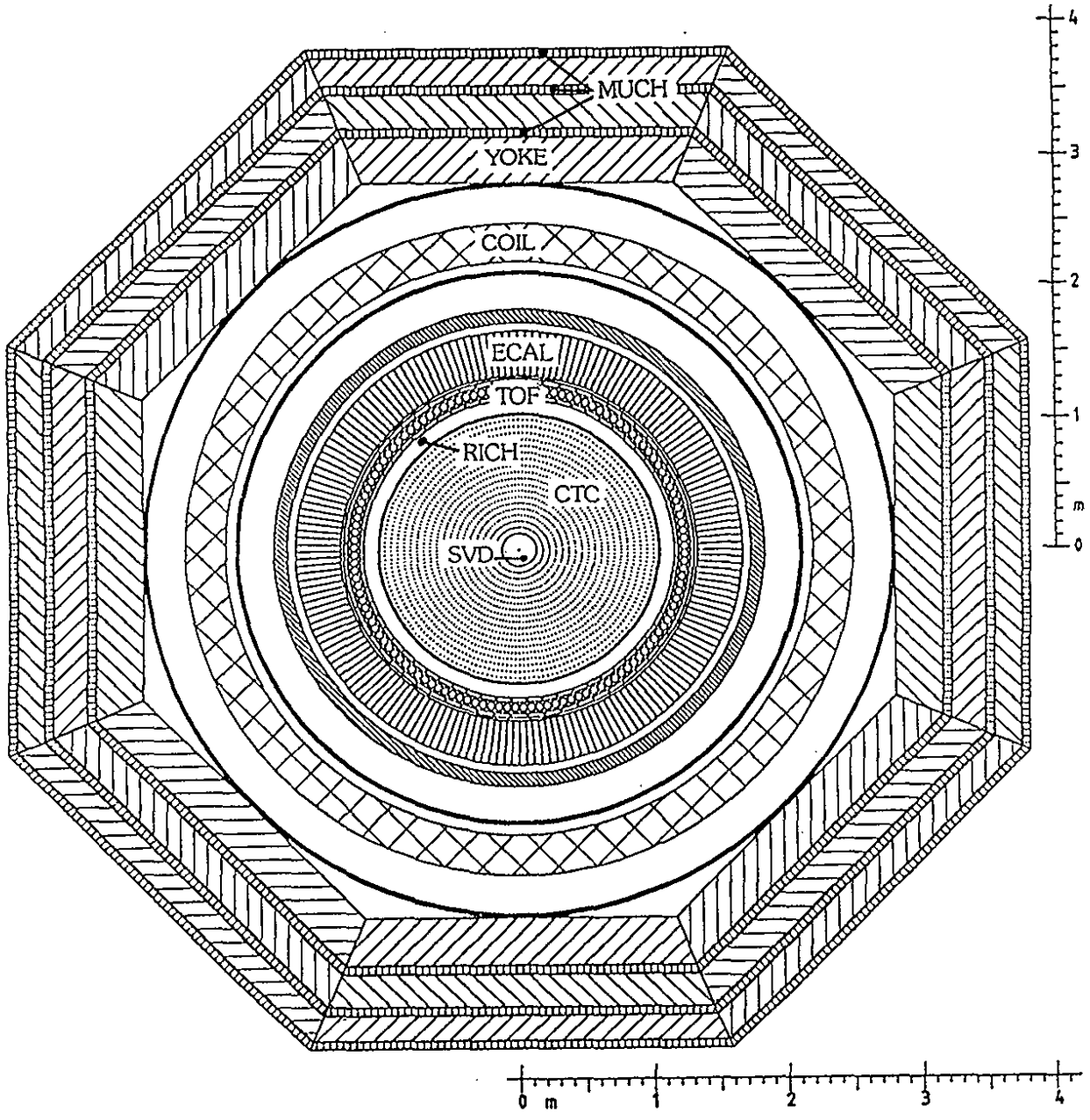

Figure 75: Cross section of the Colliding Beam Detector (r,ϕ view).

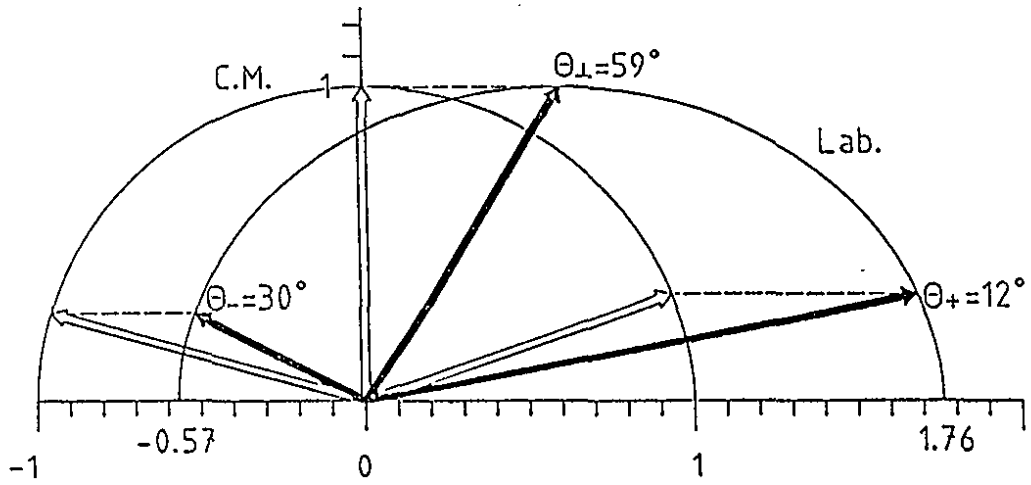

Figure 76: Effect of the Lorentz boost $\beta\gamma = 0.6$ on high momentum particles. Open arrows: *CM* momenta; black arrows: Laboratory momenta.

Correspondingly, a backward moving particle gets a laboratory momentum

$$p_- = (\gamma - \beta\gamma)\, p^* = 0.57\, p^*.$$

Small polar angles θ^* in the *CM* system are transformed into the laboratory frame like

$$\theta_+ = \frac{\theta^*}{1.76} \text{ and } \theta_- = \frac{\theta^*}{0.57}.$$

Due to a very sophisticated interaction region design, an angular coverage of the detector down to an angle of

$$\theta_+ = 12°$$

has been achieved in forward direction. This corresponds to a forward solid angle coverage in the *CM* system of

$$\Omega^*_+ = cos(1.76\,\theta_+) = 93.4\ \%\ \text{of}\ 2\pi.$$

In the backward direction we choose a coverage down to

$$\theta_- = 30°,$$

resulting in

$$\Omega^*_- = cos(0.57\theta_-) = 95.6\ \%\ \text{of}\ 2\pi.$$

Obviously the proposed detector covers an impressive solid angle range, which *Acceptance*
in total amounts to

$$\Omega = 94.5\ \%\ \text{of}\ 4\pi.$$

Ellipsoidal shape of the calorimeter

In order to provide that calorimeter elements of equal size cover equal *CM* solid angle elements, the calorimeter must have an ellipsoidal shape. The distances of the calorimeter from the interaction point in the various directions should relate like

$$\text{forward} : \text{sideward} : \text{backward} = 1.76 : 1 : 0.57.$$

The shape of the proposed calorimeter approximates this shape.

Drift chamber radius

The radius of the drift chamber r defines the scale and thus the overall size of the detector. A large radius has advantages. The momentum resolution improves like the square of the radius. Also pattern recognition and the resolution of the specific ionisation measurement improves. However, there is also a disadvantage connected with a too large chamber radius. Kaons will decay within the chamber before being identified in the identification system behind the chamber and thus get lost. As a result of simulation calculations we consider a radius of

$$r = 104 \ cm$$

the optimal choice. This specification sets the scale for all other detector components.

Conical shape of the drift chamber

The shape of the drift chamber results from the requirement to obtain the same momentum resolution for high-momentum particles regardless of their flight-direction in the *CM* frame. Since the transverse momentum resolution is proportional to the inverse square of the radius and to the transverse momentum, the forward radius should be

$$r_+ = r\sqrt{\sin(1.76 \cdot \theta_+)} = 0.60 \ r.$$

In order to keep the length of the chamber within the limits of technical feasibility, we choose $r_+ = 54 \ cm$ which is still a fair approximation to the original goal.

The backward radius should be

$$r_- = r\sqrt{\sin(0.57 \cdot \theta_-)} = 0.54 \ r.$$

Here we choose $r_- = 52cm$.

Thus the proposed conical shape of the drift chamber gives an almost constant momentum resolution, independently of the polar angle of a track, in the *CM* frame. In addition this shape minimizes the material traversed by photons flying to the calorimeter and it allows the optimal shape of the calorimeter to be implemented. The usual separation into a barrel and an end cap calorimeter, present in all classical detector designs, has been avoided here. This will lead to a more homogeneous data quality and a substantial increase in detection efficiency.

Ring imaging Čerenkov counter for particle identification

A ring imaging Čerenkov counter is the ideal instrument for particle identification at a B-factory detector. The detector design is based on the assumption that such a counter can actually be built and operated. As a fall back solution the space allocated for the RICH can be used to install a high performance time of flight system which would guarantee reliable operation at a somewhat reduced resolution. This option is illustrated in Fig. 77.

Trigger scintillators

If a RICH is used, we foresee a simple time of flight system behind the RICH which serves for triggering purposes.

CsI calorimeter

We propose a calorimeter made of CsI(Tl) crystals. Other apparently less expensive solutions have been extensively studied. In particular, a calorimeter design using scintillating glass was worked out in detail. No substantial savings could be obtained, and CsI(Tl) remained as the only reasonable choice.

Behind the calorimeter a 10 *cm* thick stainless steel housing supports the weight of the calorimeter and serves as part of the muon filter.

Magnetic field

The magnetic field is generated by a pair of superconducting Helmholtz coils. Compared to the classical solenoid coil, they are less expensive and they allow for access to the electronics of the calorimeter. The central field has a strength of 1 T.

Muon filter

The outer shell of the detector is an iron magnetic return yoke which also serves as a muon filter and contains the muon chambers.

Optimization

The detector described here has been designed for the physics at a B-factory without compromising the design because of economic reasons. It is optimized within the limitations due to technical possibilities and unavoidable conflicting requirements which tend to distort the performance of one component by optimizing another one.

However, it appears impossible to arrive at a substantially cheaper design which would be still capable of performing all the measurements of the physics programme planned.

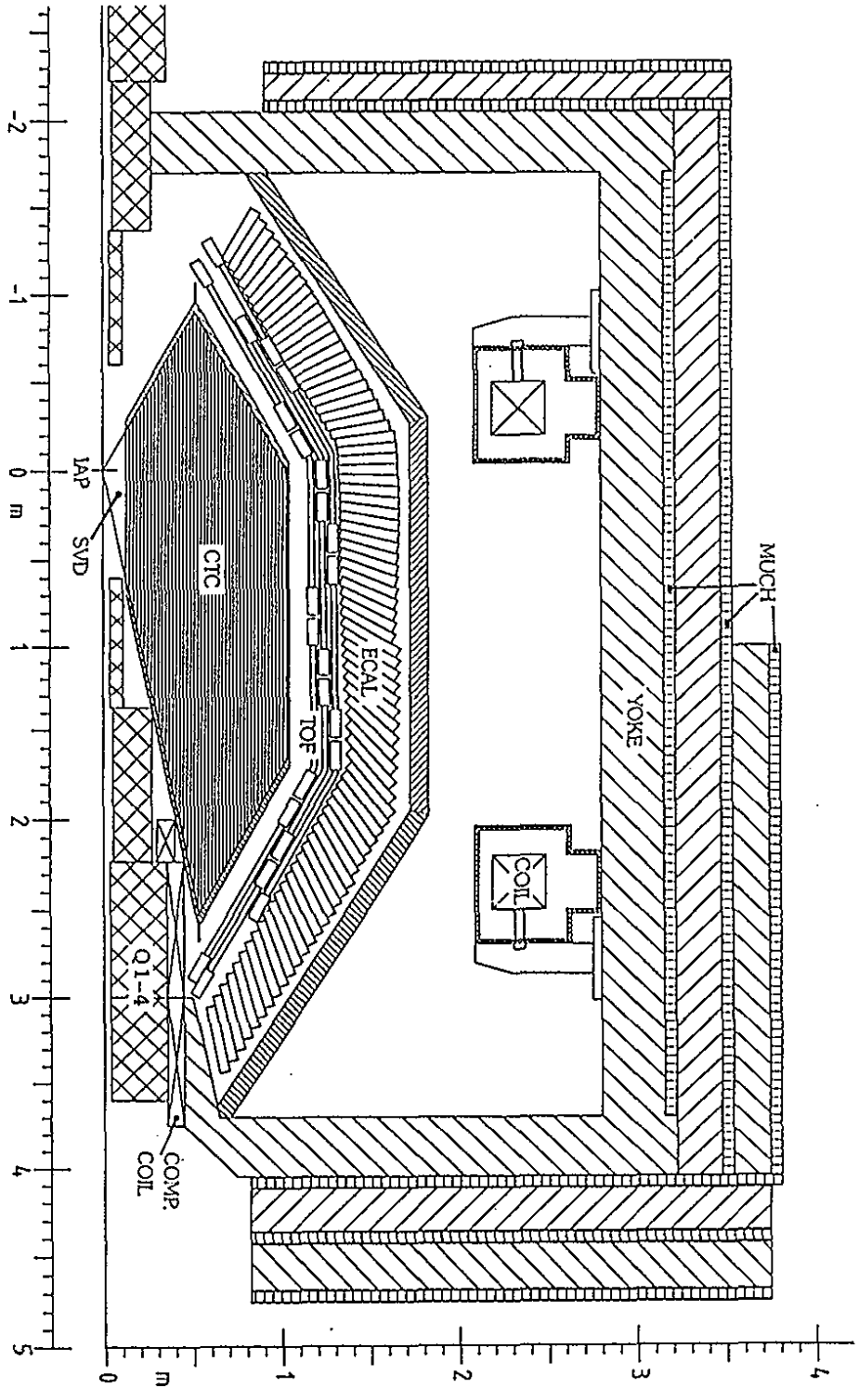

Figure 77: Detector with Time of Flight Scintillation Counters for Particle Identification instead of RICH Counters.

2 The Magnet

The momentum p of charged particles is measured by the curvature of their tracks in a magnetic field. We choose a magnetic field strength of B = 1 T.

Choice of field strength

This choice is a compromise between the requirements of good momentum resolution demanding a high field and of good acceptance for low momentum tracks, which would be curled up by a high field. These conflicting requirements are best satisfied by a low magnetic field strength and a large detector radius.

Simulation calculations for the pilot reactions to be observed by the detector have shown that the momentum resolution σ_p required is

$$\frac{\sigma_p}{p} = 0.7\% \frac{p}{GeV/c}$$

For a drift chamber with the proposed wire structure and a radius of 1 m this resolution is achieved by a field of B = 1 T.

We foresee an iron flux return yoke with flat poles and an octagonal barrel part. Two types of coils fit into this yoke: A solenoid or a pair of Helmholtz coils.

A study of these two options was performed at Saclay. It showed the feasability of both options. While a solenoid produces a more uniform field, the Helmholtz coils allow for access to the electronics of the calorimeter and they are slightly less expensive. A solenoid design would be a scaled down version of the ALEPH coil, while the Helmholtz coil would be built with the technology developed for the BEBC and EHS coils.

Helmholtz coils

For the present detector design, we choose superconducting Helmholtz coils, since access to the shower counters and easier mechanics to open the detector are considered to be very important. Field distortions, caused by the compensation coils needed to shield the beam magnets from the detector field, will arise in either scenario, and are straightforward to compensate in the analysis software. Hence this is not a decisive factor.

The coils are arranged in the classical Helmholtz coil configuration, each one in equal distance from the centre of the magnet. The distance between the two magnet poles is twice the distance between the coils. Thus the axial forces on the coils are zero, as long as both coils are excited by the same current. Nevertheless strong supports are foreseen, which will hold the coils in place in case that one of the coils fails.

Coil construction

A coil is made of flat pancakes, with spacers between pancakes for helium circulation in a pool boiling mode. The conductor is a copper stabilized tape as currently manufactured, wound under tension together with a stainless steel tape, which carries, in a distributed way, the radial magnetic load and avoids the need for an outer thick shell. In this design the winding is mechanically sound, without vacuum impregnation, and is properly cooled. The assembly

and electrical connections are easily controllable without complicated tooling and sophisticated helium joints. The large axial forces have to be sustained towards the iron yoke and require a number of axial supports. They are made of high strength glass-epoxy columns anchored in a vertical steel plate which is connected to the iron yoke and also serves as a closing vacuum flange of the cryostat. The two coils are completely separate and independent. The main parameters of the coils are collected in Table I.

Table I: The main characteristics of the coils

Inner diameter of cryostat	4.1	m
Outer diameter of cryostat	5.3	m
Length of a cryostat	0.76	m
Diameter of coil (centre)	4.7	m
Distance of coils (centre)	2.7	m
Number of pancakes per coil	10	
Number of turns per pancake	50	
Conductor size	30 x 4	mm^2
Stainless steel tape	30 x 2	mm^2
Rated current	5000	A
Central field	1	T
Peak field on conductor	5	T
Total Amp x turns	$5 \cdot 10^6$	
Current density in conductor	42	A/mm^2
Overall current density	25	A/mm^2
Axial force on single excited coil	540	t
Axial force if both coils are excited	small	
Stored energy	100	MJ

Cost

According to these specifications a cost estimate was made at Saclay. The coils will amount to 18 MDM including cryogenics, but not helium refrigeration.

The iron yoke of the magnet has a weight of 1043 t. The cost of the iron yoke is estimated to be 6.3 MDM.

Comparison of normal conducting and superconducting coils

The relatively low field required could also be achieved by a normal conducting magnet. A normal conducting copper solenoid with the same radius and central field would cost about 6 MDM and have a power consumption of 4 MW. Assuming an average electricity cost of 4 MDM per year, after a continuous operation time of 3 years both a normal- and a superconducting magnet would require about the same funds.

Field maps are shown in Fig. 78 and 79.

To facilitate an early separation of the two beams of the storage ring, the detector magnet could be tilted by 110 mrd relative to the beam direction in the horizontal plane. The detector components are not affected by this tilt.

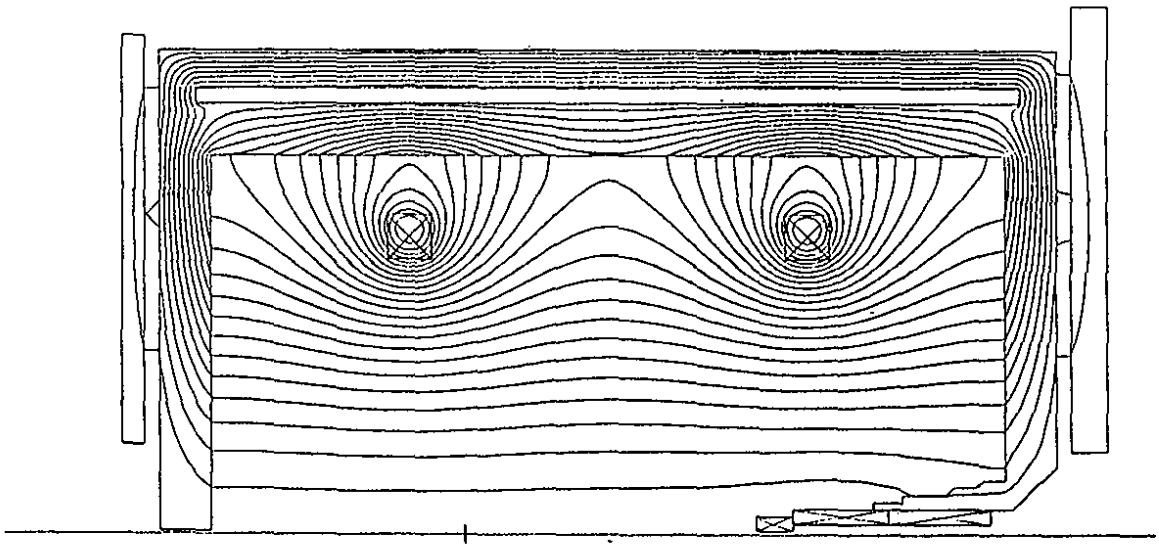

Figure 78: Field distribution in the Colliding Beam Detector.

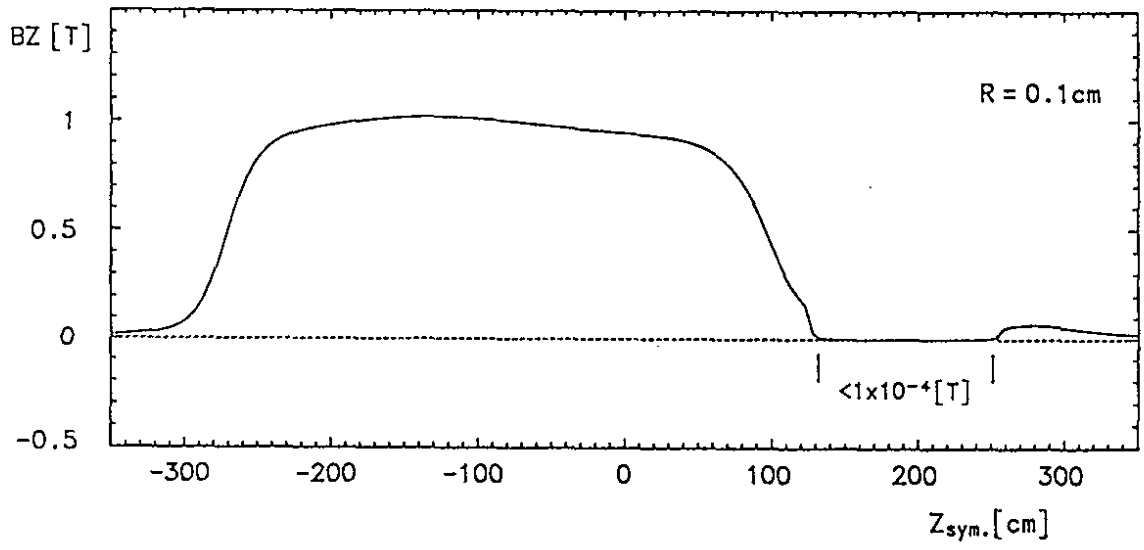

Figure 79: *Field Distribution in z Direction at* R = 0.1 cm, showing that the beam magnets at a distance from the IP of more than 1.2 m are well shielded against the main detector field by the compensation coils.

Their axes remain strictly parallel to the beam axis. Alternatively an early beam separation could also be accomplished by small permanent magnets.

3 Vertex Detector

3.1 Introduction

Combination of asymmetric collider and vertex detector gives access to fundamental time dependent effects

The potential physics output of an asymmetric B-factory depends crucially on the performance of a vertex detector, which gives access to the measurement of time dependent effects down to time differences of $\tau \sim 10^{-13}$ s by measuring space differences $\beta\gamma c\tau$, where the asymmetric collider provides the Lorentz-boost $\beta\gamma$ of the B mesons. The main objectives of a B-factory include such time measurements:

- The observation of CP violation in B decays to CP eigenstates, with $B \to J/\psi K_s$ being the most prominent example, which requires a determination of the time order of the two B decays.
- The study of the strongly time-dependent process of B_s-$\bar{B}_s$ mixing.
- The measurement of the individual lifetimes of beauty mesons and of the τ lifetime with an improved accuracy.

Furthermore a vertex detector adds to the reconstruction efficiency of reactions in two ways:

- The separation of decay vertices in three dimensions reduces the combinatorial background in B and D decays and the hadronic background in τ-lepton decays.
- Adding high precision points to the track information obtained by the drift chamber improves the momentum determination.

In addition to an excellent spatial resolution, the innermost component of a B-factory detector has to meet other demands. It is highly exposed to the radiation background and can not be accessed for maintenance during long periods of time.

3.2 Choice of Devices

3.2.1 Silicon Detectors

Strip detectors

Double-sided silicon strip detectors appear to be the obvious choice for a precise 2-dimensional position measurement:

- An intrinsic resolution better than 5 μm has been demonstrated [1]. This is due to the high ionization statistics in Si, the limited charge diffusion and the fine detector segmentation. A typical pitch size is 25 μm, but when a charge is induced in $\geq$2 strips, the computation of the centroid yields a position resolution much better than the strip pitch.

- Silicon detectors can cope with the speed requirements of high rate experiments. The charge collection time is of the order of 10 ns, depending on geometry and bias voltage, with an ultimate limit at carrier saturation of $\mathcal{O}$(1 ns). Contemporary VLSI preamps allow for a rise time of $\sim$100 ns [2].

- Self-supporting structures are possible with silicon being a strong and rigid material. The planar processing technology allows to fabricate strip diodes with a high flexibility in design and a geometrical accuracy better than 1 μm.

- The fine segmentation leads to a low probability for background hits overlapping with real tracks, i.e. a high occupancy limit.

- Silicon detectors are resistant to a radiation exposure of several 10^4 Gy [3].

- There is growing experience in the use of various types of Si-detectors in high energy physics and the development of new superior devices is an active field of research.

Thickness

A drawback of silicon strip detectors is their thickness of typically 300 μm which introduces an angular uncertainty due to multiple Coulomb scattering of the particle. For detectors fabricated on 4" wafers, the thickness can be reduced to 200 μm at the cost of a lower signal and higher fragility [4].

Radiation sensitivity

Another problem is the sensitivity of the associated VLSI electronics to radiation where the maximum dose is at present a few 10^2 Gy, but specifically radiation hard chip designs and fabrication processes do exist in prototypes [5].

Pixel devices

A severe limitation in the noise performance of strip detectors is the large interstrip capacitance of $\sim$2 pF/cm. This can only be avoided by detectors segmented into pixels where the signal is amplified locally. Several realizations of such a device have been proposed [6,7] and prototypes have already been built and tested [8]. However, with pixel devices still being in an immature state, the layout proposed in this study shall be based on strip detectors. The option of using pixel detectors instead does not affect the general design.

CCD

Charge coupled devices (CCDs) are pixel detectors that are used in some experiments [9], but the readout by shifting the signal through the device at a frequency of a few MHz per channel is far too slow for the present purpose.

3.2.2 Other Devices

Vertex drift chambers

Drift chambers with small drift cells and operated at an increased pressure have reached a considerable level of accuracy. A vertex chamber similar to the one operated at ARGUS [10] would suffice to measure CP violation in B decays, but its resolution is clearly inferior to that of a silicon detector. The amount of material in the sensitive volume appears to be in favor of a gaseous chamber, but this statement is reversed, once the walls of the pressure vessel and support structures for wires with large stereo angles are taken into account. Furthermore, the background occupancy in drift chamber cells is expected to be higher than in silicon strips [11]. This also compromises the presumed good pattern recognition ability of a drift chamber.

If the radiation background is too high to operate a silicon detector, a drift chamber would not help either. Only for a high radiation dose delivered during the injection phase, a drift chamber would be advantageous, because its aging can be retarded by switching it off during critical periods. Since an improved radiation hardness of VLSI electronics can be envisaged, the discussion of a vertex drift chamber as a fallback solution will be omitted.

A combination of vertex drift chamber and silicon detector is disfavored because it requires additional material and volume, and there is no significant benefit.

Gas microstrips

Gas microstrip detectors, where cathode and anode strips are fabricated on a resistive substrate with a pitch of 100 μm or less, are the most promising alternative to silicon detectors. Prototypes [12,13] have not yet reached the intrinsic resolution of silicon strip detectors, but further improvement is possible. Using Kapton as the substrate, these devices would be inexpensive, geometrically flexible and thinner than silicon detectors. A conceptual design of a vertex detector with this new technology has been presented in [14].

Scintillating fibres

Glass or plastic scintillating fibres [15] or capillaries filled with a scintillating liquid have been proposed as central tracking detectors of high resolution. To obtain a sufficient accuracy, 2-3 % of a radiation length material are required, by far exceeding the thickness of a silicon detector. Furthermore, there is presently no attractive readout technique. Image intensifiers followed by CCDs are clearly too slow, whereas photomultipliers would occupy too much space.

Forward TPC

In the forward* region, where the resolution of a cylindrical silicon detector is strongly degraded by multiple Coulomb scattering, the use of a small time projection chamber (TPC) has been proposed [16]. Apart from geometrical conflicts, a high occupancy and problems with the required uniformity of the magnetic field are expected. Instead, we propose to cover the forward region by a suitable silicon device.

*"forward" and "backward" refers to the direction of the Lorentz boost.

3.3 Design Considerations

3.3.1 Impact Parameter Resolution

Spatial resolution

The impact parameter resolution, i.e. the 1-σ extrapolation error perpendicular to the track direction, depends on the detector's intrinsic position error and on the angular uncertainty from multiple scattering (MS). A beam pipe of radius R_0 and thickness t_0 in units of radiation lengths ultimately limits the resolution to

$$\sigma = rms\ angle \times lever\ arm \approx \frac{z\ 0.014\ GeV}{\beta\ c\ p}\sqrt{t_0/\sin\vartheta}\ \times\ R_0/\sin\vartheta \qquad (69)$$

where z, p and ϑ are the particle's charge, momentum (in GeV/c), and polar angle, respectively.

Consider a silicon detector of two cylindrical layers with intrinsic resolutions σ_i and radii $R_i\,(i = 1, 2)$, the inner layer being close to the beam pipe $R_1 \approx R_0$. With σ_{MS} being the combined MS errors of the beam pipe and the first layer, the impact parameter resolution is approximately given by

$$\sigma^2 = \left(\frac{\sigma_1 R_2}{R_2 - R_1}\right)^2 + \left(\frac{\sigma_2 R_1}{R_2 - R_1}\right)^2 + \sigma_{MS}^2. \qquad (70)$$

The gain from increasing the gap $R_2 - R_1$ is limited by σ_{MS} and σ_1, *i.e.* the properties of the beam pipe and the inner detector layer. For more detector layers, the particle track may be written as

$$y(x_i) = \alpha_0 + \sum_{j=1}^{i} \alpha_j (x_j - x_{j-1}); \quad x_0 = 0$$

with x measured along and y perpendicular to the track, and neglecting the small bending in the magnetic field. At each layer $j > 0$, at which MS occurs, the particle is deflected by an angle $\alpha_j \approx \tan\alpha_j$ with a momentum-dependent *rms*-value. The impact parameter resolution is then given by the uncertainty in the determination of the coefficient α_0, when applying a least squares fit procedure.

It is found that a third layer of silicon strips does not further improve the resolution. Nevertheless, at least three layers are required, if track recognition is to be done from the silicon detector alone. The resolution of e.g. the two outer layers pointing to hits in the innermost layer is then given by an expression analogous to eq. 70.

Angular dependence

The intrinsic detector resolution depends on the angle of incidence. For inclined tracks, the precision of the centroid of the induced charge is deteriorated by the noise on the strips involved, and by energy straggling causing a non-uniform charge distribution along the track. At large angles, the mean coordinate of

the strips within a hit cluster becomes even more accurate than the centroid. These effects have been modelled in Monte-Carlo simulations [17] and have been measured recently, but only preliminary experimental results are available [18]. A crude parametrization of the angular dependence

$$\sigma_{intrinsic} = 5\mu m + 10\mu m \times \ (angle\ of\ inclination)^2$$

may suffice for the present purpose, since the impact parameter resolution is usually dominated by multiple scattering, particularly for inclined tracks.

3.3.2 Geometrical Limits

Geometry

The space available for the vertex detector is limited by the outer radius of the beam pipe (we assume 2.55 mm within z=±130 mm), the inner radius of the drift chamber (130 mm) and a double cone of 200 mrad opening angle ($\cos\vartheta = \pm 0.98$) centered at the z-axis, which is occupied by collider quadrupoles and compensation coils.

The drift chamber covers polar angles of $\vartheta = 12° - 150°$. The true interaction region is not pointlike, but extends longitudinally with a σ_z of 11 mm. The silicon detector will be arranged such that tracks originating from a 2-σ_z region traverse three silicon layers before entering the drift chamber.

3.3.3 Background Limits

One limit on the tolerable amount of background radiation is set by the maximum dose the detector and readout electronics can resist. The other limit is the acceptable probability for background hits interfering with real tracks (see also [11]).

Synchrotron radiation

Knowing the beam properties, the synchrotron radiation characteristics are predictable and masks can be designed to shadow the sensitive region from direct radiation (see II.5.2). Photons scattered e.g. from downstream collimators and leaking through the beam pipe are likely to be absorbed in the innermost silicon layer. Their spectrum is dominated by the 8 keV line from K-shell fluorescence in the copper coating of the beam pipe. At this energy, the mean free path in silicon is only 0.07 mm.

A limit of 0.1 Gy/h (or $2.8 \cdot 10^{-8}$ W/g) that allows readout chips available today to survive about 10^7 s, corresponds to a flux of 10^6 photons/s of 8 keV absorbed per cm^2 of a 200 μm thick silicon layer. On average, charged particles will induce charge on 4-5 strips of 50 μm width. Considering a 12 cm long detector, 300000 background hits per second from synchrotron radiation are expected in five adjacent strips. With a readout frequency of 10 MHz (see 3.4) the resulting occupancy probability of 3 % is just tolerable. The limit on synchrotron photons is further relaxed by the fact that 8 keV photons are easily discriminated from the >50 keV hit clusters of minimum ionizing particles.

However, the occupancy will become the limiting factor, when radiation hard electronics permits a dose rate orders of magnitude higher.

Lost beam particles

Another source of background are beam particles deflected by interactions with the residual gas. These lost particles and photons from interactions close to the IP may send shower debris into the detector. The significance of this process depends on the machine geometry, the vacuum profile and the beam conditions, particularly during injection, and is hard to predict. Compared to synchrotron radiation, the average energy is much higher and the tolerable flux of particles lower. Since the first detection layer has to be as close to the beam pipe as possible, there is no space for an effective shield against this radiation. For beam particles hitting the masks or the conical slopes of the beam pipe, EGS4 [19] shower simulations indicate that a shield of $\geq$30 radiation lengths of heavy material (lead or tungsten) can attenuate this radiation by a factor of $\sim$10.

3.3.4 Environmental Considerations

Apart from pile-up due to radiation background, the signals from the silicon detectors may be distorted by thermal noise, electromagnetic pickup and, to a certain extent, by the detector's magnetic field.

Temperature

The temperature in the vicinity of the vertex detector should not only be kept at a moderate level, but also equilibriated within the detector volume to avoid time-dependent and uneven thermal expansion. Contemporary CMOS readout chips have a power consumption of 1 mW per channel [2] which results in $\mathcal{O}$(100 W) for the whole vertex detector. The heat load of the beam pipe due to synchrotron radiation, image current heating, and higher order mode losses may be even larger [20].

Cooling

Cooling by forced air yields about 1.3 kWs/(m^{3}K). The forward detector described below leaves a gap of 0.016 m^2 between detector and beam tube. With a flow of a few m/s and a temperature difference of, say, 2° K, not more than 100 W can be handled. Cooling by contact to a liquid circuit or evaporative cooling is more efficient and should be employed at suitable places, possibly in combination with forced air to level out temperature variations. If the beam pipe is cooled by a liquid between two concentrical Be tubes [21], the lever arm in eq. 69 increases by 1 mm and t_0 is doubled, increasing the extrapolation error by 50%.

Noise

Besides being sensitive to RF pickup, the vertex detector itself is a potential source of noise: current VLSI chips require several 5 V driving signals transmitted continuously at the sample frequency.

Magnetic field effects

A magnetic field of 1 Tesla results in a Lorentz angle of 31 (165) mrad for holes (electrons) in silicon [22]. This causes a broadening of the signal and a systematic shift of a few μm that can be corrected for.

3.4 Layout of a Silicon Vertex Detector

3.4.1 Strip Detector Layout

A generic design of a silicon vertex detector, based on technology existing today, is presented in this section.

Double-sided strip detectors

Double-sided strip detectors with orthogonal strips are now available, providing three-dimensional position information without doubling the detector thickness. On a high-resistivity n-type substrate, p^+-strips on one and n^+-strips on the other side are introduced by ion implantation. The p^+ strips form diodes to which a reverse bias voltage is applied. They are individually biased by polysilicon lines connected to a bus which provides ohmic contact between the strips. Aluminum readout lines, congruent with the strips, are separated from the doped material by a SiO_2 layer forming capacitors for AC readout. On the n^+ side, an accumulation layer of electrons builds up that would short the n^+ strips if no measures were taken to isolate them, either by additional p^+ implantations [23] or with field-induced junctions [24].

Strip pitch

To match the diffusion width of the charge carriers, a strip pitch of 25 μm is chosen. A good resolution is achieved by taking advantage of capacitive charge division [1] and connecting only every second strip to the readout electronics.

Placement of readout electronics

The readout electronics is placed on ceramic hybrid plates glued onto the detector edges and connected via ultrasonic wire bonding. Considering a rectangular detector with orthogonal strips, it is desirable to access long and short strips from the short edge only. A way to accomplish this is currently under study [14,25]: The short aluminium lines are overlaid by a second metallization layer with readout lines running perpendicular to the short strips, spaced at the nominal strip pitch. Contact holes in the oxide layer separating the two metallization layers connect every Nth short strip to a given readout line, where N is the number of such lines fitting on the detector. This leads to an ambiguity which is removed using the drift chamber information. In the z-coordinate, the stereo angle of the drift chamber wires yields a resolution of $\mathcal{O}(1\text{ mm})$ which is more than sufficient. A rectangular detector and an analogous semi-circular design are sketched in Fig. 80.

3.4.2 VLSI Readout Electronics

Chip design

The silicon strip detectors are read out by VLSI-chips with a pad pitch of 50 μm. Although other configurations are just as possible, 128 readout channels per chip are assumed in the following. The chip is then 6.4 mm wide and of similar length, depending in detail on the functions incorporated and the technology used. Contemporary preamplifier chips with multiplexed readout [26,27,28,29] are customarily fabricated with 3 μm CMOS technology, but smaller integration is already available. The functional units required for the present purpose are:

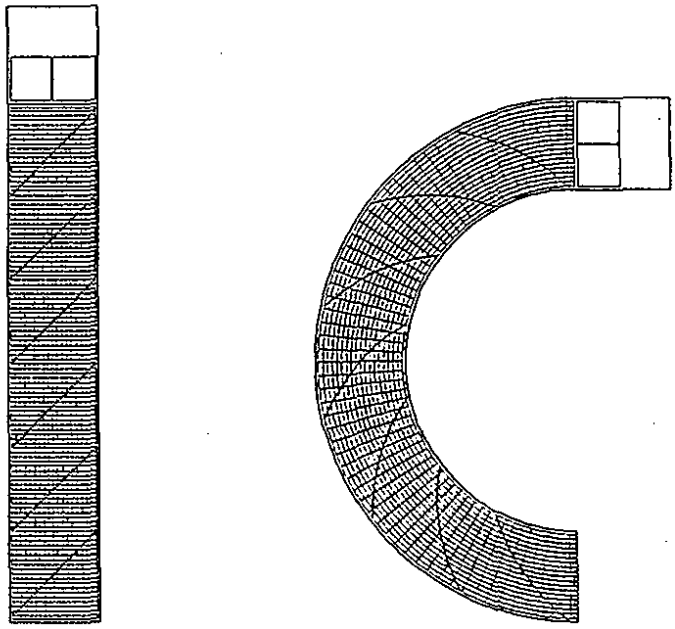

Figure 80: Schematic design of strip detectors with double strip metallization. Contact holes along the diagonal lines connect each readout line to a number of short strips.

- A charge sensitive amplifier with low noise and low power consumption.
- A discriminator providing digital information.
- An analog pipeline to store pulse heights for at least $3\mu s$ and a second buffer for $\sim$10 events accepted by the first level trigger.
- Circuitry for multiplexed readout.

Power, speed, noise

Noise performance, power consumption, speed, and detector capacitance are interdependent quantities. Using CMOS chips, a power consumption adjusted to 1 mW/channel is consistent with a rise time of 100 ns [2], i.e. $\geq$8 bunch crossings per sample. With 16000 electrons released by a minimum ionizing particle traversing 200 μm of silicon, the equivalent noise charge should not exceed $\sim$1500 electrons for a detector capacitance of $\sim$25 pF. This requires additional filtering techniques, known as double and quadruple correlated sampling [26,27], where samples are taken before and after the actual event. An analog pipeline as discussed below can provide these samples.

Digital information

A comparator provides digital information from channels above a preset threshold. The minimum requirement for a first level trigger is the OR of all channels on one chip. More detailed digital information can be used to decrease the readout time by addressing only the channels above threshold. The feasibility of such a feature has already been demonstrated [28], but the anticipated benefit has to be balanced against the additional chip area and higher power consumption.

Analog pipeline

A decision from the first level trigger is expected after 3 μs which defines the depth of the analog pipeline. None of the existing chips provides multi-event storage, since there was no immediate need to do so, but developments in view of future high rate experiments have started [2,30,31,32]. An analog pipeline can be realized with switched capacitors, standard CMOS elements with a sufficiently long memory decay time [33]. Building a ring buffer of 32 storage cells for each channel would extend the chip length by 2 mm.

Several events selected by the first level trigger are stored to await the next level decision, while data taking continues. This may happen in a shorter version of the previous pipeline or, at this stage, one may even think of pipelining the events through a successive-approximation ADC [30].

Multiplexed readout

The second level trigger initiates the readout cycle where multiplexing reduces 10^5 channels to 10^2 readout lines, i.e. 8-12 chips share a bus on a thin Kapton cable. At a cycle frequency of 5 MHz, this implies a readout time of 200 μs. The bus contains lines for the analog output, detector bias, chip power supply, driving signals for the switching sequences of sampling and readout, and possibly address lines for selective readout. There is space available between the detector and the first magnets to install cable drivers as close as 20 cm to the chips.

3.4.3 Signal Processing

Electronics

The role of further electronics depends on the functions implemented on the chip. The required tasks include noise filtering, analog-to-digital conversion by flash ADCs, elimination of time-dependent pedestals or common mode fluctuations, hit clusters identification and communicating the reduced data to a computer. Since the multiplexed readout is a bottleneck, some of these jobs may be done on-chip while awaiting a higher level trigger decision.

An example is the unit developed for the DELPHI silicon vertex detector [34]. For flexibility in the algorithm employed, a programmable processor is used which allows for a processing time of $\sim$2 ms.

To keep pace with the event builder, readout and data processing should take no longer than 1 ms which appears to be feasible with 10^2 units working in parallel.

3.4.4 The Barrel Detector

The barrel detector consists of three cylindrical layers built of rectangular modules that contain up to four double-sided strip detectors (Fig. 81a,b).

Geometry of the barrel detector

The radius R_1 of the innermost layer is determined by the fact that it should be very close to the beam pipe to minimize the multiple scattering error. For the outer layers, the module length increases with radius and so does the detector capacitance. The radius R_3 of the outermost layer is chosen as to yield a module

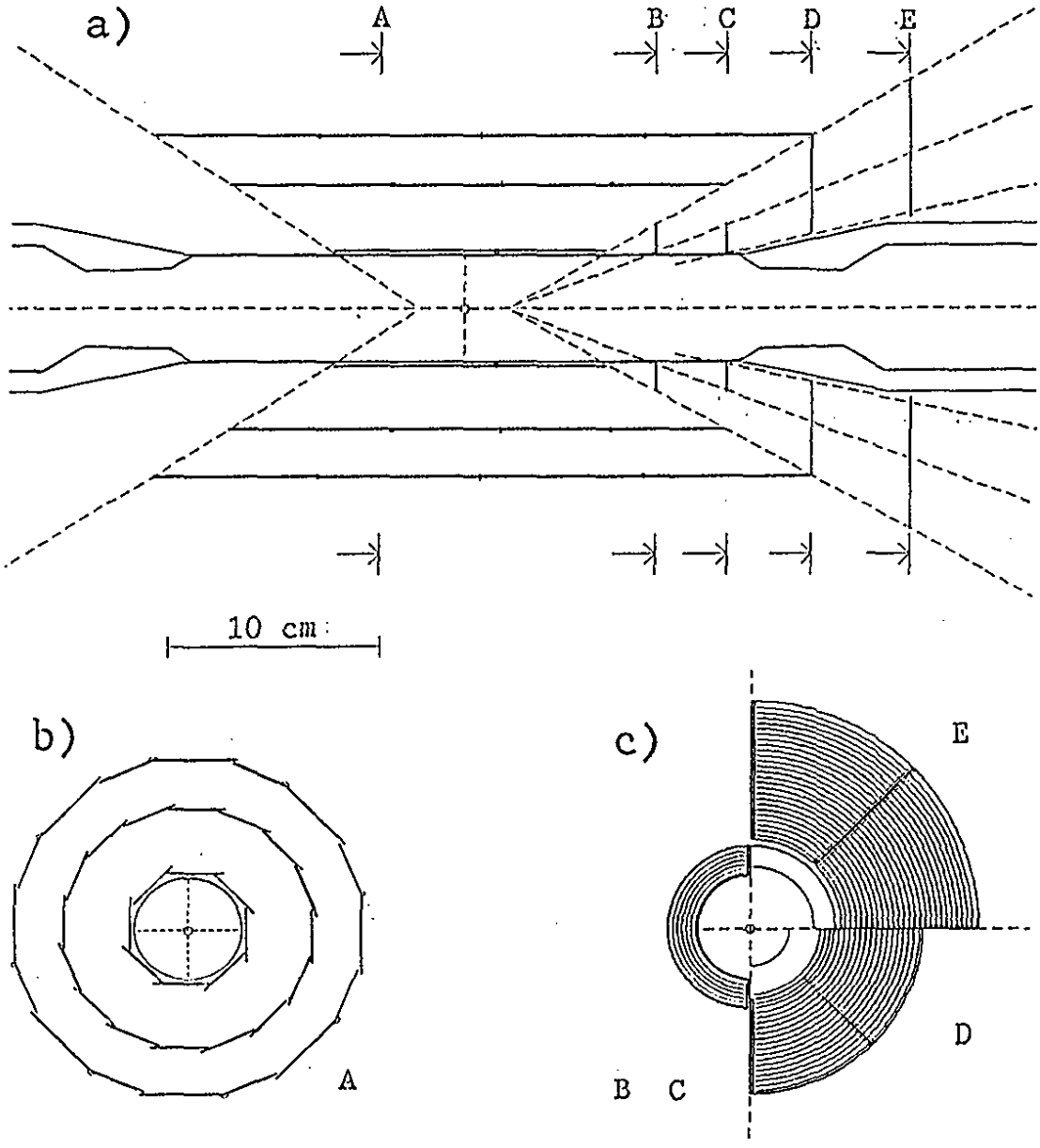

Figure 81: Arrangement of the silicon detector modules
a) in the r-z plane,
b) r-ϕ cross section at A (barrel part),
c) cross sections at B-E (forward modules).

length that equals four times the maximum length of a detector fabricated on a 4" wafer. With R_1 and R_3 fixed, the radius R_2 of the intermediate layer represents a compromise between different requirements. As shown in fig. 82, the impact parameter resolution at the IP improves slowly as $R_2 \rightarrow R_3$, whereas the highest background occupancy is expected on the innermost layer and good track recognition ability of the outer layers implies $R_2 \rightarrow R_1$. The geometrical data resulting from these considerations are given in Table II. With a thickness of 200 μm for the innermost layer and 300 μm for the outer layers, the silicon of the barrel represents $(0.85/\sin\vartheta)\%$ of a radiation length.

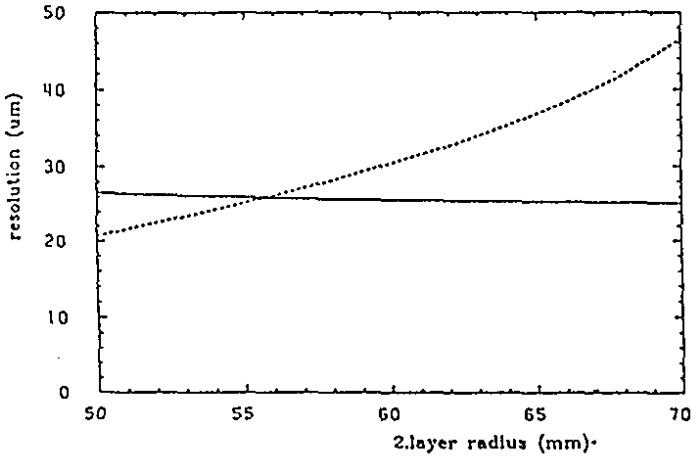

Figure 82: Errors in extrapolating 1 GeV/c pion tracks from the two inner layers to the IP (solid line) and from the two outer layers to R_1 (dashed line), depending on R_2. R_1 and R_3 are fixed to 27 mm and 81 mm, respectively.

Table II: Geometry of the silicon barrel detector. The readout pitch of all detectors is 50 μm and their sizes include a rim of 500 μm.

Layer no.	1	2	3
Number of modules	8	16	16
Number of detectors	16	64	64
r-ϕ readout channels	4096	16384	20480
r-z readout channels	4096	16384	8192
Inner radius [mm]	27.0	58.0	81.0
Detector width [mm]	26.6	26.6	26.6/39.4
Detector length [mm]	52.2/77.8	52.2/77.8	77.8
Module length [mm]	130.0	234.4	311.2
Detector thickness [μm]	200	300	300

Number and width of modules

Once the layer radii are fixed, the number and widths of the modules are the next issues. Approaching a cylindrical shape with many modules minimizes the average radius and incident track angle, but increases the amount of dead material, since state-of-the-art detectors require a $\geq 500\mu$m wide rim. However, computing the overall resolution for different polygons shows no pronounced optimum and the choice is rather a matter of mechanical feasibility. A possible solution is shown in Fig. 81b. An overlap between adjacent modules is desired for full solid angle coverage and for software alignment using tracks passing through more than one module. In the outer layer, modules of different widths are used and are daisy-chained pairwise to reduce the number of readout channels.

Mechanical construction

Individual detectors are glued together to form a module with additional pieces of ceramic or carbon fibre being included for rigidity. Modules of the first layer are built from two detectors, the outer two layers require four detectors, all fabricated from 4" wafers. The innermost modules are read out from the backward end only, whereas the modules of the two outer layers are read out from both sides to split their capacitance.

On the forward end, the ceramic hybrid boards carrying the readout electronics are tilted by 30° to minimize the obstructed solid angle. The 35 W produced by these chips can be carried away by forced air. The chips at the backward end of the barrel are out of the drift chamber's acceptance region where a solid support structure and contact cooling is possible.

Impact parameter resolution

The expected impact parameter resolution for charged pions with respect to momentum, polar, and azimuthal angle is shown in Fig. 83 and 84.

3.4.5 Forward Detector

The impact parameter resolution of the barrel detector is strongly degraded at forward angles, as shown in Fig. 84. If the resolution in z is the quantity of interest, the effect is even worse by a factor of $1/\sin\vartheta$. A suitably tailored forward detector can improve the resolution, but only within the limit set by the beam pipe (Eq. 69). Another benefit of a forward detector is that it allows to reduce the length of the barrel modules.

Geometry of the forward detector

Placing silicon detectors perpendicular to the particle tracks minimizes the effective detector thickness and optimizes the intrinsic resolution, but the average lever arm increases. The optimum could be obtained when keeping close to the beam pipe with a saw tooth like arrangement of many small detectors. Considering dead material and mechanical feasibility, the number of such detectors should however remain small. Arranging the detectors perpendicular to the beam pipe simplifies the construction without much loss in resolution. Four detector planes are forseen (Fig. 81a,c, and 85) and are arranged such that each track traverses at least three planes. Their geometrical data are given in Table III.

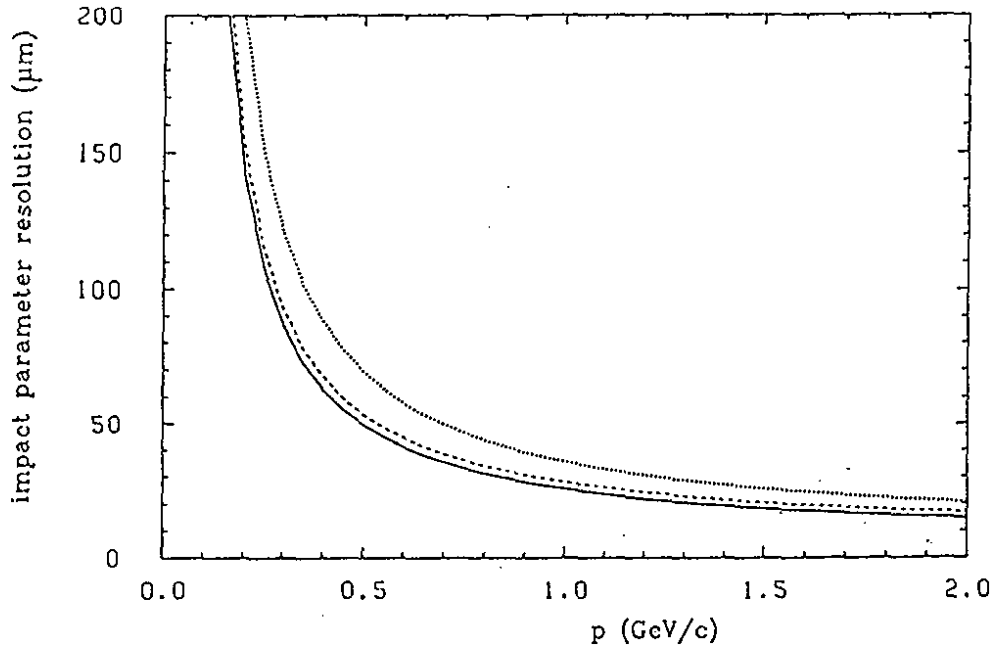

Figure 83: Momentum dependence of the impact parameter resolution for charged pions at $\vartheta = 90°$ and different azimuthal angles.
Solid line: $\phi = 0°$ (defined as perpendicular incidence).
Dashed line: $\phi = 22°$.
Dotted line: $\phi = 27°$ (overlap of two modules).

Table III: Geometry of the forward detector.
The readout pitch of the circular strips is 50 μm
and varies for the radial strips. A rim of 500 μm is included.

Plane no.	1	2	3	4
Number of detectors	2	2	8	8
r-ϕ readout channels	512	512	3584	5120
r-z readout channels	512	512	3584	5120
z[mm]	91.0	124.7	165.0	212.0
Inner radius [mm]	26.0	26.0	35.2	43.0
Outer radius [mm]	39.8	39.8	81.0	108.0
Detector thickness [μm]	200	200	300	300

The first two forward planes (seen from the IP) are built using the semi-circular type of detector shown in Fig. 80 which fits on a 4" wafer and is assumed to be 200 μm thick. The position of the second plane is given by the minimum polar angle $\vartheta = 12°$. The detectors of the first plane cover the adjacent polar angle region.

The forward detector includes two more planes built from 45° segments as shown in Fig. 81c. The position in z of the outer plane is chosen such that one octant still fits on a 4" wafer. With 300 μm for these planes, the total thickness of silicon is $(0.85/\cos\vartheta)\%$ of a radiation length for $\vartheta = 12° - 26°$.

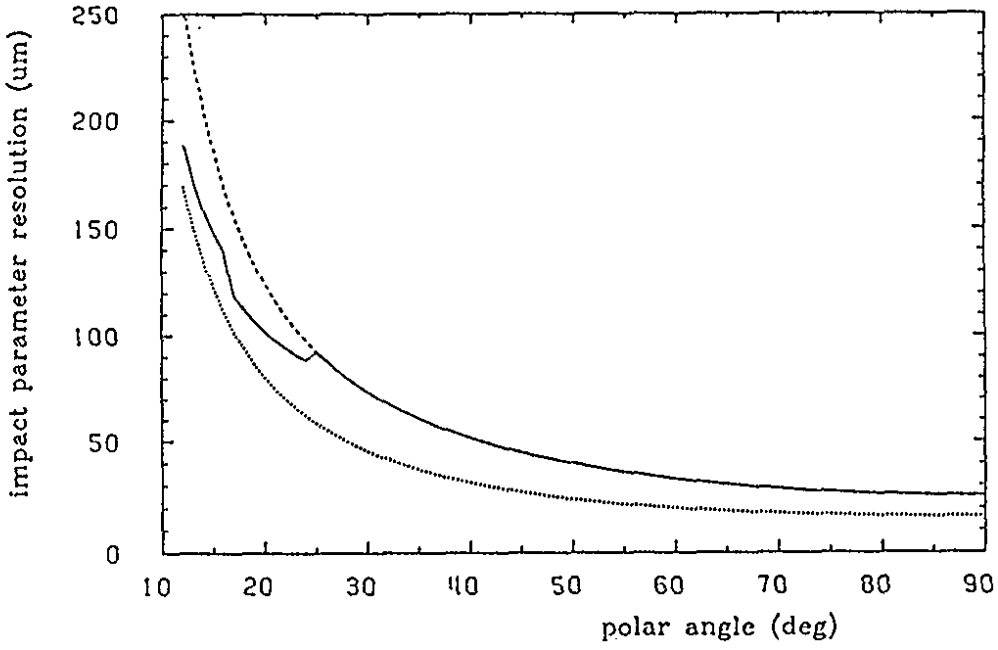

Figure 84: Impact parameter resolution for 1 GeV/c pions as function of the polar angle ϑ.
Solid line: Barrel and forward detector.
Dashed line: Barrel detector only.
Dotted line: Resolution limit given by the beam pipe (Eq. 69).
The average resolution for pions distributed isotropically in the e^+e^- rest frame is 40 μm for $\vartheta = 26° - 150°$ and 116 μm (144 μm) for $\vartheta = 12° - 26°$ with a forward (barrel type) detector.

The detectors forming the forward planes do not overlap and the sacrificed rim area of $< 2\%$ is occupied by the readout electronics. Evaporative cooling may be used here with tiny pipes running radially outwards. Each detector is read out from one end by VLSI chips on a ceramic hybrid board perpendicular to the detector plane (Fig. 85) which requires a non-trivial wire bonding technique or other bonding methods. The chips may also be bonded conventionally and placed directly on the detector at the cost of additional multiple scattering in parts of the solid angle. One more alternative is a Kapton cable connection between detector and readout chips [33].

3.4.6 Mechanical Construction

Support structure

The silicon barrel and forward detector are rigidly connected and form a self-supporting structure. It is built in two half cylinders that are closed around the beam pipe. The total weight of the silicon detectors is about 230 g, chips and hybrids add another 100 g.

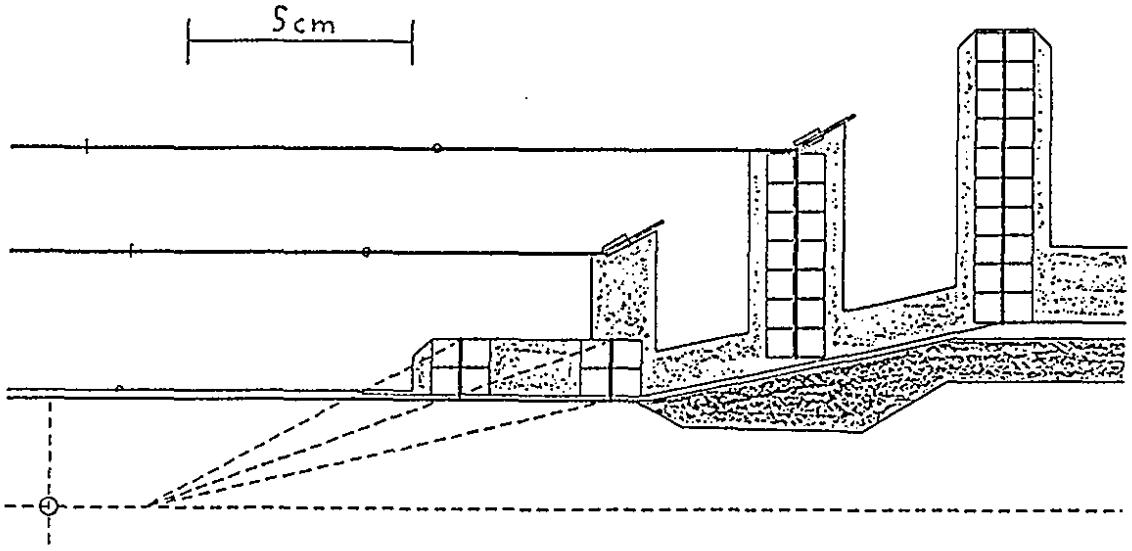

Figure 85: Side view of the forward silicon detector and part of the barrel, including VLSI electronics on ceramic hybrid boards.

The whole vertex detector requires support at both ends. The drift chamber acceptance of $\vartheta = 12° - 150°$ permits a connection between vertex detector and drift chamber at the backward end. A forward connection would have to be beyond $z = 13\ \text{cm}/\tan 12° = 61$ cm. Instead, we propose a forward support ring that slides on the beam pipe which may undergo longitudinal thermal expansion, but should be inhibited in transverse motion.

The forward ends of the barrel detector modules could be supported by thin semi-circular arcs made of carbon fibre, their backward ends would be mounted on a structure that provides the connection to the drift chamber.

The positions of the forward detectors can be defined by vanes perpendicular to the detector planes. These vanes would furthermore provide the connection between forward and barrel detector and would connect the whole detector to the forward support ring.

Alignment

Extensive survey of the detector with a coordinate measuring machine is necessary before and after a period of operation. In addition, some means of on-line position monitoring, either by capacitive probes or using laser light spots, should be employed. The final alignment information, however, comes from the off-line track analysis.

3.5 Costs

The vertex detector presented here requires six different mask designs for double-sided strip detectors and 164 individual detectors from 134 wafers of 4" diameter. A tentative cost estimate is 0.6 MDM to design and manufacture the masks and 1.2 MDM for the detectors plus spares.

Consider 0.5 MDM to design a readout chip that meets the discussed requirements, 0.3 MDM to fabricate $\sim$ 1000 chips, 0.3 MDM for the ceramic hybrid boards and Kapton bus lines, 0.8 MDM for R&D in readout electronics and the production of 10^2 units.

Building the vertex detector requires clean room equipment, microscopes, a bonding machine, a probe station, a coordinate measuring machine, computers, oscilloscopes and other lab equipment. Starting from an already existing laboratory, 1.0 MDM may be sufficient.

With another 0.5 MDM for mechanics and other small items, the estimated costs total at 5.2 MDM, excluding manpower (see also Table IV).

Table IV: Cost Estimate of a Silicon Vertex Detector

Item	Cost MDM
Masks	0.6
Detector Elements	1.2
Readout Chip Design	0.5
" " Fabrication	0.3
Ceramic Hybrid Boards + Bus Lines	0.3
Electronics. Design + Production	0.8
Laboratory Equipment	1.0
Mechanical Parts	0.5
Total	5.2

3.6 Summary

The physics goals of an asymmetric B-factory require a precise position measurement of secondary decay vertices.

The design of a vertex detector presented in this document is based on double-sided silicon strip detectors, although alternative devices (silicon pixel detectors, gas microstrip detectors) are not ruled out.

The strip detectors, fabricated on 4" wafers, would be 200 μm and 300 μm thick with a strip pitch of 25 μm. On one side, the strips would be overlaid by perpendicular readout lines to allow for readout from one edge.

VLSI-chips, that combine small size, high speed, low noise and low power consumption are required to amplify the signal from the strip diodes and to store several events in an analog pipeline. The required specifications can be met by technology available today.

The geometrical layout of the vertex detector aims at an optimized spatial resolution, full solid angle coverage and good track recognition ability, and includes two parts which are rigidly connected to each other and to the outer tracking device, i.e. the drift chamber:

- a barrel part with three concentrical, cylindrical layers of silicon
- a forward part with four planes perpendicular to the beam axis.

4 The Central Track Chamber

The Central Track Chamber (*CTC*) is the principal device for reconstructing tracks of charged particles. Its tasks are the following ones:

Track recognition

- Determine the number of charged tracks. The achievable reconstruction efficiency for charged particles mainly depends on the Central Track Chamber. Other detector components contribute only marginally to track recognition.

Momentum resolution

- Determine the charged tracks' momentum and direction. The momentum resolution, even though improved by Silicon Vertex Detector (*SVD*) information, depends essentially on the Central Track Chamber design.

Vertex detection

- Find vertices located outside the dedicated vertex detector *SVD*, *e.g.* strange particle decay vertices and photon conversion points.

Basis for the other components:

- Provide the necessary input for reconstructing charged tracks in all other detector components.

SVD,

With the Silicon Vertex Detector, there exists an interplay in the sense that, on one hand, the information of the *SVD* is of limited use without knowing the tracks' trajectories and that, on the other hand, the *SVD* may contribute itself to the momentum resolution and even to the track recognition.

RICH, TOF, ECAL, MUCH.

The analysis of the outer detector components *RICH*, *TOF*, *ECAL*, and *MUCH* unconditionally needs the charged tracks' information.

Neutral particle detection

A necessary condition for detecting neutral particles in the *ECAL* is to identify and to discard those calorimeter signals which are induced by charged particles.

dE/dx

- Identify particles by measuring their specific energy loss dE/dx in the chamber gas. This complements the dedicated particle identification system *RICH/ TOF* as well as the electron identification in the calorimeter and the muon identification in the muon chambers.

Charged particle trigger

- Allow for a fast trigger decision. Charged track information is an essential input for an efficient and selective trigger.

We propose to build a drift chamber with small drift cells. All cells are slanted with respect to the beam axis by a varying stereo angle. The shape of the chamber, formed by cylinders and truncated cones, is novel.

4.1 Design Criteria

In this section, the criteria are discussed which have been taken into consideration in the proposed design. It will become evident that different criteria frequently lead to contradictory demands on the detector. The necessary compromises and the adopted solutions will be discussed in subsequent sections. Headings of sections referred to are indicated by **bold face** characters.

Optimized for "low" energy physics

The chamber is designed for physics in the $\Upsilon(4S)$ region. At these energies, the event topology is isotropic ($\Upsilon(4S) \rightarrow B\overline{B}$ events) or only moderately jet–like ($q\overline{q}$ events). The average charged multiplicity is about 11 on the $\Upsilon(4S)$ resonance. Thus, in contrast to detectors for physics at higher energies, disentangling complicated jet structures does not impose a major problem on the chamber design (see section **Cell Structure**). Instead, the aspect of optimizing the reconstruction of low momentum tracks has been placed into the foreground.

4.1.1 Geometrical Acceptance

Novel shape of the CTC

To achieve an optimum geometrical acceptance for a detector at an asymmetric e^+e^- storage ring requires finding new solutions for the chamber's geometrical design. The Central Track Chamber's novel shape and its geometrical acceptance are described in the section **Chamber Geometry**.

4.1.2 Track Parameter Resolution

Resolutions: σ_p; σ_{p_T}, σ_ϑ,

The following discussion of accuracies will mainly refer to the momentum resolution σ_p which, in turn, depends on the transverse momentum resolution σ_{p_T} and on the polar angle resolution σ_ϑ:

$$\sigma_p^2 = (\sigma_{p_T}^2 + p_z^2\sigma_\vartheta^2)/\sin^2\vartheta.$$

σ_φ,

The azimuthal resolution σ_φ is not treated here as it is hardly ever a limiting factor in B physics analyses. The spatial resolutions of the tracks' origin, σ_d and σ_z, was addresssed earlier in context with the vertex chamber.

σ_d, σ_z

4.1.3 Spatial Resolution

Choice of CTC: Drift chamber

A drift chamber has been chosen to be used as Central Track Chamber as it provides an optimum spatial resolution over a large volume in connection with a relatively low density. The achievable spatial resolution in the drift cells σ_D depends on the **Cell Structure** and on the chamber gas (see section **Gas and Wire Materials**).

σ_D

Furthermore, all angular and momentum accuracies depend on the number of measurements N_{meas} along the track trajectory (see **Stereo Layers**).

N_{meas}

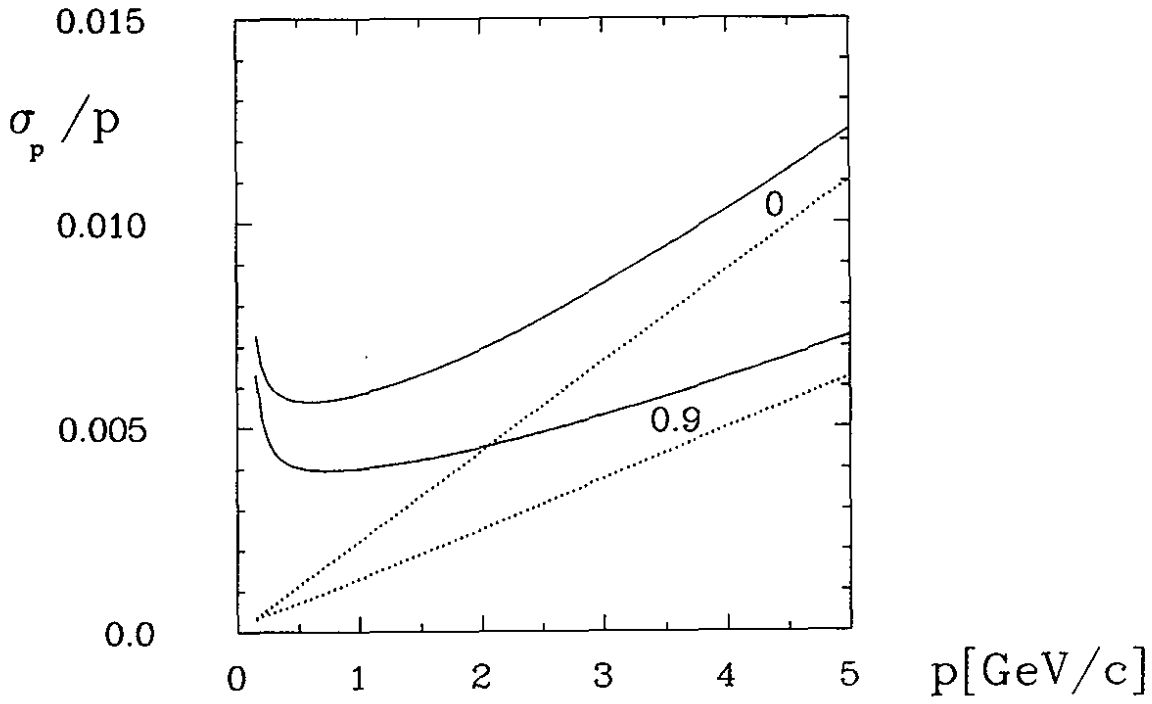

Figure 86: *Pion momentum resolution σ_p/p vs. p for the proposed design (full lines). In addition, the resolution of a hypothetical detector without multiple scattering is shown (dotted lines). Both resolutions are given for polar angles $\cos\vartheta = 0$ and $\cos\vartheta = 0.9$ as indicated in the figure.*

4.1.4 Momentum Resolution

Multiple scattering

Multiple scattering effects in the chamber's active volume * are non-negligeable even at the highest interesting momenta. This is demonstrated in figure 86 which shows the finally obtained resolution together with the resolution of a hypothetical detector with the same characteristics but without any multiple scattering. In the following discussion on σ_{p_T} and σ_ϑ, multiple scattering will first be ignored and taken into account later.

σ_{p_T} resolution

The transverse momentum resolution σ_{p_T} depends on the **Magnetic Field** B and on the **Chamber Size** given in terms of the radii of the innermost and outermost drift layers R_{inner} and R_{outer}:

$$\sigma_{p_T} \propto \sigma_D \cdot N_{meas}^{-1/2} \cdot B^{-1} \cdot (R_{outer} - R_{inner})^{-2}.$$

Consequently, an increase of the chamber size by 10% results in the same resolution improvement as an increase of the magnetic field by 20%.

For high momentum tracks where multiple scattering in the inner *CTC* wall is small and thus the Silicon Vertex Detector contributes to the momentum determination, R_{inner} in the above formula should be replaced by the *SVD* outer radius R_{SVD}.

*To a good approximation, multiple scattering in the chamber's inner wall does not deteriorate the momentum resolution of the *CTC* and is consequently ignored here. It determines, however, to which extent the vertex chamber *SVD* contributes to the momentum measurement (see below: Interplay with the vertex chamber).

3D reconstruction: Stereo wires

In a drift chamber, the best polar angle resolution σ_ϑ is obtained by using stereo wires for the three–dimensional track reconstruction. This solution has been chosen. The complications concerning the trigger and the track recognition procedure are well understood from existing detectors; see, *e.g.*, [35] for the reconstruction programme and [36] for the trigger. The polar angle resolution σ_ϑ depends on the track length s inside the active chamber volume and hence on the **Chamber Size**. Furthermore, σ_ϑ is a function of the stereo angle α and of the number of stereo wires along the track trajectory N_{stereo} as paraxial wires do not contribute to the ϑ measurement (see section **Stereo Layers**):

σ_ϑ resolution

$$\sigma_\vartheta \propto \sigma_D \cdot N_{stereo}^{-1/2} \cdot \sin^{-1}\alpha \cdot (R_{outer} - R_{inner})^{-1}.$$

4.1.5 Multiple Scattering

Taking multiple scattering effects into account, the above statements on resolutions remain true with the restriction that, with increasing distance covered along the track trajectory, measurements are more and more spoilt by multiple scattering and contribute less to the track parameter accuracy.

Dependence on: σ_D, B, α,

Thus, even when considering multiple scattering, σ_{p_T} and σ_ϑ depend on the spatial resolution σ_D, on the magnetic field B, and on the stereo angle α in the same way as described above: $\sigma_{p_T} \propto \sigma_D \cdot B^{-1}$ and $\sigma_\vartheta \propto \sigma_D \cdot \sin^{-1}\alpha$.

$\langle N_{meas}\rangle$, $\langle N_{stereo}\rangle$,

Furthermore, the σ_{p_T} and σ_ϑ dependence on N_{meas} and N_{stereo} is similar with and without multiple scattering: $\sigma_{p_T} \propto \langle N_{meas}\rangle^{-1/2}$ and $\sigma_\vartheta \propto \langle N_{stereo}\rangle^{-1/2}$ if these numbers are interpreted as density of measurements at the beginning of the track and not as total number of measurements.

$R_{outer} - R_{inner}$

The dependence of the momentum resolution on the **Chamber Size** $R_{outer} - R_{inner}$ is weaker than described in the above formulae due to multiple scattering effects. Nevertheless, a large chamber size is the most efficient way to improve the momentum resolution for high momentum particles. This is demonstrated in figure 87. For high momenta ($p > 1$ GeV/c), the relations $\sigma_{p_T} \propto (R_{outer} - R_{inner})^{-2}$ and $\sigma_\vartheta \propto (R_{outer} - R_{inner})^{-1}$ are still a good approximation.

Appropriate materials

The most efficient way to keep multiple scattering effects small is to choose appropriate **Gas and Wire Materials** with low Z, and to minimize the number and thickness of wires (see **Cell Structure**).

The optimum choice for the wires and for the gas is still under discussion. Test measurements have been done [37,38] and will be continued in future in order to investigate, for example, the usablity of gas mixtures containing helium and DME.

Present choice of gas and wire materials

In the present paper, we assume propane to be used as the chamber gas and copper–beryllium for the cathode wires. These materials fulfil all requirements on drift chamber materials except that conceivably they do not represent the optimum choice with respect to multiple scattering. They have been used since

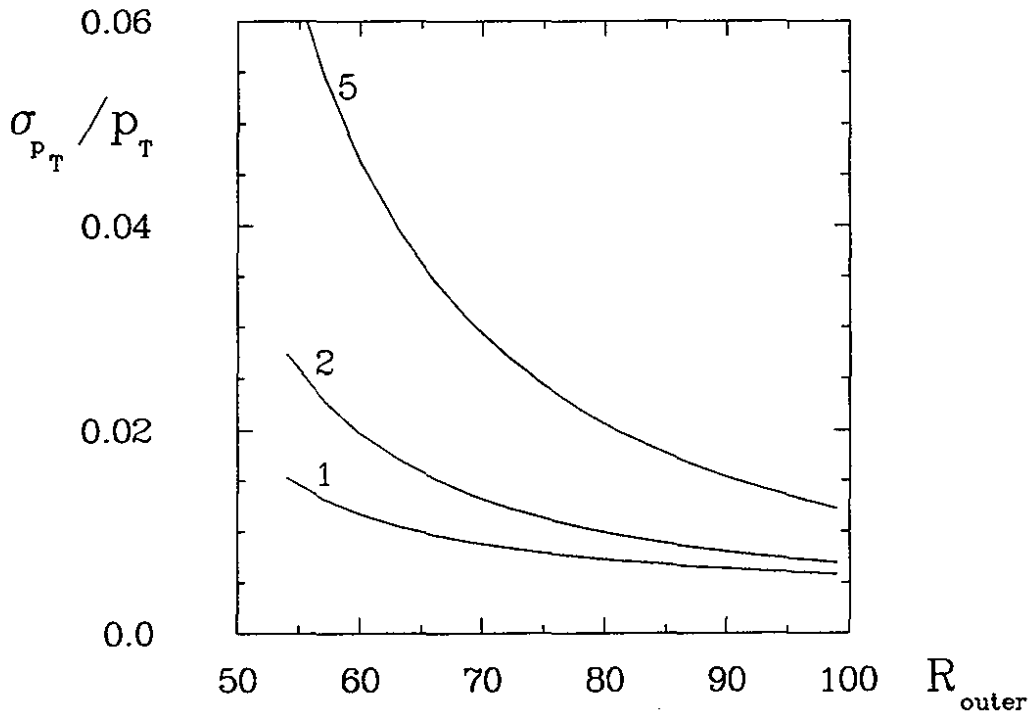

Figure 87: *Transverse momentum resolution σ_{p_T}/p_T for pions vs. outer chamber radius R_{outer} for various momenta indicated in units of GeV/c. Multiple scattering effects are taken into account assuming a polar angle $\vartheta = 90°$.*

many years in the experiment ARGUS [35], thus allowing for accurate predictions on the performance of the new chamber.

As soon as other materials will be found which provide less multiple scattering and, at the same time, match all other requirements, they can and will be chosen without any major impact on the overall chamber design. The requirements imposed on those new materials are discussed in the sections **Gas and Wire Materials**.

4.1.6 Detection Efficiency for Low Momentum Tracks

We strongly emphasize that for low momentum particles the aspect of the track parameter resolutions is of secondary importance compared to the aspect of detection efficiencies. The efficiency at low momenta definitely influences the physics analysis potential of a B-factory detector. It imposes intricate problems on the chamber design and on the analysis software.

Inefficiencies due to lack of hits

For performing a track fit, at least six coordinate measurements are necessary. Pattern recognition requires that the track passes through seven layers [†]. A larger number of layers definitely does improve the efficiency. Thus, a track

[†]Here, optimistically we suppose that different stereo views contribute about equally to the measurements at the begin of the track. This is a specific feature of the proposed chamber (see section **Stereo Layers**). A smaller number may be sufficient if the vertex chamber contributes to the track recognition, too.

must reach at least the radius of the seventh layer:

$$R_7 = R_{inner} + 6 \cdot \Delta R_{layer}$$

with ΔR_{layer} being the radial distance between adjacent layers. The maximum distance from the beam line to the outermost point on a track originating at the interaction point is given by twice the bending radius ρ:

$$\rho[cm] = 333 \cdot p_T\,[\mathrm{GeV}/c]\,/B[T].$$

Using these formulae one can calculate the transverse momentum p_{Tmin} below which the track recognition efficiency completely vanishes:

$$p_{Tmin}[\mathrm{GeV}/c] = 0.0015 \cdot B[T] \cdot (R_{inner} + 6 \cdot \Delta R_{layer})[cm].$$

Thus, the demand for high efficiencies at low particle momenta requires a low **Magnetic Field**, a small inner chamber radius (see **Chamber Size**) and a small radial distance between layers (see **Stereo Layers**). In the design presented here, a value $p_{Tmin} = 30\ MeV/c$ has been achieved which provides full detection efficiency for transverse momenta $p_T > 50\ MeV/c$.

Low vs. high magnetic field

Obviously, the above request for a low magnetic field is in contradiction to the momentum resolution requirements discussed before, and a compromise has to be made. Other arguments favouring a moderate **Magnetic Field** (*q.v.*) concern cell efficiencies and track recognition efficiencies. Another problem with achieving high efficiencies at low momenta is that soft particles, instead of leaving the chamber through one of the outer walls, perform one and more full turns inside the active volume. Only the first turn really contributes to the track measurement whereas the rest is a matter of background (see below: "curling tracks"). Such curling tracks pass through drift cells not only in radial but also in azimuthal direction. Actually, the point on the track where the azimuthal direction dominates provides the most reliable starting point for the track recognition procedure.

Isotropy: Precondition for good efficiency

Choice of a drift chamber with small cells

Consequently, for an efficient track recognition, the single drift cells must be equally efficient for tracks passing through in any direction. This need for isotropy has lead to the decision that the drift chamber consist of small square and rectangular cells ("small cell" solution; see section **Cell Structure**).

4.1.7 Efficiency for Tracks not Pointing to the Interaction Region

There is another argument which also leads to the isotropy requirement: Tracks which do not point to the beam axis and thus can penetrate the drift cells in any direction should be reconstructed with the same efficiency as tracks originating at the interaction point.

Strange particle decays

This concerns, above all, decay particles coming from secondary vertices far

from the interaction point, in particular products of strange particle decays. In addition, background particles of any kind belong to this category. There is, in fact, necessity to reconstruct background for the following two reasons:

Necessity to reconstruct background: Fake photons,

First, background particles which reach the calorimeter, *e.g.* scatters in the interaction region material and backscatters from the calorimeter itself, fake a photon if the charged track is not reconstructed and the corresponding *ECAL* signal is not associated to a track.

Curling tracks

Second, low momentum tracks may perform several turns in the chamber ("curling tracks") and obscure large areas therein. A good efficiency for relevant tracks hidden in those areas can only be granted if the background tracks are reconstructed, too.

Even though the chamber's isotropy allows for reconstructing most of the curling tracks, their abundance should be kept small. In particular, low momentum tracks with a polar angle close to 90° can perform many loops in the chamber. Helpful would be a low **Magnetic Field** and absorbing material close to the beam line, *i.e.* a small **Chamber Size**.

At an asymmetric storage ring, however, one may as well decide to live with these curling tracks. The probability that low momentum particles have a polar angle of 90° is by far smaller than at a symmetric machine due to the Lorentz transformation which boosts particles into forward direction (for details see section **Chamber Geometry** and figure 90).

4.1.8 Interplay with the Vertex Chamber

σ_z^{SVD}, σ_d^{SVD}

A reliable extrapolation of the track trajectories from the Central Track Chamber to the Silicon Vertex Detector must be guaranteed in order to allow for the unambiguous assignment of *SVD* signals to tracks found in the *CTC*. The relevant quantities are the track's spatial resolutions σ_z^{SVD} along the beam line and σ_d^{SVD} in azimuthal direction, both defined at the point where the track intersects with the outermost *SVD* layer.

There exist three contributions to the resolutions σ_z^{SVD} and σ_d^{SVD}: The spatial resolution of the track's intersect with the inner drift chamber wall σ_z^{CTC} and σ_d^{CTC}, the uncertainty of the angles measured in the drift chamber σ_ϑ and σ_φ, and multiple scattering. The size of the two latter effects depends on the lever arm used in the extrapolation.

The question of an intermediate chamber

As the *SVD* is limited in size, either the *CTC*'s inner radius has to be kept as small as possible in order to minimize the length of the lever arm, or one needs an intermediate chamber between *SVD* and *CTC*. An intermediate chamber would add more material to the detector at a location where it matters. Its benefits would be only to bridge the gap between *SVD* and *CTC* for tracking purposes but hardly to improve the momentum resolution or the reconstruction

efficiency. Consequently, we propose to build a *CTC* with a small inner radius (see section **Chamber Size**).

Small inner radius

The amount of material between the two detector components has to be kept as small as possible in order to minimize multiple scattering effects. This concerns mainly the inner wall of the drift chamber (see section **Chamber Walls**) which, in the design presented here, can be built extremely thin due to the **Chamber Geometry** and the mechanical stability following therefrom. The benefit of such a thin wall is not only the ability to extrapolate reliably between *CTC* and *SVD* but also the fact that the *SVD* contributes already at low momenta to the momentum measurement accuracy.

Drift chamber inner wall

SVD: Impact on momentum resolution

Note that all momentum resolution specifications given in this chapter are based on the *CTC* only. The improvement due to the *SVD* is not taken into account.

4.1.9 Particle Identification

In a detector for an asymmetric B–factory, unique particle identification in the full momentum range is indispensable for properly performing the Lorentz transformation from the detector rest system into the centre–of–mass (*CM*) frame of the e^+e^- system. Momentum spectra, for example, cannot be obtained without unambiguous identification. For the analysis of invariant masses and other Lorentz–invariant quantities, the consequences are less severe. Here, problems with ambiguous mass hypotheses are well understood from present experiments at symmetric storage rings.

Necessity for unique particle identification

The specific ionisation measurement dE/dx complements the dedicated particle identification system *RICH* at low particle momenta. For high momentum particles in the region of the relativistic rise of the ionisation, it provides additional information on identification even though full particle separation needs a coherent analysis of all detector components. Moreover, the existence of two independent identification systems allows to extract identification efficiencies and misidentification rates from data. The size of the relativistic rise is a property of the chosen gas (see **Gas and Wire Materials**).

dE/dx

Relativistic rise

The dE/dx resolution depends again on the gas, on the track length inside the active chamber volume (see **Chamber Size**), and on the number of measurements (see **Cell Structure** and **Stereo Layers**). Note that for a dE/dx analysis, by far more measurements are necessary than for a good track recognition in order to calculate an appropriate mean value of the Landau distribution ("truncated mean"). This has to be kept in mind in particular for a detector at an asymmetric storage ring where the particle density in forward direction is high. Even in extreme forward direction, a sufficient gas length and a sufficient number of measurements have to be provided (see sections **Chamber Geometry** and **Cell Structure**).

dE/dx resolution

It is worth mentioning that for exclusive B meson analyses a good momentum

Kinematical separation

resolution, in particular at the highest reachable particle momenta, contributes to particle identification, too. It allows to kinematically separate different particle hypotheses: The B meson energy E_B in the decay $\Upsilon(4S) \rightarrow B\overline{B}$ is known. The sum of the energies of the B meson decay products $\sum E_i$ must be equal to E_B. A wrong mass hypothesis for one decay particle leads to a wrong $\sum E_i$.

4.2 Chamber Geometry

In this section, the chamber's shape will be described. To a large extent, its size is independent of the shape and will be discussed in the next section.

Novel chamber geometry with truncated cones

The chamber geometry which makes optimum use of the available space is shown in figures 88 and 89. It consists of a short inner cylinder A and an outer cylinder D which are closed by truncated cones (B, C, E, and F). Details of the **Mechanical Construction** are described in the corresponding section.

Excellent mechanical stability

The major advantage of this novel structure is its extraordinary mechanical stability. As a consequence, all chamber walls can be built by far thinner than those of an ordinary cylinder chamber. In particular, the inner wall A is not subjected to any mechanical force and is laid out for providing the minimum achievable multiple scattering (see section **Chamber Walls**).

Optimum space occupancy around the beam pipe

The cones B and F in backward and forward directions (see figure 88) fit smoothly around the beam optics elements whose diameters increase with increasing distance from the interaction point. Compared to a cylinder chamber, the conical structure leaves more space for beam focusing elements while keeping the chamber's inner diameter smaller in the region close to the interaction point.

97.8% solid angle coverage in forward direction

The geometrical acceptance in the laboratory system is limited by the opening angles of the cones F and B, $\theta_F = 12°$ and $\theta_B = 30°$, respectively. These numbers refer to the active chamber volume. In forward direction, this leads to a remarkable solid angle coverage of $\eta_F = \cos\theta_F = 97.8\%$. This has been achieved by the interaction region layout and by the fact that the drift chamber electronics and the access to the vertex detector and to the beam pipe are located in backward direction only. Consequently, the backward solid angle coverage is smaller: $\eta_B = 86.6\%$.

This asymmetric shape fits nicely to the Lorentz boost of the detector system with respect to the *CM* frame of the e^+e^- system. Relevant for physics analyses are acceptances in the *CM* system, *viz.* $\eta^*_{F/B} = \cos\theta^*_{F/B}$ where asterisks denote quantities given in the *CM* frame.

Approximately symmetric chamber in the CM frame

For particles with velocities $\beta^* \approx 1$ and for the proposed Lorentz boost with $\beta\gamma = 0.6$, the angles $\theta_{F/B}$ given above transform into *CM* acceptances $\eta^*_F = 93.4\%$ and $\eta^*_B = 95.6\%$. Thus, in the *CM* frame, the asymmetric detector shape

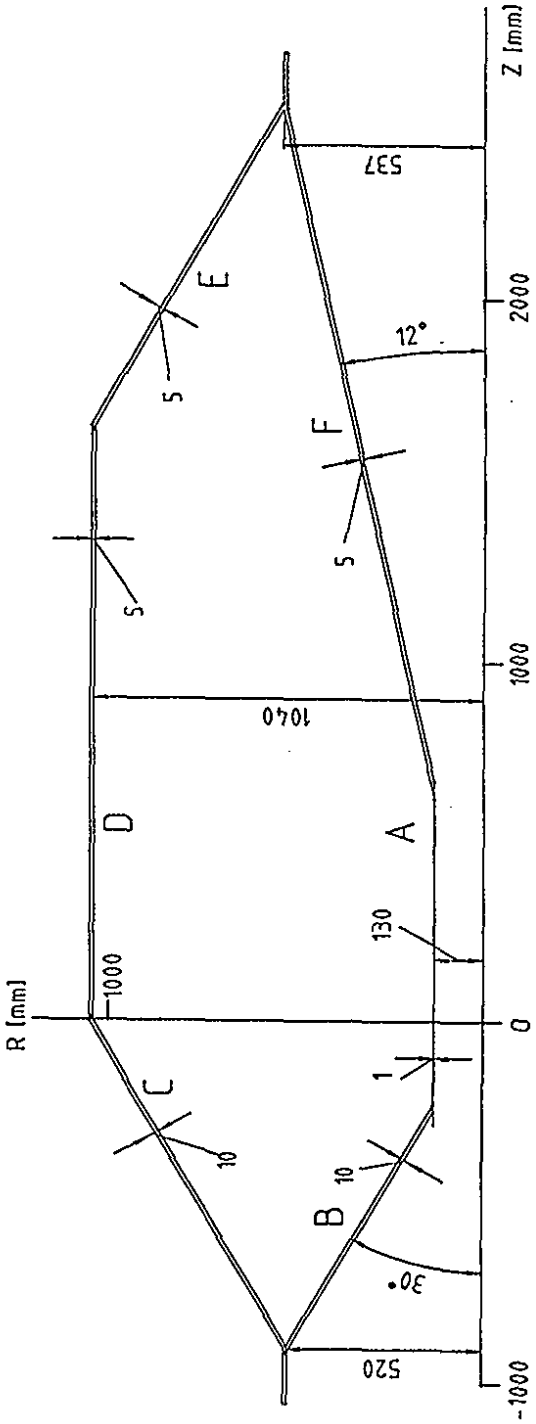

Figure 88: *The Central Drift Chamber in the R – z projection*

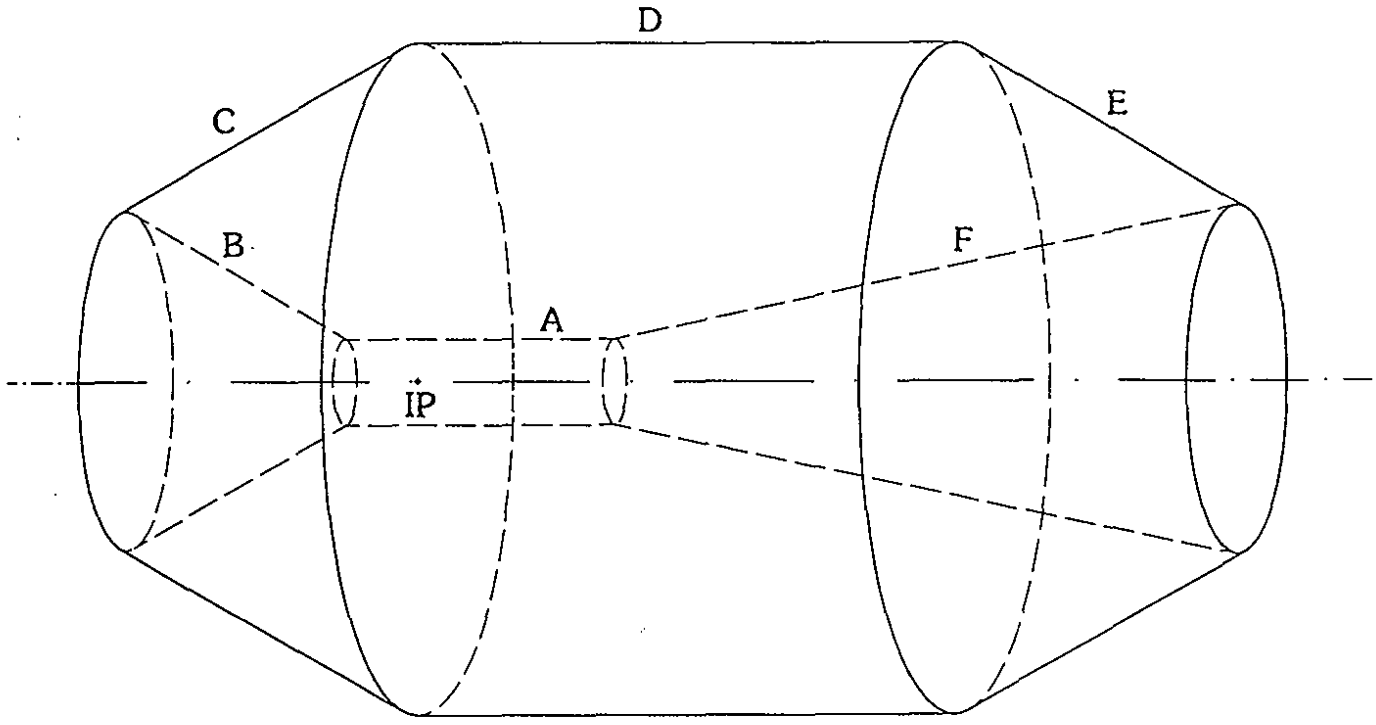

Figure 89: *Perspectivic view of the Central Drift Chamber*

provides approximately equal geometrical acceptance in forward and backward direction. The total geometrical acceptance η^* is 94.5%.

$\eta^* = 94.5\%$.

Necessity for an asymmetric detector

Since η_B^* is even slightly larger than η_F^*, one could argue that the detector is still too symmetric. Such a discussion fails due to lack of technical feasability. The acceptances in backward and, above all, in forward direction are squeezed to the utmost. It demonstrates, however, that a detector for an asymmetric B–factory necessarily must be asymmetric in order to achieve a reasonable geometrical acceptance.

Acceptance for low momentum particles

At small velocities β^*, the effect of the Lorentz boost is most pronounced. For π mesons of various momenta, figure 90 shows the transformation of the polar angle ϑ^* in the *CM* system into the corresponding angle ϑ in the detector system. Particles with a momentum below $p^* = 80\ MeV/c$ are always boosted into the forward direction.

Resulting geometrical acceptance

The geometrical acceptance achieved in the proposed design is shown in figure 91 (solid lines). It demonstrates again the excellent performance for high momentum particles. At low momenta, the chamber geometry is actually not the factor which limits the total track acceptance (*c.f.* the discussion on the inner drift chamber radius in section **Chamber Size**). This statement, as a matter of fact, depends crucially on the forward solid angle coverage $\eta_F = 97.8\%$.

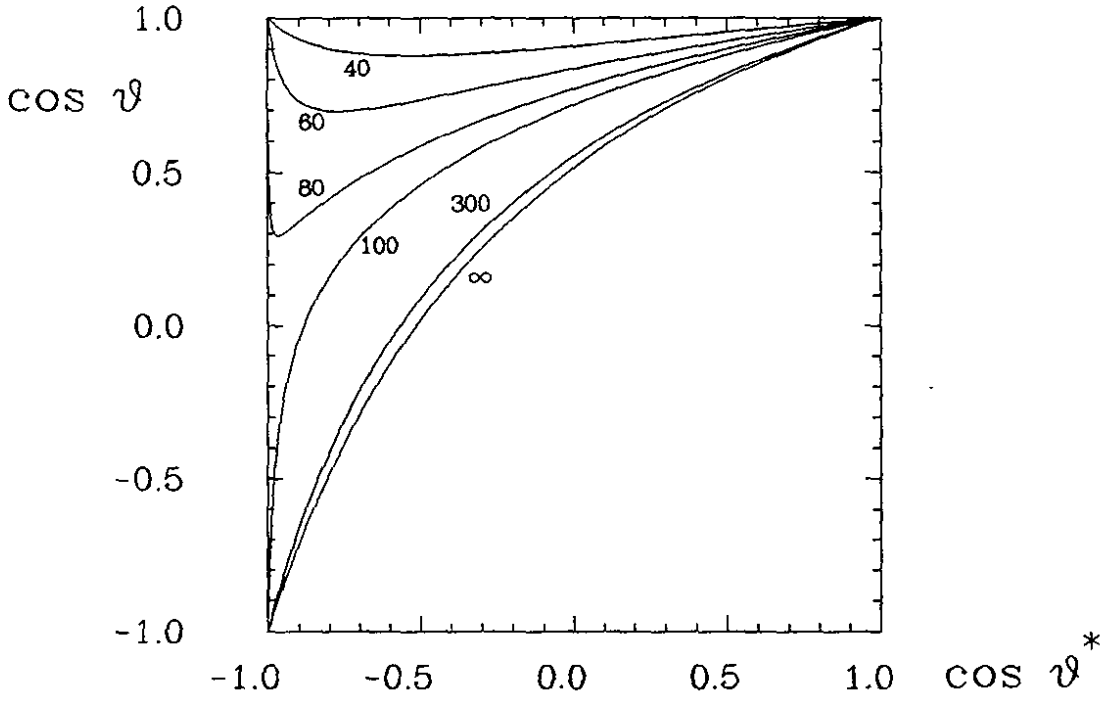

Figure 90: *Polar angle* $\cos\vartheta$ *vs.* $\cos\vartheta^*$ *for pions with various momenta indicated in units of MeV/c.*

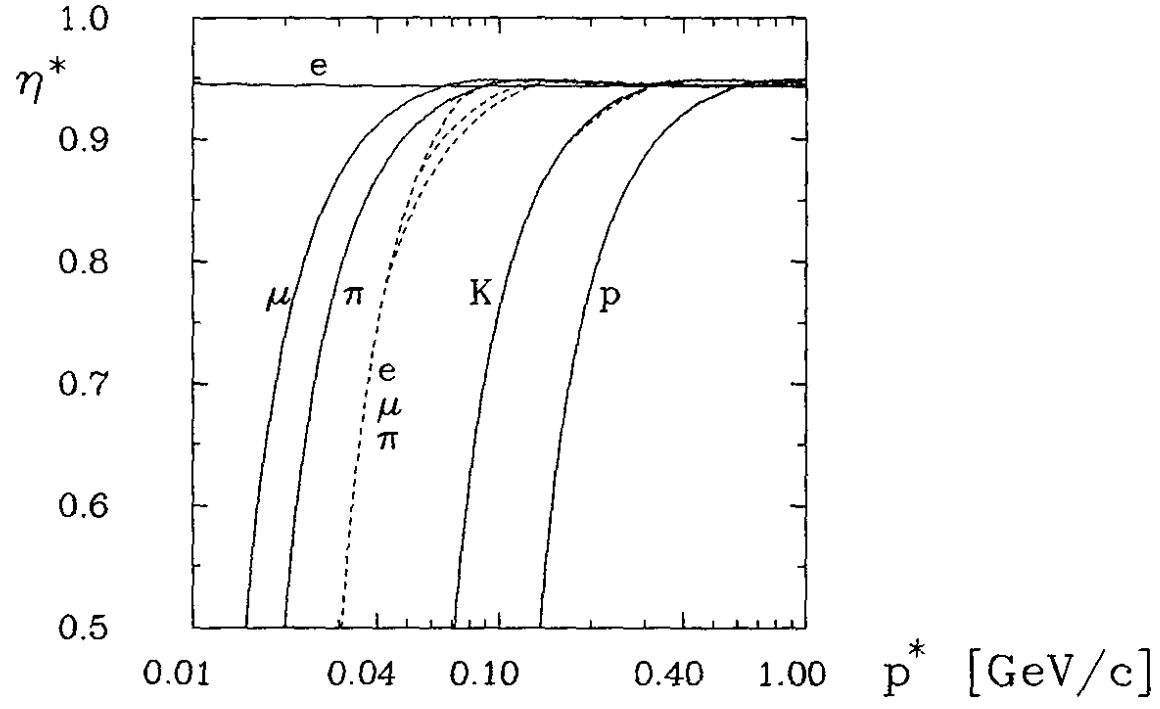

Figure 91: *Geometrical acceptance vs. CM momentum (solid lines). Dashed lines: Acceptance with the additional requirement that particles pass through at least seven layers.*

Momentum resolution σ_{p^*}

The momentum resolution σ_p/p σ_{p^*}/p^* in the CM system is approximately independent of the polar angle ϑ^* as shown in section **Drift Chamber Resolutions.**

Immediate onset of the geometrical acceptance

There are two more advantages of the novel drift chamber shape. First, it grants an immediate onset of the acceptance if the track's polar angle ϑ is close to the acceptance limits denoted by θ_F and θ_B. There is no region where the efficiencies slowly vary with ϑ and where the acceptance determination strongly depends on details of Monte Carlo simulations as it does in cylinder chambers.

dE / dx useful even in extreme forward direction

There is either zero or full geometrical detection efficiency. The validity of this statement is slightly affected by the p_T dependence of the acceptance described in the following section. More concisely: All particles with $p_T \geq 75\ MeV/c$ will traverse at least 30 layers of the chamber provided they pass through the chamber at all. Beyond the acceptance argument given above, the true benefit of this fact is that dE / dx analysis can be performed even in the extreme forward direction (see section **Cell Structure**).

Only useful space

Lastly, the chamber shape fulfills the condition that the whole chamber volume is usable for particles coming from the interaction point. There are no corners which can only be reached by background or, less likely, by decay particles. This is in contrast to cylinder chambers where such corners exist close to the beam line where they are most dangerous. In the design presented here, the wire occupancy is minimized. Only particles originating in a volume around the interaction point pass through the innermost layers whereas many background particles do not. Note that this volume is also restricted in the z coordinate along the beam line. The charged particle trigger and the pattern recognition programme strongly benefit from this fact.

4.3 Chamber Size

The chamber size is given by the radii of the outer cylinder D (see figure 88) and of the outer cones C and E. The chamber's inner radius (cylinder A) is also discussed in this section as well as the implications following from the length of the chamber and of the wires. The wall materials will be described in the next section **Chamber Walls.**

4.3.1 Outer Radius

The advantages and disadvantages of a large chamber size are the following:

μ misidentification due to π and K decays

- An important background for muon identification and an inefficiency for hadron identification is caused by $\pi^{\pm}$ and $K^{\pm}$ mesons which decay before being absorbed in the detector material or in the iron. The decay muons may reach the muon chambers and fake genuine muons if the track

trajectories determined in the drift chamber are consistent with the measured impact points in the muon chambers. The probability for this kind of misidentification increases with the decay volume and thus with the size of the drift chamber. Nevertheless, this argument did not lead to the choice of a small outer radius because a significant reduction of the chamber size with severe consequences on the overall performance results in a modest reduction of the decay volume only.

Misidentification rate vs. chamber size

On the contrary, the chosen large size enhances the probability of detecting π and K meson decays inside the chamber volume [‡] even in the typical cases where the decay vertices cannot be reconstructed. It allows to divide the chamber into an inner and an outer part in either of which track momenta and angles as well as dE/dx can be determined separately. Inconsistencies between both parts indicate hadron decays.

π and K decays inside the chamber

- To a large extent, the chamber's outer radius is related to the total expenses for the detector. It is one of the factors which determine the size and thus the cost of the outside detector components *RICH*, *TOF*, *ECAL*, *MUCH*, and of the magnet. Compared to this, the cost of the drift chamber alone does not depend that much on the size but rather on the number of drift cells (see section **Drift Chamber Cost**).

Impact on the total cost

- The chamber size determines the gas length, *i.e.* the length of the trajectory inside the active gas volume, and thus the dE/dx resolution.

dE/dx resolution

- To choose a large chamber size is the optimum way to improve the momentum resolution σ_p for high momentum tracks when other factors, namely reducing the multiple scattering and improving the spatial resolution, are exhausted. The dependence of the resolution σ_{p_T} on the chamber's outer radius is shown in figure 87.

  The reasons why we optimize the momentum resolution by choosing the largest feasible chamber size and not the largest feasible magnetic field are described in the section **Design Criteria**.

Momentum resolution

The chosen radius of the outer wall of the chamber, $R_{wallD} = 104\ cm$ which leads to $R_{outer} \approx 1\ m$,[§] is a compromise between the cost argument given above on one hand and the momentum and dE/dx resolution arguments on the other hand.

$R_{wallD} = 104\ cm$

[‡] The appropriate way to deal with π and K meson decays located outside the chamber is to install an extra hadron absorber as close as possible to the outer wall.

[§] The radii of the wire layers vary slightly along wire direction due to the stereo angle; see section **Stereo Layers**).

4.3.2 Inner Radius

The reasons for choosing the smallest feasible inner radius for the drift chamber have already been mentioned in the section **Design Criteria:**

Extrapolation CTC → SVD

- The distance between *SVD* and *CTC* must be as small as possible in order to provide a reliable assignment of *SVD* hits to tracks found in the *CTC*.

Soft particle detection efficiency

- The detection efficiency for low momentum particles increases with decreasing R_{inner}: $p_{Tmin}[\mathrm{GeV/c}] = 0.0015 \cdot B[T] \cdot (R_{inner} + 6 \cdot \Delta R_{layer})[cm]$.

dE/dx resolution

- A small inner radius is the cheapest way to increase the gas length and thus to improve the *dE/dx* resolution.

Momentum resolution

The momentum resolution for high momentum particles, $\sigma_{p_T} \propto (R_{outer} - R_{inner})^{-2}$, is noticeably improved by a small inner radius only in those rare cases where the *SVD* does not contribute to the momentum measurement.

$R_{wallA} = 13\ cm$

Ultimately, the drift chamber inner radius is determined by technical considerations. During the drift chamber assembly phase, a long support bar ($\approx 10\ m$) is needed in the hole formed by the inner wall. The radius of the support bar which is necessary for the mechanical stability leads to a radius of the inner wall of 13 *cm*.

The accessibility of the *SVD* and of the beam tube does not represent the limiting factor. In the design presented here, the support for the beam optics elements and their proper adjustment do not depend on the drift chamber inner wall.

The acceptance for low momentum particles obtained with $R_{wallA} = 13\ cm$ is shown in figure 91 (dashed lines). Here, it is assumed that particles are detected if they pass through at least seven layers of the *CTC*. The accuracy of the track extrapolation from the *CTC* to the *SVD* is described in the chapter **Drift Chamber Resolutions**.

4.3.3 Chamber Length

The size of the chamber leads to a maximum wire length of about 350 cm. At these lengths, the gravitational and the electrostatic forces acting on the wires impose non–negligeable problems (gravitational sag and electrostatic sag).

Gravitational sag

The gravitational sag cannot be the same for signal and for cathode wires. This would lead either to an unmanageably small mechanical tension for the light signal wires or to such high tensions for the heavy cathode wires that, even though the elasticity limit is not exceeded, severe problems arise for the wire fixation.

Electrostatic sag

The electrostatic forces normally cause unstable equilibria of the wire positions.

wall (see figure 88)	material	average thickness (mm)	radiation length / X_0
A	Carbon fibre	1	0.004
B	Aluminum	10	*irrelevant*
	preamplifiers, cables, *etc.*	50	*irrelevant*
C	Aluminum	10	0.11
	preamplifiers, cables, *etc.*	50	0.12
D	Carbon fibre	5	0.02
E	Carbon fibre	5	0.02
F	Carbon fibre	5	*irrelevant*

Table V: *The drift chamber walls*

The presence of asymmetries, *e.g.* of the gravitational sag, leads to a large, stable total sag. The problems are reduced if the chamber can operate with a relatively low voltage (see chapter **Gas and Wire Materials**).

Test measurements

Test measurements on this topic are currently being done at DESY. First results indicate that the effects are sizable but smaller than in the ARGUS drift chamber [35] where a deviation of the signal wire position from the drift cell centre of up to ± 1 *mm* has been intentionally introduced for reasons which will be described in the section **Stereo Layers**.

4.4 Chamber Walls

Materials and thicknesses of the chamber walls are summarized in table V. Some comments:

Inner wall: 0.4% *of a rad. length*

- The inner wall *A* (see figures 88 and 89) needs not to stand any mechanical force. Specifically, the sum of the mechanical tensions of all wires which in total corresponds to more than seven tons leads to a length deformation of this wall of 200 μm only. It must stand, however, the difference between the varying outside air pressure and the gas pressure inside the chamber which must be kept constant. The chamber runs at a slight overpressure. Thus, this wall must consist of a rigid material.

  Extrapolation accuracy

  The uncertainty of the track extrapolation from the *CTC* to the *SVD* due to multiple scattering effects in the inner wall is described in the section **Drift Chamber Resolutions**.

Electronics on backward side only

- All preamplifiers, cables, *etc.* are located on the backward side only (walls B and C in figure 88). These walls should consist of a conductive material in order to simplify the electrical connection amongst the potential wires and to provide a good ground definition for the electronics. In a metal, drilling holes for the signal wires does not deteriorate the mechanical stability as much as it would do in carbon fibre material.

24% rad.l. in 23% of 4π

  For particles going through wall C, the material of the whole drift chamber (gas, wires, walls, read–out electronics, and cables) corresponds to 24% of a radiation length. Note that this happens only in a solid angle η^* which covers less than 23% of 4π in the *CM* system (see figure 90).

3.5...5.5% rad.l. in 72% of 4π

- The walls D and E consist of carbon fibre material without any holes except some gas connections. The drift chamber material seen by particles passing through these walls is between 3.5% and 5.5% of a radiation length depending on the polar angle ϑ.

Thus, wall C, the bad case, still represents less material than the endplate of a corresponding cylinder chamber. In a region which covers more than than 72% of 4π in the *CM* system, *i.e.* in the solid angle corresponding to the walls D and E, the detector material is minute.

4.5 Magnetic Field

4.5.1 Field Strength

Two criteria for choosing the appropriate strength of the magnetic field have already been described in the section **Design Criteria**:

High field

- Good momentum resolution requires a high field as $\sigma_{p_T} \propto B^{-1}$.

Low field

- Good detection efficiency for low momentum particles needs a low field as $p_{Tmin} \propto B$.

There are two more arguments, both in favour of a moderate field:

Technical restrictions of charged particle trigger and track reconstruction

- There exist intrinsic technical reasons why the charged particle trigger and the pattern recognition can cover only a limited range of track bending radii ρ: $\rho \geq \rho_{min}$. A typical value is $\rho_{min} = 15\ cm$ for the pattern recognition procedure. For the trigger, the corresponding value is larger.

  One of these reasons is that for an efficient trigger and for an efficient track recognition the track's bending radius has to be much larger than the typical distance between subsequent measurements along the track.

Fake tracks

  More specific: Fake tracks, consisting in reality of hits belonging to dif-

ferent particles and of background hits, tend to have small ρ, typically a few times the distance between hit wires. One gets swamped by this background if the cut-off ρ_{min} is chosen too small. This problem is serious in a drift chamber even in absence of background hits: It is a priory unknown on which side a track passes a hit wire ("left-right ambiguity"). Choosing the wrong side leads to fake tracks, most of which can efficiently be discarded by requiring $\rho \geq \rho_{min}$ with an appropriate ρ_{min}.

Left-right ambiguities

Another reason is that the expenditure for the trigger is roughly proportional to the range of radii it covers. [¶]

Trigger complexity

The requirement to detect particles with the lowest feasible transverse momentum p_T which have at the same time large bending radii ρ, leads to the requirement of a small magnetic field B because $p_T = c \cdot B \cdot \rho$.

- The single cell efficiency depends on the Lorentz angle and thus on the magnetic field. The size of dead corners where the drift time is extremely large or where the charge never arrives at the proper signal wire increases with the magnetic field. More details are described in the section **Cell Structure.**

Single cell efficiency
Dead corners

The final choice of the magnetic field is $B = 1\ T$.

At a much higher magnetic field, rising cell inefficiencies partly compensate the expected gain in momentum resolution. The low momentum particle acceptance is severely reduced.

At a lower magnetic field, the low momentum particle acceptance is only slightly improved since other factors (multiple scattering *etc.*) start to play the dominant rôle.

4.5.2 Inhomogeneities and Tilted Magnetic Field

The treatment of an inhomogeneous magnetic field is well understood from existing experiments [35]. Field variations in the order of several percent along track trajectories in the active chamber volume, as is the case for the magnet proposed here, do not impose any major problem for the charged particle trigger, for the track recognition procedure, and for the final track parameter determination. There is no advantage if the field would be more homogeneous unless the homogeneity would be exactly 100%.

Moderately inhomogeneous magnetic field

The axis of the magnetic field is tilted by 7° with respect to the beam / detector axis in order to provide a sufficient separation of the e^+ and e^- beams. Relevant for the transverse momentum resolution σ_{p_T} is the polar angle ϑ^B with respect to the field and not, as used for simplification throughout this paper, the angle ϑ with respect to the beam axis. The approximation $\vartheta^B = \vartheta$ is slightly optimistic.

Tilted magnetic field

[¶] More exactly, it is proportional to the range of curvatures $\kappa = 1/\rho$ which makes it even more difficult to reach a small ρ_{min}.

σ_{p_T} resolution

In the extreme forward direction, $\vartheta = 12°$ translates into an angle ϑ^B between 5° and 19°, depending on the azimuth φ. Compared to an angle of 12° the accuracy σ_{p_T} is worse for $\vartheta^B = 5°$ and better for $\vartheta^B = 19°$. The deterioration of the accuracy, however, is not compensated by the improvement. A similar imbalance occurs for the reconstruction efficiency of particles with extremely low transverse momentum p_T in forward direction.

Reconstruction efficiency for low momentum particles

There remains a solid angle of 1% of 4π where the resolution of the tilted detector is worse compared to the case where the detector and magnet axis coincide. Even if taking into account that this occurs in the important forward direction, the implications of the tilted magnetic field are small enough to be neglected.

4.6 Cell Structure

We propose to build a drift chamber with small quadratic and rectangular cells ("small cell" solution). Pictures of these cells are shown in figures 92 and 93. The advantages of having two different cell types will be described below.

Small cell vs. jet cell

In the following, the features of the small cell solution will be discussed and compared to an alternative solution, the "jet cell" structure [39,40]. It should be well understood that some of the arguments given below are valid only for the "low energy" regime of a B–factory detector.

Number of channels

- The small cell solution needs more signal wires and thus more electronic channels than the jet cell solution. Comparing existing jet chambers with the chamber proposed here, the factor is two to three. This is not considered to be a problem as there exist other detectors, *e.g.* the ARGUS drift chamber [35], with more channels than the chamber proposed here.

Multiple scattering

- The small cell solution needs more wires (signal and cathode wires) and thus gives rise for more multiple scattering. The validity of this statement depends on design details of either chamber type. Anyway, the gas and not the wires will most likely be the factor which determines multiple scattering (see table VI and section **Gas and Wire Materials**).

Separation of closely neighbouring tracks

- In small cells, signals from different particles going through the same cell overlap in time and cannot be separated from each other. In such a case, only the track with the smallest distance to the anode wire gives a useful signal.

Granularity

In the design presented here and for $\Upsilon(4S) \rightarrow B\overline{B}$ events, 10% of the hits in the innermost drift chamber layer are not usable because of this "track overlap". Only 1% of all tracks have no useful hit in the two innermost layers due to this effect. For the outer layers, the track overlap probability more and more vanishes.

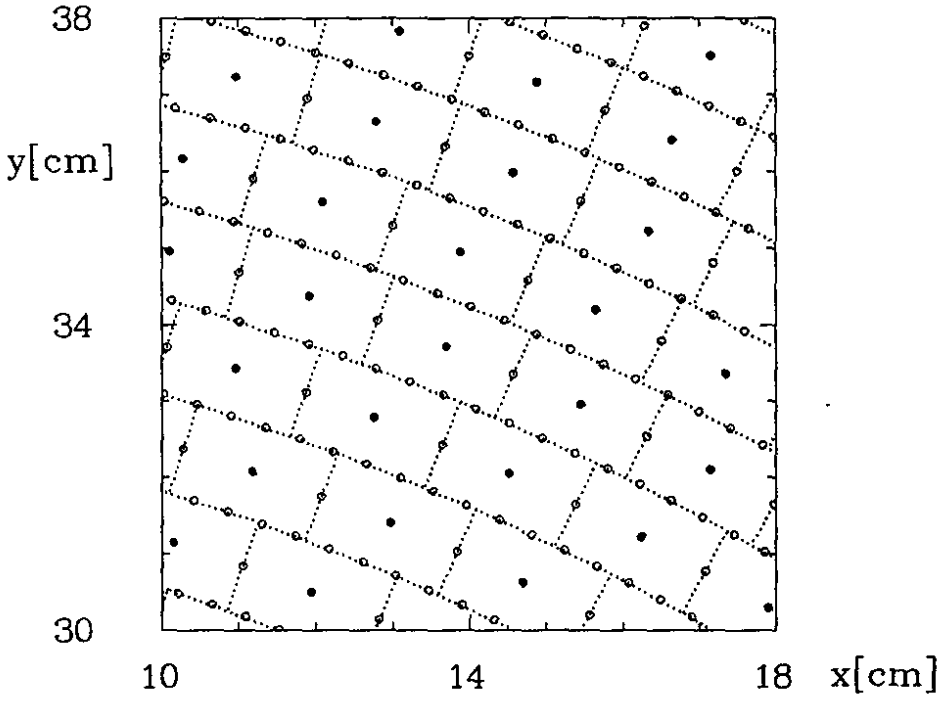

Figure 92: *Rectangular drift chamber cells: Pattern of signal wires (full dots) and cathode wires (open dots) in $x - y$ projection. The dotted lines indicate approximately the cell boundaries. Except for the wire diameter, the scale is* 1 : 1.

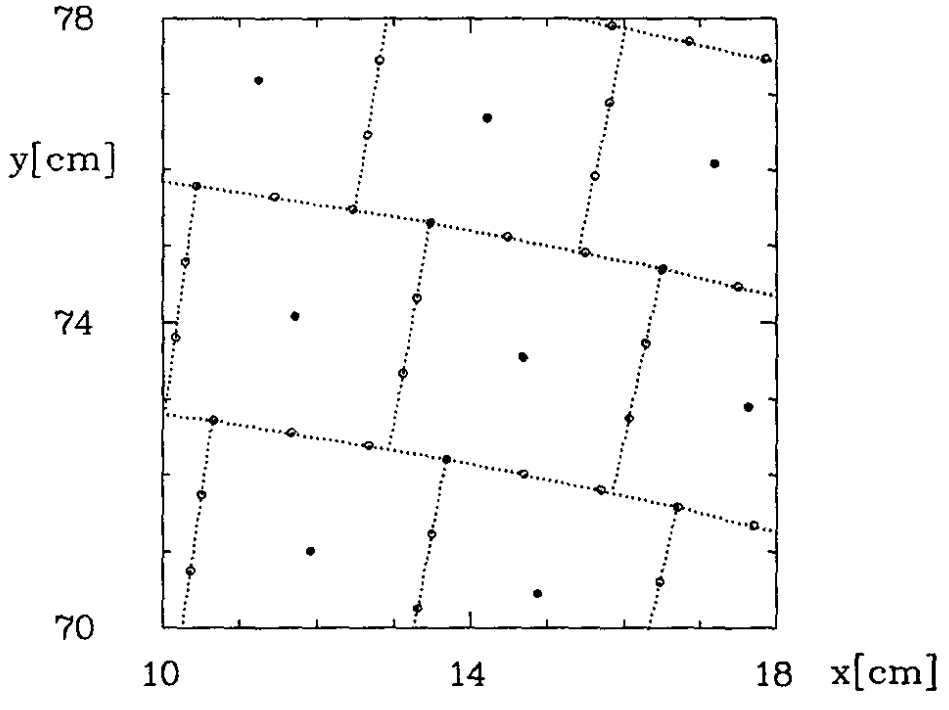

Figure 93: *Square drift chamber cells: Wire pattern as described for figure 92.*

No superlayers

- A benefit of the small cell solution is that there is no need for superlayers (many subsequent layers of wires with the same stereo angle). Details will be discussed in the following section **Stereo Layers**.

No dead space

- There is no dead space in a chamber with small cells as other solutions would have.

Only few calibration constants

- The calibration is extremely simplified for small cells. In this respect, all signal wires in square cells are identical, and the same holds for all wires in rectangular cells. For either cell type, only one set of calibration constants describes the drift time – space relation and the dE/dx behaviour. Thus, a very small number of constants describes the entire drift chamber.

Isotropy

- The principal reason for choosing the small cell solution is the requirement of isotropy in the drift chamber. This argument has been discussed in the section **Design Criteria**.

The chamber can be completely filled with square cells if the number of wires is increased by six from one layer to the next one and if the relation of height to width is $\pi : 3$, *i.e.*, the "square" cells are only approximately quadratic. For the rectangular cells, the increase must be four wires per layer and the relation height : width $= \pi : 2$ in order to avoid dead space in the chamber. As will be explained in section **Stereo Layers**, the cell sizes vary slightly along the wire direction.

Isochrones

An overview over the important numbers of the proposed chamber is given in table VI. The wire pattern, the drift paths, and the isochrones for single cells are shown in figures 94 and 95. The isochrones indicated in these figures represent the set of all points with equal drift time. Particles passing through a cell have, in general, many points where ionizations occur. Only that ionization centre matters which leads to the smallest drift time. Thus, the drift time – space relation is based on curves which are related to but different from the isochrones.

Varying position of cathode wires

Some cathode wires, namely those which delimit the drift cells in radial direction, have no fixed position with respect to the signal wire. Their position varies along the vector $\vec{e}_\varphi$, *i.e.* in horizontal direction in figures 94 and 95. This effect is a consequence of the different stereo angles of signal wires and cathode wires. It is well understood from the ARGUS detector [35] and does not impose any major problem.

5 cathode wires / cell

As can be deduced from figures 92 and 93, there are five cathode wires per signal wire for either cell type. The reasons for this large number are listed below:

More wires = less material

- Installing more wires means, in fact, less material. This can be explained as follows:

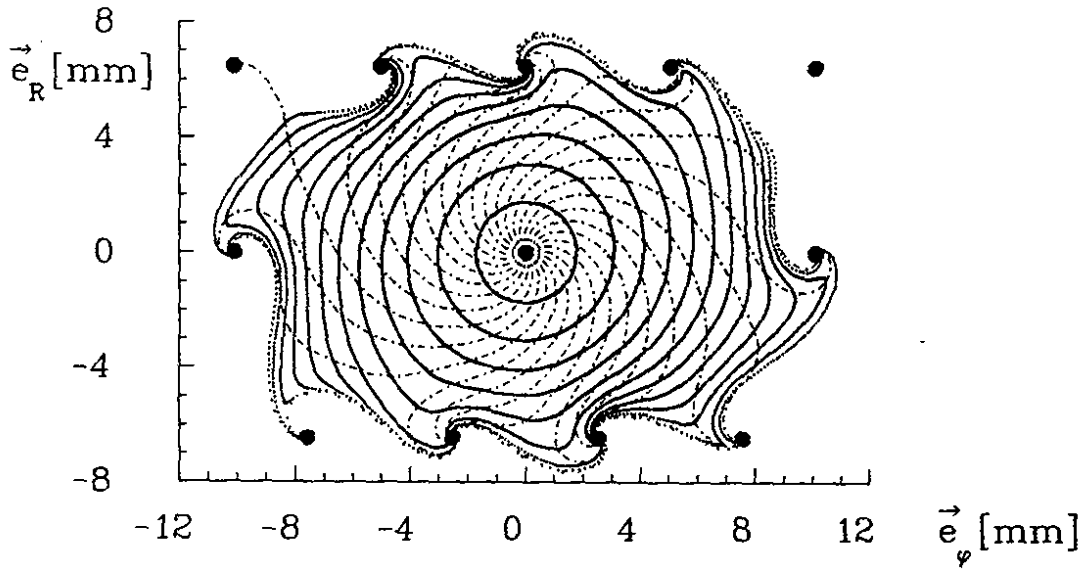

Figure 94: *Rectangular drift chamber cells. The central black dot represents the signal wire and the other ones the cathode wires. Full lines: Isochrones for t = 20, 40, 60, ..., 240 ns; dashed-dotted lines: Drift paths.*

	rectangular cells	square cells	Σ
Number of layers	30	16	46
Cell size (cm^2)	1.286×2.020	$3.0 \times \pi$	
Number of signal wires	3180	2544	5724
High voltage (V)	2500	2900	
Signal wire diameter (μm)	20	20	
Cathode wire diameter (μm)	50, 60	60	
Cathode wires / cell	5	5	
Number of cathode wires	16572	13350	29922
radiation lengths: wires	0.0016	0.0006	0.0022
radiation lengths: gas			0.0037

Table VI: *Drift chamber cells. The cell size is slightly varying and given here at the most forward point along the wire. For the high voltages and for calculating radiation lengths, propane for the chamber gas, W signal wires, and Cu-Be for the cathode wires are taken.*

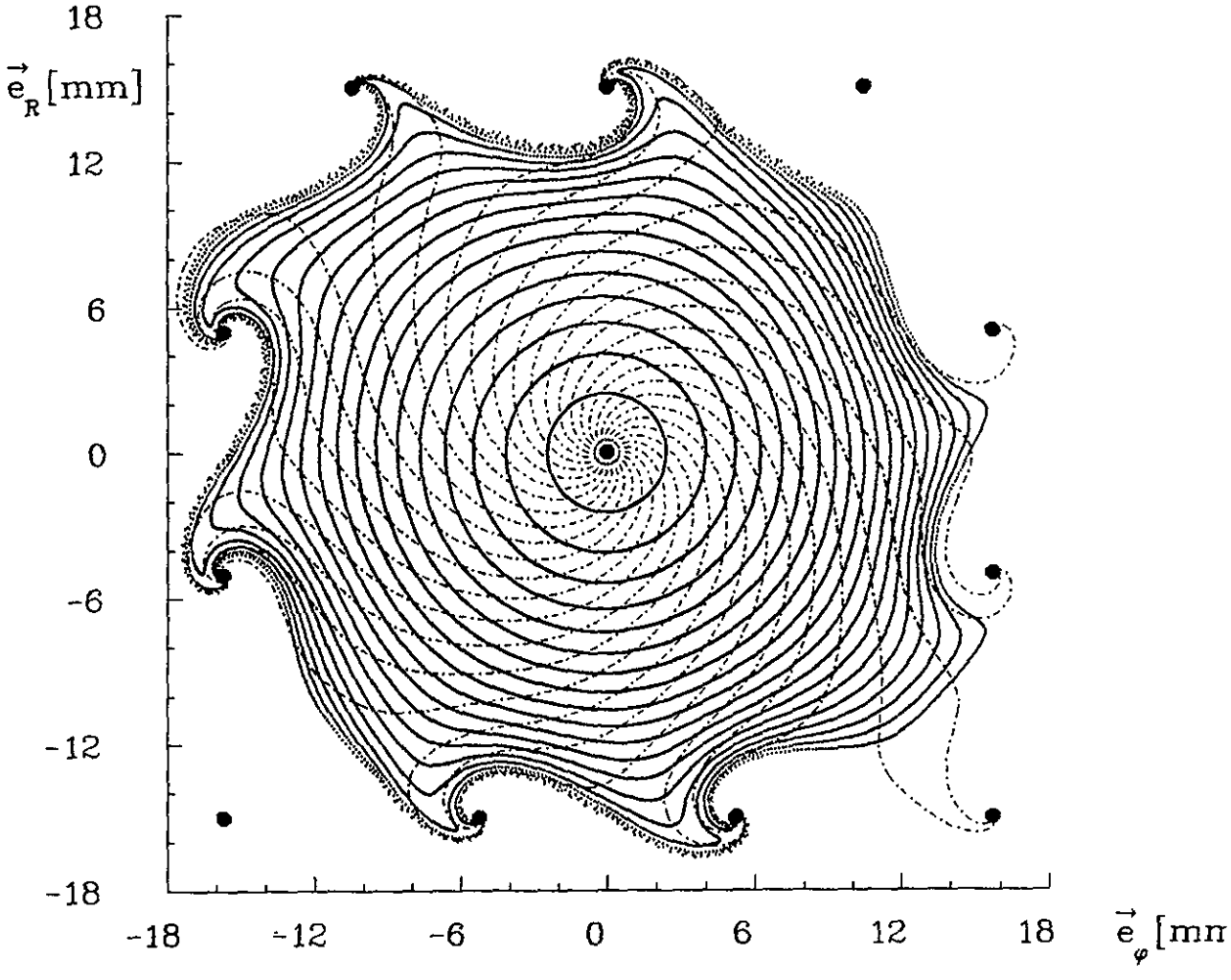

Figure 95: *Square drift chamber cells. The central black dot represents the signal wire and the other ones the cathode wires. Full lines: Isochrones for t = 30, 60, 90, ..., 570 ns; dashed-dotted lines: Drift paths. The scale is the same as in figure 94.*

– The electric field on the surface of cathode wires must be kept small in order to avoid aging processes. For being on the safe side, the proposed field of 23 kV/cm is 25% smaller than for the ARGUS detector [35]. *Aging: Small field at the cathode wires*

– For a given high voltage, usually a large wire diameter is chosen for keeping the field low at the cathode wire surface. Another approach, however, is made here: To increase the number of wires by simultaneously decreasing the wire diameter so that the product $N_{wire} \times r_{wire}$ is kept constant. This improves the multiple scattering behaviour since this effect is proportional to $N_{wire} \times r_{wire}^2$. *In praxi*, compromises have to be made because parallel wires which are too close together impose problems due to electrostatic forces (*c.f.* the discussion on wire lengths in section **Chamber Size**). *Large wire diameter or many wires*

In total, material is saved and multiple scattering effects are reduced by the solution which uses more wires with a smaller diameter.

- More cathode wires reduce the size of dead corners in the cells. In either drift cell shown in figures 94 and 95, two corners where no isochrones are drawn are dead. With the chosen **Magnetic Field** (*q.v.*) and the large number of cathode wires, however, it has been achieved that this fact has no consequence for the overall track reconstruction efficiency. It is a factor only in those cells where tracks exactly go through one of the dead corners with an angle of incidence of exactly 45° or 135°. *Almost no dead corners*

- As demonstrated in figures 94 and 95, the isochrones are to a good approximation circles. This holds for the rectangular cells almost as well as for the square cells. Circular isochrones simplify the track recognition procedure considerably. *Circular isochrones*

4.6.1 Spatial Resolution

The spatial resolution σ_D which will be obtained with these drift cells is shown in figure 96. This is an extrapolation from the ARGUS drift chamber [35] where the resolution has been measured by analysing the residua, *i.e.* by comparing the drift distance D expected from the final track reconstruction with the actually measured distance.

At small distances D, the accuracy is poor due to ionisation statistics effects. Here, the measured drift time is not only a function of the distance between the wire and the track but depends also on the positions along the track where ionisations actually occur. *Ionisation statistics*

For large distances, the observed steep rise is a sum of several effects occurring close to the cell boundary. For example, the exact parametrisation of the drift time – space relation at large drift distances is extremely intricate as can be *Resolution at the cell boundary*

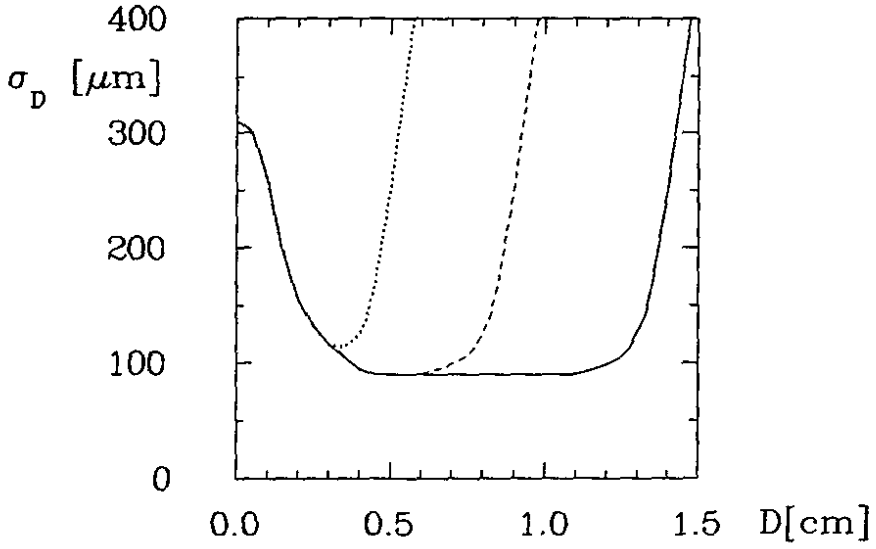

Figure 96: *Spatial resolution σ_D vs. distance D between wire and track. Full line: large (square) cells. Dashed line: small (rectangular) cells for tracks with radial incidence. Dotted line: small cells with azimuthal incidence.*

deduced from the shape of the isochrones shown in figures 94 and 95. As a pessimistic approximation, the calculation of spatial resolutions given here are based on the assumption that the actual non–circular shape of the isochrones can be described by circles everywhere in the cell.

$\langle\sigma_D\rangle$

In order to calculate the spatial resolution averaged over the full cell size, the proper weights $1/\sigma_D^2$ have to be taken into account with which every measurement contributes to the track parameter determination:

$$\langle\sigma_D\rangle = \frac{\int_{cell} dD/\sigma_D(D)}{\int_{cell} dD/\sigma_D^2(D)}.$$

In the large square cell, $\langle\sigma_D\rangle$ is 105 μm. In the rectangular cell, the most frequent case is approximately radial track incidence with $\langle\sigma_D\rangle$ = 120 μm. The worst case is azimuthal incidence into a rectangular cell with $\langle\sigma_D\rangle$ = 170 μm.

Momentum resolution independent of cell cize

In general, the average spatial resolution $\langle\sigma_D\rangle$ is improved by choosing a larger cell size. It turns out, however, that this gain in spatial resolution is counterbalanced by the reduced number of measurements per track length $\langle N_{meas}\rangle$. The product $\langle\sigma_D\rangle \cdot \langle N_{meas}\rangle^{-1/2}$ which is relevant for the momentum accuracy is at its optimum value for lateral cell lengths between 1 *cm* and 3 *cm*, *i.e.* for the range of cell sizes discussed here.

4.6.2 Different Cell Sizes

The following reasons support the choice of two different cell sizes:

- The number of cells in each layer must be sufficiently large in order to reduce the "track overlap" probability, *i.e.* the probability that more than one particle pass through a cell (see above). This request for granularity limits the cell size in the inner part of the chamber.

  Granularity

- In the outer part of the chamber where the granularity is good enough anyway, it would be a waste of material, electronics, and manpower to use the same small cell size as in the inner part.

  Minimum number of wires

- For the drift chamber calibration, the additional expenditure caused by having two different cell sizes is justifiable as the total set of calibration constants still remains small.

  Calibration

Choosing more than two different cell types does not reduce the number of wires considerably. Instead, this procedure would require a larger effort for the calibration and would lead to more problems in areas where different cell types border on each other (*c.f.* the discussion of an intermediate layer in section **Stereo Layers**).

4.6.3 Rectangular Cells and Square Cells

The shape of the smaller cells in the inner part of the chamber is chosen to be rectangular instead of quadratic. The advantages of the rectangular shape are described in the following:

- The resolution in rectangular cells depends on the track's angle of incidence into the cell. Comparing particles passing through a rectangular cell in radial direction with particles going through a square cell with the same area, the rectangular cell provides a better average spatial resolution $\langle \sigma_D \rangle$ as the cell width seen by those tracks is larger. At the same time, the number of measurements $\langle N_{meas} \rangle$ is higher as the lateral cell length is smaller. Thus, both factors in the product $\langle \sigma_D \rangle \cdot \langle N_{meas} \rangle^{-1/2}$ lead to an improvement of the momentum resolution. The gain for radial track incidence has to be paid by a deterioration for azimuthal incidence.

  Better momentum resolution for radial tracks

  For high momentum tracks coming from the interaction point and for the beginning of low momentum tracks, the radial component of the particle momentum vector dominates. Consequently, the larger impact on the momentum accuracy for radial incidence compared to azimuthal incidence is advantageous.

- The most important reason for choosing a rectangular cell shape is the requirement for a good dE/dx resolution in extreme forward direction. Here, the gas length is up to 190 *cm*, larger than anywhere else in the chamber and thus fully adequate. This fact, however, can be exploited only if a sufficient number of measurements or, in other words, a large

  dE/dx in forward direction

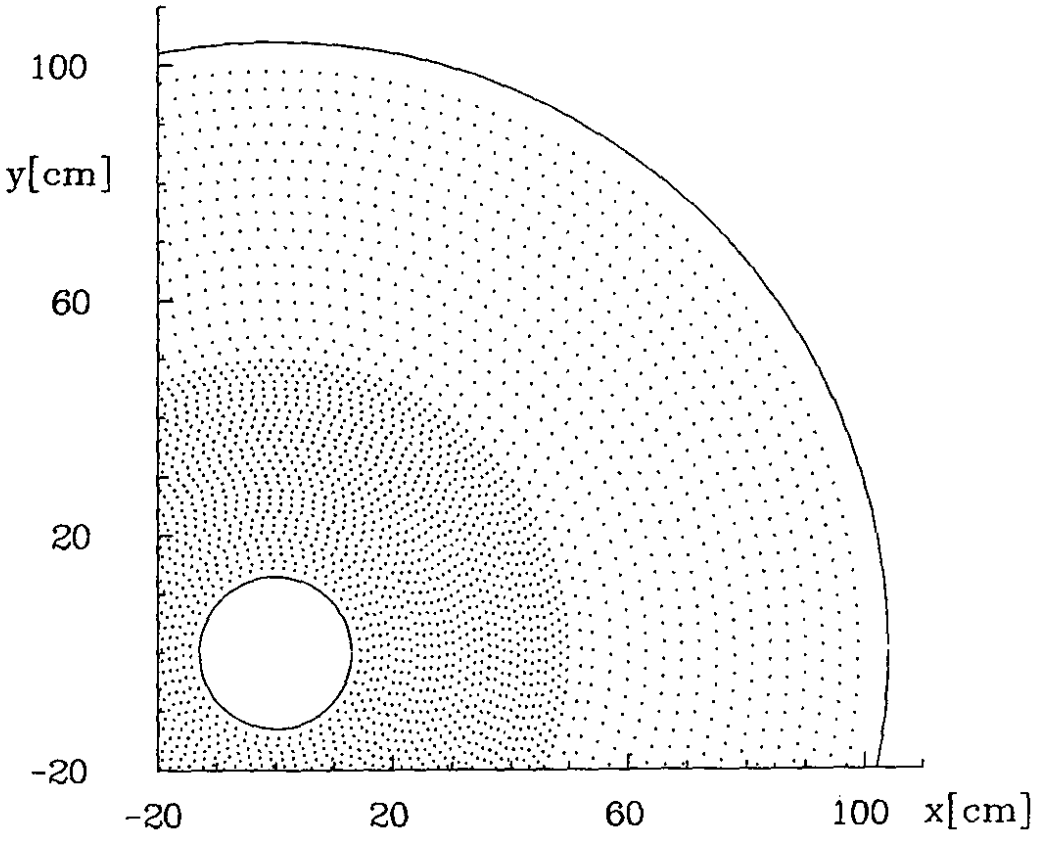

Figure 97: *Pattern of signal wires in $x - y$ projection.*

number of layers is available. The demand for a large number of layers together with the demand that the total number of cells must be kept manageably small automatically leads to a rectangular cell shape.

Granularity

- Rectangular cells provide the same granularity as square cells with the same area (cell width $\times$ cell height). For a given track length, the area and not the cell width determines the "track overlap" probability (see above) provided that the cells in different layers are staggered.

Circular isochrones

- Even in rectangular cells, the isochrones form approximately circles.

4.7 Stereo Layers

4.7.1 Layer Configuration

The layer structure is described in table VII. A picture of the signal wire pattern is shown in figure 97. The innermost 30 layers consist of rectangular cells. The outermost 16 layers are formed by larger square cells. Inbetween the rectangular cells and the square cells, an intermediate layer (layer 31 in table VII)

Intermediate layer

layer	cells / layer	R_{min} (cm)	R_{max} (cm)	wire length (cm)	cell size at $R = R_{min}$ (cm^2)	stereo angle $(mrad)$
1	48	14.56	15.43	99.1	1.21×1.91	+80.0
2	52	15.77	16.71	107.4		−80.0
3	56	16.98	18.00	115.6		+80.0
⋮	⋮	⋮	⋮	⋮	⋮	⋮
28	156	47.30	50.14	322.1		−80.0
29	160	48.52	51.43	330.4		+80.0
30	164	49.73	52.71	338.6	1.21×1.91	−80.0
31	168	51.42	54.42	352.4	2.16×1.91	+80.0
32	114	54.0	57.0	327.6	3.0×2.98	−84.8
33	120	57.0	60.0	317.2	3.0×2.98	+89.9
34	126	60.0	63.0	316.9	3.0×2.99	−95.3
⋮	⋮	⋮	⋮	⋮	⋮	⋮
45	192	93.0	96.0	192.5	3.0×3.04	+188.3
46	198	96.0	99.0	182.1	3.0×3.04	−202.1
47	204	99.0	102.0	171.8	3.0×3.05	+217.6

Table VII: *Drift chamber layers. R_{min} and R_{max} are described in the text.*

is foreseen. The main purpose of this layer is to provide an electric field for the outer rectangular cells (layer 30) and for the inner square cells (layer 32) which is similar to all other cells of the respective type. Thus, the existence of layer 31 simplifies the calibration of layer 30 and 32.[‖] In addition, this layer has the potential to contribute to track recognition, momentum determination, and dE / dx measurement even though the electric field in these cells is asymmetric. For the resolution specifications given here, this layer has been ignored.

4.7.2 Stereo Angle

A drift chamber with stereo wires has usually also layers of paraxial wires. Paraxial cells are supposed to simplify the charged particle trigger and the track recognition procedure.

Layers of paraxial wires form cylinders, in contrast to layers of stereo wires which form hyperboloids. The radius of stereo wire layers is slightly varying

[‖]For the same reason, an additional layer of anode wires is foreseen between layer 1 and the inner chamber wall. An analogous layer close to the outer wall is renounced as its benefits are smaller.

Hyperboloidal sag

along the wire direction ("hyperboloidal sag"). The smallest and the largest distance between the beam line and a wire are denoted by R_{min} and R_{max} (see table VII).

Even though the hyperboloidal sag is small, the problem remains how to fill the drift chamber with cylindric layers and, at the same time, with hyperboloidal layers. Two solutions have been chosen up to now:

Superlayers

- In the superlayer solution, several paraxial layers (cylinders) are placed in sequence followed by several layers with an equal stereo angle (hyperboloids). The layers belonging to the same stereo view fit nicely one into the other even though the stereo layers are not exactly parallel (see below). At the border between paraxial and stereo cells, however, dead space is unavoidable. Note that dead space normally affects the adjacent cells because there the electric field is irregular.

  Moreover, the superlayer solution is in contradiction to the requirement that the different stereo views contribute about equally to the measurements at the beginning of tracks. The reason for this requirement is to improve the reconstruction efficiency for low momentum tracks (see section **Design Criteria**).

Alternating paraxial and stereo wires

- In the other solution, applied for the ARGUS detector [35], paraxial layers alternate with stereo layers. The cathode wires inbetween two layers have a stereo angle which leads to exactly half the hyperboloidal sag as the sag of the stereo signal wires. Thus, the position of signal wires varies with respect to the surrounding cathode wires or, in other words, with respect to the cell centre. This variation is equal for stereo and for paraxial wires and leads to a signal wire displacement of up to ± 1 *mm* in the ARGUS case. The resulting maximum stereo angle, (which depends strongly on the chamber length), is 80 *mrad*. As the chamber presented here is 75% longer than the ARGUS chamber, this solution allows only for very small stereo angles or it leads to an unacceptably large sag.

Only stereo wires

Thus, a third solution is chosen here: To relinquish the paraxial wires. The chamber consists of stereo cells only, forming hyperboloidal layers which are nicely nested one into the other. There exist two stereo views, one with positive and one with negative stereo angles. The layers belong in alternating sequence to either view.

The track recognition programme being used for the ARGUS drift chamber [35] does not depend on the existence of paraxial wires. Here, the necessary condition is that track trajectories viewed in any stereo projection can locally be approximated by circle segments. This is fulfilled for the chamber presented here. Moreover, new track recognition procedures are conceivable which take advantage of the fact that there are only two stereo views and that the lay-

ers belonging to either view are distributed to the highest possible degree of homogeneity.

The charged particle trigger currently being installed at ARGUS [36] which exploits the large stereo angle in the ARGUS Micro Vertex Chamber [10] is an example for a trigger based mainly on stereo wires.

Maximum stereo angle

The finally chosen stereo angles are shown in table VII. Note that even in this solution with stereo wires only, geometrical considerations remain according to which the size of the stereo angle should be limited.

- The hyperboloidal sag in the innermost layer must be small in order not to interfere with the cylindric shape of the inner drift chamber wall. Similarly, the stereo angle in layer 32 must not be too large. As will be explained in section **Chamber Construction**, it must be granted that the whole inner part of the chamber, consisting of layers 1 to 31 and of the walls A, B, and F, can be shoved through the hyperboloid formed by layer 32.

  As a consequence, the stereo angle is kept at a constant value of ± 80 *mrad* for the inner layers 1 to 31.**

- The cell size is varying along the wire even in this solution. This is a consequence of the fact that the distance between any two different hyperbolae is not constant. The size of the variation depends on the wire length and on the stereo angle. In the outer part of the chamber, *i.e.* in layers 32 to 47, the stereo angles are chosen in a way that the cell size variation does not exceed 1 *mm*.

In summary, the chamber design presented here provides an optimum polar angle resolution σ_ϑ. This is a consequence of the facts that there are no paraxial wires, *i.e.* that all measurements contribute to the ϑ accuracy, and that the stereo angles can be chosen to be very large. For physics analyses, σ_ϑ hardly ever represents a limiting factor.

4.8 Gas and Wire Materials

All resolution specifications given in this section are based on the assumption that propane be used as chamber gas, Cu–Be for the cathode wires and W for the signal wires. Test measurements on other chamber gases are currently in progress [37,38]. The aim is to find materials with less multiple scattering, *i.e.* to improve the momentum resolution. In the following, the requirements will be listed which have to be fulfilled by new materials.

**In general, one does not profit by choosing a constant stereo angle. A marginal benefit could be that the event display looks more convenient.

Wires

For all wires, it is most important to avoid wire breakings with the highest possible probability (see section **Chamber Construction**). This depends mainly on the wire fixation. Alternative choices of cathode wire materials [††] are Al [41] or Ti-Be which would reduce the radiation lengths from $0.22\%x_0$ to $0.04\%x_0$ and $0.10\%x_0$, respectively.

Gas

Using He based gas mixtures can reduce the material from $0.37\%x_0$ for propane to typically $0.15\%x_0$. It is worth mentioning that, at least with respect to multiple scattering, propane is a good choice when compared to, *e.g.*, argon. The requirements to be matched by the chamber gas are the following ones:

Spatial resolution

- To some extent, a degradation of the spatial resolution can be accepted if, at the same time, multiple scattering is strongly reduced compared to propane. For example: Reducing the size of multiple scattering effects by a factor of two in connection with a two times worse spatial resolution leads to an improvement of the momentum resolution for pions with momenta $p < 1$ GeV/c. At higher momenta, however, the momentum resolution is deteriorated to such a degree that this example cannot be regarded as a viable solution.

dE/dx: Low momentum particles

- For low momentum particles, particle separation by means of measuring the specific ionisation loss dE/dx is rather insensitive to the dE/dx resolution (see figure 99). With propane, the separation of pions and kaons is better than 4σ for all momenta below 800 MeV/c. In a gas with a dE/dx resolution twice as bad, this limit is at 630 MeV/c.

dE/dx: Relativistic rise

The situation is different for high momentum particles. In order to exploit the relativistic rise of dE/dx, a good resolution as well as a large size of the rise is necessary both of which depend on the choice of the gas. In the design presented here, a $\pi - K$ separation of 2 – 3 standard deviations is achieved with propane for momenta above 2 GeV/c(see section **Drift Chamber Resolutions**). In the ARGUS experiment, the separation is less than 2σ and nevertheless contributes fruitfully to exclusive analyses.

A $\pi - K$ separation below 1σ would even not allow for the minimum task of the dE/dx measurement at high momenta, namely for determining the identification efficiencies and fake rates of the *RICH* system from data.

High voltage

- Aging effects strongly depend on the high voltage necessary for running with a specific gas. Moreover, a lower voltage allows for thinner wire diameters.

[††] The contribution of the signal wires to multiple scattering is small and neglected here.

4.9 Mechanical Construction

No holes for cathode wires

A basically new aspect of constructing the chamber proposed here is that in forward direction, *i.e.* at the walls E and F in figure 88, no electronics and even no holes for wires are foreseen. The reasons are summarized in the following:

- The total amount of material must be minimal in forward direction. Consequently, all electronics, cables, *etc.* are placed in backward direction only (see section **Chamber Walls**).
- Holes degrade the stability of carbon fiber material substantially. Thus, all holes except some gas connections are drilled in the backward cones B and C which consist of aluminium.
- The truncated cone E has a length of 190 *cm* and an opening angle of 12°. No procedure of passing wires through holes in such a cone is conceivable due to lack of space.

Wire feed throughs are not only renounced in forward direction but also for cathode wires in backward direction. Essentially, only the holes for the signal wires, for the high voltage, and for the gas connection remain in this chamber.

Wire fixation from inside

The consequence of this design is that the wires have to be fixed from inside the chamber (see below). Once the chamber is closed or even as soon as more wires are strung, there is no more access to them.

This means that wire breakings have to be excluded with the highest conceivable probability. The experience with the ARGUS main drift chamber [35] has shown that it is well possible to run a detector since almost a decade without a single wire breaking.

The mechanical construction ptocedure will shortly be sketched here:

Wiring in two chamber parts

- During the wiring phase, the chamber consists of two separate parts, an inner one (walls A, B, and F) and an outer one (walls C, D, and E). In contrast to the outer part, the inner part is an unstable structure because the wall A must not be subjected to any mechanical force at any time. For this reason, the walls B and F are kept at a constant relative position by means of a support bar fed through the hole formed by wall A. This bar determines the inner chamber radius (see section **Chamber Size**).
- In the inner part, the wiring proceeds from inside to outside, and in opposite direction in the outer part.
- The inner sides of the conical chamber walls have a steplike shape leading to a surface consisting of many short cylinders. For every radius of wire fixation points, one such cylinder exists.

Fixation boards

- The wires are attached to fixation boards on either end. On every board, the wires belonging to many cells of the same layer are fixed, taking into account the proper wire length and stereo angle. This work is done in a separate clean room outside the chamber. The mechanical wire tension can be tested before the wires are installed in the chamber.

- Every pair of fixation boards with all wires belonging to it is mounted on the cylindrical surfaces on the inner side of the chamber walls. A sufficient geometrical accuracy of about 100 μm can be achieved.[‡‡]

Assemblage

- When both parts are shoved one into the other, the support bar described above serves as a guide for the outer part. During this procedure, the hyperbolic sag of layer 32 (the innermost layer of the outer part; see section **Stereo Layers**) imposes a specific problem because the inner part must fit through the hyperboloid formed by this layer. It has been achieved to avoid dead space due to this effect by choosing slightly different radii of the wire fixation points in forward and backward direction.

A similar wire mounting scheme has been applied for the ARGUS Micro Vertex Chamber [10].

The fact that the wires are fixed at the inner side of the chamber walls has the following advantages: After a separate stringing procedure, the wires belonging to many cells are installed simultaneously. The wire fixations can be tested outside the chamber. This minimizes the time necessary for assembling the drift chamber substantially. Manpower is saved, and the period during which the chamber is open and, even in a clean room, exposed to dust is as short as possible.

4.10 Drift Chamber Resolutions

4.10.1 Accuracy of the Extrapolation from *CTC* to *SVD*

The accuracy of determining the tracks' intersect with the *SVD* is denoted by σ_z^{SVD} and σ_d^{SVD} (see section **Design Criteria**). As σ_d^{SVD} is always smaller than σ_z^{SVD}, only the contributions to σ_z^{SVD} are described here. The following numbers are valid for π mesons with a momentum $p = 300\ MeV/c$.

The spatial resolution of the track's intersect with the inner drift chamber wall is $\sigma_z^{CTC} = 500\ \mu m$. The contribution from multiple scattering in the inner drift chamber wall amounts to $\sigma_{z,mult.scatt.}^{SVD} = 160\ \mu$m. The uncertainty due to the angular resolution σ_ϑ in the *CTC* is $\sigma_{z,angle}^{SVD} = 140\ \mu m$. The two latter numbers

[‡‡] A precise determination of every individual wire position has to be performed in the reconstruction programme.

are valid for a polar angle $\vartheta = 90°$ and have to be increased by factors up to 2 ($\sigma^{SVD}_{z,mult.scatt.}$) and 1.6 ($\sigma^{SVD}_{z,angle}$) for other polar angles.

The three contributions σ^{CTC}_z, $\sigma^{SVD}_{z,mult.scatt.}$, and $\sigma^{SVD}_{z,angle}$ can be added in quadrature.* At lower momenta, the multiple scattering term dominates which scales with $1/(p \cdot \beta)$ of the particle.

The accuracy of the extrapolation from the *CTC* to the *SVD* is fully sufficient. This is a consequence of the small radius and the small thickness of the drift chamber inner wall and of the large stereo angle.

4.10.2 dE/dx Resolution

Landau distribution

Particle identification by means of the specific energy loss is complicated by the fact that dE/dx measurements follow a Landau distribution where mean values cannot be calculated. The remedy which will be applied in all following considerations is to use the "truncated mean". Following ref. [35], the 10% lowest lying and the 30% highest lying measurements are discarded. The average value calculated from the remaining 60% of the measurements is Gaussian–distributed with tails correctly described in a region of more than three standard deviations.

Truncated mean

For various particles, the energy loss in propane is shown in figure 98. The curves represent measurements of truncated means obtained with the detector ARGUS [35]. For propane, it is not necessary to rely on predictions (see, *e.g.* [42,43,44]) rather than on measurements. For other gases, test measurements are currently in progress [37,38].

dE/dx resolution extrapolated from ARGUS

In order to calculate the resolution of the chamber proposed here by extrapolating from the resolution achieved in the ARGUS detector [35], the following scaling predictions [45] have been used:

$$\sigma_{dE/dx} \propto (\textit{Sample Thickness})^{-0.32} \cdot (\textit{Number of Samples})^{-0.43}.$$

The ARGUS drift chamber has 36 layers and, at a polar angle $\vartheta = 90°$, a gas length of 64 *cm*. The achieved relative dE/dx resolution in ARGUS is 4.4% for simple events (Bhabha events) and 5.0% for complicated events. The extrapolation to the chamber presented here with 46 layers and a gas length of 85 *cm* leads to a resolution of 3.9% for Bhabha events and 4.4% for hadronic events.

$\sigma_{dEdx} \leq 4.4\%$

This extrapolation is pessimistic because particles are boosted into the forward direction due to the Lorentz transformation. Consequently, the particle density at $\vartheta = 90°$ is smaller than at a symmetric storage ring, and the average gas length is increased by more than a factor 85/64 as supposed above. The best dE/dx resolution is achieved in the extreme forward direction where the gas length is 190 *cm*, even though there are only 30 layers.

*This is somewhat pessimistic as the correlation between σ^{CTC}_z and $\sigma^{SVD}_{z,angle}$ is large and negative.

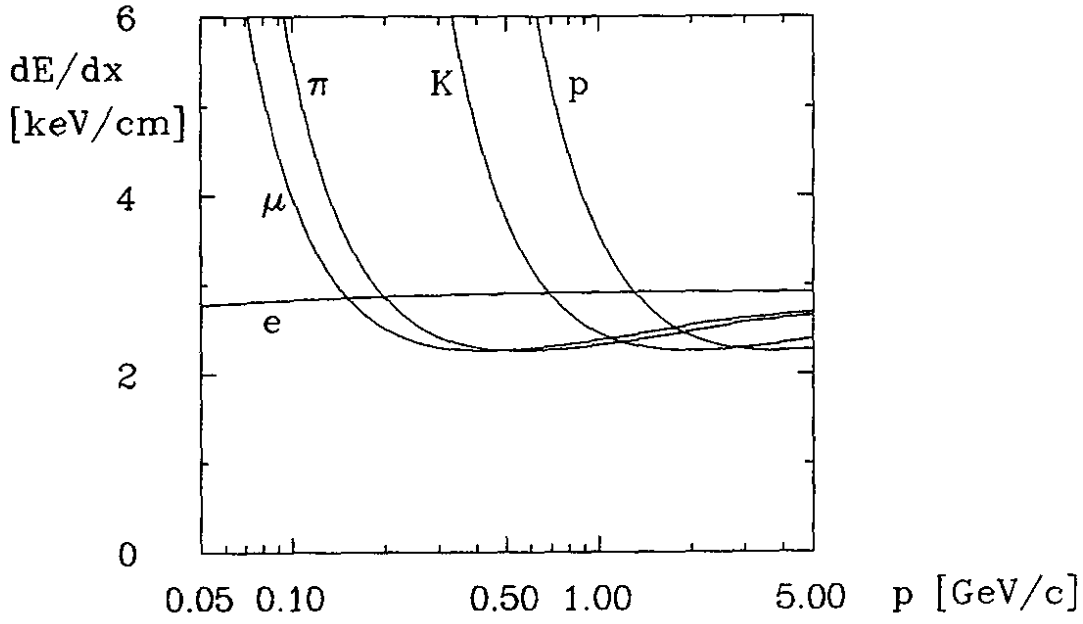

Figure 98: *dE/dx truncated means for e, μ, π, K, and p vs. momentum p.*

4σ π − K separation below 800 MeV/c

The energy loss differences for various particle hypotheses relative to the *dE/dx* for the pion hypothesis is given in figure 99. Assuming the conceivably worst resolution of 4.4% (see above), the energy losses of pions and kaons are separated by more than 4 standard deviations for all momenta below 800 *MeV/c*.

2 − 3σ π − K separation in the relativistic rise

In the region of the relativistic rise, a $\pi - K$ separation of two to three standard deviations is achieved for momenta larger than 2 GeV/*c*. This separation is insufficient for an independent particle identification procedure. Experience with the ARGUS detector [35] demonstrates, however, that even this kind of separation is valuable when the information of all detector components is coherently taken into account.

4.10.3 Momentum Resolution

The momentum resolution is calculated from the spatial resolution described in the section **Cell Structure** and from the layer configuration (see **Stereo Layers**). An approximation has been used similar to the procedure described in ref. [46] but modified in order to correctly deal with different cell sizes and varying stereo angles.

Comparison with the resolution at ARGUS

This method has been compared with the more elaborate procedure used in the ARGUS reconstruction programme [35] where multiple scattering is treated literally as a series of many small scattering angles. For invariant mass calculations *etc.*, this procedure leads to correct χ^2 distributions. Down to momenta of 150 *MeV/c*, both methods agree perfectly.

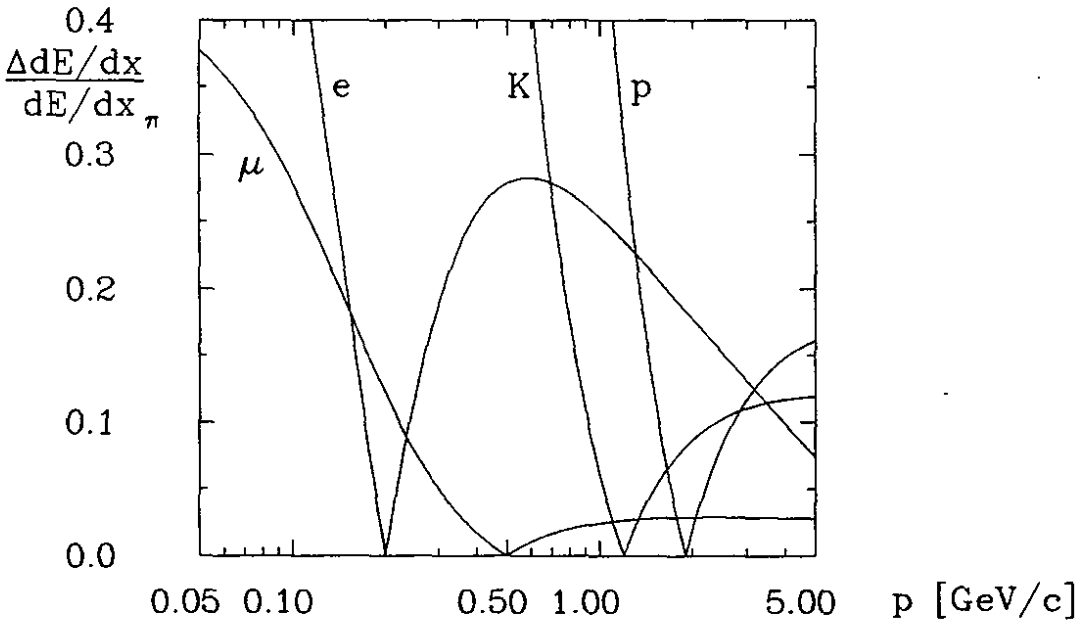

Figure 99: *Relative dE/dx differences* $|\ (dE/dx)_\pi - (dE/dx)_h\ |\ /(dE/dx)_\pi$ *for particle hypotheses* $h = e, \mu, K$, *and* p *as indicated in the figure.*

Momentum resolution in complex events

In multihadron events, crossing tracks *etc.* lead to a deterioration of the momentum resolution of 10% [35] compared to the calculation described above. This factor is taken into account for all following resolution specifications.

SVD not taken into account

In order to make comparisons with other track chambers possible, the improvement of the momentum resolution due to the Silicon vertex detector *SVD* is not taken into account here.

Resolution in the lab system

The momentum resolution for charged tracks in the detector rest system is shown in figure 100. The zigzag of the curves in backward and, less pronounced, in forward direction is caused by the fact that the number of hit layers depends on the polar angle ϑ and that every decrease of the number of layers leads to a noticeable deterioration of the resolution.

As expected from the drift chamber shape, the momentum resolution for high momentum particles in the detector rest system is asymmetric and depends strongly on the polar angle ϑ.

Resolution in the CM system

The design criterion of the chamber, however, is to achieve an optimum resolution in the *CM* system. This is shown in figure 101. Here, all quantities (ϑ^*, p^*, and σ_{p^*}) are given in the *CM* frame. Except the curve corresponding to the lowest momentum (150 MeV/c), the resolutions are almost symmetric and flat in a wide range of $\cos\vartheta^*$.

Resolution for low momentum particles in Backward Direction

The deterioration for low momentum particles in backward direction cannot be avoided in detectors at asymmetric storage rings. It results from the fact that the Lorentz transformation from the *CM* frame to the lab frame leads to so small lab momenta p that multiple scattering ultimately limits the resolution.

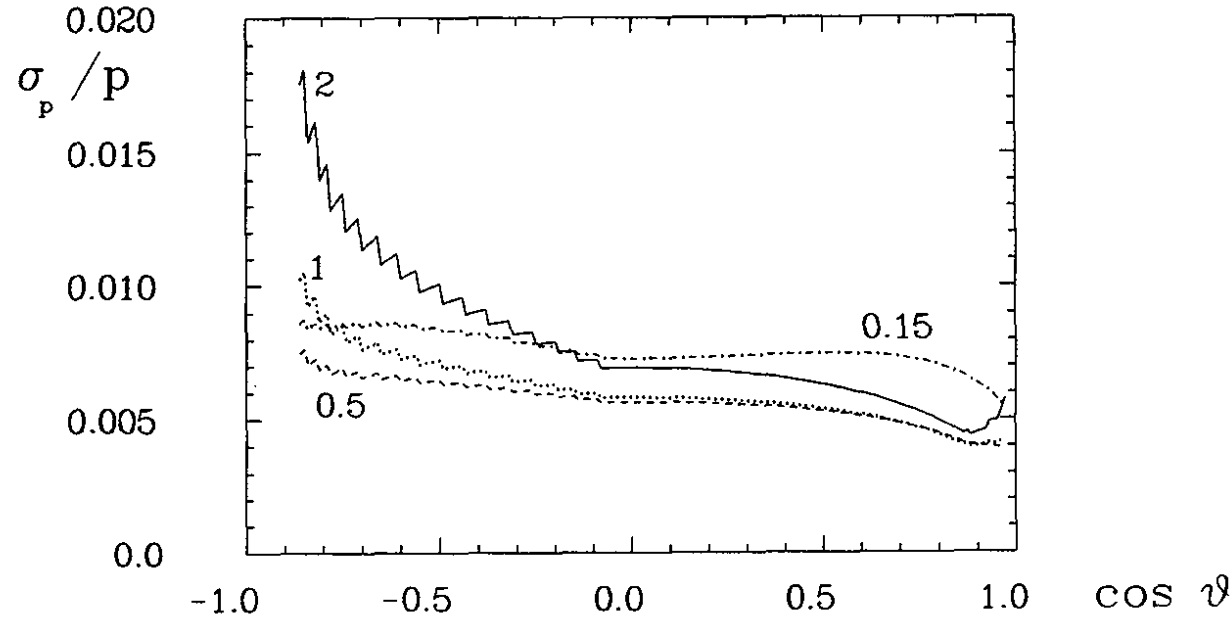

Figure 100: *Pion momentum resolution σ_p/p vs. $\cos\vartheta$ for various momenta indicated in units of GeV/c.*

At these momenta, however, the resolution has hardly any impact on physics analyses.

Resolution for high momentum particles

At momenta around $p^* = 2.5$ GeV/c, the momentum resolution is better than 17 *MeV/c* in 80% of the full solid angle. Even though this resolution alone does not allow for a kinematical separation of two–body B meson decays, *e.g.* $B^0 \to \pi^+\pi^-$ and $B^0 \to \pi^+K^-$, it contributes to an analysis which coherently uses all information from particle identification and event kinematics.

4.11 Drift Chamber Cost Estimate

The cost of the drift chamber electronics (preamplifiers and flash–adc's) is 400 DM per channel. This can be deduced from the price for the similar electronics in the track chamber of the experiment H-1 [40]. Thus, the total cost for electronics is 2.4 MDM.

The chamber mechanics, including the chamber walls and the mounting rack, amount to 1.0 MDM. The gas system costs 0.3 MDM.

The total cost for the central track chamber is 3.7 MDM.

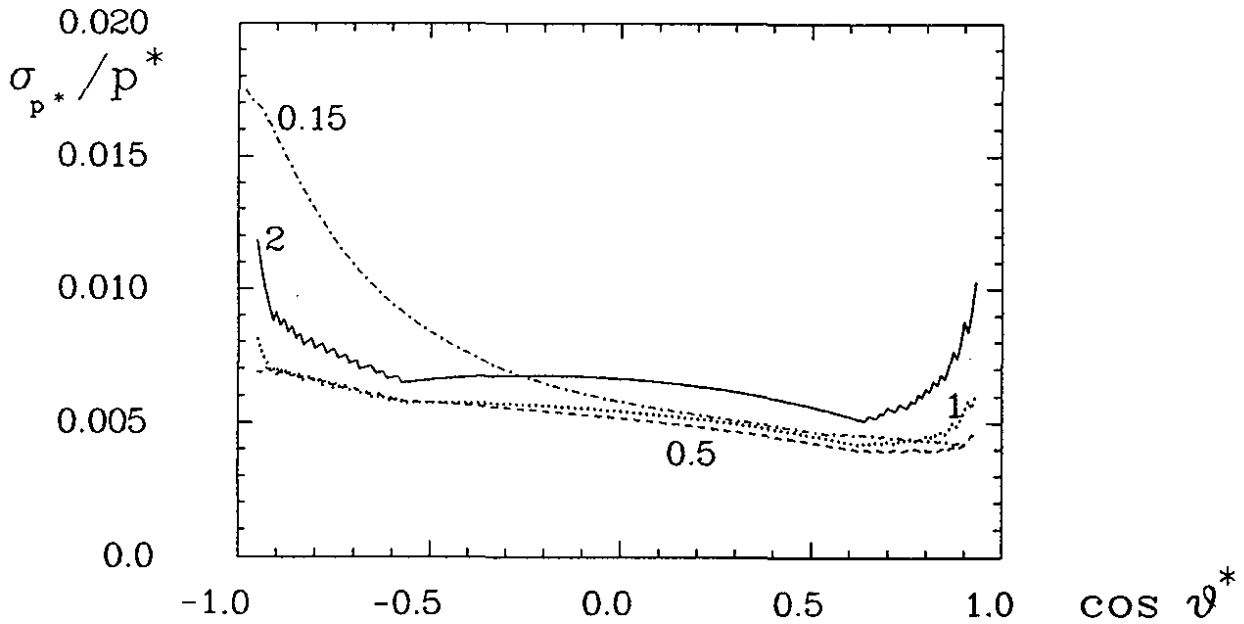

Figure 101: *Centre–of–mass π momentum resolution σ_{p^*}/p^* vs. $\cos\vartheta^*$ for various CM momenta indicated in units of GeV/c.*

5 The Ring Imaging Čerenkov Counter

5.1 Requirements for Particle Identification

Identification of charged particles (PID) over a wide range of particle momenta is one of the basic requirements for a B factory detector (see Part I). Several components of the detector contribute to this task:

- Muon chambers (for muons with momenta above 1 GeV/c),
- Electromagnetic calorimeter (electron-hadron separation above 0.4 GeV/c),
- Drift chamber via dE/dx (3σ separation π/K up to 0.9 GeV/c, K/p up to 1.5 GeV/c).
- Ring Imaging Čerenkov Counter (RICH), necessary to complement the other techniques and extend the PID to higher momenta.

The RICH, as described in this section, has been designed to separate pions, kaons and protons up to the kinematic limits in B meson decays. For a center of mass system moving with $\beta\gamma = 0.6$ these limits correspond to a maximal momentum of about 4.7 GeV/c. The counter described below fulfils these requirements. It provides, in addition, a good e/μ, e/π and even μ/π separation at low momenta, thus supplementing the information from the other components of the detector.

5.2 The Choice of the Radiator and the Photon Detector

Elements

The elements of the RICH counter are (Fig. 102):

- a *radiator* where Čerenkov photons may be produced by passing charged particles,
- a wire chamber cathode plane acting as a *photo-cathode*,
- a *wire chamber*, capable of detecting photo-electrons from the photo-cathode with high efficiency and with good resolution in two dimensions,
- a *drift space* separating the radiator and the wire chamber, wide enough to obtain an accurate Čerenkov angle from the measured photon absorption coordinates, and
- a *wire chamber read-out system.*

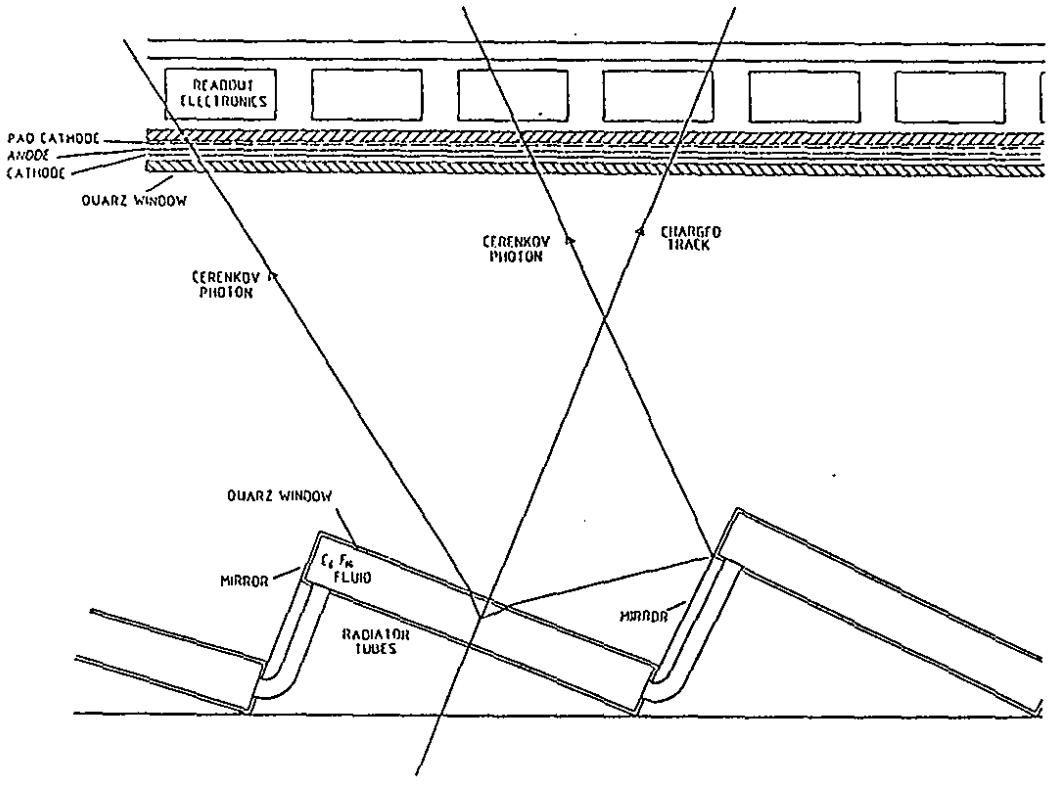

Figure 102: Side view of a section of the RICH counter.

Radiator

The radiator consists of 1 cm of a special liquid, C_6F_{14} (known as FC72), which has also been used in the RICH of the DELPHI experiment [47]. The liquid is contained in a box made of aluminum and equipped with a 3 mm thick fused quartz exit window for the Čerenkov photons.

Threshold momenta

This radiator was chosen since it combines low dispersion (less then 2% variation in refractive index for photon energies between 6 eV and 8 eV) and a low Čerenkov threshold. For the mean value of the refractive index (1.278) the Čerenkov threshold momenta for pions, kaons, and protons amount to 0.18, 0.62 and 1.18 GeV/c, respectively. The Čerenkov angle corresponding to $\beta = 1$ particles is 39° and amounts to 53° after refraction in the air (for tracks that enter the radiator perpendicularly).

Cleaning system of liquid radiator

We plan to use a cleaning system for the liquid radiator similar to the one used in the DELPHI detector [47]. This system has proven to be reliable even on a large scale [48].

Photocathode

Čerenkov photons are detected by a reflective photocathode made of a 500 nm thick layer of CsI on aluminum, activated by TMAE (tetrakis-dimethyl aminoethylen), a chemically highly active photosensitive substance. TMAE is added to the chamber gas by letting the gas flow through a cooled bubbler. Such a photocathode was recently [49] shown to be sensitive to photons with energies above 5.5 eV (Fig. 103).

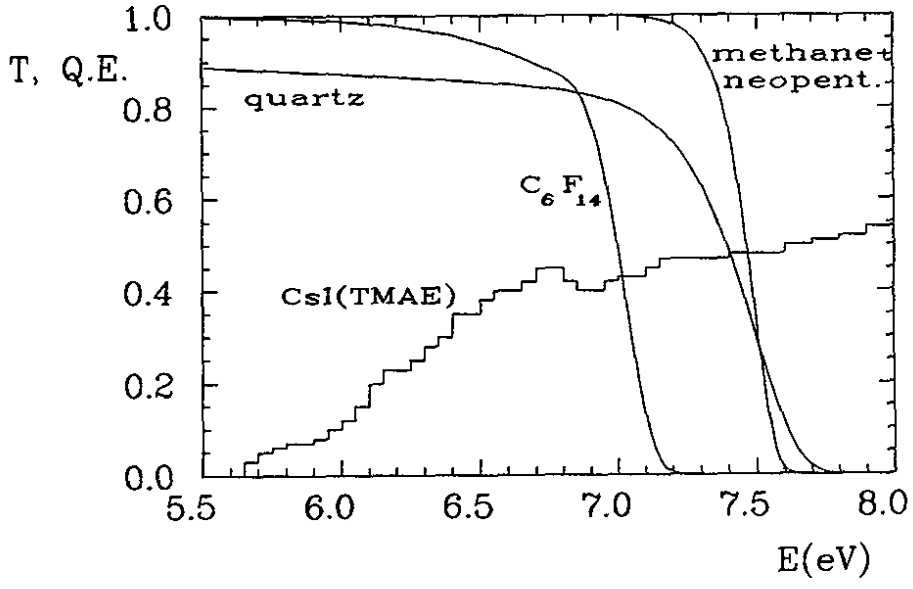

Figure 103: Quantum efficiency of a TMAE activated CsI photocathode vs. photon energy [49]. Also shown are transmission curves for C_6F_{14} (1 cm) [47], fused quartz (6 mm) [47] and a 90:10 methane-neopentane mixture (2 mm) [50].

Wire chamber

The photocathode is one of the two cathodes of a multiwire proportional chamber (MWPC) with a 3 mm thick fused quartz entrance window, 2 mm anode wire spacing and a 3 mm cathode to cathode distance. The photosensitive cathode is divided into CsI covered aluminum pads 7×7 mm^2 large. The other cathode, close to the quartz window, is made of 50 μm thick wires with a pitch of 2 mm. The anode wires are 10 μm thick. The chamber is filled with methane at room temperature. A small amount of neopentane is added to the chamber gas in order to absorb feedback photons from avalanches in methane (their energies being at 6.42, 7.48 and 7.94 eV). Neopentane is chosen as a quencher since its transmission characteristics [50] matches the spectrum of Čerenkov photons arriving from the radiator (Fig. 103), while it absorbs about 60% of methane feedback photons. Such a chamber can be operated at gas amplification factors of up to 10^6. Combined with low noise read-out electronics (ENC $\approx 1000\,e$) the single electron detection efficiency can be as high as 80% [51,52,53].

Space resolution

Three-dimensional information on the photon absorption is provided by reading out each of the 7×7 mm^2 large cathode pads separately. The pad dimension is larger than the width of the electric charge distribution induced by an avalanche on the cathode [54,52], so that on average only slightly more than one pad gives

a signal for a single photon. The pads are, on the other hand, small enough not to deteriorate the space resolution of the counter.

Drift space

For the gas in the drift space between radiator and MWPC we have chosen nitrogen.

Read-out electronics

The read-out electronics will be mounted on the back side of the MWPC. A low noise highly integrated system of the type designed and developed for the NaF-TEA RICH [33,52] seems to be a good solution. Pads are read out by a shift register technique at 50 MHz. Since this can be performed in parallel in several counter segments, the read-out time will be below 10 μs. To allow for pipelining each pad is equipped with a digital delay (shift register) of a few microseconds.

The amount of material of the RICH counter is summarized in Table VIII.

Table VIII: Thickness of materials in the RICH in units of radiation length X_0.

Layer	Thickness mm	X_0
Radiator		
C_6F_{14}	10	0.050
Quartz window	3	0.024
Support (Al)	2	0.022
Photon detector		
Quartz window	3	0.024
Chambers	3.5	0.020
Electronics (Si)	1	0.011
Cabling (Al)	1	0.011
Total		0.162

Comparison to other RICH types

Due to the relatively small dispersion of the FC72 liquid radiator, the measurement errors in combination with a TMEA activated CsI photo cathode are much smaller than in the alternative combination of a NaF radiator and TEA photon detector [33,55].

Compared to the TMEA gas photon detector of DELPHI [47] the present design has several advantages. Since only the cathode is photosensitive (the partial pressure of the TMAE gas in the MWPC is kept very low), the feedback photon problem is easier to handle. Moreover, the detector does not have to be heated to reach its full efficiency. Finally, the quantum efficiency is expected to be even slightly better than for TMAE in the gas phase.

5.3 Resolution of the RICH

Input parameters for the simulation

The properties of the counter were studied by computer simulation. A charged particle of velocity βc was tracked through the radiator. Čerenkov photons were generated by taking into account the variation of the refractive index $n(E)$ according to the relation $n = 1.2177 + 0.00928\,E$ [47]. Photon refraction and possible reflections at the boundary were handled by taking into account the energy and the polarization of the photon. The photon was then followed through the drift space. We have assumed contamination of the gas in the drift space with 20 ppm oxygen (as e.g. has been observed in the ARGUS drift chamber) and with 20 ppm water, and we have used the value of the photon absorption cross-section from [56,57]. The energy dependence of the quantum efficiency of TMAE activated CsI was taken from the measurement of *Seguinot et al.* [49]. The detection efficiency for single photo-electrons was assumed to be 80%. Finally, the position of the hit in the MWPC was found from the coordinate of the corresponding cathode pad. From the photon hit coordinate as measured by the photon detector MWPC and from the particle trajectory as given by the drift chamber the photon path was reconstructed to obtain the Čerenkov angle and thus the velocity of the particle.

Sources of errors

Sources of errors in the velocity determination from single photons were studied by comparing the generated and the reconstructed Čerenkov angle. The leading contributions are:

- The chromatic error, a consequence of the variation of the refractive index over the energy range of those Čerenkov photons that are seen by the photon detector.
- The parallax error, due to the limited information on the position of the emission point.
- The finite coordinate resolution of the photon detector.

While the chromatic error is a property of the material, the remaining errors depend on the geometry. The parallax error depends linearly on the radiator thickness, the absorption point coordinate error is linear in pad size, and both of them are inversely proportional to the length of the drift space.

Average number of detected photons

The dependence of the average number of detected photons on the angle of incidence of a charged particle with respect to the radiator plane is shown in Fig. 104 for a particle with $\beta = 1$. This functional dependence can be qualitatively understood in a simple picture. The index of refraction of C_6F_{14} is small enough ($n < \sqrt{2}$), so that the Čerenkov angle (38°) is smaller than the angle of total reflection (51°). As a consequence none of the Čerenkov photons, which are produced by a particle that enters the radiator perpendicularly (i.e. with angle of incidence $\theta_i = 0°$), is lost due to total reflection. The number of detected photons remains essentially constant (about 30) with rising angle of

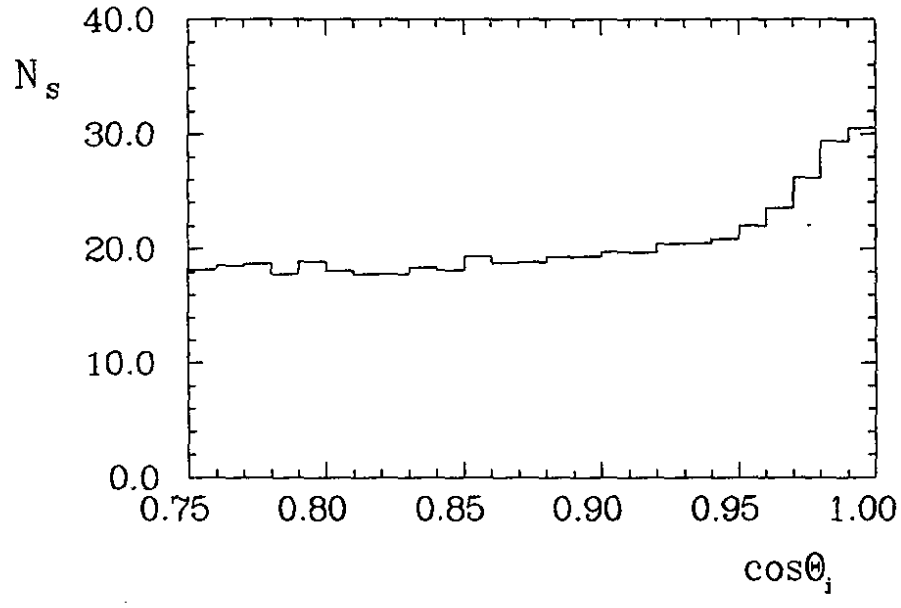

Figure 104: Average number of detected photons as a function of the angle of incidence of a charged particle with $\beta = 1$ hitting the radiator plane.

incidence until at $\theta_i > 10°$ part of the Čerenkov photons on the emission cone are lost by internal total reflection at the radiator surface. This cut into the cone produces at first a sharp drop in the number of detected photons which then levels out to a fairly constant value of about 20 for angles of incidence above 20°.

Performance

Since the average single photon resolution also improves if perpendicular incidence is approached, the overall performance of the counter is by far the best for charged particles that enter the radiator perpendicularly (Fig. 105). Fig. 106 demonstrates the PID ability in this case: A 3σ pion-kaon separation is possible up to 5.4 GeV/c. Electrons can be well resolved from pions and muons below 1.6 and 1.2 GeV/c, respectively. Even muons can be separated from pions below 1.0 GeV/c.

Error induced by particle track uncertainty

We note that there is an additional error in the velocity measurement which was not discussed above. It arises from the measurement of the particle trajectory as it leaves the tracking chamber. A rough estimate shows that for a drift chamber discussed in the previous section this error in the velocity measurement is of the order of $0.001\,c$ and is thus not negligible. We note, however, that this error is common to all detected photons of a single track. Due to the rather large number of detected photons it is possible to remove the uncertainty by including the track parameters into the fit of the Čerenkov angle.

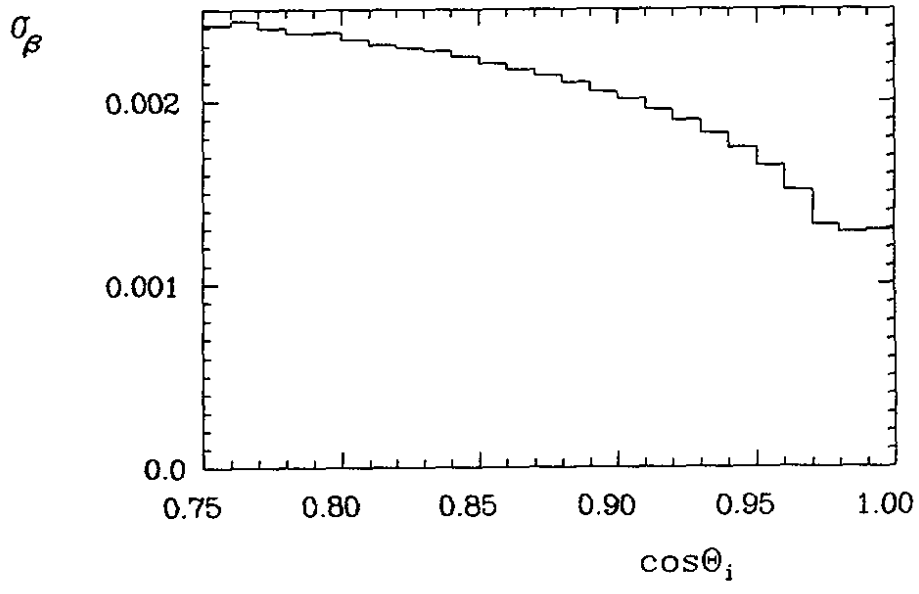

Figure 105: Velocity resolution as a function of the angle of incidence of the particle upon the radiator for charged particles with $\beta = 1$.

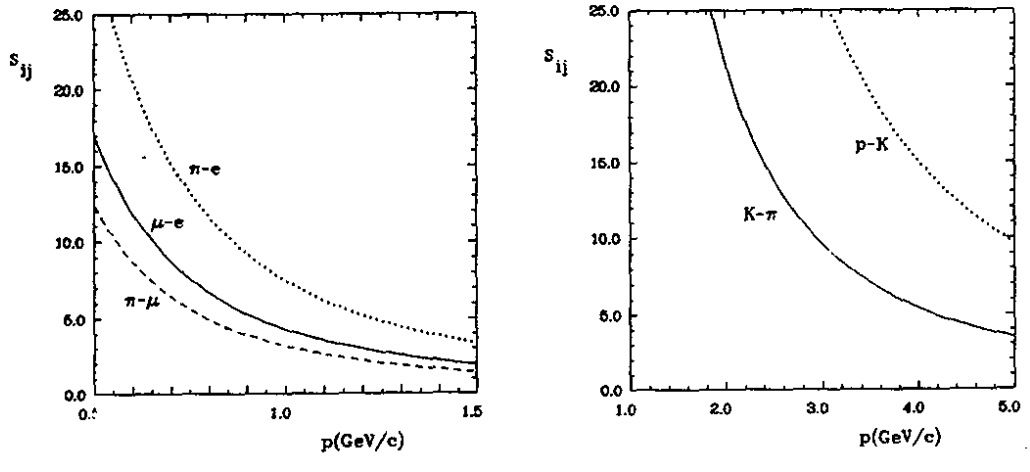

Figure 106: Expected particle separation, velocity difference in units of resolution $s_{ij} = |\beta_i - \beta_j|/\sigma_\beta$ for various pairs. Particles are assumed to enter the radiator perpendicularly.

5.4 Detector Geometry

Geometrical design

As already discussed in the introduction, the aim of the proposed RICH is to enable π/K separation up to the kinematical limit defined by the decay $B \rightarrow \pi\pi$. Since the center of mass system is moving, this limit depends on the direction of the decay particle. Specifically, in the forward direction ($\vartheta_\pi = 0°$), the maximal momentum is 4.76 GeV/c in the case of $\beta^*\gamma^* = 0.6$. The corresponding momenta in the backward direction and in the equatorial plane are 1.52 and 2.38 GeV/c, respectively. From Fig. 105 we conclude that in the forward direction a reliable identification is possible only if the counter is designed in such a way that charged particles enter it at angles of incidence below 10°.

There are additional reasons why one should aim for perpendicular incidence also in other parts of the detector. First of all, the large number of photons associated with normal incidence makes the counter less sensitive to possible backgrounds, and allows for a simultaneous fit of the track parameters. Moreover, in this case Čerenkov photons emitted in the quartz window get trapped in the quartz and do not contribute to the background in the photon detector.

Subdivision

Bearing in mind these arguments we have designed the counter in such a way that everywhere, except in the backward direction, particles enter the radiator at angles of incidence close to 0° . To achieve this, the radiator is divided into 15 sections of the polar angle, and each of the sections is further divided into 16 segments of the azimuthal angle (Figs. 74 and 75).

Mirrors

In order to allow all of the Čerenkov photons leaving the radiator to reach the photon detector we have to add a mirror to each of the radiator segments (Fig. 102). It is worth noting that this planar reflecting surface is slightly tilted with respect to the direction towards the interaction point. For tracks which pass the radiator close to the mirror plane this tilt helps to resolve the ambiguity as to whether the Čerenkov photon emitted in the radiator has arrived at the MWPC in a direct way or has been reflected. Mirrors are made with an $Al + MgF_2$ coating which has a reflection coefficient of about 90% [47] in the wavelength region of interest. The same type of mirrors has been used in the DELPHI experiment with the gas radiator system.

5.5 Background

Background effects

The spread in the Čerenkov angle of individual photons due to dispersion as well as uncertainties in emission point and charged particle direction transform into an uncertainty of the coordinate on the photon detector surface. This uncertainty is typically much larger than the pad dimension, the actual error of the position measurement. In order to collect all the candidate hits possibly

belonging to a particle track, a certain region of the photon detector surface A has to be scanned, taking this uncertainty into account. The number of background hits collected in addition to N_S signal hits becomes then $A \cdot \rho_B$, where ρ_B is the background hit density. Thus the background level in the signal region does not only depend on the background hit density ρ_B, but also on the geometry of the detector via the surface area A.

Throughout the study it was assumed that background hits are uniformly distributed over the photon detector surface. This assumption is at least locally valid in case of uncorrelated background (electronic noise, background events such as synchrotron radiation and beam-gas scattering on top of a true event). On the other hand, correlated background hits do occur due to Čerenkov photons from other charged tracks in the same event. These hits can, however, only be considered as background until the pattern recognition in the RICH (i.e. the assignment of hits to tracks) has been completed. As it will become clear at the end of this section, the estimated background levels are low enough so that the assumption of an uniform background is not critical.

It is worth noting that the results of the background study depend strongly on the refractive index of the radiator. In particular the conclusions would be much less favourable if the mean refractive index exceeded $\sqrt{2}$ so that the Čerenkov angle were larger than the angle of total reflection (as e.g. in the case of the NaF-TEA combination).

The performance of the RICH in the presence of background was studied by analysing simulated events. In addition to signal hits background hits were simulated for different uniform background densities ρ_B. The particle identification efficiency in the presence of background was calculated using the extended likelihood method [58]. Results from this study are summarized in Fig. 107. For the particularly interesting case of the π/K separation, we conclude that critical values of ρ_B start above 200 hits per square meter of detector surface corresponding to a 1% probability of a pad to have a background hit.

Simulation study

To determine the amount of background to be expected in the RICH photon detector during normal operation, a Monte Carlo study has been performed. Simulated were real events and the following sources of background:

(1) Čerenkov photons emitted by products of primary photon conversion in the material in front of the RICH radiator (drift chamber wall and RICH support structure) and in the radiator itself,

(2) Shower electrons backscattered from the calorimeter,

(3) Interactions of particles from beam-gas and beam-wall interactions,

(4) Electronic noise.

Levels of backgrounds (1) and (2) were estimated by a computer simulation. By using the EGS4 code (see 7.7) one learns that interaction products of a primary

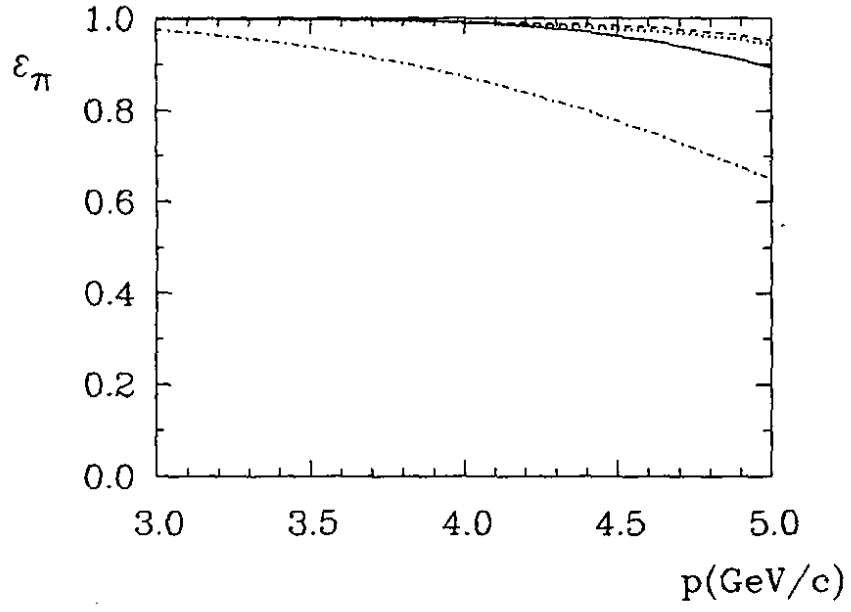

Figure 107: Pion identification efficiency in the presence of background, i.e. the fraction of real pions for which the analysis results in a kaon probability larger than 1%, for background densities ρ_B of 2000 (dash-dotted), 200 (solid), 20 (dotted) and 2 (dashed) m^{-2}.

photon shower produce in average 5 hits in the RICH MWPC, largely independent of the photon energy for photons between 0.05 and 5 GeV. Assuming a primary photon multiplicity of less than ten we arrive at a $\rho_B < 2$ m^{-2}. For primary electron showers a similar estimation, again using EGS4, yields $\rho_B < 2$ m^{-2}.

As far as source (3) is concerned, its intensity depends on details of the accelerator and interaction region design, and can at present be estimated only roughly. This type of background affects the performance of the main tracking chamber as well. Since 10 background tracks in the drift chamber are considered to be the limit that can be tolerated, we take this number and compute the corresponding background level in the RICH counter. In a simple model we have estimated the energy distribution of photons and electrons, corresponding to the background (3), and propagated it through the drift chamber gas into the RICH MWPC. Assuming that the hit information in the RICH is collected every 100 ns, we were able to relate the number of background tracks in the drift chamber to the number of hits in the RICH MWPC.

Background hit density

The results of the background studies are summarized in Table IX. Comparing these conservative estimates to the limit of $\rho_B = 200$ m^{-2} as deduced from

Table IX: Estimated background hit density ρ_B in the photon detector of the RICH	
Type of background	ρ_B m^{-2}/100 ns
Photon and electron showers in good events	4
Electronic noise	6
Charged particles from background events	<30
Total	<40

Fig. 107, we find that the background level is expected to be at least a factor of 5 smaller.

It is worth noting that there is yet another limitation for the allowed background level. The average read-out time depends linearly on the background hit density ρ_B [33] and amounts to 5 μs in case of 32 x 128 pad read-out sectors and ρ_B = 40 m^{-2}. A larger background level would either prolong the read-out time unacceptably, or smaller and consequently more sectors would have to be used.

5.6 Cost Estimate

Cost estimate

The estimated cost of the RICH counter is summarized in Table X.

Table X: RICH Cost Estimate.	
Item	MDM
Chambers (33 m^2)	3.30
Quartz windows (60 m^2)	1.80
Liquid radiator with cleaning system	1.00
Electronics (630000 pads)	6.30
Mechanical structure	0.50
Total	12.90

5.7 Particle Identification by a High Resolution Time of Flight Measurement: An Alternative to the RICH.

Time of flight measurement as an alternative to the RICH

The Ring Imaging Čerenkov Counter described above is a very promising solution. It employs, however, techniques for which the experience is growing, but is still limited. We therefore foresee an alternative in form of a novel time of flight (TOF) measurement, where the time resolution is improved by increasing the light output and by measuring the particle's TOF with four or eight clocks (instead of the conventional two). Averaging the flight times measured by n independent clocks, the timing uncertainty can be reduced approximately by a factor of $1/\sqrt{n}$. The particle separation power reached in this scheme will, as discussed below, be considerably inferior to what one expects from the RICH. It will, however, still allow to perform the main physics program described in this paper.

Improving the time Resolution

The particle separation power of any PID system based on a velocity measurement deteriorates with momentum as $\sigma(M^2) = p^2 \cdot \sigma(\beta^{-2})$, where p is the particle's momentum, β its velocity in units of the speed of light, and M^2 its rest mass squared as reconstructed from the measured velocity and momentum. In contrast to the RICH system discussed above, TOF systems do not measure a particle's velocity directly but only its flight time over track length l. Rewriting the above relation in terms of these quantities gives

$$\sigma(M^2) = 2 \cdot p^2/l^2 \cdot TOF \cdot \sigma(TOF).$$

Since TOF is proportional to l, one power of l is lost. Furthermore, the possible flight path length l is limited to a few meters in 4π-detectors operating at storage rings. The only remaining parameter to be improved is the time resolution σ(TOF). Typical resolutions achieved with operating detectors at e^+e^- machines, e.g. ARGUS and CLEO, reach from 220 to 150 ps. For the particle separation power required at HELENA one needs time resolutions of at least 100 ps.

Time resolutions of 50 ps and below can easily be achieved with small scintillator pieces; it is, however, difficult to reach this region with counters of several meters length. A TOF system for HELENA would therefore be highly segmented in order to have short counters and little light attenuation; in addition, the counter thickness would be chosen to match the phototube cathode diameter in order to maximize the light output, and to minimize light losses and velocity dispersion.

Further, equipping a single scintillator module with several phototubes (PMs) would enable one to average the individual times measured. Assuming each PM to perform independently of its partner tubes, one is able to reduce the timing error by a factor of $1/\sqrt{number\ of\ tubes}$. Test measurements [59] as well as

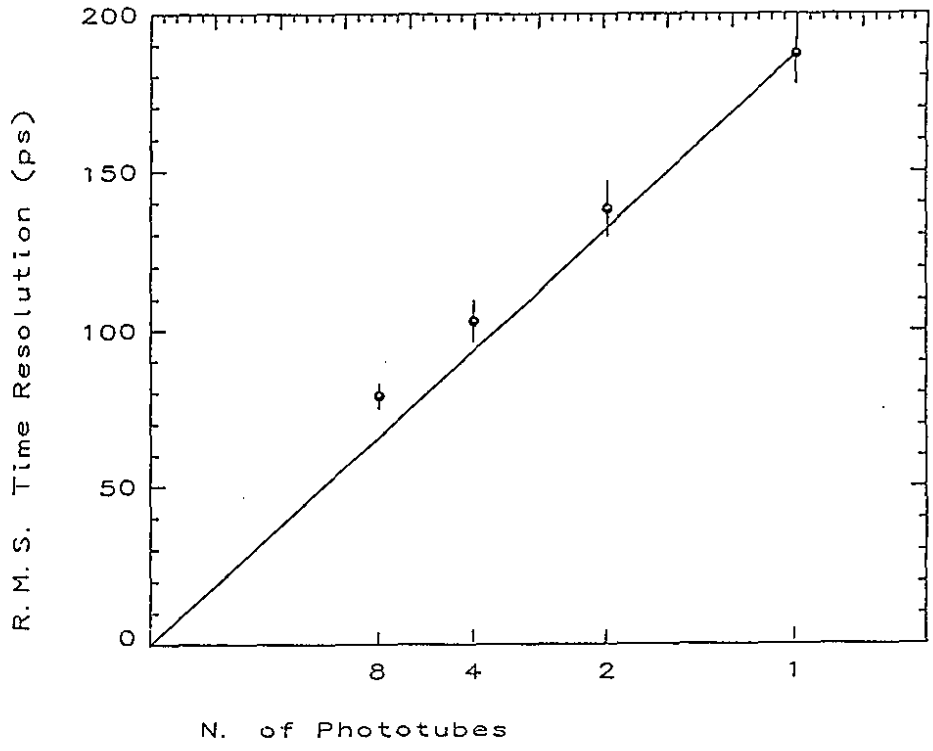

Figure 108: Time resolution as a function of the number of phototubes used for read-out (Monte Carlo simulation).

Monte Carlo simulations [60] demonstrate that this 'one-over-square-root' scaling law is in fact true to a very good approximation. Fig. 108 shows the result of a simulation for a counter of dimensions $60 \cdot 20 \cdot 5$ cm^3; the material was Pilot U, the tubes used for the simulation Hamamatsu R2490 with timing properties as described in the technical data sheet. The graph shows the variation of the counter's resolution when read out by one, two, four, and eight phototubes.

Finally, the resolution could be further improved by having two independent layers of counters.

Design of a high resolution TOF system

A possible design of a TOF system is sketched in Fig. 109. The principle idea is to have each track traversing at least two counters. To cover dead space where PM's are located, in total three layers of counters and phototubes are necessary, each layer containing four counters in $\cos\theta$. The individual counter thickness is 3 cm, the segmentation in azimuth is 32-fold. This leaves space for equipping the counters with 4, 6, 7 or 8 phototubes each, depending on its position in $\cos\theta$. The length of an individual counter module would be around 80 cm, its width varying between 12.5 and 35 cm. The phototube foreseen is Hamamatsu R2490-05. This is an upgrade of Hamamatsu R2490-01, a fine mesh proximity tube designed for operation in magnetic fields up to and beyond 1 T. A test of the timing behaviour of R2490-01 is described in [61]. The scintillator material could be either BI 408 or Pilot U. The tubes would be glued directly onto the counter surface, without any light guides. The number of tubes per counter could vary between four and eight, depending on the space available. The tube

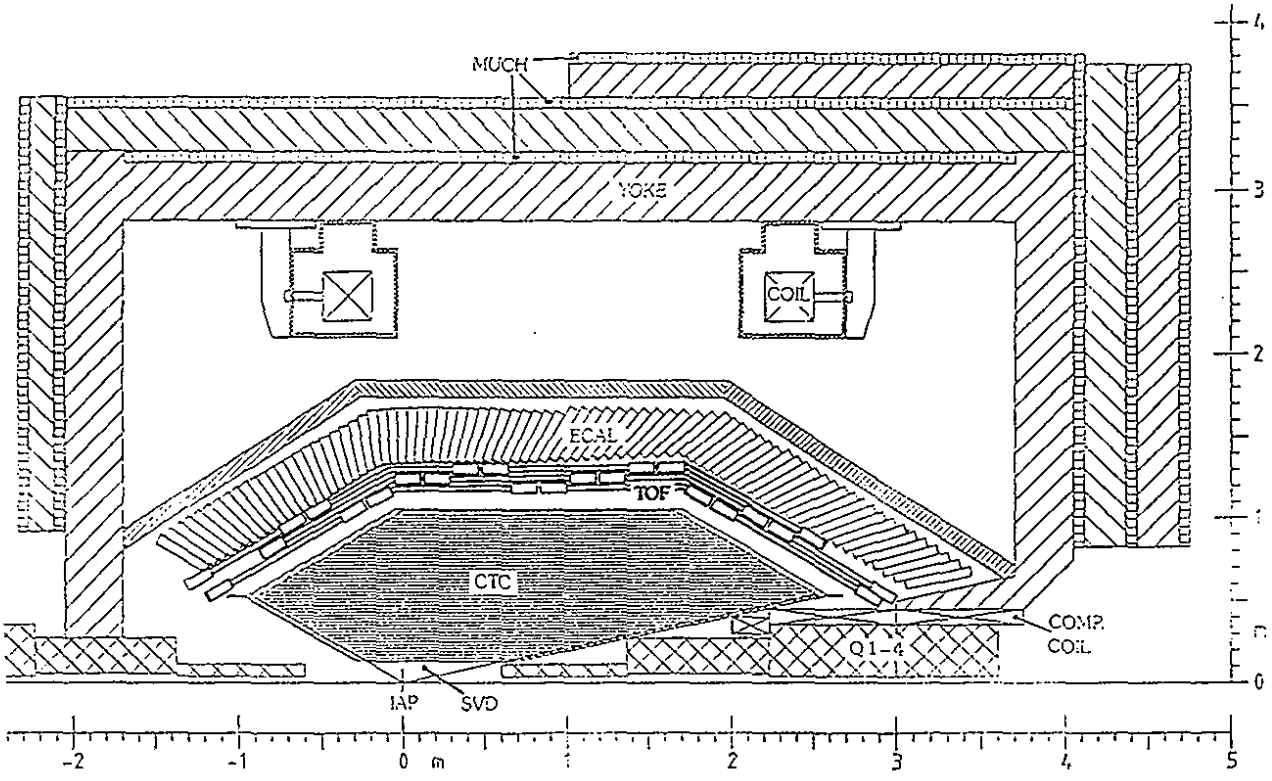

Figure 109: Design sketch of a TOF system for particle identification.

need not be perfectly aligned with the magnetic field; its performance should not deteriorate as long as the angle of inclination of its axis with respect to the field does not exceed 30 degrees. The use of several tubes per counter does not only improve the time resolution, but in addition improves the reliability and the spatial information available from the TOF counters; it finally helps in resolving ambiguities and double hits.

Particle separation capability

Using the scaling law mentioned above and extrapolating from existing measurements, one expects a nearly uniform time resolution of around 60 ps. Here one meets the influence of the finite lengths of the e^+ and e^- bunches which introduces an a priori uncertainty in the annihilation time of about 50 ps. This uncertainty could, however, be removed in an off line analysis taking into account TOF values and geometrical and kinematical parameters of all tracks measured in the event. Then the expected particle identification capability in terms of significance of separation is shown in Fig. 110. The separation power sketched above is considerably inferior to the design performance of a RICH. Especially the two-body B meson decays like e.g. $B \to \pi\pi$ and $B \to \rho\pi$ cannot be identified by the TOF system. On the other hand, the key reactions for the measurement of CP violation in B meson decays would be well accessible. A Monte Carlo study has shown that even with a resolution not worse than 100 ps the tagging of B mesons by well identified kaons is still possible, the loss of kaon tags being then only of the order of 10% .

Readout and use as a fast trigger

The time between bunch crossings (12 ns) is much smaller than the time needed for a trigger decision ($\sim$ 3 μs). Therefore all information on an event candidate

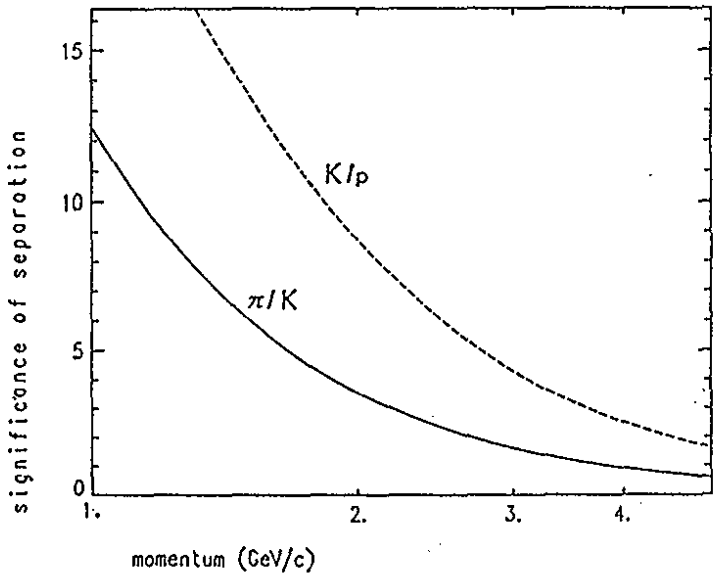

Figure 110: Expected particle separation with a multiple readout time-of-flight system

has to be stored in pipelines until the trigger decision is available. This excludes the use of conventional TDCs on the TOF counters. Instead, novel techniques have to be used, some of which are listed here:

- a high speed FADC system. While a 1 GHz clock for an FADC might be within reach, it does not seem realistic to think of higher speeds. Sampling the TOF phototube pulse in 1 ns steps, however, leaves the possibility to derive the particle impact time, with the resolution wanted, in a fitting procedure of the signal shape as a part of the offline analysis.
- an analogue pipeline (e.g. the SLAC AMU [62]);
- a pipelined high resolution TDC [63];
- a mixing of analogue and digital pipelines [64]; here, a medium speed FADC could be used in connection with a capacitor: charging starts after the pulse fires a discriminator, and is stopped by the FADC cycle. The charge is digitized and stored by the FADC. Assuming an 8 bit FADC resolution, the time resolution of this device equals the FADC cycle time divided by 256.

The techniques mentioned are still under development and have at present not yet reached the performance necessary in our case. But the progress is fast, and

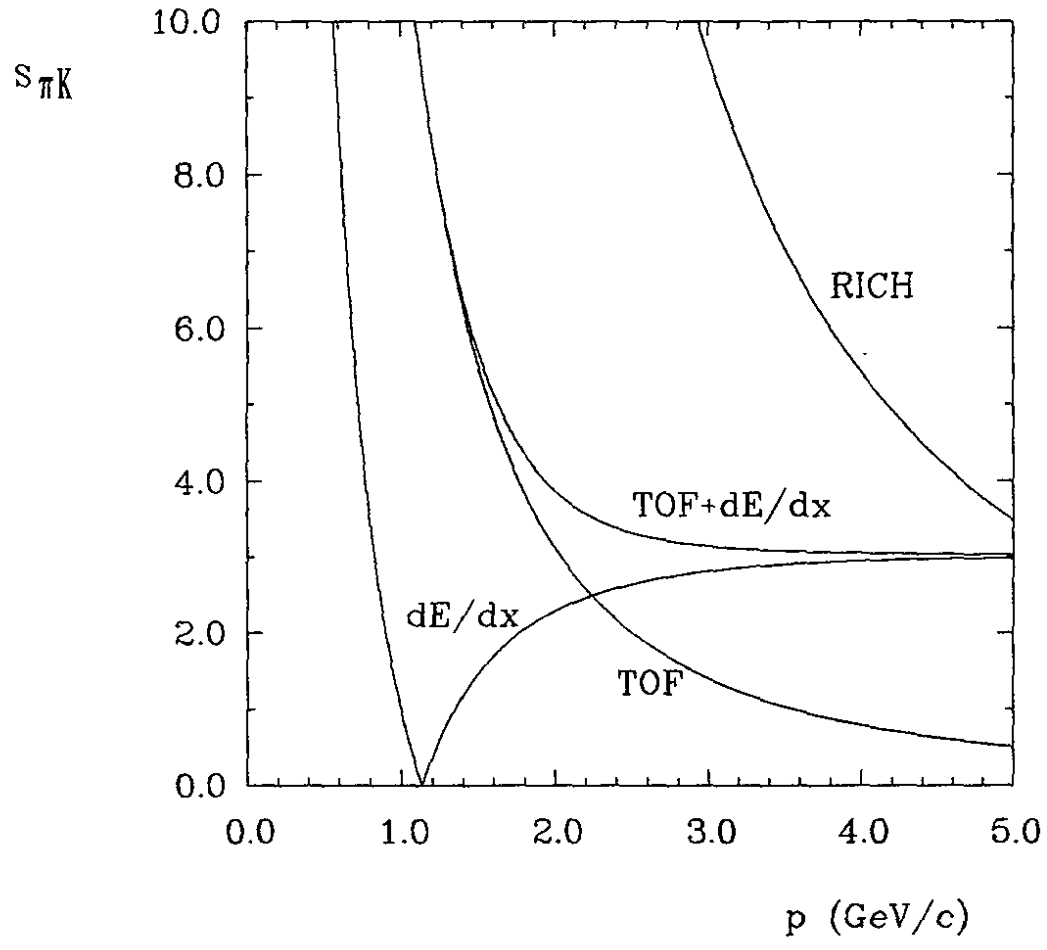

Figure 111: Expected π/K separation, velocity difference in units of resolution $s_{ij} = |\beta_i - \beta_j|/\sigma_\beta$, with the RICH or TOF, as described in this section, and by measuring the specific ionization in the central tracking chamber (see section 4.10.2).

it seems realistic that one of these methods will soon fulfill the requirements of a TOF readout system at a high luminosity B factory.

A TOF system as described here would at the same time serve as part of the fast trigger. The necessity of a scintillator based trigger device is discussed in chapter 6.

Summary

To summarize, the design of a TOF system with a time resolution of about 60 ps seems possible, and a readout scheme which matches this precision will most likely be available in the near future.

The separation of pions from kaons in both cases, with RICH or with TOF is summarized in Fig. 111. Also shown is the separation by combining the measurements of time-of-flight and dE/dx in the CTC.

6 The Trigger Scintillator System

6.1 Purpose and General Layout

Determination of reference time

The time between bunch crossings in the interaction region of HELENA is 12 ns. For each detected interaction one has to identify uniquely the bunch crossing in which the event occurred to provide the time reference t_0 for the event analysis. The precise knowledge of t_0 is mandatory, e.g. for drift time measurements in the CTC and the integration of signals from the ECAL. In addition, t_0 will be used to mark the time windows for transferring event specific information from pipelines into the event buffers.

Scintillation counter array

The time resolution of the device to be used for determining t_0 must be smaller than the time between bunch crossings, $\sigma_t < 12\,\text{ns}$. The technically most simple solution is the introduction of a scintillation counter array of the time-of-flight (TOF) type between RICH and ECAL, (see Fig.112).

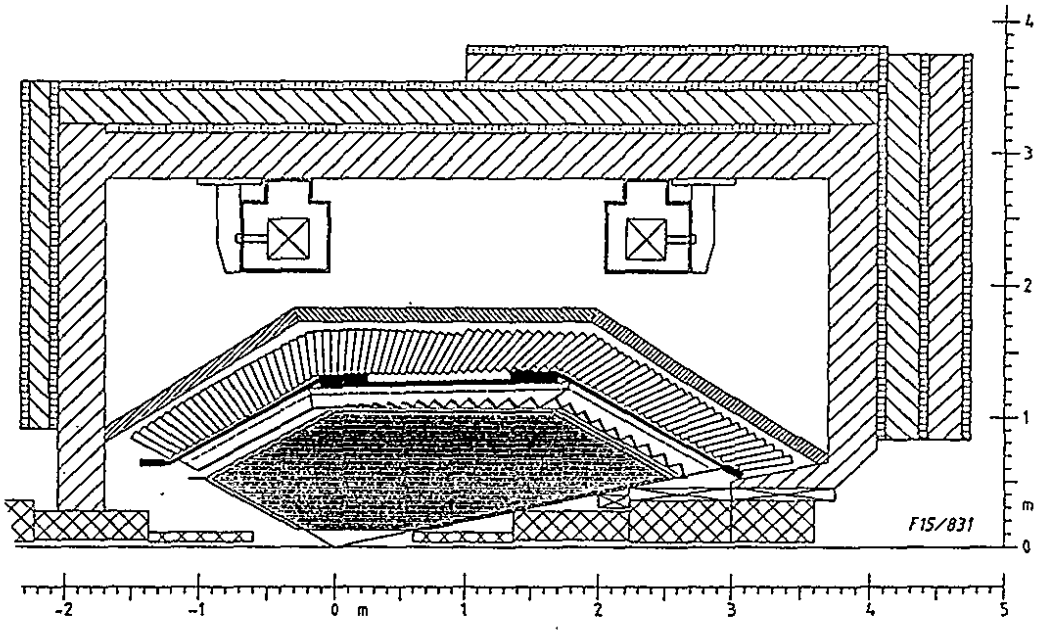

Figure 112: Arrangement of scintillation counters.

The information from such an array will also be valuable input for the first level trigger and will in addition procure trigger signals for testing the detector with cosmic radiation.

Timing requirements

The intrinsic time resolution of a simple trigger TOF system (TTS) will be of the order of 300 ps or even better, depending on the counter thickness and the choice of material. In order to be able to assign arrival times of scintillation

light at the PM's of the TOF modules uniquely to bunch crossing times, one must ensure that timing uncertainties due to different particle flight times and varying track impact points on the counters are well below 12 ns.

To match these timing requirements and to fit into the detector geometry, the TTS must be segmented in polar as well as azimuthal direction. The TTS should cover more than 90 % of the full solid angle in the centre-of-mass frame. The thickness of the counter modules is defined by the time resolution wanted, which in turn depends on the scintillation light output. The TTS discussed here is expected to give only a binary information on whether a hit occurred or not. Additionally, the readout of the TTS could be designed in a way as to deliver information on charged particles' flight times, adding a modest contribution to the detector's particle identification capability. The technical implications of this additional option are, however, not discussed here.

If the High Resolution Time of Flight Option, described in Section 5.7, will be chosen for particle identification instead of the RICH, it will also perform the functions of the TTS, which is obsolete then.

6.2 Segmentation and Time Resolution

Geometry

Segmentation of the TTS is done in a way that there are 3 counter modules in the polar angle interval $-0.87 < cos\,\theta < 0.98$ (see Fig.112) and 64 in azimuth. The counter lengths vary between 1.5 and 2 m, the widths between 6.9 and 12.8 cm. The thickness could be 2 cm, corresponding to 5% of a radiation length. The time resolution of such a counter array, with the scintillator material assumed to be Bicron BI 408 and each counter viewed by two photomultiplier tubes (PMs) is estimated to be around 200 ps rms. The phototubes are assumed to be Hamamatsu R2490-5, a recently developed tube based on the model R2490-1 which can be operated in a magnetic field as high as 1.5 T [61].

Time spread

The basic information element, input to the first level trigger, is the 'yes' from a single counter module, realized by the AND of its two PMs. Timing uncertainties of the order of several nanoseconds arise from particle flight time differences, and different track impact points on a counter module, making the scintillation light arrive at the PM photocathodes in a time interval depending on particle momentum and the counter size. With the above dimensions and an effective speed of light of 15 cm/ns inside the counter, the time spread due to scintillation light propagation is about 7 ns. The time spread due to different particle momenta above β of 0.8 amounts to 3 ns. Timing uncertainties arising from properties varying between individual modules have to be controlled by calibration.

Signal processing

There is one overall clock which is synchronized with the bunch crossing. The TTS modules have their own pipelines, data buffers filled by 'yes/no' information per bunch crossing. The stepsize of the TTS pipeline is defined by the time between bunch crossings which is 12 ns. This corresponds to a 83 MHz clock. The information from the TTS pipelines is read and used by the first level trigger.

7 The Electromagnetic Calorimeter

7.1 Physics Requirements

The wide range of research topics to be addressed at a B factory requires a universal detector which measures neutral and charged tracks with comparable precision. To fulfill this requirement, a state of the art electromagnetic calorimeter has to be designed.

Physics requirements

The main purpose of an electromagnetic calorimeter is to reconstruct decays $\pi^0 \to \gamma\,\gamma$. In average B decays, 5.5 charged particles and 5.0 photons [65,66] are produced. The complete reconstruction of a B meson thus requires the detection of photons at all energies and the measurement of their direction and energy with high precision.

From Monte Carlo studies of physics reactions one obtains the following desirable properties of the electromagnetic calorimeter:

- High detection efficiency ($\geq 80\,\%$):
  pointing geometry, large hadronic absorption length, little dead space.
- Good energy resolution ($< 5\,\%$ at 100 MeV) and low energy threshold ($\sim 30\,\mathrm{MeV}$) :
  large signal, low noise readout, little material in front of the calorimeter.
- Good spatial resolution ($\leq 1\,\mathrm{cm} \doteq 7\,\mathrm{mrad}$):
  extensive segmentation of the calorimeter and/or readout.
- Good double hit resolution ($\sim 10\,\mathrm{cm}$):
  high granularity, pointing geometry, large distance to the IP.
- Good electron/hadron separation down to $\sim 400\,\mathrm{MeV}$:
  good energy resolution, large hadronic absorption length, pointing geometry.

The importance of a low energy cutoff of the calorimeter is demonstrated in Fig. 113, where the average reconstruction efficiencies for individual π^0 mesons from B decays and for complete B mesons are plotted as a function of the photon energy cutoff. Cutoff values below 50 MeV are obviously very desirable for efficient B meson reconstruction.

7.2 Choice of Medium

Fully active medium

The requirements listed above imply a fully active medium which can either be

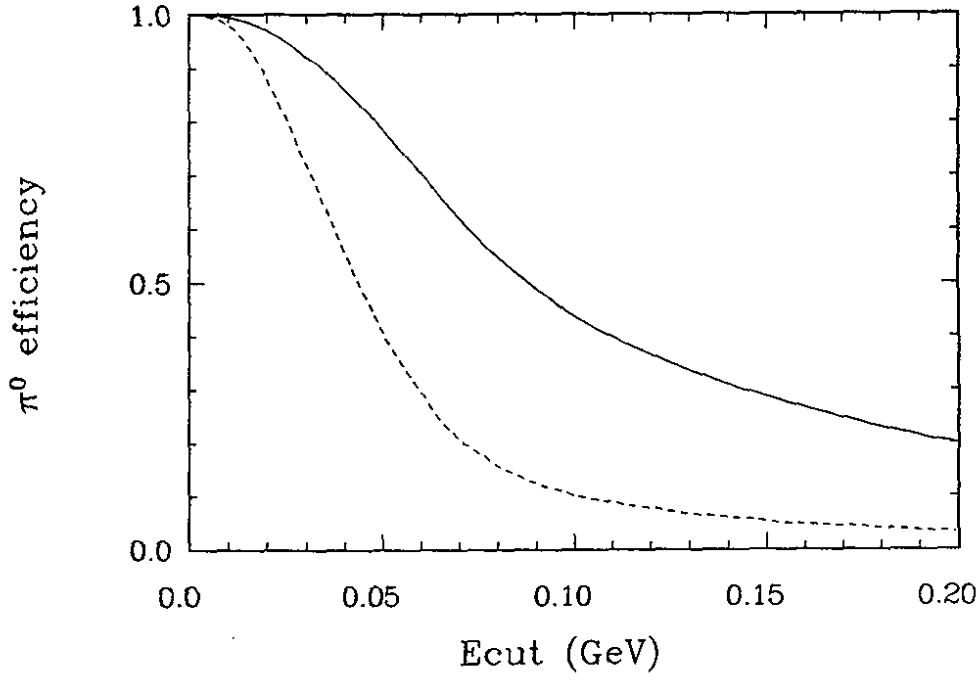

Figure 113: π^0 - (full line) and B meson reconstruction efficiency (dashed line) vs. photon energy threshold

a solid scintillator material or a noble liquid like Krypton or Xenon [67].

Scintillating liquids

Liquid calorimeters exhibit some quite attractive features. They can be segmented into small cells, thus measuring both the longitudinal and transversal shower development. These liquids are insensitive to radiation damage. The scintillation output of liquid Xenon is comparable to that of NaI(Tl) and the decay time is about 3 nsec [68]. Liquid Xenon has to be excluded, however, due to its price which is about one order of magnitude higher than what has to be paid *e.g.* for a CsI calorimeter [69]. The radiation length of liquid Krypton is 4.6 cm which requires a very large and expensive cryostat with an inner volume of 45 m^3. The results obtained so far with liquid Krypton detectors [70] are not superior to those obtained with crystal calorimeters. In addition, there exists no experience with large systems of this material up to now.

Solid scintillators

Among the many solid scintillator materials which are available, only scintillating glass and CsI(Tl) were considered [71]. All other materials like BGO, BaF_2, CsI, CsI(Na), CeF_3, NaI(Tl), GSO(Ce), and lead glass have been excluded for at least one of the following reasons:

- too expensive;
- not enough light-output per deposited energy;
- unfavorable mechanical properties;

- no experience with large systems.

However, it should be kept in mind that the SSC and LHC projects stimulated an enormous R&D effort in precision electromagnetic calorimetry. BaF_2 and liquid Xenon have been proposed as options [72]. Therefore the arguments made in this section have to be reviewed when the final decision on the B factory detector is taken.

Comparison of scintillating glass and CsI(Tl)

The relevant features of the scintillating glass HED-1 [73] and CsI(Tl) are listed in Table XI. The advantages of the glass are the short decay time, sufficient

Table XI: Properties of some scintillating materials.

	HED-1	**CsI(Tl)**	**BaF_2**	**LXe**
References	[73,74]	[75,76]	[72,77,33]	[68,69,72]
Density (g/cm^3)	3.44	4.51	4.89	3.05
Radiation length (cm)	4.12	1.86	2.05	2.77
Interaction length (cm)	43	37	30	55
Moliere radius (cm)	3.9	3.8	4.3	5.6
Critical energy (MeV)	22	10.2	12	10
dE/dx_{min} (MeV/cm)	5.2	5.6	6.6	3.9
Decay const. (nsec)	87±5	900	630/0.9	25/3
Temp. coeff. (%/ ^{0}C)	0.18	0.25	−0.6	–
λ_{peak}(nm)	435	550	320/210	–/170
Photoelec. / MeV	12.5±1.2	2500	–	–
Photons / MeV	330±42	$4.5 \cdot 10^4$	5000/1000	$2000/4 \cdot 10^4$
Price (DM/cm^3)	0.58	2.6	11	8 - 24
Rad. hardness (Gy)	6000	1000	10^5	large

radiation hardness and a low price /cm^3. However, the last point is partially compensated by the large radiation length as compared to CsI(Tl), resulting in a volume three times as large. The amount of scintillation light [74] is small compared to the light output of crystals which makes the readout by photomultipliers necessary. PM's with sufficient amplification in magnetic fields are very expensive [78]. For these reasons, the total price for a glass calorimeter including PM's will be about the same as for CsI(Tl) with silicon photodiode readout. In addition, a careful comparison of both materials reveals the superior quality of CsI(Tl). The performance of the CLEO II calorimeter based on CsI(Tl) crystals [79] is somewhat better than the expected performance of an ideal glass detector. According to the manufacturer [73], no substantial improvement in the light output of the HED-1 glass can be expected, whereas the following improvements have been reported for the crystal performance:

- The intrinsic resolution of CsI crystals doped with Thallium was limited in the past by a large variation of the Tl concentration along the longitudinal

axis of the crystal [75]. Meanwhile, the homogeneity of crystals has been improved by using the "Kyropoulos" method [76].

- The widespread use of PIN Si photodiodes triggered the development of types [78] having a larger sensitive area combined with a smaller capacity/cm^2. Together with the reduction in dark current, these new diodes show an improved signal to noise ratio.

CsI(Tl) crystals chosen

The above mentioned points justify the assumption that a CsI(Tl) calorimeter can be designed and constructed with a quality even superior to the existing CLEO II or Crystal Barrel calorimeters. Accordingly we propose an electromagnetic calorimeter for HELENA based on CsI(Tl) crystals.

7.3 Choice of Crystal Sizes, Support Structure

Length of crystals

The length of the crystals is determined by the amount of longitudinal leakage allowed at the maximum energies of electrons/photons to be measured with the calorimeter. Since electrons and positrons from Bhabha scattering are important for calibrating the calorimeter, a good resolution at their energy is important. Longitudinal leakage should be limited here to 2 %.

The maximum electron momentum and consequently the necessary length of the crystals are a function of the polar angle. The required length has been derived from a Monte Carlo simulation which will be described in more detail below. In the forward region the crystal length should be 39 cm $\hat{=}$ 21 rad. length and 33.5 cm $\hat{=}$ 18 rad. length in the backward hemisphere.

Arrangement of crystals

The arrangement of the crystals follows the inverse flie's eye principle, namely that the longitudinal axis of each crystal points to the IP (see section 1, Fig. 74). The proposed ellipsoidal shape avoids the barrel/endcap separation which is typical for many colliding beam detectors. Thus, the same performance is guaranteed for all polar angles.

Crystal shape

The granularity of the calorimeter is determined by the transverse dimensions of the crystals. The cross section at the front side has been chosen to be about 5 x 5 cm^2. The counters will be shaped like an obelisk with a trapezoidal longitudinal cross section. The obtained granularity is a compromise between the wish to optimize the spatial resolution and to minimize the dead space between the crystals and the cost for the readout. This choice has been verified in a Monte Carlo study. The results are presented in section 7.7.

Support structure

The support structure of the calorimeter will follow the concept of the L3 design [80]. The crystals are mounted in a honeycomb structure providing a separate compartment for each counter. Special care has been taken to guarantee that

the planes separating the crystals are slightly tilted (15 mrad) with respect to the direction to the main vertex. The honeycomb structure is connected to the iron support shell around the calorimeter and is stabilized by an inner cylinder made of 0.5 cm carbon fiber composite material. The walls between the crystals are made from the same material and have a thickness of 0.1 cm (0.4% of a radiation length) including the wrapping of the counters.

Number of crystals

The calorimeter is subdivided in 80 rings (see section 1, Fig. 74) with the number of crystals per ring varying between 75 and 173. The total number of crystals amounts to 11000.

7.4 Readout

Readout by Si-diodes

Recent tests of new CsI(Tl) crystals and new Si diodes have demonstrated that excellent energy resolutions can be obtained. Using a large crystal of 34 cm length [76] and the Si PIN diode S3204-3 [78], 9700 photoelectrons per MeV and a noise of about 100 keV were observed [81,82]. Both results are much better than the corresponding numbers of CLEO II or the Crystal Barrel (Table XII). Another appealing feature of Si photodiodes is their easy handling and their

Table XII: Results obtained with different CsI(Tl) detectors.

	CLEO II[79]	Crystal Barrel[83]	Test[81,82]
Crystal cross section	5 x 5 cm^2	$\sim$ 5 x 5 cm^2	4.5 x 4.5 cm^2
Crystal length	30 cm	30 cm	34 cm
Readout	4 diodes of 1cm^2	WLS + diode	1.8 x 1.8 cm^2
n_{pe} / MeV	2500	2300	9700
Noise (keV)	400	250	100

excellent long term stability. Encouraged by these results, we plan to use just one large area Si photodiode per crystal which will be followed by a low noise charge sensitive preamplifier. The noise contribution of the preamp should not exceed 400 e^- (rms) which corresponds to 80 keV using the assumptions of section 7.7. Following the preamp, a pole-zero circuit eliminates the long tail of the preamp pulse. Finally the pulses are shaped with a time constant of about 2 μsec.

Digitization

To digitize the pulses a flash ADC (FADC) system would be very attractive for the following reasons. At a beam crossing rate of 83 MHz, pileup from beam gas interactions might occur. If a signal is sampled in 50 time slices, such an overlap can be recognized. In addition, a pulse shape analysis of the signal might help to distinguish photons from energy depositions due to hadronic showers (split offs) [84]. However, for the time being, a FADC system operating at 25 MHz and with a dynamical range of 13-14 bits does not yet exist.

A more conventional solution foresees a 16 bit ADC using the dual-range technique. Sample and Hold circuits then have to buffer the analog pulses, because the long conversion time of the ADC's (about hundred μsec) might otherwise introduce deadtime.

Calorimeter and trigger

A calorimeter trigger is accomplished by summing neighbouring crystals into towers of 36 elements. The summed signals are shaped with a time constant of 0.5 μsec . If the signals of the individual crystals can not be digitized with FADC's, the signals of the trigger towers are analyzed with 10 bit FADC's, in order to compensate for the missing time information. At the $\Upsilon(4S)$, about 250 crystals will have an energy deposition above threshold. Based on this number, the calorimeter will contribute at most 2 kbyte to the event record including the FADC information of the trigger sums.

7.5 Calibration

Calibration monitoring

The precise intercalibration of the whole calorimeter and its time stability over long periods are essential to obtain the desired energy resolution. The error introduced by the calibration should be kept below 0.4%.

The absolute light output as well as the light collection along the crystal axis will be measured as a part of the acception test. The photodiode including the following electronic chain can be calibrated absolutely by measuring the photopeak of low energetic photons from a radioactive source [85]. The electronics itself can be monitored by injecting pulses of known charge into the preamplifier. With these numbers at hand, an absolute precalibration of the calorimeter at the level of 1% seems to be possible. The final calibration and the long term monitoring can be obtained from Bhabha events [86]. The observable Bhabha rate is about 300 Hz at a luminosity of $3 \cdot 10^{33}/\mathrm{cm}^2\mathrm{sec}$. Although the Bhabha events will be prescaled in the second level trigger, at least hundred hits per crystal and day will be recorded, allowing for an absolute calibration of all counters every week. The energy range can be extended by using radiative Bhabha events. The linearity of the calorimeter response is checked by reconstructing π^0's with one photon measured in the shower counters and the second one measured as converted photon in the CTC.

Temperature control

The calibration scheme presented here will not allow to correct for short term variations like temperature drifts. The temperature gradient of CsI(Tl) has been reported to be $2.5 \cdot 10^{-3}/^0\mathrm{C}$ at room temperature [82] which means that the temperature in the detector has to be stabilized within $\pm 0.5^0$ C. Short term fluctuations can be corrected by using a radioactive source calibration or a light pulser system. From our present experience [86] it seems to be very difficult to design a light pulser system with an intrinsic stability at the level of 0.1% due to the many components which are involved in such a system. Therefore

preference is given to a radioactive source calibration which has the additional advantage of providing a measurement at very low energies.

7.6 Radiation Damage

Radiation effects

Sufficient radiation hardness of the shower counters is very important to maintain the quality of performance. Radiation damage will result in reduced light output and nonlinear energy response which is very difficult if not impossible to correct for. In the literature CsI(Tl) has been reported to be very sensitive to radiation [87]. A substantial reduction in light output at a dose level of 1 Gy was observed. However, in the context of the PSI B factory study [33] a careful measurement has been performed [88] using small crystals ($\sim$ 1 cm^3) grown by different manufacturers. From this study it can be concluded that the radiation hardness is strongly effected by impurities. Using CsI powder of highest purity crystals were grown withstanding doses up to 1000 Gy without any deterioration. For comparison, a CsI(Tl) block hit by 1 MHz of minimum ionizing particles during 10^8 sec (= 10 "Snowmass years") accumulates a dose of 1000 Gy. Thus we do not expect any problems due to radiation damage with high purity CsI(Tl) crystals, provided that proper care is taken during the whole manufacturing process.

7.7 Expected Performance

Performance, simulation studies

In order to estimate the expected performance of the electromagnetic calorimeter and to examine the interaction with the adjacent detector components, a Monte Carlo simulation was performed using the EGS4 code [89]. In this study we concentrated on the most critical forward part of the calorimeter ($0.88 \leq \cos\vartheta \leq 0.975$). The material in front of the shower counters includes the drift chamber (6% of a radiation length), the RICH detector with C_6F_{14} radiator, quartz windows, MWPC and electronics (17%) and 5% for trigger counters and calorimeter support, summing up to a total of 28% of a radiation length at perpendicular impact. The magnetic field of the detector was taken into account in the region in front of the calorimeter which is essential for a correct estimation of the background. However, the magnetic field can be neglected for the tracking in the shower counters because its influence is negligible here.

Input parameters

A matrix of 15 x 15 crystals belonging to the innermost 15 rings was simulated (see section 1, Fig. 74). The material between the crystals amounts to 0.1 cm of carbon fiber material. Photons and electrons were generated in an energy interval of 0.02 - 5 GeV and 0.1 - 10 GeV, respectively. For simplicity, the

carbon fiber walls pointed to the main vertex. The particles were generated off origin to simulate the tilt of the walls.

A readout noise level of 200 keV/crystal and a light output of 5000 photoelectrons/MeV have been assumed (Table XII). In addition, a readout threshold of 0.2 MeV per crystal (= 1 ADC channel) has been applied. The MC events were analyzed using a simple cluster algorithm. Due to shower fluctuations or interaction in the material some crystals above threshold can be separated from the main cluster which reduces its visible energy and therefore deteriorates the energy resolution. In addition, the separated crystals can fake photons if their energy is large enough.

Further effects which influence the performance of the calorimeter and which have been taken into account in the simulation study are discussed one by one in the following paragraphs.

Intrinsic resolution of the crystal

It is known since many years that the response of crystals is not exactly proportional to the energy of the incoming particle. This is due to the fact that the scintillation efficiency depends on the specific energy loss. At high ionization densities (protons, alphas), recombination effects occur which can be described by Birks law [90]. At small dE/dx (electrons), the scintillation efficiency is rising with the specific energy loss. This effect can be easily observed by measuring the CsI(Tl) response with γ sources of different energies [82]. However, we do not expect that this effect contributes much at higher energies. Therefore it has been neglected in the present study.

Nonuniform light collection

The uniformity of crystals has been improved during the last years. The manufacturing techniques have been modified resulting in a very stable Thallium concentration along the whole crystal [76]. Furthermore, variations in the light collection can be corrected for by a careful surface treatment reducing nonuniformities along the crystal to 1%, leading to a negligible effect on the energy resolution. For comparison, the CsI(Tl) blocks of the Crystal Barrel experiment show nonuniformities of up to 5% [83].

Electronic noise

The effect of electronic noise of the readout on the energy resolution increases with the number of crystals contributing to a cluster. The cluster size is approximately proportional to $\sqrt{E}$. Assuming a noise level of 0.2 MeV per block, the contribution to the energy resolution is $\sigma_E/E \approx 0.001/E^{0.75}$.

Backscattering and longitudinal leakage

Photons of 50 MeV lose about 1% of their energy by backscattering. The loss at 1 GeV is below 0.4%. The energy deposition as a function of the length of the crystals is shown in Fig. 114. To obtain less than 2% leakage, the length of the crystals has been fixed to 39 cm in the forward hemisphere (see Fig. 115).

Calibration

The intercalibration error has been taken into account by adding 0.4% to the energy resolution (see sect. 7.5).

Support structure effects

The energy loss in the honeycomb structure which is the same for incident electrons and photons, is proportional to the thickness of the material and

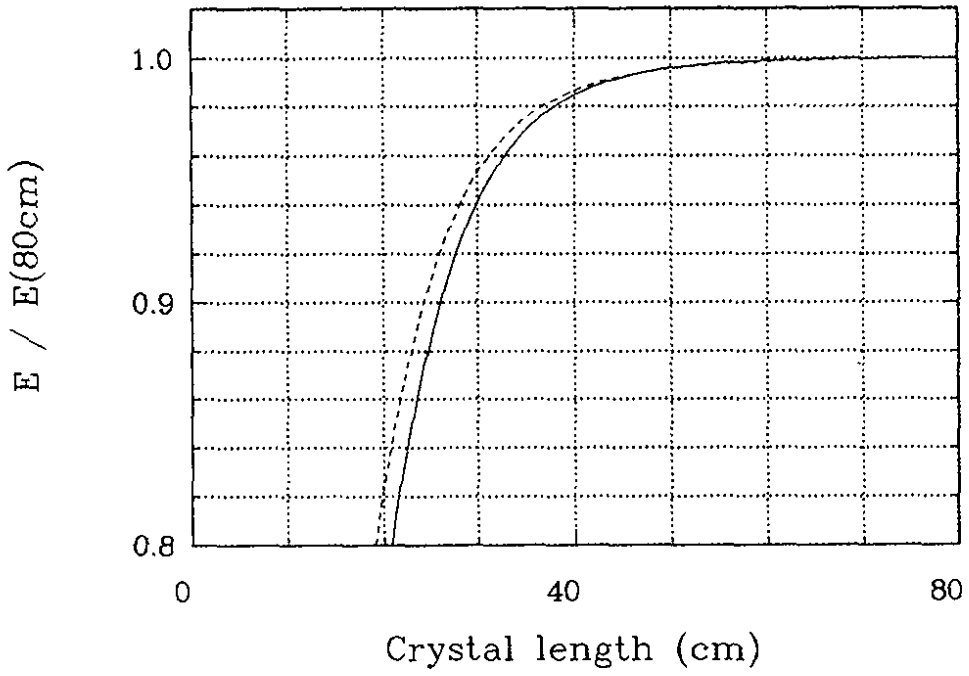

Figure 114: Deposited energy, normalized at 80 cm, as a function of the crystal length for 10 GeV e^- (full line), 5 GeV e^- (dashed line) and 5 GeV γ (dotted line which is almost identical to the full line).

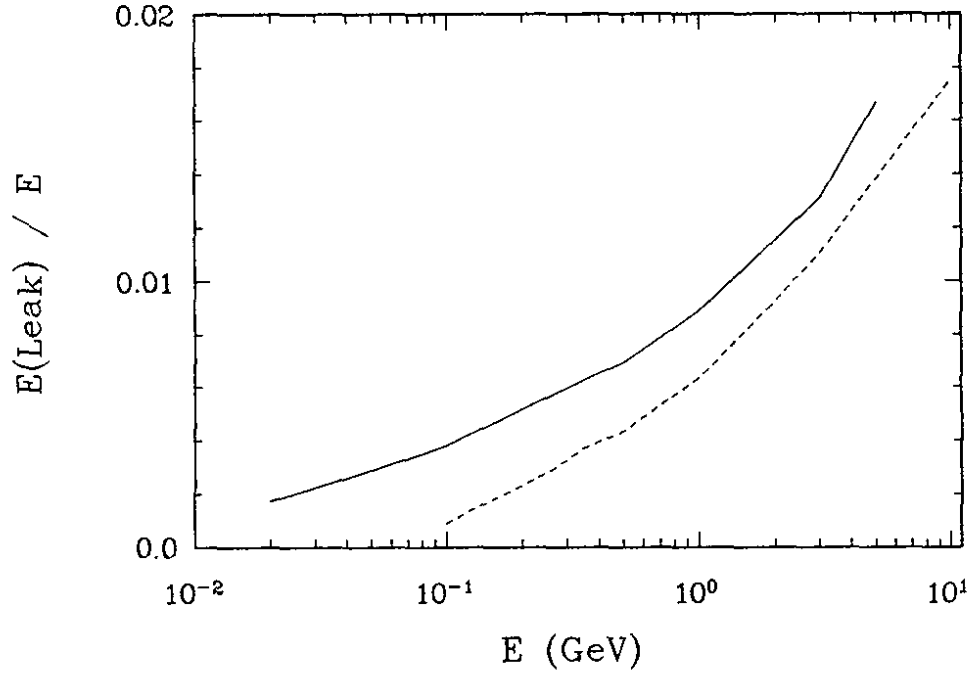

Figure 115: Relative energy loss due to longitudinal leakage for incident photons (full line) and electrons (dashed line) for crystals of 39 cm length.

shows almost no energy dependence. Both electrons and photons lose about 1.3% of their energy. The particles have to pass the trigger counters and the support structure in front of the crystals where electrons deposit about 20 MeV and photons at most 10 MeV.

Effects of materials in front of the calorimeter

Photons from B decays have to pass 32% of a radiation length on average. This material has a severe influence, and it should be tried to reduce it in the final design. 20 - 30% of all photons convert before entering the calorimeter. However, in most cases the products of conversion of photons with energies above 250 MeV form one cluster in the crystals. Using the additional information made available by the RICH and the scintillation counters it will be possible to distinguish these overlaps from accidental overlaps of two photons and to correct for the energy loss in the material.

Backscattering

In addition to extra $e^{\pm}$ tracks and photons produced by showering particles in the CTC endplates and the radiator of the RICH detector, many low energetic electrons and photons are backscattered from the calorimeter which increases the background in the RICH detector. In Fig. 116 the number of additional $e^{\pm}$

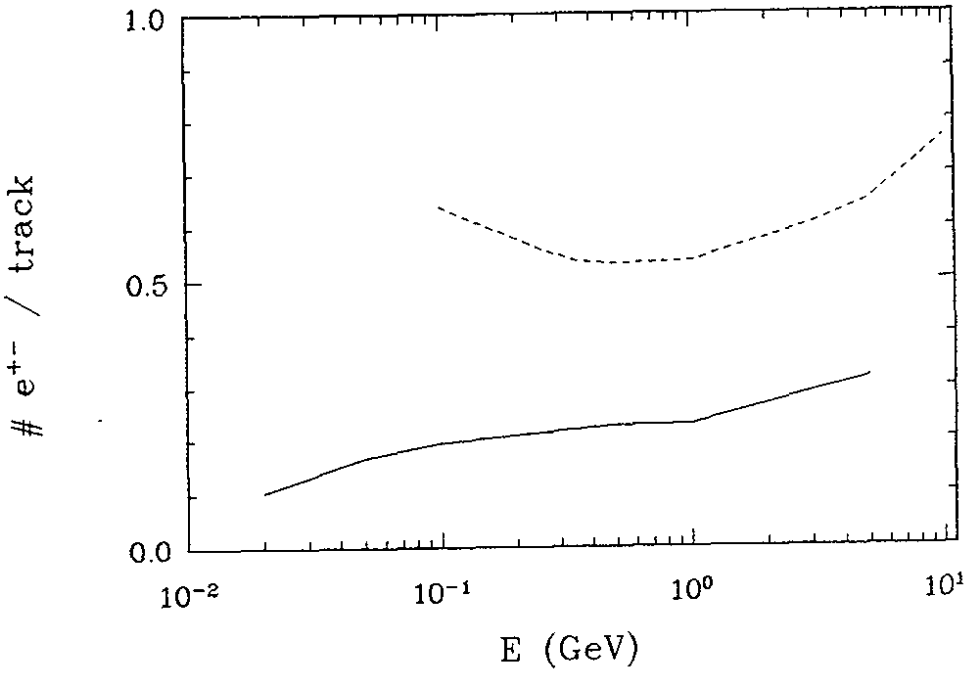

Figure 116: Number of additional $e^{\pm}$ passing the RICH detector per incident photon (full line) or electron (dashed line).

tracks due to these effects is plotted. Only electrons passing through the radiator contribute to the background in the RICH, whereas photons have no effect if they do not interact in the radiator or in the MWPC. Using this information,

the number of background hits in the RICH detector and in the calorimeter can be estimated.

Energy loss

The amount of energy which the incident particles lose due to interactions in the detector components in front of the calorimeter can be derived from Fig. 117 where the average fraction of visible energy is plotted. These losses can be corrected for in the offline analysis, but they deteriorate the energy resolution. As an example, the visible energy distribution for 100 MeV photons is shown in Fig. 118. The spectrum can be described by a Gaussian plus an exponential tail. However, the interaction in the material in front of the crystals results in an almost flat tail down to very low energies. This tail strongly decreases at higher energies, because the energy loss is roughly constant. To get an estimate for the background in the calorimeter, Fig. 119 shows the energy spectrum of photons produced in connection with primary 1 GeV photons. Most of these additional photons have such small opening angles with respect to the primary particle that they do not show up as extra clusters. However, some clusters with an energy above 10 MeV are left which can fake photons (Fig. 120).

Energy resolution

Due to the different components contributing to the energy resolution, no simple algorithm is available which takes into account the energy dependence of each contribution. Therefore the energy resolution is described by an empirical function fitted to the results of the MC simulation. The resolution quoted here is derived from FWHM/2.35. To describe the tails quantitatively, the fraction of particles measured with an energy within $3\,\sigma$ of the peak value is given. The energy resolution expected for photons is parametrized (Fig. 121) by

Photons

$$\frac{\sigma_E}{E} = \sqrt{0.004^2 + \left(\frac{0.012}{E^{0.25}}\right)^2}$$

where 65% of all photons at 20 MeV are measured with this accuracy and 80% at 5 GeV. The rest is contained in the low energy tail. The above energy dependence indicates that neither the photoelectron statistics ($\sim E^{-0.5}$) nor the electronic noise ($\sim E^{-0.75}$) are the limiting factors. The resolution for electrons is worse for energies below 1 GeV due to bremsstrahlung in the material in front of the crystals

Electrons

$$\frac{\sigma_E}{E} = \sqrt{0.007^2 + \left(\frac{0.01}{E^{0.67}}\right)^2}; \quad 0.2\ \text{GeV} \leq E \leq 1\ \text{GeV}.$$

About 80% of the electrons are measured with this precision. At energies above 1 GeV electrons are measured with slightly better precision compared to photons, because they have less longitudinal leakage.

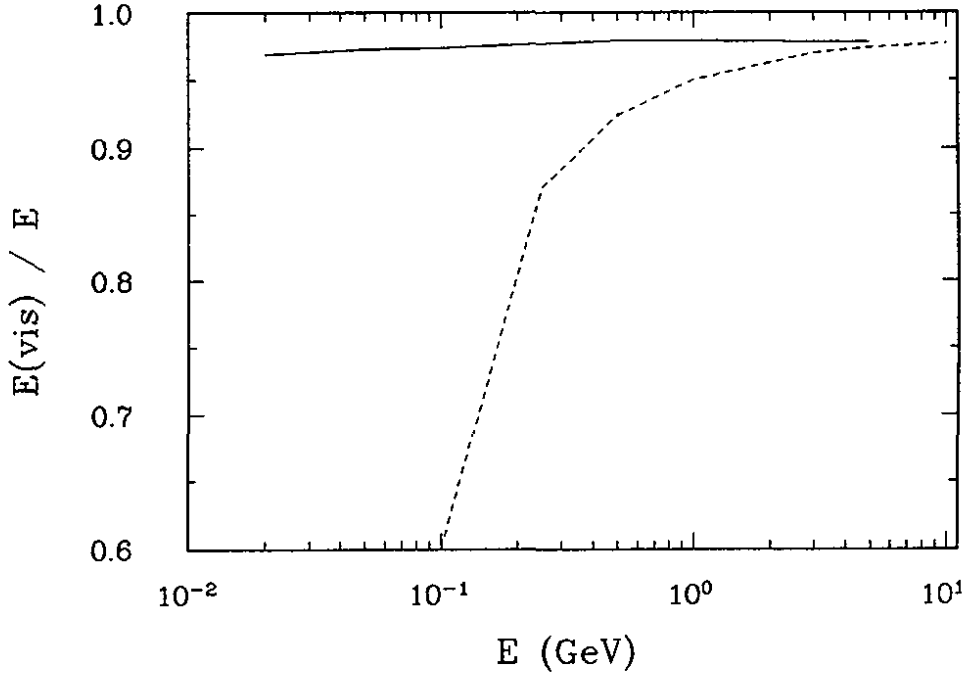

Figure 117: Fraction of visible energy (peak value) for photons (full line) and electrons (dashed line).

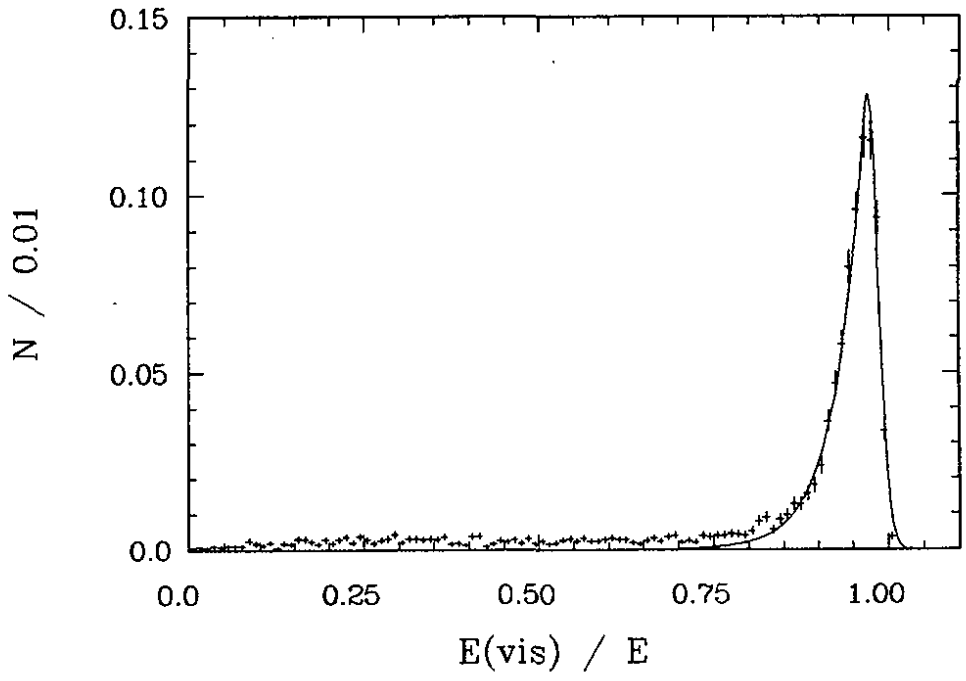

Figure 118: Spectrum of 100 MeV photons. A Gaussian plus an exponential (full curve) has been used to determine the width.

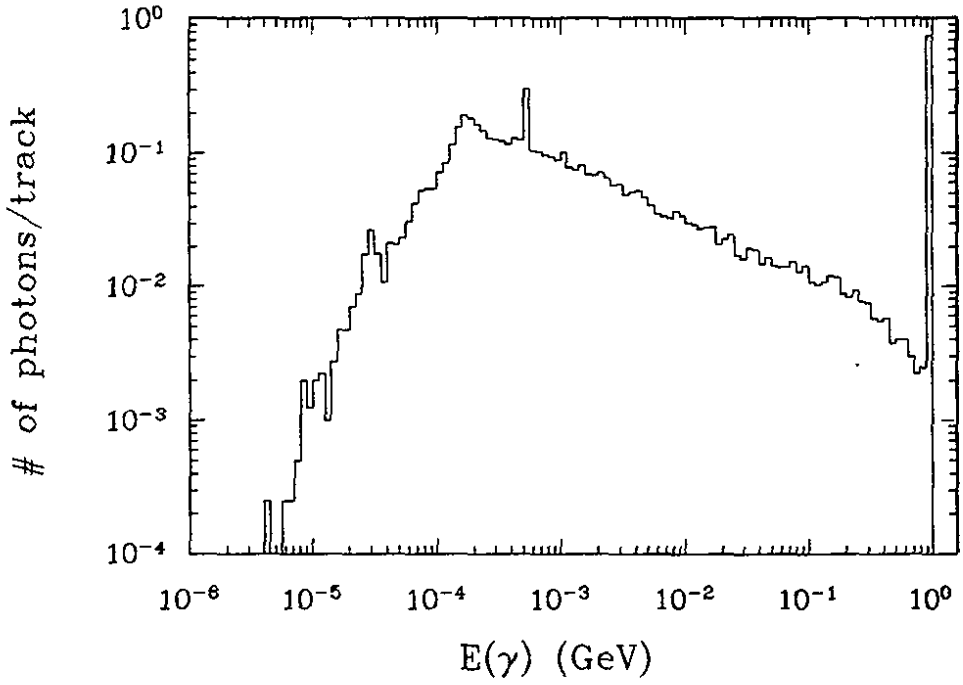

Figure 119: Energy spectrum of photons hitting the calorimeter for incident photons of 1 GeV.

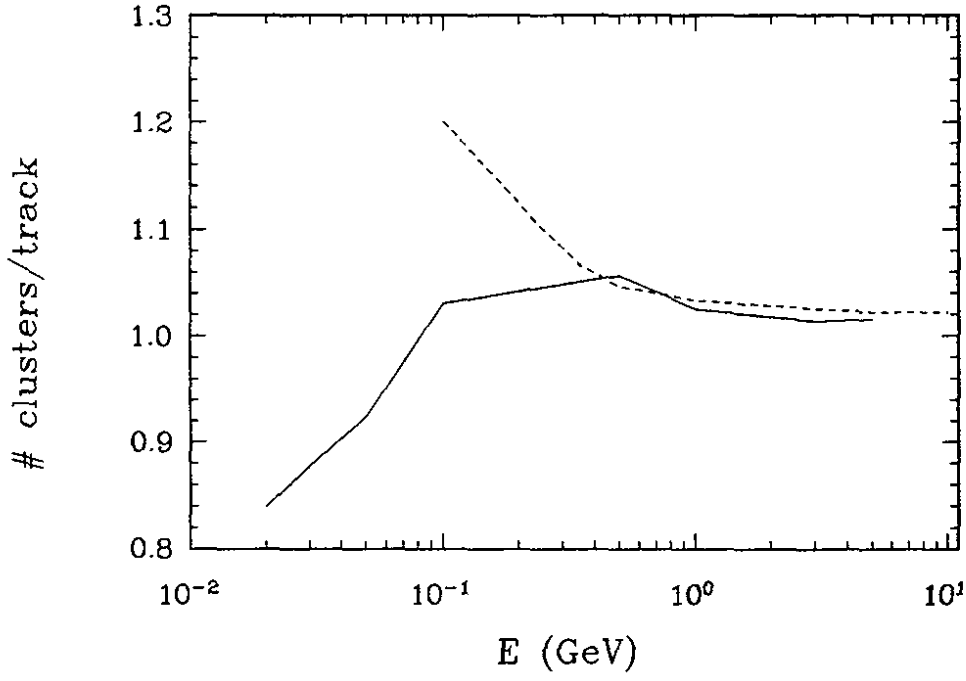

Figure 120: Number of reconstructed clusters with E > 0.01 GeV per incident photon (full line) or electron (dashed line).

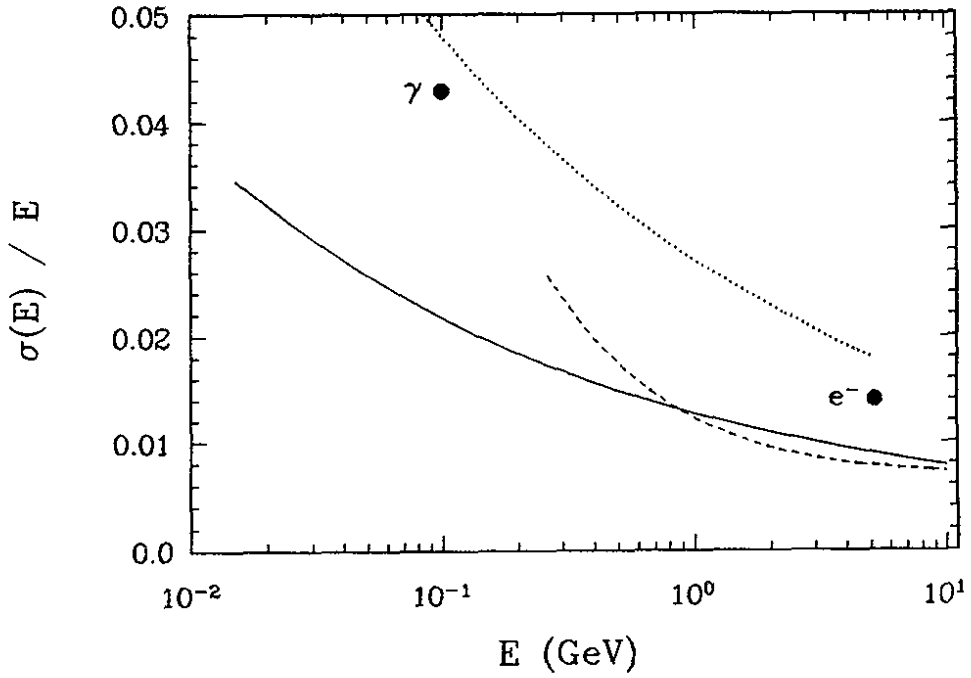

Figure 121: Energy resolution for photons (full line) and electrons (dashed line). Results of CLEO II [79] (full points) and Crystal Ball [92] (dotted line) are included for comparison.

Angular resolution

In ref. [74], a parametrization of the position resolution is given. Adopting this for our calorimeter, we obtain the following expression

$$\sigma_x[\mathrm{cm}] = \frac{\mathrm{D}/\sqrt{12}}{\sqrt{7\mathrm{E}+1}}$$

with D being the crystal width. The angular resolution is $\sigma_\varphi = \sigma_x/\mathrm{R}$ and $\sigma_\vartheta = \sigma_x/\mathrm{L} = \sigma_x \cdot \sin\vartheta/\mathrm{R}$. L is the distance between the impact point of the photon and the interaction point; R is the radial distance to the beam line. In the barrel region of the calorimeter we obtain

$$\sigma_\varphi = \frac{10\mathrm{mrad}}{\sqrt{7\mathrm{E}+1}} \quad \text{and} \quad \sigma_\vartheta = \frac{10\mathrm{mrad}}{\sqrt{7\mathrm{E}+1}} \cdot \sin\vartheta \ .$$

Mass resolution of π^0

The influence of the granularity and of the angular resolution will be demonstrated with three examples. First, the mass resolution of reconstructed π^0's is considered. Fig. 122 shows the mass resolution as a function of the π^0 momentum. According to the expression

$$\frac{\sigma_\mathrm{m}}{\mathrm{m}_{\pi^0}} = \frac{1}{2} \cdot \left(\left(\frac{\sigma_{\cos\alpha}}{1-\cos\alpha} \right)^2 + \left(\frac{\sigma_{\mathrm{E}_1}}{\mathrm{E}_1} \right)^2 + \left(\frac{\sigma_{\mathrm{E}_2}}{\mathrm{E}_2} \right)^2 \right)^{\frac{1}{2}}$$

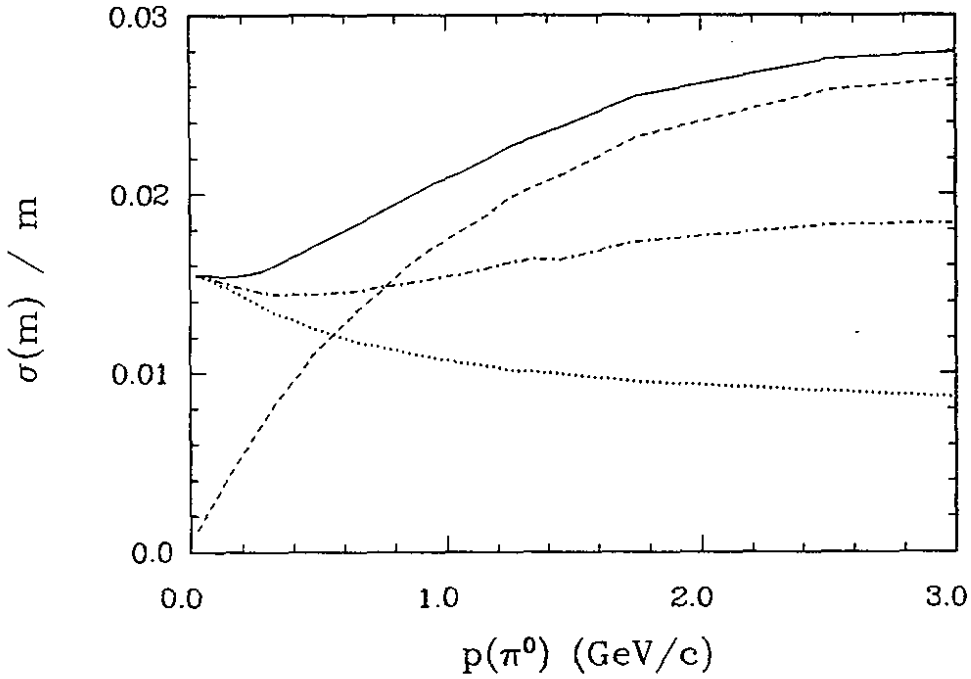

Figure 122: Mass resolution versus momentum for reconstructed π^0's (full line) with separate contributions from energy resolution (dotted line) and angular resolution (dashed line). The expected mass resolution of crystals with D=3 cm is included as a dashed-dotted line.

the mass resolution is dominated by the error on the opening angle α at large momentum. To obtain a flat (momentum independent) mass resolution, the crystal cross section would have to be reduced to 3 x 3 cm^2 (see Fig. 122), which, on the other hand, would increase the dead space, and the number of crystals would go up by almost a factor of three.

Monochromatic photons

The second example refers to the measurement of monochromatic photons which are produced in radiative Υ decays or decays of excited B mesons $B^* \rightarrow B\gamma$. In an asymmetric B factory, these photons are not monochromatic in the laboratory system. Transforming them into the cm system, energy and angular resolution determine the width of the energy distribution. Thus it has to be checked that the excellent energy resolution is not deteriorated. A Monte Carlo simulation of the decay $B^* \rightarrow B\gamma$ confirmed that the accuracy of the direction measurement is sufficient. The relative energy resolution of 52 MeV photons is 2.54% according to the above mentioned formula. The resolution is slightly better in the lab system (2.48%) due to the boost. Transforming the reconstructed photon in the B^* system results in a minimal degradation to 2.52% which is negligible.

π^0/γ separation

Third, the π^0/γ separation will be discussed. For high energetic π^0's the energy depositions of both photons merge into one cluster. To distinguish these clusters

from single photons of the same energy, the distance x between both impact points must be at least three times the crystal size D: $x = \alpha \cdot L \geq 3 \cdot D$ where L denotes the distance to the interaction point. Since the minimum opening angle of a π^0 is $\alpha = 2m_\pi/E_\pi$, D is 5 cm for a π^0 of the maximum possible energy from B decays in the asymmetric collider. This simple calculation was substantiated by a Monte Carlo study. The energy deposition of 4.5 GeV π^0's (α = 60 mrad) emitted in the forward region has been analyzed using a cluster algorithm which is based on neural networks [91]. For all events it was possible to reconstruct two separate photon clusters. In average, the energies assigned to these two clusters were 98.2% and 95.7% of the nominal photon energies. This demonstrates that the granularity chosen allows to distinguish single photons from π^0's over the whole momentum range.

7.8 Cost Estimate

The price of the electromagnetic calorimeter is determined by the total volume of the crystals and the number of readout channels. Given a volume of 13 m^3, the cost for the crystals amounts to 34 MDM. The price for the readout chain has been estimated to be 400 DM per channel including the Si diode, amplifiers, and ADC. Assuming a price for the honeycomb structure of 1.5 MDM, we end up with a total price of 40 MDM for the calorimeter.

As a summary, the most important features of the proposed calorimeter are collected in the following Table XIII.

Table XIII: Cost estimate of the proposed electromagnetic calorimeter

material	CsI(Tl)
size of crystals	$\sim$ 5x5x(33.5 - 39) cm^3
readout	1 PIN photodiode of $\sim$ 4 cm^2
volume	13 m^3
# of crystals	11000 arranged in 80 rings
signal	> 5000 photoelectrons / MeV
noise	< 200 keV / crystal
photon energy resolution	2.6% at 50 MeV, 1.3% at 1 GeV
π^0 mass resolution	1.5 - 2.8%
total cost	40 MDM

8 Muon Identification

Muon identification

Muon tracks are detected and their momenta are measured in the main drift chamber. They are distinguished from kaons and protons by the RICH system and by dE/dx measurements in the main drift chamber. In order to distinguish them from pions two methods will be used, depending on the momentum of the particle.

$p < 1\ GeV/c$

For momenta below 1 GeV/c, the separation of muons and pions is achieved by the RICH system. The separation is $3\,\sigma$ at 1.0 GeV/c and $4\,\sigma$ at 0.9 GeV/c.

$p > 1\ GeV/c$

For momenta above 1 GeV/c the separation of muons from pions is achieved by exploiting their ability to penetrate matter without interaction other than ionization. The existing CsI calorimeter, its iron support, and the magnet yoke are used as hadron filter. The design of the muon detection system is mainly dictated by background considerations.

Backgrounds

The main backgrounds to muon identification by range measurements are the following ones [33]:

- Punch-through of noninteracting pions is indistinguishable from muons. Its rate falls off roughly as $\exp\left(-\frac{d}{\lambda_I}\right)$ where λ_I is the nuclear interaction length in the filter [93]. This behavior calls for a thick absorber which, however, has to be weighed against an increased momentum cut-off for real muons due to their finite range. Fig. 123 shows punch-through probability and cut-off momentum vs. absorber thickness.
- Shower leakage also falls off exponentially but not as fast as punch-through. This background can largely be eliminated by extrapolating the muon trajectory through the absorber using at least two planes of the muon detection chambers and checking whether position and direction of the track is consistent with being a primary muon.
- π, K decays: The probability for a pion to decay into muon and neutrino within a cylindrical radius of 1.3 m is $2.3\%/p_T$ (p_T in GeV/c) and for a kaon $11\%/p_T$. Kaons are less critical, however, since their decays within the driftchamber are more readily detected by observing a kink and/or a change in curvature of the track. Kaons decaying behind the RICH were already identified. For pions passing the RICH there is strong competition between decay and nuclear interaction, depending on the distribution of absorbing materials along the track. Pions decaying here can be recognized by determining the momentum of the decay muon which is lower than that of the parent pion measured in the CTC.

Both shower leakage and pion decay background can be strongly reduced by a rough momentum measurement of the track in the absorber. This requires either to use a finely segmented range telescope or to detect the bending of

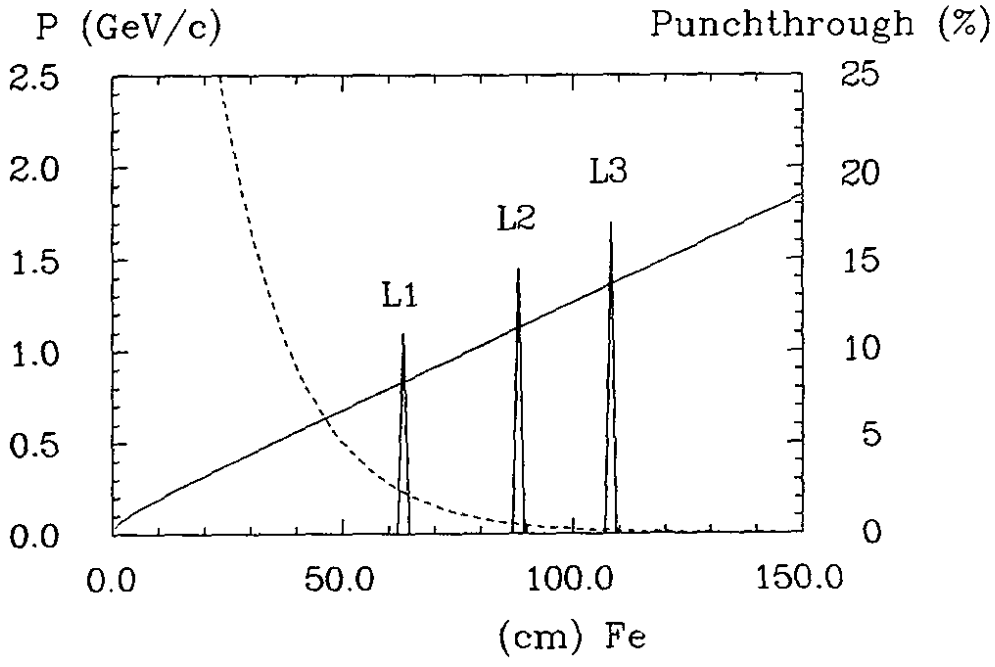

Figure 123: Pion punch-through probability (dashed line, right scale) and muon cutoff momentum (solid line, left scale) vs. iron absorber thickness. L1, L2 and L3 mark the position of muon detection chambers in the proposed design (the CsI calorimeter has been set equivalent to 17 cm of iron).

charged particles in the magnetic field outside the CTC. Considering the huge area that would have to be covered by muon detection chambers in the range telescope approach, we prefer the latter technique.

8.1 Design of the Hadron Filter

Design of the hadron absorber

Our design of the hadron filter is shown in Fig. 124. The CsI calorimeter provides one nuclear interaction length (= 1.0 λ_I). It is directly surrounded by a layer of 10 cm nonmagnetic iron (= 0.6 λ_I) in order to further reduce the number of pions that otherwise may decay in the free space between calorimeter and magnet yoke, giving rise to fake muons. The gap of ca. 100 cm between calorimeter and magnet yoke, containing almost the full magnetic field, helps in separating low momentum secondary particles from primary muons in the subsequent muon detector. The iron return yoke is 35 cm thick and corresponds to 2.1 λ_I at normal incidence. The total thickness of absorbing material until here (= 3.7 λ_I) corresponds to a muon cutoff momentum of 0.9 GeV/c and a nominal pion punch-through probability of 2.5% at normal incidence. Here the

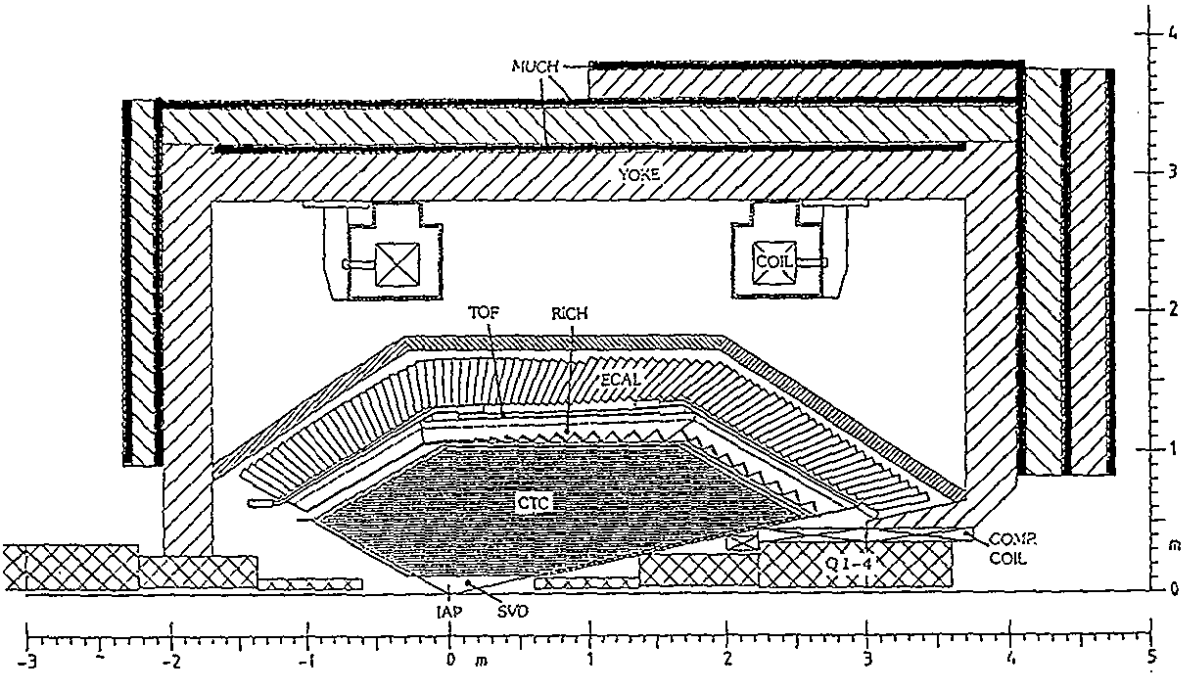

Figure 124: Arrangement of muon detection chambers.

first layer of muon detection chambers is positioned. Together with a second, and in forward direction, a third layer with additional iron absorbers, it measures position and angle of penetrating particles. If these parameters fit to the parameters measured in the CTC, the particle is identified as a muon.

Solid angle, momentum cutoff

The muon detection system covers 95% of 4π. The geometrical arrangement of muon chambers and iron (see Fig.124) takes into account the effect of the Lorentz boost with high momentum particles produced predominantly in the forward direction and low momenta in the backward hemisphere. The respective muon cutoff momenta as function of the lab polar angle are plotted in Fig. 125. For comparison, CMS momenta of 1.0, 1.5, and 2.0 GeV/c boosted into the lab system with ($\beta\gamma = 0.6$), are also shown.

Fake rate

Estimates of the probability of fake muons reconstructed in this detector have been obtained by a Monte Carlo simulation and by scaling experimental results from the ARGUS detector to the new geometry. The ARGUS collaboration obtained experimentally a probability to misidentify a pion as a muon of 1 – 2% for momenta between 1 and 3.5 GeV/c [94] with a total absorber thickness of 5.1 λ_I . In the same momentum band we expect a fake rate of less than 1% .

8.2 The Muon Chambers

Proportional tubes

The muon chambers (MUCH) have to cover a large area with a good efficiency and a moderate spatial accuracy of track detection. This can be economically

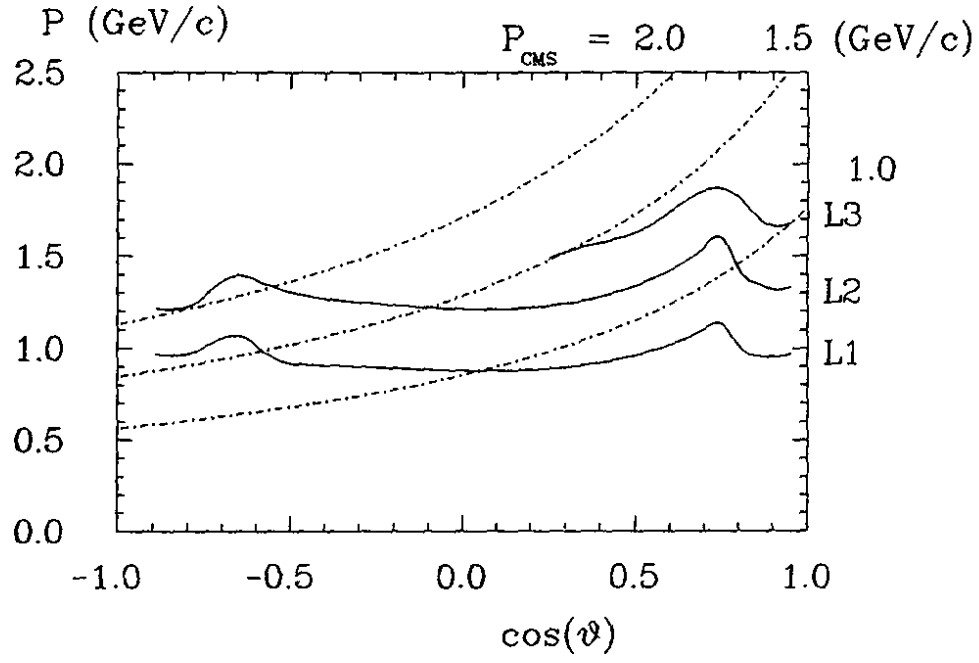

Figure 125: Muon cutoff momentum vs. $\cos\vartheta$ for the three muon chamber layers $L_{1,2,3}$ (solid lines). Dash–dotted lines show p_{lab} vs. $\cos\vartheta$ for constant p_{cms} = 1.0, 1.5, 2.0 GeV/c.

accomplished with proportional tubes or with limited streamer tubes. Since simple proportional tubes, used in the ARGUS detector, have shown excellent reliability during 10 years of operation, we prefer this type of detection system.

Modules

The basic unit consists of a double layer of 16 stainless steel tubes of 30 mm diameter staggered by half the width (see Fig. 126). The length of the tubes depends on the position of the module and varies from 2.7 to 3 m. In total 560 m^2 have to be covered with muon chambers, corresponding to 35 km of tubes.

Spatial resolution

The spatial resolution perpendicular to the wire direction is given by the tube diameter and the layer staggering, and is 15 mm. The coordinate along the wire is obtained by measuring the difference of arrival times of the signals at opposite ends of the tube. The coordinate is proportional to the measured time difference. The coefficient for the conversion of the time difference to a coordinate is 6.7 ps/mm. With electronic channels, each consisting of two amplifier/discriminator combinations, connected to the ends of a tube, plus a time stretcher and a TDC module, resolutions between 23 and 33 mm along the wire have been obtained [95]. This compares well with the average radius of 56 mm for the spot of intersection of a muon of 2 GeV/c with the first plane of muon chambers due to multiple scattering in the preceding material.

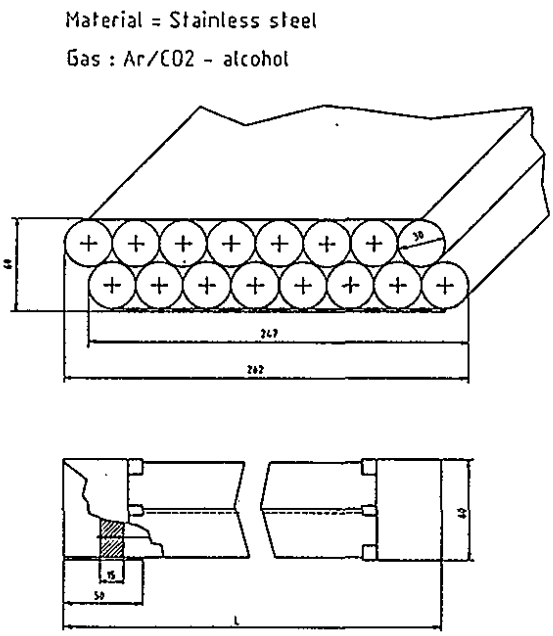

Figure 126: Design of a muon chamber module.

Chaining tubes

The above method allows a better ultimate resolution to be obtained than the charge division technique [96]. It is also more economic since only one "analog to digital" converter is necessary for a tube instead of two. Further savings can be obtained by connecting several tubes to a chain and using only one set of electronics at the ends of the chain, since in the muon detection system the particle flux is small.

9 Trigger, Rates and Data Acquisition

9.1 General Considerations

Boundary conditions

The trigger system of a B-factory detector has to handle very high luminosities at large bunch crossing frequencies. In order not to limit the development potential of the machine we want to assume in this chapter that a luminosity of $L = 10^{34}\ cm^{-2}s^{-1}$ with a bunch crossing frequency of 83 MHz or even twice that may ultimately be reached. These conditions are certainly very different and much more demanding than for current e^+e^- experiments with one to two orders of magnitude less luminosity and bunch crossing frequencies around 1 MHz or less.

However, the conditions of a B-factory are also not so unusual: the requirements lie somewhere between HERA with about 10 MHz bunch crossing frequencies and LHC/SSC with similar luminosities and bunch crossing frequencies. Compared to LHC/SSC a B-factory has the advantage that the event probability per bunch crossing is orders of magnitude lower. We will certainly profit from ongoing research and development for hadron machines [97]. However, our trigger and data acquisition system outlined below can be built from electronic components available today.

A trigger has the task to efficiently recognize good physics events and sufficiently suppress background while keeping the deadtime low. Therefore we first discuss the event topologies we want to trigger on and the features of the backgrounds we want to reject before we turn to the description of a trigger and data acquisition system.

9.2 Event Topologies and Rates

Physics processes

In the energy range of the proposed machine the events are either one-photon or two-photon reactions:

$$e^+e^- \rightarrow q\bar{q} \rightarrow hadrons \tag{71}$$
$$e^+e^- \rightarrow l^+l^- \qquad (l = e, \mu, \tau) \tag{72}$$
$$e^+e^- \rightarrow \gamma\gamma \tag{73}$$
$$e^+e^- \rightarrow e^+e^- + hadrons \tag{74}$$
$$e^+e^- \rightarrow e^+e^- + l^+l^- \qquad (l = e, \mu, \tau) \tag{75}$$

Multihadron events

The first reaction covers quark pair production in the continuum as well as

hadronic decays of the Υ resonances, in particular $\Upsilon(4S)$ production with subsequent decay into $B\overline{B}$ pairs. All these processes lead to multihadronic final states, and most of them have many charged and neutral particles which can hardly be missed by the trigger. No attempt will be made to select $B\overline{B}$ events on the trigger level.

QED events

The QED processes

$$e^+e^- \rightarrow e^+e^-,\ \mu^+\mu^-,\ \gamma\gamma$$

can be identified by their two- or zero-track topology together with a large energy deposition in the calorimeter or hits in the muon chambers. They are useful as monitor reactions to measure the luminosity, and to calibrate detector efficiencies and resolutions. However, the rate of Bhabha scattering will be so large that it has to be prescaled. In the Υ energy region with a luminosity of $L = 10^{34}\ cm^{-2}s^{-1}$ the Bhabha rate will be about 1000 Hz. Prescaling of this rate requires a clean recognition of Bhabha scattering at the trigger level. About 10 to 20% of the QED events radiate a sufficiently hard photon to make these events more difficult to recognize as QED events.

The remaining QED process, $\tau^+\tau^-$ production, is an important topic in the physics program of the B-factory. The τ leptons decay dominantly into one or three charged particles plus any number of neutrals. Due to the undetected neutrinos the events are in general not momentum balanced. Particularly difficult to trigger on is the 1-1 topology (e.g. $\tau^+ \rightarrow \pi^+\overline{\nu}_\tau$, $\tau^- \rightarrow \pi^-\nu_\tau$).

Two-photon reactions

In the two-photon reactions (74) and (75), the scattered e^+ and e^- usually disappear in the beam pipe. Low multiplicity and low particle energies and momenta are characteristic of the remaining final state. With respect to the trigger two-photon annihilation events are similar to τ pairs, since both require low multiplicity triggers which may be troubled by the backgrounds. For the two-photon reactions it is not so simple to quote event rates, since only a small fraction of the total cross section is seen in the detector. For a beam energy of 5 GeV and a two-photon invariant mass $W_{\gamma\gamma} > 0.5$ GeV the hadronic $\gamma\gamma$ reaction (74) contributes about 13 nb. The QED process (75) with the additional restriction $|\cos\theta^*| < 0.7$ (θ^* is the lepton angle in the $\gamma\gamma$ CM-system) adds roughly the same amount. These estimates depend critically on the kinematical restrictions, since the cross section increases very fast for smaller $W_{\gamma\gamma}$ or smaller θ^*. A trigger requiring at least two charged particles with $p_T > 150$ MeV/c will accept about 150 Hz from $\gamma\gamma$ events. A more stringent trigger requirement, in general, cuts also into τ events. If it is required that trigger tracks have to hit the scintillation counters, their transverse momentum p_T has to be larger than 200 MeV/c for a magnetic field of 1 Tesla.

Rates

The expected event rates are summarized in Table XIV. It follows that the total rate from physics events will be about 200 Hz ($L = 10^{34}\ cm^{-2}s^{-1}$) with the Bhabha rate already prescaled.

Conclusion

The full range of the physics program can be covered if one could afford a

Table XIV: Event rates for an assumed luminosity of 10^{34} cm^{-2}s^{-1} at the $\Upsilon(4S)$

Process		Rate [Hz]
$e^+e^- \rightarrow$	$b\bar{b}$	10
	$u\bar{u}$, $d\bar{d}$, $s\bar{s}$, $c\bar{c}$	35
	e^+e^- (prescaled)	10
	$\mu^+\mu^-$	10
	$\tau^+\tau^-$	10
	$\gamma\gamma$	10
Sum one-photon events		85
Two-photon events $n_{ch} \geq 2$, $p_T > 250$ MeV/c		85
Total sum		170

charged particle trigger with a low-p_T cut-off requiring at least 2 tracks or at least 1 track with an additional neutral energy cluster.

9.3 Background Sources and Rates

In the following we discuss the known background sources, their characteristics and the means to reduce their rates.

Beam-gas interactions

Electron scattering off the rest gas in the beam pipe creates mainly events with low-p_T tracks. This background can be reduced by improving the vacuum in the interaction region, by setting appropriate p_T cuts for the track triggers, and by restricting tracks to a limited volume around the interaction point (in particular along the beam axis to about ± 5 cm). As an example: with $5 \cdot 10^{-9}$ Torr and a beam current of 2 A, one expects a rate of 2 Hz per cm in z from events with at least one track with $p_T > 150$ MeV/c and 0.4 Hz/cm with at least two such tracks.

Off-momentum beam particles

This rate depends on machine conditions and the vacuum in the beam pipe. If beam lifetimes of the order of 5 hours are achieved, a beam current of 2 A yields a rate of lost particles of about 3 kHz/m (see II.5.3). Using scrapers at suitable positions in the machine, the loss rate near the detector can be reduced to obtain acceptable running conditions. At small angles off-momentum particles initiate showers in the IR which lead to both charged particles in the tracking chambers and large energy deposits in the detector parts closest to the beam pipe. With a p_T cut of 100 MeV/c, the rate of background tracks passing the CTC is at most 1 kHz. The trigger rates can be further reduced below 100 Hz

by requiring charged tracks to originate from the IR in r-z (e.g. $\Delta z = \pm 5$ cm) and r-ϕ (e.g. distance from origin $d_0 < 0.5$ cm).

Cosmic ray particles

The detector is continuously sensitive to cosmic rays since the bunch spacing of the machine is comparable to the time resolution of all detector components. However, requiring in the trigger charged tracks to originate from the IR in r-z and r-ϕ reduces the cosmic ray rate well below 1 Hz.

Synchrotron radiation

The synchrotron radiation from the beam optical elements near the IR is particularly dangerous. A major effort went into the design of the IR to minimize the radiation into the detector (see II.5.2). To avoid aging problems of the drift chamber not more than one photon per bunch crossing should be absorbed in the chamber (corresponding to a total drift chamber current of about 30 to 50 μA). For the trigger this will not cause any problems even if this number goes up by an order of magnitude.

Conclusion

In summary, the most effective background reduction is achieved by restricting on the trigger level charged tracks to come within some allowances from the IR. A low bias trigger, requiring at least 2 tracks with $p_T > 150$ MeV would then be acceptable, with a signal-to-background ratio around 1:1.

9.4 Trigger Types

Trigger types

The most important trigger types are:

- charged track trigger
- energy trigger
- muon chamber trigger

In addition calibration and monitor triggers have to be provided:

- luminosity monitor trigger from endcap crystals (prescaled)
- Bhabha trigger (prescaled)
- cosmic ray trigger
- random trigger
- electronic test triggers (pulsers etc.)

Flexibility of the trigger

The triggers derived from the different components are usually OR'ed together. Some low bias triggers may require a logical AND with other components. Redundancy in the trigger system is important for cross checks and trigger efficiency calculations. This also requires a complete recording of all fulfilled

trigger criteria. The flexibility to allow for adjustments to the background conditions is provided by variable thresholds for transverse momenta, energies and multiplicities. The goal is to work with low bias triggers, e.g. requiring two charged tracks with $p_T > 150$ MeV/c, or one charged track plus a neutral energy cluster. Turning thresholds up cuts into two-photon and certain τ events, but will not cause losses of multihadronic events, including $B\overline{B}$ events.

9.5 General Trigger Concept

Requirements

The main requirements on the trigger system are

- efficiency for good events
- effective rejection of background
- operation without or with little dead time (say $\leq 1\%$).

Deadtime

In the environment of the planned B-factory the largest challenge for the design of the trigger arises from the high bunch crossing frequency. To keep the deadtime reasonable the trigger decisions have to be made on several levels with stepwise decreasing rates. The input rates on each trigger level have to match the deadtime per event on this level such that the total deadtime stays below about 1%.

There are different ways how this matching can be done depending on the relation between the input rate ν_{in}^i and the decision time Δt^i at the level i:

(a) $\nu_{in}^i \Delta t^i \ll 1$: In this case one can stop the experiment and wait for a decision with a deadtime ratio $\nu_{in}^i \Delta t^i$.

(b) $\nu_{in}^i \Delta t^i \approx 1$: This case allows for most efficient running, provided the events are equally spaced in time (e.g. if ν_{in}^i is the bunch crossing rate). Otherwise one has to derandomize the events by buffering the events at the input. The buffer should have a depth of about 10 events [98].

(c) $\nu_{in}^i \Delta t^i \gg 1$: This case can only be handled if many decisions are made in parallel. There are three (or maybe more) ways to realize parallelism:

(i) multiplexing the events into n identical decision chains;

(ii) making the decision for an OR of n sequential "events" (e.g. bunch crossings) and deciding at a later stage which of the events actually fired;

(iii) pipelining the decision, i.e. dividing the decision in n time slices such that $\nu_{in}^i \Delta t^i / n \leq 1$ (= 1 applies for equally distributed input, random input may have to be derandomized, see above). At any given time

such a trigger pipeline works on n events at the same time, but each event is in another process stage.

Applying the methods (i) to (iii), n times higher input rates can be accepted than without them.

Necessity for a 1st level trigger pipeline

Most critical is the first trigger decision which has to cope with the bunch crossing rate. A trigger decision with a frequency of 80 or 160 MHz could, if at all, only be achieved with fast scintillation counters. In the simplest scheme such a "pre-trigger" would have to stop the experiment to give time for a more sophisticated decision. Assuming a decision can be made in about 3 μs, the pre-trigger rate has to be smaller than 3 kHz to keep the deadtime below 1%.

An extrapolation from the current situation at ARGUS shows that such a low pre-trigger rate cannot be achieved with scintillation counters alone. Scaling the ARGUS pre-trigger rate of about 200 Hz by the luminosity increase of 10^2 to 10^3 yields a rate of 20 to 200 kHz. Besides, at ARGUS the pre-trigger includes also information from shower counters (fast scintillators) which is, within a bunch crossing, not available from the CsI readout of the B-factory detector.

Thus the 1st level trigger needs already a lot of sophistication before one can afford a stop of the experiment for some microseconds. We encounter here the case where the product of the input rate times the decision time is much larger than 1. The appropriate solution, in particular since the input is equally spaced, is a pipeline scheme where the trigger logic is divided into many small steps as discussed above.

Cycle frequency

It is important to note that the cycle frequency of the trigger pipeline has not to be the same as the bunch-crossing frequency. The time interval for each trigger step can span over several bunch crossings (*i.e.* one can combine method (ii) and (iii) listed above). With today's technology we would feel comfortable with cycle frequencies of about 20 MHz which, taking the design values of the machine, corresponds to 4 bunch crossings within one cycle. Such a scheme allows for an arbitrary high bunch crossing frequency, including the d.c. case.

A complication arises from the fact that at some point one has to identify the bunch crossing in which the event occurred to provide the time reference t_0. An accurate timing is needed, *e.g.* for the drift time measurements and the integration of the CsI signals. We will discuss this below when we work out a realistic scheme for the first level trigger.

Data pipeline

While waiting for a trigger decision the relevant detector signals have to be delayed or stored. To keep the 1st level decision deadtime-free the fast signals of all detector components have to be stored in analogue or digital pipelines which are part of the front end electronics of each detector component. Examples for analogue storage devices are CCD's or Analogue Memory Units. Digital pipelines can be realized by shift registers and fast dual port memory,

an example being the buffer of a flash ADC. The delay or the depth of the pipeline is adjusted to the time required by the trigger.

In general, pipelining digital signals is in many respects more comfortable (no noise problems, no signal degradation with time etc.) [99]. However, fast digitization is only possible with a limited resolution, *e.g.* 100 MHz FADC accomplish today resolutions of up to 8 bit. Calorimeters require a dynamic range of 14 to 16 bit. At the moment this can only be reached with conversion times of the order of 1 μs.

The 1st level data pipeline has to run synchronously with the bunch crossing but will have, in general, a different time structure. The buffers for the following levels could run asynchronously, data driven, and are in general less deep.

9.6 The Multi-Level Trigger System

9.6.1 General Scheme

Three levels

A scheme for a three-level trigger system and the corresponding timing estimate is shown in Fig. 127. To be specific, examples for trigger rates and for the necessary time intervals at the different steps are given at the left and right side of the diagram, respectively. If after about 3 μs a 1st level trigger (FLT) is generated the pipeline is stopped. The data will be digitized if necessary and then be transferred to local, asynchronous buffers within less than 5 μs. These 2nd level (SL) buffers have a depth of about 10 events to derandomize the triggered events for the 2nd level trigger (SLT). When the transfer is completed the necessary resets are distributed and the FLT pipeline is started again.

The SLT marks the events which are to be further processed by the 3rd level trigger (TLT). In this step the data of all detector components have to be combined in one memory ('event builder'). We estimate that after data reduction by 'fast local processors' (zero suppression, peak finding, parametrization of FADC data, etc.) the transfer from the SL buffer into the memory will have to proceed with a bandwidth of 25 to 100 Mbyte/s. This appears today as the most critical requirement on the system since it cannot be achieved by conventional bus systems. However, novel techniques of accessing memory are being developed [97].

The TLT consists of a farm of microprocessors, each of which works on one event at a time. A manager processor organizes the distribution of the events which are stored in a random access memory. Suitable systems are meanwhile commercially available (see, *e.g.*, the new third level trigger of the CDF experiment [100]).

The events kept by the TLT will be recorded on a permanent storage device at a speed of up to 5 Mbyte/s. Recording with this speed should be available

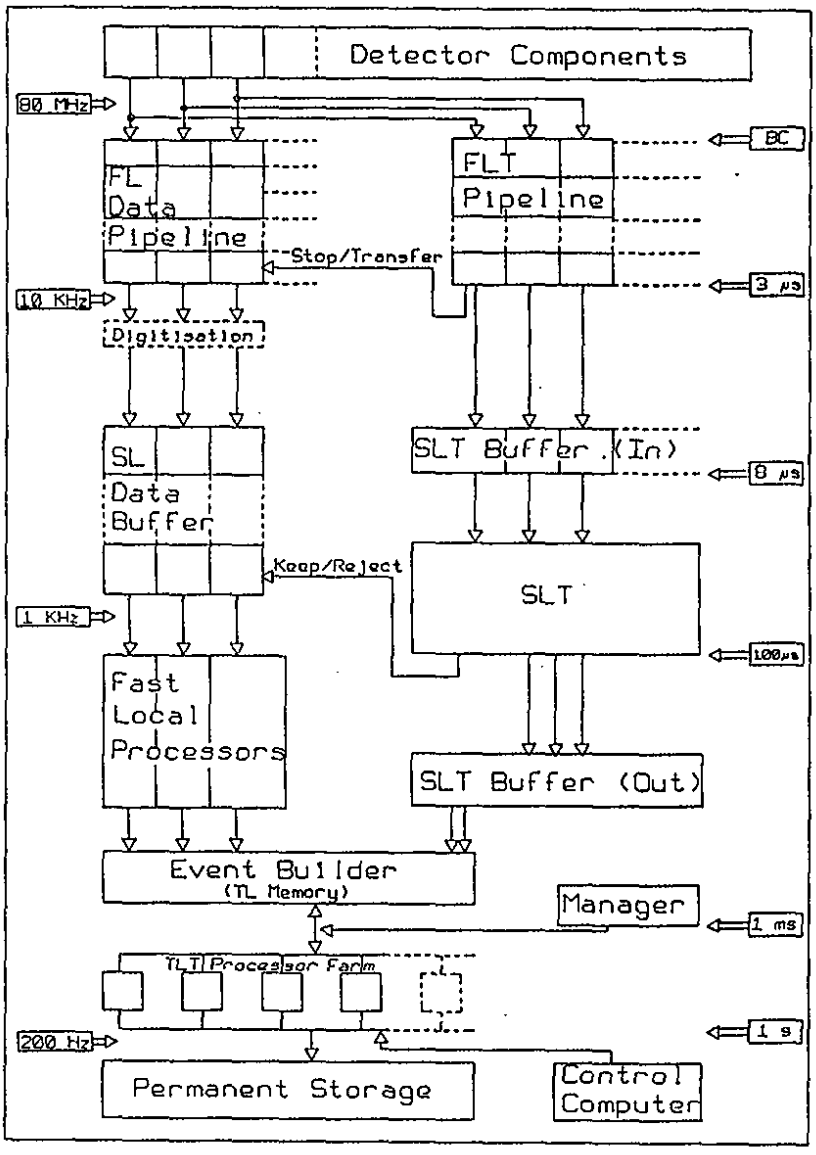

Figure 127: Diagram for the data flow (left) and the three-level trigger decisions (right). The rates and the timing are given as an example, the actual numbers will depend on the final design of the data acquisition system.

when the experiment starts, otherwise the speed can effectively be reached by routing the output to several devices installed in parallel.

9.6.2 Time Constraints on the Trigger System

CsI calorimeter

The CsI signals have to be integrated for about 2 to 4 μs. Since the integrated charge has to be measured with a resolution of about 14 to 16 bits it seems not to be possible to pipeline the signals in usual flash ADCs or fast analogue storage devices. We will therefore employ a scheme where the FLT generates a gate after about 2 to 4 μs to hold the integrated charges on precision capacitors. This fixes the time available for the FLT decision to 2 to 4 μs and thus the depth of the 1st level data pipeline. The digitization with the required resolution can be achieved within about 1 to 2 μs. In principle, this introduces the only unavoidable deadtime.

Need for a 2nd level buffer

We expect the FLT rate not to be much lower than about 10 kHz since the physics rate at this level (without Bhabha prescaling) is already above 1 kHz. A reduction by an order of magnitude by the SLT certainly requires a decision time of at least 10 μs, probably more something like 100 μs. Therefore the pipeline cannot be stopped during the time required by the SLT. Furthermore, since the product of the input rate times the decision time will be close to 1, a buffer for about 10 events is needed to decouple the SLT from the random occurrence of the FLTs (see sect. 9.5). The buffer runs asynchronously, driven by the FLT, and has to store the data in a sufficiently large time window around the FLT.

The first level pipeline has probably to be stopped during the data transfer into the 2nd level buffer. Creating deadtime, the transfer should therefore be as fast as possible, at least below 5 μs to comply with a 5 % deadtime limit. This can only be achieved if the transfer between pipeline and buffer, which should preferably be placed on the same electronics board, is mainly parallel.

A SLT causes the data to be transferred from the local 2nd level buffers to memory storage which can be accessed by microprocessors. Allowing 1 ms for accomplishing this transfer the SLT rate has to be smaller than about 1 kHz. On the other hand, it cannot be expected to be much smaller since the physics rates at this level are several 100 Hz (assuming the Bhabhas to be prescaled). Therefore a buffering of the 2nd level output before it can be transferred to the memories has to be provided. This buffering could be achieved by the same SL buffer described above.

9.7 The Three Trigger Levels

9.7.1 The First Level Trigger (FLT)

Prompt data which can be used for the FLT are available from the following subdetectors:

- drift chamber,
- scintillation counters,
- CsI calorimeter,
- possibly Si-microstrip detector.

From these subdetectors we can derive

- charged track triggers,
- neutral energy triggers (total energy and topology),
- combinations thereof.

The drift chamber signals are available after the maximal drift time of about 200 to 300 ns. We will probably restrict ourselves to the inner 30 layers with the small cells and correspondingly smaller maximal drift times. The CsI signals will be split into a pulse for the relatively slow precision charge measurement and a pulse going into a fast shaping circuit which provides within less than 500 ns energy information for trigger purposes (see sect. 7.4).

The scintillation counter signals (see chapt. 6) have a much better time resolution than the bunch crossing interval and serve the only purpose to provide a good timing information at an early stage. It is possible that a solution for the trigger which works also without scintillation counters can be found.

The silicon vertex detector (SVD) could provide for the FLT fast ORs of strips with a resolution of a few millimeters. These fast ORs have to be formed in the readout chips on the detector and have to be read out with the cycle frequency of the FLT.

The charged track trigger

The charged track trigger is formed by the hit patterns of the central drift chamber, the scintillation counters, and possibly the Si-microstrip detector. The basic principle is to compare the measured hit patterns with predefined masks. Desirable is a fully three-dimensional track recognition exploiting the stereo wire arrangement of the planned drift chamber. The masks would be defined for certain values of the variables: polar angle θ, azimuth angle ϕ, transverse momentum p_T and vertex coordinate z_V. This allows a restriction on p_T and on the vertex in r-z and r-ϕ. If the SVD could be included into the FLT the geometry alone would already lead to an effective restriction of track origins.

Trigger processor

A trigger processor could work as follows: Adjacent layers in the drift chamber are paired yielding 15 double layers in the inner small cell part. For all double layers all possible coincidences between wires are made, the total number of coincidences being about 30000. Each coincidence corresponds to a certain r-ϕ-z bin with a width of about 20 mm in r-ϕ and about 125 mm in z. The number of bins in each layer varies with the radius. Table XV gives the number of r-ϕ and z divisions together with the total number of coincidences for each double layer. Taking the coincidences of the outermost layer as reference points we

Table XV: Number of coincidences in the first 15 double layers of the CTC used for the definition of track masks in the FLT processor.

Double layer	r-ϕ bins	z bins	coincidences
1	52	7	364
2	60	8	480
3	68	10	680
4	76	11	836
5	84	12	1008
6	92	14	1288
7	100	15	1500
8	108	16	1728
9	116	18	2088
10	124	19	2356
11	132	20	2640
12	140	22	3080
13	148	23	3404
14	156	24	3744
15	164	26	4264
Sum	1620	245	29460

define 4264 masks for straight tracks. For each straight track we add another 30 masks for curved tracks (15 for each curvature sign) to cover a p_T range down to about 150 MeV. This yields a total of about 130000 masks. The steps in p_T are listed in Table XVI. The vertex resolution in the r-ϕ projection will be around 10 mm and in z about 100 mm.

Both resolutions can still be improved at the cost of multiplying the number of masks which may, however, be prohibitive for parallel processing. Therefore a fully three-dimensional track recognition with higher resolution, possibly using also the drift time information [101] should be left to the SLT where the time is long enough for serial decisions.

Timing considerations

Given an 83 MHz bunch crossing frequency the trigger pipeline cycle frequency could be around 20 MHz (at somewhat higher cost also 40 MHz) spanning over

Table XVI: Nominal p_T values of a set of masks of the CTC charged track trigger.

Mask	Track radius [mm]	p_T [GeV]
0	∞	∞
1	6876	2.06
2	3440	1.03
3	2296	0.69
4	1725	0.52
5	1383	0.42
6	1155	0.35
7	993	0.30
8	872	0.26
9	779	0.23
10	704	0.21
11	643	0.19
12	593	0.18
13	551	0.17
14	515	0.15
15	484	0.14

4 (2) bunch crossings (BC). If a track passes the chamber at a certain BC, each hit wire sets a logical 1 for a time interval which allows for a coincidence of all track hits after the maximal drift time plus an allowance for the 4 (2) BCs. That means that each hit has the chance to be registered in several adjacent pipeline cycles. The pipeline cycle is resolved in the mask processors where the properly delayed scintillation counter hits are included. The scintillation counter timing also defines the range in the data pipeline which has, after a FLT has fired, to be transferred to the 2nd level buffer (the case where only a neutral energy trigger fired is discussed below).

Example: ARGUS trigger processor

A trigger processor which has many of the required features for a FLT is currently being built for the ARGUS experiment [102]. It uses the information of the ARGUS μVDC whose most distinguished characteristics are $\pm 45°$ stereo layers (in addition to $0°$ layers) which are fully exploited for a three dimensional track recognition.

The processor compares hit patterns seen by the chamber with masks stored in random access memories. A decision is made in 20 steps, each step 50 ns long (the cycle time of the used RAMs is about 20 ns). The processor works out 512 masks in parallel but repeats the process 500 times for different chamber segments and vertex constraints. Since the system works in a pipeline mode

the trigger decision takes only 500 × 50 ns = 25 μs plus a constant time of 5 μs.

Some of the features of the ARGUS μVDC trigger can be directly applied for a charged track FLT, *e.g.* the pipeline with a cycle time of 50 ns (implying averaging over an acceptable number of bunch crossings). However, the 500 serial steps have to be made in parallel, which should be possible by employing VLSI techniques for the logical connections (probably custom made chips).

The neutral energy trigger

For the FLT the calorimeter provides fast signals with information on the energy flow. The signals of groups of crystals, defining a "trigger segment", are linearly summed and shaped with an integration time of less than 500 ns. From the pulse heights in the trigger segments one can form total or topological energy triggers. The trigger pipeline could be build from rather conventional electronics.

The neutral triggers can be combined with charged track triggers. In this case the timing can be obtained from the scintillation counters. For a stand-alone neutral trigger the timing resolution is about 50 ns which is sufficient to determine the range of data to be transferred to the 2nd level buffer.

9.7.2 The Second Level Trigger (SLT)

Filter refinement on 2nd level

The SLT has to achieve a rate reduction by about an order of magnitude. The available input will essentially be supplied by the same subdetectors as for the FLT (drift chamber, scintillation counters, calorimeter), but also by the Si-microstrip detector and the muon chambers. The necessary refinement will mainly come from serial processing. For the charged track trigger masks with higher resolution, in particular of the track vertex, can be defined.

Bhabha prescaling

An important task of the SLT processing is the clean recognition of Bhabha events by their back-to-back topology both for the charged tracks and the energy deposition. Prescaling of Bhabha events has probably to be done at this level.

The SLT marks the events which have to be transferred to the memory of the 3rd level processor farm.

9.7.3 The Third Level Trigger (TLT)

Full event reconstruction

At the third level the data will be buffered in random access memory. A manager processor distributes the events to a farm of microprocessors which have access to the memory. All microprocessors in parallel carry out a full event reconstruction and a 3rd level event selection, i.e. the TLT is actually a software trigger. The rate of events which pass the selection is close to the interesting physics rate (about 100 to 200 Hz). These events are dumped to a permanent storage device.

9.8 The Data Acquisition System

Data flow

The data flow in each detector component is shown in Table XVII. The large amount of data on the first and second level are moved locally and fully parallel in each component. At any given time the total of the data in the FL pipeline amounts to about 2.5 Gbit and in the SL buffer to about 10 Mbit. From the first to the second level data are reduced by rate reduction while before the transfer to the TL memory the amount of data per event is reduced by fast local processors.

The average event length will be about 10 kbyte with contributions from the different subdetectors as shown in Table XVII. At the ultimate luminosity of $L = 10^{34}$ cm^{-2}s^{-1} we may reach TLT rates of up to 200 Hz which means that the recording capacity has to be 2 Mbyte/s. Devices which are able to record at this speed are now becoming available [97].

Table XVII: Amount of data expected from each detector component.

Detector component	Number of channels	Bits per channel	Pipel. [MHz]	Channels fired	TL data [kbyte]	Perm.stored [kbyte]
SVD	89088	10	5	2000	4	2
CTC	5724	8	100	400	5	3
RICH	400000	8	83	400	4	1
TOF	2432	8	1000	200	1	0.5
ECAL	11000	analog	analog	250	2	2
MUCH	5000	8	no	100	0.8	0.2
Sum	527244			3270	16	9

10 Detector Cost Estimate

Table XVIII: Cost Estimate of the Asymmetric Detector

		Subtotal MDM	Total MDM
1. Silicon Vertex Counter			
Silicon counters		1.8	
Read out chips		0.8	
Read out electronics		0.8	
Mechanics and support		0.8	
Laboratory equipment		1.0	
Total		5.2	5.2
2. Central Track Chamber			
Gas volume	6.2 m^3		
Number of cathode wires	6.000		
Cost per electronic channel	400 DM		
Total electronics cost		2.4	
Chamber mechanics		1.0	
Gas system		0.3	
Total		3.7	3.7
3. Ring Image Čerenkov Counter			
Total area	33 m^2		
Area of quartz windows	60 m^2		
Quartz window cost per area	30.000 DM/m^2		
Quartz windows total		1.8	
Number of pads	646.122		
Cost per electronic channel	10 DM		
Electronics, total		6.5	
Chamber mechanics		3.2	
Gas system		0.3	
Liquid radiator system		0.5	
Total		12.3	12.3

Continuation Table XVIII

		Subtotal MDM	Total MDM
4. Time of Flight System			
Total area	32.4 m^2		
Scintillator cost per area	2.500 DM/m^2		
Scintillator, total		0.1	
Number of counters	195		
Number of channels	384		
Cost of one photomultiplier	1.500 DM		
Photomultipliers, total		0.6	
Cost per electronic channel	500 DM		
Electronics, total		0.2	
Total		0.9	0.9
5. Electromagnetic Calorimeter			
Total volume	13.0 m^3		
Total weight	59 t		
Crystal cost per volume	2.6 DM/cm^3		
Crystals, total		34	
Number of channels	11.000		
Cost per electronic channel	400 DM		
Electronics, total		4.4	
Support structure		1.5	
Weight of steel housing	43 t		
Cost of steel housing		0.4	
Total		40.3	40.3
6. Magnet			
Two superconducting coils		17.0	
Refrigerator		1.2	
Power supply		0.3	
Compensation coils		1.0	
Weight of magnet yoke	1043 t		
Magnet yoke cost per mass	4 DM/kg		
Magnet yoke, total		4.5	
Total		24.0	24.0

Continuation Table XVIII

		Subtotal MDM	Total MDM
7. Muon Chambers			
Area	534 m^2		
Cost per area of chambers	150 DM/m^2		
Total cost of chambers		0.1	
Number of electronic channels	1984		
Cost per channel	100 DM		
Electronics, total		0.2	
Gas system		0.3	
Total		0.6	0.6
8. Electronics Hut			
Area	300 m^2		
Cost per area	1.100 DM/m^2		
Total		0.4	0.4
9. Trigger Electronics (Estimated by considering the effort at other comparable detectors)			
Total		5.0	5.0
10. Data acquisition and Online computing			
Data acquisition system		0.7	
Computers		1.0	
Network		0.1	
Total		1.8	1.8
Grand Total			94.2
10 % contingency			9.4
Total cost of the HELENA detector		MioDM	103.6

Bibliography

[1] M.Caccia et.al., Nucl.Inst.Meth. A260 (1987) 124

[2] P.Jarron, ECFA Study Week on Instrumentation Technology for High-Luminosity Hadron Colliders, Barcelona, Spain, CERN 89-10, ECFA 89-124 (1989) 287 and 678

[3] T.Ohsugi et.al., Nucl.Inst.Meth. A265 (1988) 105

[4] L.Evensen, ECFA Study Week on Instrumentation Technology for High-Luminosity Hadron Colliders, Barcelona, Spain, CERN 89-10, ECFA 89-124 (1989) 351

[5] H.F.-W.Sadrozinski et.al., SCIPP 90/36 (1990)

[6] J.Kemmer, G.Lutz, Nucl.Inst.Meth. A253 (1987) 365

[7] R.Horisberger, Nucl.Inst.Meth. A288 (1990) 87

[8] J.Kemmer et.al., Nucl.Inst.Meth. A288 (1990) 92

[9] S.J.Watts, Nucl.Inst.Meth. A265 (1988) 99

[10] E.Michel et.al., Nucl.Inst.Meth. A283 (1989) 544

[11] Th.Browder, M.Witherell, CLNS 90-1019 (1990)

[12] F.Angelini et al., Nucl.Inst.and Meth.A283 (1989) 755

[13] F.Angelini et al., Nucl.Inst.and Meth.A292 (1990) 199

[14] "Detector for a B-Factory" M. Ogg *et al.*, CLNS 91-1047 (1991)

[15] H.Leutz, in Proceedings of the ECFA Study Week on Instrumentation for High-Luminosity Hadron Colliders, September 1989, Barcelona, Spain, CERN 89-10 (1989) (and related contributions)

[16] G.Wormser, in Proceedings of the Workshop on Physics and Detector Issues for a High-Luminosity Asymmetric B-Factory at SLAC, SLAC-373 (1991) 365

[17] V.Lüth, in Proceedings of the Workshop on Physics and Detector Issues for a High-Luminosity Asymmetric B-Factory at SLAC, SLAC-373 (1991) 337

[18] R.Turchetta, *Contribution* to the European B Factory meeting, Paris (December 1990)

[19] W.R.Nelson, H.Hirayama, D.W.O.Rogers, The EGS4 Code System, SLAC-Report 265 (1985)

[20] H.DeStaebler, SLAC-PUB-5299 (1990)

[21] R.Erbacher and W.Vernon, in Proceedings of the Workshop on Physics and Detector Issues for a High-Luminosity Asymmetric B-Factory at SLAC, SLAC-373 (1991) 373

[22] E.Belau et.al., Nucl.Inst.Meth. 214 (1983) 253

[23] P.Holl et.al., IEEE Trans.Nucl.Sc.36 No.1 (1988) 251

[24] B.S.Avset et.al., presented by P.Weilhammer at IEEE Nuclear Science Symposium (1989) and CERN EP/90-11

[25] R.Horisberger, priv.comm. (1991)

[26] P.Allport, P.Seller, M.Tyndel Nucl.Inst.Meth. A273 (1988) 630

[27] W.Buttler et.al. Nucl.Inst.Meth. A273 (1988) 778

[28] S.Kleinfelder et.al., IEEE Trans.Nucl.Sc.35 No.1 (1988) 171

[29] E.Beuville et.al., Nucl.Inst.Meth. A288 (1990) 157

[30] F.Anghinolfi et.al., CERN/EF 89-14 (1989)

[31] J.Möschen et.al., Nucl.Inst.Meth. A288 (1990) 180

[32] J.DeWitt, Nucl.Inst.Meth. A288 (1990) 209

[33] Proposal of an Electron Positron Collider for Heavy Flavour Particle Physics and Synchrotron Radiation, PR-88-09, PSI, Villigen, 1988.

[34] N.Bingefors, Contr. to Conference on Impact of Digital Microelectronics and Microprocessors on Particle Physics, Trieste, Italy (1988)

[35] H. Albrecht *et al.*, Nucl. Instr. Meth. **A275** (1989), 1.

[36] D. Reßing, Diploma thesis, Karlsruhe (1990).

[37] V. Cindro *et al.*, Nucl. Instr. Meth. **A309** (1991), 411.

[38] S.M. Playfer *et al.*, ETH-preprint ETHZ-IMP PR/91-3 (1991).

[39] H. Drumm *et al.*, Nucl. Instr. Meth. **176** (1980), 333.

[40] J. Bürger *et al.*, Nucl. Instr. Meth. **A279** (1989), 217.

[41] D.G. Cassel *et al.*, Nucl Instr. Meth. **A252** (1986), 325.

[42] G. Lynch, LBL–TPC–81.

[43] J. Va'vra *et al.*, *Nucl. Instr. and Meth* **203** (1982), 109.

[44] W. Alison and P. Wright, *Exp. Tech.*, in *High Energy Physics*, Addison–Wesley Publ., 1987.

[45] I. Lehraus, R. Matthewson, and W. Tejessy, *Phys. Scr.* **23** (1981), 727.

[46] R.L. Gluckstern, Nucl. Instr. Meth. **24** (1963), 381.

[47] R. Arnold *et al.*, Nucl. Instr. Meth. A270 (1988) 255.

[48] G. Lenzen, private communication.

[49] J. Seguinot *et al.*, Nucl. Inst. and Meth. A297(1990) 133.

[50] T. Ypsilantis, private communication.

[51] E. Chesi *et al.*, Nucl. Inst. and Meth. A283 (1989) 602.

[52] J. Seguinot *et al.*, in preparation.

[53] M. Starič, A. Stanovnik and P. Križan, Nucl. Inst. and Meth. A300 (1991) 213, and Nucl. Inst. and Meth. A307 (1991) 145.

[54] B. Lund-Jensen *et al.*, TSL-ISV 17, University, Uppsala, 1988.

[55] P. Križan, DESY 89-172, and Annals of the New York Academy of Sciences 619 (1991) 202.

[56] R. Goldstein *et al.*, J. Opt. Soc. Amer. 56 (1966) 256.

[57] J. Seguinot, CERN-EP/89-92, CERN, Geneva, 1989.

[58] P. Baillon, Nucl. Inst. and Meth. A238 (1985) 341.

[59] J. Biegansky, Diplomarbeit, MPI Heidelberg, 1990

[60] E. Križnič, Master Thesis, University of Ljubljana, Ljubljana, 1990.

[61] S. Mordhorst, Untersuchungen von Photomultipliern im Magnetfeld, Diplomarbeit, Hamburg 1989

[62] J. T. Walker et al., IEEE Trans. Nucl. Sci. **32** (1985) 616; D. F. Freytag and J. T. Walker, ibid., 622

[63] O. Sasaki, Tsukuba KEK Preprint 90-142, November 1990

[64] E. Michel, DESY, Private Communication

[65] H. Albrecht et al. (ARGUS collaboration), DESY 91-092, submitted to Z. Phys. C

[66] B. Gittelmann and S. Stone, Cornell preprint CLNS 87/81.

[67] M. Chen et al., CERN 89-10, Vol.2, ECFA Workshop Barcelona.

[68] A. Incicchitti et al., INFN/TC-89/09.

[69] G. Kessler, Desy Internal Report DESY Z-89-1 (1989).

[70] V.M. Aulchenko et al., Novosibirsk preprint IYF-89-124.

[71] J. Spengler, Workshop on Detectors for an Asymmetric B Factory, Heidelberg, MPI H-1990-V6.

[72] Expression of Interest by the L* Collaboration, SSC-EOI0010;
H.B. Newmann, CALT-69-1687 (1990).

[73] Schott GmbH, Mainz, FRG.

[74] U. Buchner et al., Nucl.Instr.Methods A272 (1988) 695.

[75] CLEO II Updated Proposal CLNS-85/634;
E. Blucher et al., Nucl.Instr.Methods A249 (1986) 201.

[76] Quartz et Silice, Nemours Cedex, France.

[77] Particle Data Group, Phys.Lett. B239 (1990) 1.

[78] Hamamatsu Photonics, Japan.

[79] B. Barish et al., Paper submitted to the Int. Conf. on High Energy Physics, Singapore (1990);
C. Bebek, Nucl.Instr.Methods A265, 258 (1988).

[80] M. Schneegans, Nucl.Instr.Methods A257 (1987) 528.

[81] E. Lorenz, European B Factory Meeting, Paris, 1990.

[82] U. Kilgus et al., Nucl.Instr.Methods A297 (1990) 425.

[83] W. Schott, Das CsI(Tl) Kalorimeter des Crystal Barrel Detektors, Karlsruhe preprint, IEKP-KA/89-7.

[84] P. Kreutz et al., Nucl.Instr.Methods A260 (1987) 120.

[85] I. Holl et al., IEEE Trans. Nucl. Sci. NS-35 (1988) 105.

[86] A. Drescher et al., Nucl.Instr.Methods A249 (1986) 277.

[87] M. Kobayashi et al., Nucl.Instr.Methods A254 (1987) 275;
S. Schloegl et al., Nucl.Instr.Methods A234 (1985) 435.

[88] D. Renker, Radiation damage of CsI(Tl) crystals, PSI, Villigen, 1990.

[89] W. Nelson et al., SLAC report 265 (1985).

[90] J. Birks, Theory and Practice of Scintillation Counting 1964.

[91] T. Altherr and J.C. Seixas, CERN preprint TH.5758/90.

[92] P. Nernst et al., Phys.Rev.Lett. 54 (1985) 2195.

[93] Particle Data Group, Phys.Lett. B 239, (1990).

[94] H. Albrecht et al. (ARGUS-Collab.) Phys.Lett. B 249 (1990) 359.

[95] V.V.Anashin et al., KEDR Collaboration, Status Report, (May 1990).

[96] S.F.Biagi et al., Nucl. Inst. and Meth. A 252 (1986) 586.

[97] see e.g.:
N.Ellis, S.Cittolin and L.Mapelli, Signal Processing, Triggering and Data Acquisition, Proceedings of the ECFA LHC Workshop in Aachen 1990, Vol.I, p.505
A.J. Lankford et al., Nucl.Instr.Methods A289 (1990) 597
R.K.Bock et al., Embedded Architectures for Second-Level Triggering in LHC Experiments, (EAST-Collab.), CERN/DRDC/90-56, 1990

[98] Ph. Gavillet, Nucl. Inst. Meth. A235 (1985) 363.

[99] J.Altaker et al., Pipeline Digital Signal Processors, CERN DRDC/90-62.

[100] U.Joshi et al., Nucl.Phys.B (Proc.Suppl.) 23A (1991) 365.

[101] R. Eichler et al., Technical Proposal for a Drift Chamber r-ϕ Trigger, H1 internal report H1-01/91-161.

[102] ARGUS Coll., ARGUS Plans for 1991-1993, paper submitted to the Physics Research Committee of DESY, PRC 91-03 (April 1991).

[103] H. Albrecht et al., The ARGUS Collaboration, Nucl. Instr. and Methods **A275** (1989) 1

SUMMARY

This study shows that an asymmetric B factory in the PETRA tunnel is feasible, and that it provides excellent scientific value.

Physics

Most important is the unique possibility to observe CP violation in B meson decays and thereby to measure one of the last yet unknown parameters of the Standard Model, the imaginary part of the CKM-matrix.

Furthermore an extremely rich range of fundamental experiments and measurements in many fields of elementary particle physics is offered. Thus a B factory is by far the most attractive project at the high luminosity frontier of particle physics. A luminosity of at least 10^{33} $cm^{-2}s^{-1}$ is required for a successful physics program, including the measurement of CP violation.

For the observation of CP violation it is essential that B mesons are produced by electrons and positrons colliding with asymmetric energies. Beam energies around 3 GeV on 9.3 GeV are found to provide optimal conditions.

Collider

We show that an electron positron storage ring, named HELENA, can be built in the PETRA tunnel, and which will reach a luminosity of 10^{33} $cm^{-2}s^{-1}$ and probably even $3 \cdot 10^{33}$ $cm^{-2}s^{-1}$. For some components of the collider major development work is still required, but this can be accomplished during the construction period of the machine.

It turns out that the circumference of PETRA is close to optimum for an asymmetric B factory. In addition to the existing PETRA, which serves as an injector, two new rings have to be built and accomodated in the PETRA tunnel. The cost of these new rings amounts to 175 Mio DM.

Detector

The design of an asymmetric detector is relatively straightforward, as demonstrated in this study. The cost of an adequate detector is around 100 Mio DM. A significant fraction of the cost arises from the crystals of the electromagnetic calorimeter.

Time schedule

The construction of both the collider and the detector can be completed four years after approval.

HELENA can be constructed while HERA is operating and while a future large project to succeed HERA is being prepared. Thus HELENA fits well into the research program of DESY. Due to the large number of fields of particle physics opened up, the project is ideal for the universities which use DESY for their research.

If approved, HELENA will be, at the time of its completion, a unique research facility with a new research potential for elementary particle physics in Germany and Europe.